# Late Pleistocene to Holocene changes in upper-ocean stratification and its impact on marine productivity, sea surface temperatures, and salinity in the subarctic northwest Pacific

## Dissertation

Zur Erlangung des Doktorgrades
der Mathematisch-Naturwissenschaftlichen Fakultät
der Christian-Albrechts-Universität zu Kiel

vorgelegt von
**Jan-Rainer Riethdorf**
Kiel, 2012

| | |
|---|---|
| **Referent:** | **Prof. Dr. Dirk Nürnberg** |
| **Koreferent:** | **Prof. Dr. Martin Frank** |
| **Tag der mündlichen Prüfung:** | **9. August 2012** |
| **Zum Druck genehmigt:** | **9. August 2012** |

**gez. Prof. Dr. Wolfgang J. Duschl, Dekan**

# Erklärung

Hiermit erkläre ich, dass ich diese Dissertation, abgesehen von der Beratung durch meine akademischen Betreuer, selbstständig und nur mit Hilfe der angegebenen Quellen und Hilfsmittel erstellt habe. Weiterhin versichere ich, dass der Inhalt dieses Dokumentes weder in dieser, noch in veränderter Form einer anderen Stelle im Rahmen eines Prüfungsverfahrens vorgelegen hat, veröffentlicht wurde oder zur Veröffentlichung eingereicht worden ist. Diese Arbeit ist unter Einhaltung der Regeln guter wissenschaftlicher Praxis der Deutschen Forschungsgemeinschaft entstanden.

Kiel, 30. Mai 2012 (Jan-Rainer Riethdorf)

"I don't know anything,
but I do know that *everything is interesting*
if you go into it deeply enough."

*Richard Phillips Feynman*

# Abstract

The modern subarctic North Pacific realm is characterized by a steep vertical gradient in salinity, the permanent halocline. The halocline not only hampers the exchange of gas and heat between the deep ocean and the atmosphere, it also restricts the supply of nutrients from the subsurface into the photic zone, thereby limiting marine productivity. However, for the subarctic North Pacific and its marginal seas it remains unclear whether low glacial productivity was controlled by upper-ocean stratification or by sea-ice dynamics. Recent proxy and modelling studies indicate that the halocline weakened during the last glacial termination.

This thesis is based on piston cores recovered from intermediate water levels in the hitherto only poorly studied western Bering Sea, the continental slope off eastern Kamchatka, and the southern Okhotsk Sea. Age models rely on a combination of benthic oxygen isotope stratigraphy, magnetostratigraphy, radiocarbon dating, and intercore correlations via high-resolution core logging data. Millennial-scale changes in marine productivity and terrigenous matter supply were reconstructed over the past 180 kyr applying a geochemical multi-proxy approach in combination with XRF logging data. Special emphasis is given to the last glacial termination, for which high-resolution sea surface temperature (SST), as well as subsurface temperature and salinity-approximating records were produced. These records stem from alkenone-thermometry, and from the combined measurement of stable oxygen isotope and Mg/Ca ratios of the planktonic foraminifera *Neogloboquadrina pachyderma* (sin.). Direct comparison between both temperature reconstructions allowed to infer oceanographic changes in the mixed layer. Deglacial changes in the ventilation of intermediate and deep waters are inferred from marine radiocarbon ages and stable carbon isotope records.

Results point towards low marine productivity but high terrigenous inputs during most of the last glacial-interglacial cycle and Marine Isotope Stage (MIS) 6. Increases in marine productivity occurred during warm stages of MIS5, interglacials, and the last glacial termination. These changes are supposedly controlled by insolation and sea-level changes, thereby influencing the strength of atmospheric pressure systems, seasonal contrasts, and sea-ice rafting. Sea-ice dynamics are thought to drive changes in surface productivity, terrigenous inputs, and upper-ocean stratification. Abrupt environmental changes recorded during the last 180 kyr apply to the deglacial situation and are potentially related to North Atlantic Dansgaard-Oeschger events.

During the last glacial termination SST records matched the variability in sea-ice extent, thereby resembling climate oscillations registered in Greenland ice cores. This variability is explained by perturbations of the Atlantic Meridional Overturning Circulation and suggests a quasi-synchronous atmospheric coupling between the North Pacific and the North Atlantic. Subsurface conditions differed on a regional scale, thereby reflecting different sea-ice influence. Deglacial thermocline changes are proposed with reduced thermal stratification of the upper water column during the Heinrich Stadial 1 (H1) and the Younger Dryas cold phases, but strengthened thermal stratification during

the Bølling-Allerød warm phase. Moreover, enhanced intermediate water formation in the Bering and Okhotsk seas and according shallow overturning in the subarctic northwest Pacific occurred during H1, supporting the notion of fast atmospheric interactions between the North Pacific and the North Atlantic which are held responsible for this situation. Results for the Holocene surface and subsurface development do not support the hypothesis of the Atlantic–Pacific Seesaw, but imply that modern upper-ocean conditions were established in the early Holocene.

# Zusammenfassung

Der heutige subarktische Nordpazifik ist durch eine permanente salzgehalts-gesteuerte Stratifizierung der oberen Wassersäule gekennzeichnet (Halokline). Die Halokline fungiert als eine Art Barriere für den Gas- und Wärmeaustausch zwischen dem tiefen Ozean und der Atmosphäre. Gleichzeitig beeinträchtigt sie die Zufuhr von Nährstoffen in die photische Zone und damit die Primärproduktivität. Dennoch ist unklar, ob die im subarktischen Nordpazifik und seiner Randmeere während vergangener Glaziale registrierte geringe Produktivität durch den Einfluss der Stratifizierung oder durch Meereisprozesse gesteuert wurde. Neueste paläozeanographische Daten und Modellierungsergebnisse legen nahe, dass die Halokline zumindest während der letzten Deglaziation Veränderungen unterworfen war.

Diese Arbeit basiert auf Sedimentkernen, die aus intermediären Wassertiefen der bisher kaum untersuchten westlichen Beringsee, des östlichen Kontinentalhanges von Kamchatka und dem südlichen Ochotskischen Meer geborgen wurden. Entsprechende Altersmodelle wurden durch die Anwendung von benthischer Sauerstoffisotopenstratigraphie, Magnetostratigraphie, Radiokohlenstoffdatierungen, sowie mittels hochauflösender Kern-zu-Kern-Korrelationen erstellt. Mit einer zeitlichen Auflösung von Jahrhunderten bis Jahrtausenden konnten Veränderungen in der Primärproduktion und im Terrigenfluss während der letzten 180.000 Jahre rekonstruiert werden. Dazu wurde ein geochemischer Multi-Proxy-Ansatz in Kombination mit XRF-basierten Loggingdaten angewandt. Der Schwerpunkt dieser Arbeit liegt auf der Rekonstruktion von Umweltveränderungen während der letzten Deglaziation, wofür Meerestemperaturen der Oberfläche (SST), sowie der Temperaturen und (indirekt) Salzgehaltsänderungen der darunter liegenden Wassersäule rekonstruiert wurden. Diese Rekonstruktionen basieren auf der Messung von Alkenonen, sowie auf der kombinierten Messung von stabilen Sauerstoffisotopen- und Mg/Ca-Verhältnissen an Schalen der planktischen Foraminiferenart *Neogloboquadrina pachyderma* (sin.). Der direkte Vergleich zwischen Alkenon- und Mg/Ca-Ansatz erlaubte den Rückschluss auf ozeanographische Veränderungen in der oberen, durchmischten Wassersäule. Weiterhin wurden deglaziale Veränderungen in der Bildung bzw. Durchlüftung intermediärer Wassermassen anhand der Bestimmung von marinen Radiokohlenstoffaltern und stabilen Kohlenstoffisotopenverhältnissen abgeleitet.

Die Ergebnisse zeigen, dass während des letzten Glazial-Interglazial Zyklus und während des Marinen Isotopen Stadiums (MIS) 6 in den untersuchten Gebieten eine stark verringerte Primärproduktivität, dafür aber erhöhter Terrigenfluss vorherrschte. Erhöhte Produktivität hat während warmer Stufen des MIS5, der Interglaziale, und im Zuge der letzten Deglaziation stattgefunden. Diese Veränderungen werden vermutlich hauptsächlich durch Insolationsänderungen und Meeresspiegelschwankungen verursacht, die wiederum die Stärke der vorherrschenden Luftdrucksysteme, der Saisonalität und der Meereisbildung beeinflussen. Die Dynamik von Meereisprozessen steuert seinerseits Veränderungen in der Primärproduktivität, des terrigenen Eintrags und der Statifizierung der oberen Wassersäule. Abrupte Umweltveränderungen, die während der let-

zten 180.000 Jahre aufgezeichnet worden sind, scheinen denen der Deglaziation ähnlich zu sein und stehen potentiell in Zusammenhang mit den Dansgaard-Oeschger Ereignissen im Nordatlantik.

Während der letzten Deglaziation stimmt die zeitliche Variabilität der Meeresoberflächentemperaturen mit jener der Meereisverbreitung überein, wobei sie gleichzeitig der Klimaentwicklung ähnelt, die in grönländischen Eiskernen registriert worden ist. Diese Variabilität wird durch Störungen in der Atlantischen Umwälzzirkulation erklärt und weist gleichzeitig auf eine quasi-synchrone, atmosphärische Klimakopplung zwischen dem Nordpazifik und dem Nordatlantik hin. Die ozeanographischen Bedingungen in der oberen Wassersäule unterscheiden sich in den jeweiligen Untersuchungsgebieten, was auf einen regional unterschiedlichen Meereiseinfluss zurückgeführt wird. Entsprechend werden Szenarien für Thermoklinenveränderungen während der Deglaziation vorgeschlagen. So war die thermische Stratifizierung der oberen Wassersäule während der Kaltzeiten des Heinrich Stadials 1 (H1) und der Jüngeren Dryas generell reduziert, aber verstärkt während der Warmzeit des Bølling-Allerød. Weiterhin finden sich Hinweise darauf, dass während H1 eine verstärkte Bildung von Zwischenwassermassen in der Beringsee und im Ochotskischen Meer stattgefunden hat. Dadurch erfolgte eine stärkere Umwälzung von intermediären Wassermassen im subarktischen Nordwest-Pazifik, was die Schlussfolgerung bekräftigt, dass relativ schnell ablaufende, atmosphärische Fernwirkungen zwischen dem Nordpazifik und dem Nordatlantik der kausale Ursprung dieser Beobachtungen sind. Die Rekonstruktion der ozeanographischen Entwicklung der oberen Wassersäule während des Holozäns zeigt keine Hinweise auf die Existenz der in der Literatur beschriebenen Atlantik–Pazifik Temperaturschaukel, aber die Ergebnisse lassen vermuten, dass sich die heutige ozeanographische Situation erst im frühen Holozän eingestellt hat.

# Acknowledgements

Ich möchte mich in erster Linie bei Prof. Dr. Dirk Nürnberg für die Vergabe dieser Arbeit, die intensive Betreuung und sämtliche Unterstützung während der letzten drei Jahre bedanken. Ferner danke ich neben Prof. Dr. Dirk Nürnberg auch Prof. Dr. Ralf Tiedemann als PI's von KALMAR-Teilprojekt 4 für die nützlichen Ratschläge und Diskussionen, sowie für die Möglichkeit eines Kamchatka-Aufenthaltes und der Mitfahrt auf Polarstern. Einen Dank auch an die Leiter des KALMAR-Projektes, Prof. Dr. W.-Chr. Dullo und Prof. Dr. B. Baranov. Kapitän Meyer und der Besatzung der Sonne gebührt meine Hochachtung für die harte und engagierte Arbeit während SO201-KALMAR Leg 2, die diese Arbeit erst ermöglicht haben, und ich danke allen KALMAR-Mitgliedern für die gute Zusammenarbeit.

Diese Arbeit wäre ebenfalls nicht möglich gewesen ohne die breite Unterstützung der MitarbeiterInnen des GEOMAR. Ich bedanke mich vor allem bei Nadine Gehre für die großartige Hilfe im Labor und bei der Probenaufbereitung, und bei Bettina Domeyer für einen enormen Probendurchsatz an der Kugelmühle und der Carlo Erba. Bei Lulzim Haxhiaj bedanke ich mich vielmals für die Hilfe im Isotopenlabor. Die Arbeit an der Opalanlage wäre unmöglich gewesen ohne Jutta Heinze. Dafür und für die XRD-Analysen vielen Dank. Ferner danke ich Dr. Peter Appel für die RFA-Analysen, Ute Schuldt und Sebastian Meier für die Betreuung am Rasterelektronenmikroskop, sowie Prof. Dr. Martin Frank und seiner gesamten Arbeitsgruppe, vor allem aber Dr. Cecile Blanchet, für die Unterstützung im Cleanlab (*feel the science!*). Allen HiWis, Praktikanten, Bachelorstudenten und Diplomanden sei an dieser Stelle gedankt für ihre Arbeit: David Poggemann, Kristin Doering, Lisa Griehm, Miriam Ibenthal, Eva Zimmer, Timo Hohmann, Yuki Weber, Martin Bartels, Katrin Schulz, Philipp Hildebrandt und Harald Meyer.

Lars Max danke ich dafür, dass wir uns gegenseitig immer wieder motivieren konnten und nun dieses Projekt erfolgreich abgeschlossen haben. Ohne unsere enge Zusammenarbeit während der letzten drei Jahre wäre dieses Ergebnis nicht denkbar. Ich danke Dir auch für schöne Tage in Bremen, Tokyo, San Francisco, Las Vegas und den *California road trip*!

Für alle Arten von Diskussionen und Ratschlägen bedanke ich mich sehr herzlich bei Lester Lembke-Jene und Dr. Nabil Khelifi. Besonderen Dank auch an die russischen Kollegen Dr. Sergey Gorbarenko, Dr. Mikhail Malakhov und Dr. Alexander Matul für die gute Kooperation. Ein großes Dankeschön auch an Dr. Christel van den Bogaard und Jutta Bothmann für die organisatorische Arbeit in KALMAR.

Dr. Jacek Raddatz, Hauke Vollstaedt und David Poggemann danke ich vor allem für ihre Freundschaft, die tolle Büroatmosphäre und die großartige Zeit im Wulfsbrook. Jacek, Dir vielen Dank für das eine oder andere Korrekturlesen! Eddie, Anne und Claudia, Euch ein liebes Dankeschön für die Motivation aus der Ferne.

Zuletzt danke ich meiner Familie und meinen Freunden. Vor allem Dir, Annika. Mein Herz, ich danke Dir für deine Motivation, deinen Beistand in schweren Zeiten, deine Hilfe und einfach alles! Letztendlich und im Besonderen danke ich meinen Eltern und meinen Großeltern für alle nur denkbare Unterstützung, und eine durch Euch begründete, ewige Begeisterung für das Meer. Danke für alles.

Euch allen *fair winds and following seas* und immer eine Handbreit Wasser unterm Kiel!

# Table of Contents

# 1. Introduction

## 1.1. Motivation and major objectives of this thesis

Earth's climate evolution during the Quaternary is characterized by the quasi-regular occurrence of glacial-interglacial cycles, i.e. the alternating pattern of ice ages and intercalated warm intervals. At least since the last 800,000 years changes in global climate and atmospheric $CO_2$ concentrations are correlated, as recorded in ice cores from Antarctica (e.g. Jouzel et al., 2007; Sigman et al., 2010;). The modern subarctic North Pacific (N Pacific) and its marginal seas are marked by high biological productivity and salinity-driven upper-ocean stratification (permanent halocline). Since the halocline directly influences the extent of marine productivity and atmospheric-oceanic gas exchange, the subarctic N Pacific may hold an important key for the understanding of the observed variations. Accordingly, it was speculated that the halocline weakened during the last deglaciation (e.g. Okazaki et al., 2010; Menviel et al., 2012), thereby contributing to the deglacial rise in atmospheric $CO_2$. However, paleoceanographic records allowing for decadal to millennial-scale reconstructions in the subarctic N Pacific are rare. Especially for the last glacial-interglacial cycle and deglaciation, when the North Atlantic (N Atlantic) was subject to strong oceanographic changes, according highly resolved reconstructions are missing.

Paleoceanographic studies in the subarctic N Pacific allowing for glacial-interglacial climate reconstructions rely on marine sediment cores. Only few high-quality records exist from the open N Pacific (e.g. Sarnthein et al., 2004; Jaccard et al., 2005; Gebhardt et al., 2008), the Okhotsk Sea (e.g. Nürnberg and Tiedemann, 2004), and the northern (e.g. Kim et al., 2011) and southern Bering Sea (e.g. Brunelle et al., 2007). In summer and fall 2009, three marine expeditions set sail to decipher the paleoceanography of the subarctic N Pacific and its marginal seas on different timescales: The Integrated Ocean Drilling Program (IODP) Expedition 323 performed deep drilling in the southern and eastern parts of the Bering Sea, while SO202-INOPEX also focused on these areas and the adjacent N Pacific.

This thesis was generated within the framework of the joint German-Russian research project "KALMAR–Kurile-Kamchatka and Aleutean Marginal Sea-Island Arc Systems: Geodynamic and Climate Interaction in Space and Time", and is based on sample material recovered during R/V Sonne expedition SO201-KALMAR Leg 2 (Dullo et al., 2009). In contrast to the beforementioned expeditions, the paleoceanographic goal of SO201-2 was to discover and retrieve high-resolution sediment cores from the continental slope off eastern Kamchatka (NW Pacific), and from the hitherto only poorly studied western Bering Sea. These cores provide unique climate archives to study the dynamics of the subarctic N Pacific climate system in response to external forcing mechanisms (insolation, sea-level changes), as well as its interacting components (sea-ice, upper-ocean stratification) on centennial to orbital timescales during the last ∼180,000 years.

The major objectives of this thesis are:

- to establish high-resolution core stratigraphies for cores recovered during SO201-2 for the last glacial-interglacial cycle and Marine Isotope Stage (MIS) 6,
- to reconstruct the processes that control ocean-atmosphere interactions and feedbacks (sea-ice, upper-ocean stratification), ocean circulation, and marine productivity (nutrient cycles) in the subarctic NW Pacific and its marginal seas during the late Pleistocene to Holocene in centennial to millennial-scale time-resolution, and
- to find out whether upper-ocean stratification persisted or changed during the last glacial termination, since a stratified upper water column might significantly influence marine productivity and the oceanic release of $CO_2$ to the atmosphere.

## 1.2. Strategy and structure of this thesis

### 1.2.1. Structure of this thesis

This thesis is divided into seven chapters. **Chapter 1** provides the introduction to the thesis with the underlying motivation and major objectives, as well as background information on the hydrographic situation, and an overview on previous paleoceanographic studies conducted in the study area. Detailed additional information on the applied methodologies, as well as the setup of the age models for the last 180 kyr is given in **chapter 2**.

**Chapters 3** to **6** are in the form of manuscripts which are either submitted to or are in preparation for submission to internationally peer-reviewed journals. Since a consistent stratigraphic framework is essential for paleoceanographic studies to compare different proxy records from different sites, **chapters 3** and **4** focus on the establishment of age models for the studied sediment records. The age models were generated by applying a combination of oxygen isotope stratigraphy, magnetostratigraphy, and radiocarbon ($^{14}C$) dating. Respective proxy records were compared with globally valid reference stacks, tested by spectral analysis, and age model consistency was ensured by intercore correlations.

**Chapters 3** and **5** represent the manuscripts that the author of this thesis prepared for submission as a first author. Focus of **chapter 3** is the variability of marine productivity and terrigenous matter supply during the last glacial-interglacial cycle. Therefore, a suite of different geochemical proxies was applied and results were compared with high-resolution core logging data to assess millennial-scale changes. In **chapter 4** sea surface temperatures and past changes in the sea-ice distribution are reconstructed for the last glacial termination based on alkenone paleothermometry and the sea-ice related occurrence of specific diatoms and the $IP_{25}$ biomarker. **Chapter 5** deals with the reconstruction of changes in subsurface temperature and salinity during the last glacial termination, which was achieved by performing combined measurements of Mg/Ca and stable oxygen isotope ratios ($\delta^{18}O$) on tests of planktonic foraminifera. Deglacial changes in the thermal structure of the upper water column were assessed by comparing these records with the alkenone-based sea surface temperature estimates presented in **chapter 4**. Whether the formation of intermediate and deep water masses

in the subarctic N Pacific during the last glacial termination occurred in the Bering and Okhotsk seas is assessed in **chapter 6** via marine radiocarbon ages and stable isotope ventilation records.

Finally, **chapter 7** gives a summary of the main conclusions of this thesis, and suggests perspectives for future work. Additional information on the studied sediment records as well as on the contents of **chapters 4** and **6** is presented in the Ph.D thesis of Lars Max (2012).

## 1.2.2. Site selection

Four sediment cores recovered during SO201-2 (SO201-2-12KL, -77KL, 85KL, -101KL) and one additional sediment core retrieved during cruise LV29-KOMEX Leg 2 with RV Akademik Lavrentyev in summer 2002 (LV29-114-3) were chosen for this thesis (Fig. 1.1). Detailled information about coring procedures is given in the respective cruise reports of SO201-2 (Dullo et al., 2009) and LV29-2 (Biebow et al., 2003). SO201-2 cores 77KL, 85KL, and 101KL were recovered from Shirshov Ridge in the western Bering Sea and lie on a north-south transect covering shallow to deep intermediate water levels (630–2135 m). Site 12KL (2145 m w.d.) is located on the continental slope off eastern Kamchatka (NW Pacific), and core LV29-114-3 (1765 m w.d.) was retrieved from the Kurile Basin in the southern Okhotsk Sea.

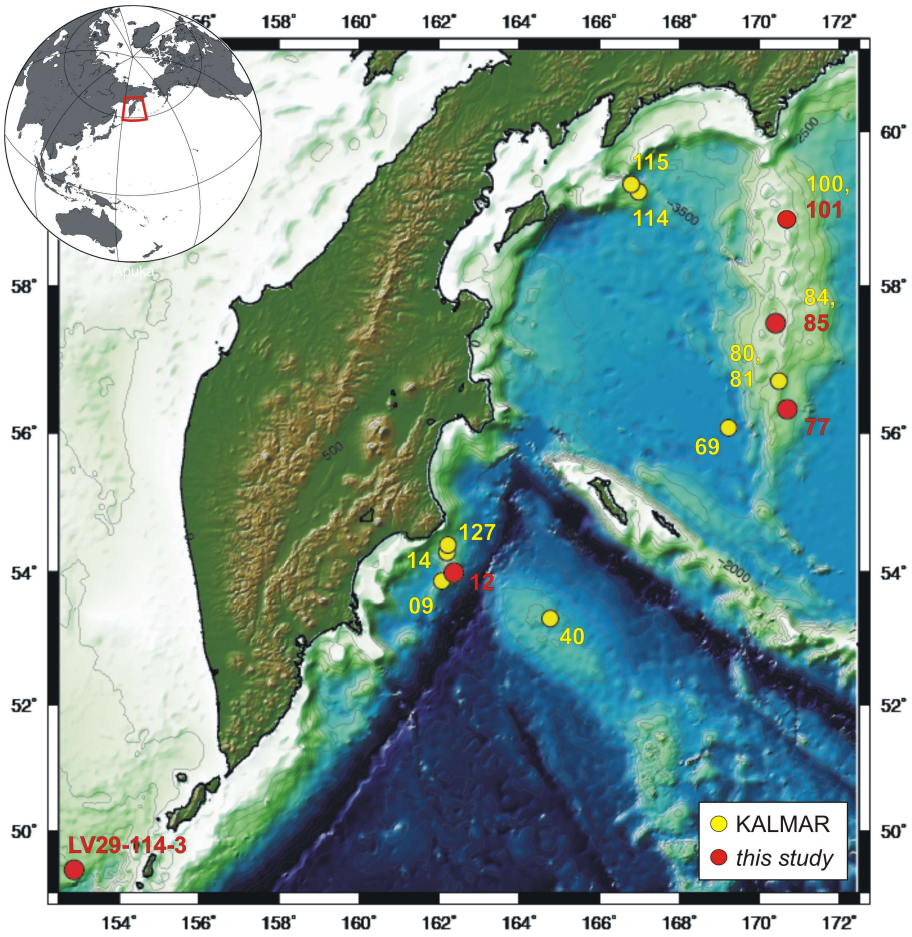


**Figure 1.1.:** Position of sediment cores recovered during SO201-KALMAR Leg 2 in the subarctic NW Pacific. Site locations chosen for this thesis are indicated by red dots.

## 1.3. Modern hydrographic situation

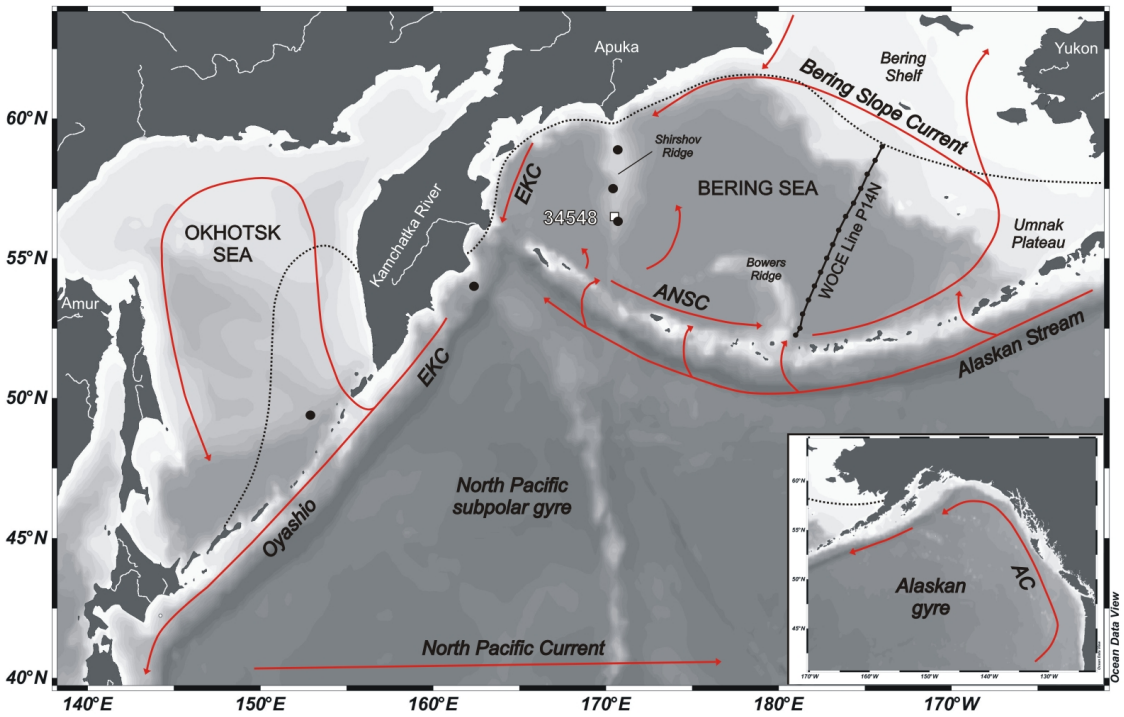


**Figure 1.2.:** Regional setting of the subarctic NW Pacific, the Okhotsk and Bering seas, and the NE Pacific (inlet). The surface circulation pattern (after Tomczak and Godfrey, 1994, Stabeno et al., 1999) is indicated by red arrows showing the major currents. The dotted black line represents the mean winter sea-ice extent (after Niebauer et al., 1999). Black dots mark sites related to this thesis. The white square represents World Ocean Atlas (WOA) station 34548 (Locarnini et al., 2010), and the position of World Ocean Circulation Experiment (WOCE) Line P14N (stations 1-15) is shown as well. AC = Alaskan Current, ANSC = Aleutian North Slope Current, EKC = East Kamchatka Current.

Fig. 1.2 shows the surface circulation pattern in the subarctic N Pacific, the Okhotsk Sea and the Bering Sea, which is characterized by a large-scale cyclonic (counterclockwise) pattern. Major currents fostering this pattern are the North Pacific Current (the Kuroshio Extension), the Alaskan Current, the Alaskan Stream, the East Kamchatka Current (EKC) and the Oyashio. While the North Pacific Current transports relatively warm and saline waters into the Alaskan gyre (NE Pacific), the westward flowing Alaskan Stream receives fresher waters from the Alaskan Current, which is fed by discharge from North America (Kowalik et al., 1994; Weingartner et al., 2005). Several passes in the Aleutian Island Arc allow waters from the Alaskan Stream to enter the Bering Sea, where the general surface circulation is also cyclonic. Here, the Bering Slope Current (BSC) and the EKC act as boundary currents. Outflow of Bering Sea waters mainly occurs through the shallow (∼50 m) Bering Strait into the Arctic Ocean, and through Kamchatka Strait into the NW Pacific. The EKC subsequently flows along eastern Kamchatka, transporting the cold and nutrient-rich waters to the south. South of the Kamchatkan peninsula, the EKC enters the Okhotsk Sea, while the Oyashio flows southwards along the Kurile Islands (for more detailed information see Tomczak and Godfrey, 1994, and Stabeno et al., 1999).

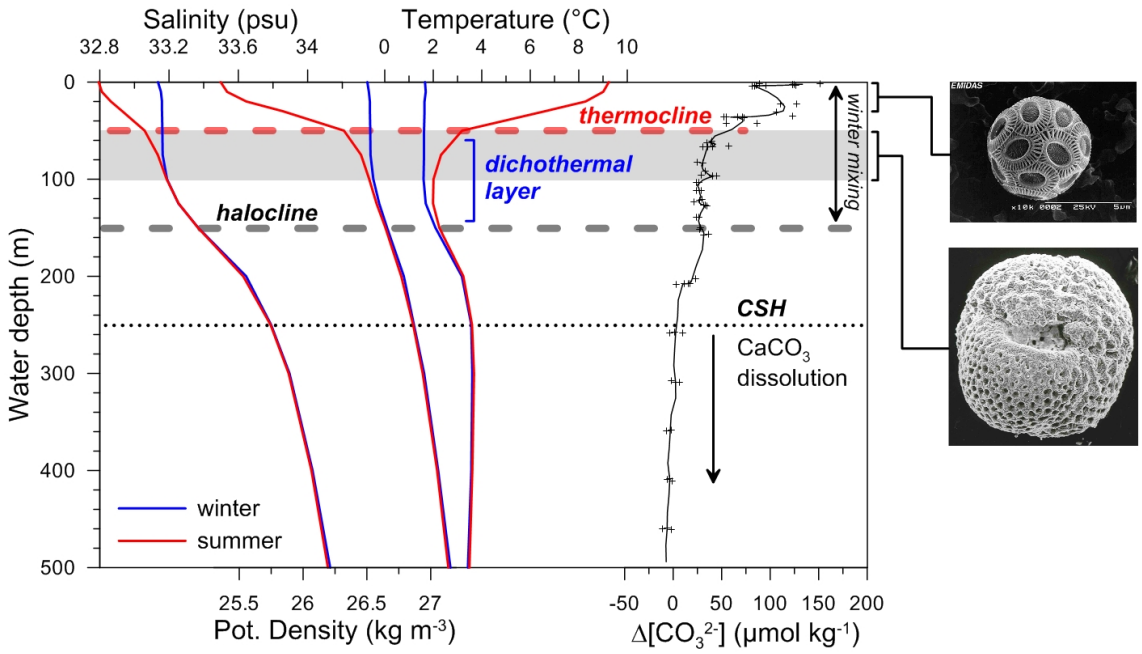


**Figure 1.3.:** Seasonal profiles of salinity, potential density, and temperature for WOA station 34548 (Locarnini et al., 2010), and the seawater calcite saturation state ($\Delta[CO_3^{2-}]$) along WOCE Line P14N (stations 1-15, available at http://cchdo.ucsd.edu/; see also Fig. 1.2). The summer (July–September, red lines) and winter situations (January–March, blue lines) reflect a strong seasonality of upper-ocean properties, leading to the formation of a summer thermo- and pycnocline (dashed red line), as well as the dichothermal layer. Winter mixing affects water depths down to ∼150 m, where a permanent halocline characterizes the whole subarctic N Pacific realm (dashed grey line). The halocline hampers atmospheric-oceanic gas exchange, which results in corrosive bottom waters and a shallow-lying calcite saturation horizon (CSH; dotted black line), below which the ocean is undersaturated with respect to calcite. Plankton organisms like coccolithophores occupy the surface layer (SEM-imagery of a coccosphere of *Emiliania huxleyi*, available at the Electronic Microfossil Image DAtabase System, http://www.emidas.org/), while planktonic foraminifer species *Neogloboquadrina pachyderma* (sin.) in this thesis is assumed to live at 50-100 m water depth (grey horizontal bar).

The modern subarctic NW Pacific realm is subject to a strong seasonality of sea surface temperature (SST) and salinity, resulting from the interplay of the atmospheric pressure cells of the Siberian High and the Aleutian Low. In consequence, intense winter mixing and sea-ice formation occur during winter (e.g. Niebauer et al., 1999), while during summer the stratification of the upper water column is the result of increased insolation and subsequent sea-ice melting. At the study sites of this thesis, the summer thermo- and pycnoclines lie within 30–70 m of the water column (Fig. 1.3). A steep vertical gradient in salinity between ∼100–200 m represents the permanent halocline (e.g. Haug et al., 1999) (Fig. 1.3), which is not affected by vertical mixing and consequently hampers atmospheric-oceanic gas exchange as well as the supply of nutrients from the subsurface. Nutrients, however, are resupplied to the surface layer by winter mixing and then used by phytoplankton during the following sea-ice-free seasons. Today, siliceous plankton organisms (diatoms) blooming during spring dominate marine productivity, but a second productivity maximum with enhanced $CaCO_3$ fluxes (coccolithophores and planktonic foraminifera) occurs during late summer/early fall (e.g. Takahashi et al., 2002a). The modern subarctic N Pacific shows a very high carbon export efficiency (Honda et al., 2002), and in the Bering Sea very high annual

production rates are associated with the eastern Bering Sea shelf areas (e.g. Arzhanova et al., 1995; Springer et al., 1996; Stabeno et al., 1999). Winter mixing also leads to the formation of the dichothermal layer, a temperature minimum layer at ∼100 m water depth that persists during summer (Ohtani et al., 1972; Miura et al., 2002) (Fig. 1.3).

Sea-ice formation during winter results from the advection of cold Arctic air masses and mainly northerly wind directions due to a strong Siberian High (Stabeno et al., 1999). In the Bering Sea, sea-ice formation starts in the northern shelf areas during October/November and sea-ice reaches its maximum distribution in March/April (e.g. Niebauer et al., 1999). In the Okhotsk Sea, sea-ice formation leads to the production of Okhotsk Sea Intermediate Water (e.g. Yasuda, 1997), a major component of North Pacific Intermediate Water (NPIW), due to brine rejection. Accordingly, sea-ice formation is influencing water mass ventilation in the subarctic N Pacific (e.g. Niebauer et al., 1999; Stabeno et al., 1999).

Carbonate preservation in the subarctic N Pacific realm is limited due to the shallow lysocline, thereby restricting most carbonate-bearing records to shallow shelf areas and morphological highs. Calculations based on data obtained from the World Ocean Circulation Experiment (WOCE) (see **chapter 5**) reveals that at the study sites of this thesis the calcite saturation horizon (CSH, i.e. the approximate top of the lysocline) already lies between 150-300 m w.d. (Fig. 1.3). Calcite dissolution starting below the CSH affects the preservation of calcitic foraminiferal tests, thereby limiting the use of carbonate-based paleoceanographic proxies.

## 1.4. Background information

### 1.4.1. Polar stratification and low glacial marine productivity

Since about 2.7 million years, the subarctic Pacific is characterized by salinity-driven stratification (e.g. Haug et al., 1999), which today is maintained by several processes including the restriction of meridional water mass exchange and atmospheric moisture fluxes (Warren, 1983; Emile-Geay et al., 2003; Kiefer, 2010). In contrast, the modern Southern Ocean is a source of atmospheric $CO_2$, which is stored in deep waters. This observation led to the hypothesis that polar stratification drives glacial-interglacial changes in atmospheric $CO_2$ concentrations (Haug et al., 1999; Sigman and Boyle, 2000; Sigman et al., 2004; Jaccard et al., 2005; Sigman et al., 2010). Haug et al. (1999) from concurrent changes in magnetic susceptibility, biogenic opal, and nitrogen isotope ratios ($\delta^{15}N$) at Ocean Drilling Program (ODP) Site 882 speculated about different stratification states during preglacial (i.e. before 2.7 Ma), interglacial, and glacial periods (Fig. 1.4). They suggested that enhanced polar stratification during glacial periods kept $CO_2$ in the ocean interior, and that it was subsequently released to the atmosphere during interglacials when stratification weakened.

Marine productivity in the subarctic N Pacific was low during glacial times, but it remains unclear whether this was the result of increased polar stratification or enhanced sea-ice cover, since both processes can influence the efficiency of the "biological pump" (e.g. Narita et al., 2002; Kienast et al., 2004; Jaccard et al., 2005; Brunelle et al., 2010). For ODP Site 882, Jaccard et al. (2005) ruled out sea-ice influence and related

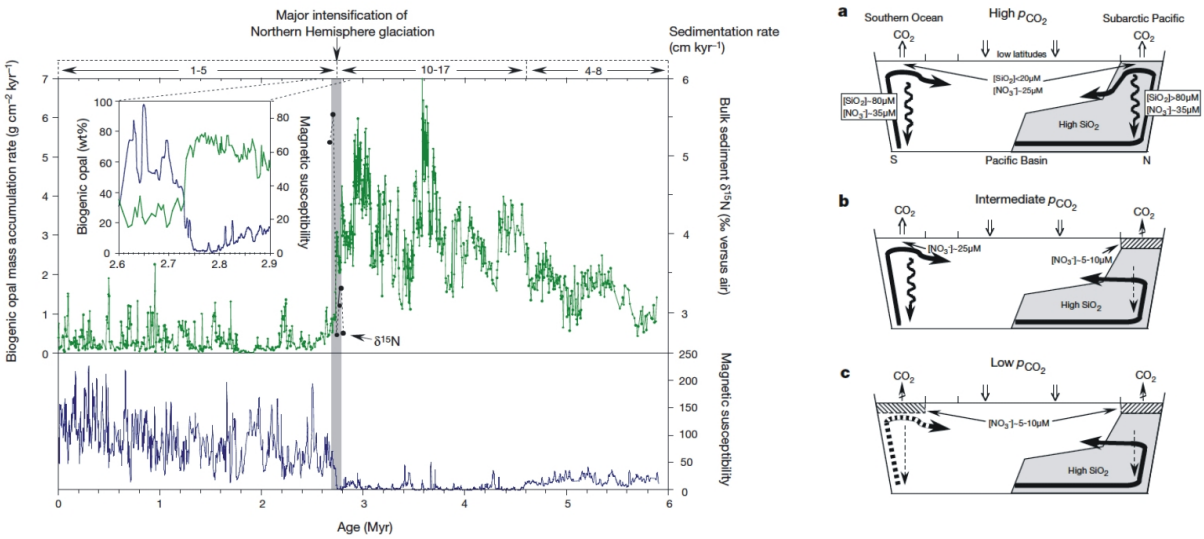


**Figure 1.4.:** Left hand: Records of magnetic susceptibility, biogenic opal, and nitrogen isotopes ($\delta^{15}$N) for ODP Site 882 covering the last 6 Ma (from Haug et al., 1999). Right hand: Paleoceanographic models, reflecting the influence of changes in deep water exposure and nutrient utilization on atmospheric concentrations of $CO_2$ along a section through the Pacific Ocean during preglacial (a), interglacial (b), and glacial (c) periods (from Haug et al., 1999).

interglacial maxima in export productivity to reduced stratification. This mechanism must not necessarily apply to the Bering Sea, which today is characterized by high marine productivity, or to other sea-ice influenced regions. Previous studies conducted in the Bering Sea confirmed low glacial and high interglacial productivity with strong changes occurring during the last glacial termination (Cook et al., 2005; Gorbarenko et al., 2005; Okazaki et al., 2005a; Brunelle et al., 2007; Kim et al., 2011). They were attributed to the interplay of changes in insolation, sea-ice dynamics, oceanography, and stratification (e.g. Katsuki and Takahashi, 2005). These studies, however, at most cover the last ∼120 kyr and/or provide insufficient temporal resolution for centennial to millennial-scale reconstructions.

Only recently, evidence for abrupt climate changes during the last glaciation was found in sediments from the Bering Sea (Cook et al., 2005; Gorbarenko et al., 2005; Okazaki et al., 2005a; Brunelle et al., 2010; Gorbarenko et al., 2010; Khim et al., 2010; Kim et al., 2011). Although being restricted to the last 70 kyr, these studies not only indicate pronounced millennial-scale climate variability during the last glaciation, but also conditions similar to those recorded during the last glacial termination. Moreover, and along with results from the NE Pacific (e.g. Hendy and Kennett, 2000) this could imply a connection to interstadials registered in ice cores from Greenland. However, a direct comparison between marine sediment and ice core records covering the full last glacial-interglacial cycle is needed to test this hypothesis, which, if correct, would argue for fast-acting teleconnections between the climates of the N Pacific and the N Atlantic.

### 1.4.2. Sea-ice and its impact on intermediate water formation

The reconstruction of sea-ice dynamics is necessary to understand changes in upper-ocean stratification and intermediate water mass formation in the subarctic NW Pacific and its marginal seas. Sea-ice rafting acts as an important transport agent for the supply of terrigenous matter to the sea-floor, as deduced from studies conducted in the Okhotsk Sea (Nürnberg and Tiedemann, 2004; Nürnberg et al., 2011), which might also be valid for the Bering Sea. Most studies focusing on sea-ice dynamics in the Bering Sea reconstructed past sea-ice extent and variability by means of diatom and radiolarian assemblages (e.g. Cook et al., 2005; Katsuki and Takahashi, 2005; Tanaka and Takahashi, 2005). The existing studies from the adjacent Okhotsk Sea indicate strong relationships to changes in marine productivity. However, only few provenance studies are available for the Bering Sea (Gardner et al., 1980; Lisitzin, 2002), and investigations assessing past changes in terrigenous matter composition and supply are clearly missing. Hence, it remains unknown how sources and transport mechanisms of terrigenous matter in the Bering Sea compare to those suggested for the Okhtosk Sea and to what extent terrigenous matter supply varied during the last glacial-interglacial cycle.

Another important aspect regarding sea-ice processes involves the formation of North Pacific Intermediate Water (NPIW). Today, important components of NPIW are formed in the Okhtosk Sea due to sea-ice formation (e.g. Yasuda, 1997). Since the modern Bering Sea is also characterized by seasonal sea-ice formation, speculation on better ventilated intermediate waters during glacials arose (e.g. Gorbarenko, 1996; Keigwin, 1998), leading to the assumption that their source region shifted to the Okhotsk Sea only since the Last Glacial Maximum (LGM) (Ohkushi et al., 2003; Tanaka and Takahashi, 2005). Recent studies support the view that at least during the last glacial termination strong oceanographic changes occurred in the subarctic N Pacific eventually leading to the formation of deep water and to a weakening of the halocline (Okazaki et al., 2010; Chikamoto et al., 2012; Menviel et al., 2012).

### 1.4.3. Deglacial climate variability and the re-opening of the Bering Strait

Reconstructions of SST, subsurface temperatures, and salinity are indicative of strong oceanographic changes in the subarctic N Pacific during the last glacial termination and the early Holocene (e.g. Sarnthein et al., 2004; Seki et al., 2004a; Sarnthein et al., 2006; Sagawa and Ikehara, 2008; Caissie et al., 2010). SST records show a temporal evolution resembling that recorded in Greenland ice with four distinct phases: the Heinrich Stadial 1 (H1) and Younger Dryas (YD) cold phases, which are intercalated and followed, respectively, by the Bølling-Allerød (B/A) and Preboreal (PB) warm phases. However, modeling studies controversially argue either for an atmosphere-controlled in-phase relationship (Mikolajewicz et al., 1997; Krebs and Timmermann, 2007; Okumura et al., 2009) or for an ocean-controlled anti-phase relationship (Schmittner et al., 2003; Saenko et al., 2004; Schmittner et al., 2007) between the N Pacific and the N Atlantic climates.

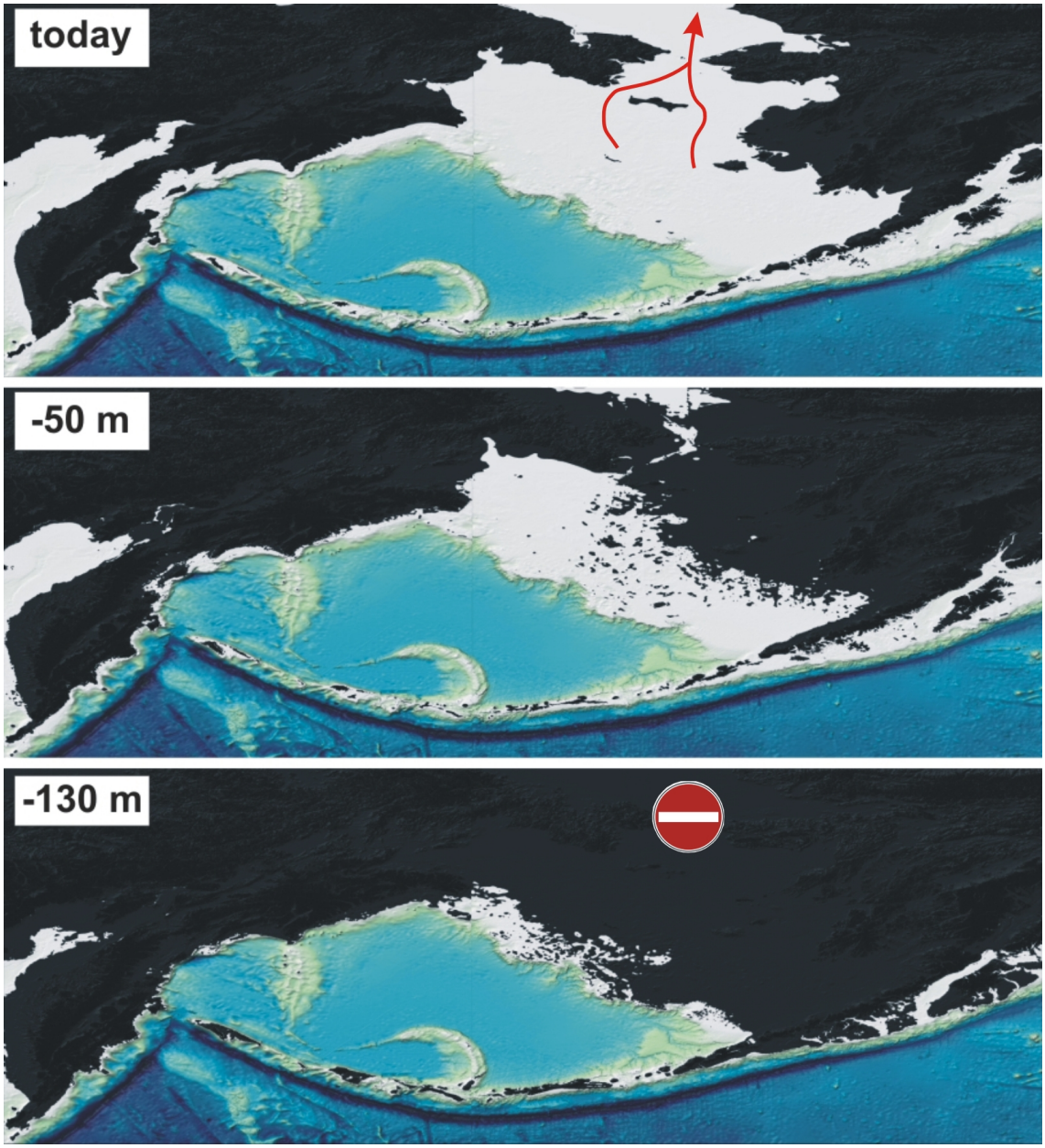


**Figure 1.5.:** Bathymetric map of the Bering Sea showing the influence of sea-level changes on the drowning/exposure of shallow shelf areas, as well as on the opening/closure of the Bering Strait. Today, most of the Bering Shelf lies below sea-level and the open Bering Strait allows net outflow of relatively fresh surface waters into the Arctic Ocean. The opening of the Bering Strait, which has an approximate sill depth of ∼50 m, is assumed to have (last) occurred between 12–11 ka BP (Keigwin et al., 2006). During the Last Glacial Maximum (LGM) and other glacial stages, sea-level was significantly lower and resulted in exposure of Bering Shelf areas and a closed Bering Strait. Accordingly, there was no connection to the Arctic and inflow of Pacific water masses into the Bering Sea might have been reduced as well. Notably, this land bridge was the prerequisite for paleoindian immigration from northeastern Asia to America (see also Sarnthein et al., 2006, and references therein). Imagery was reproduced from the GEBCO_08 Grid (30 arc-seconds resolution, version 20100927, http://www.gebco.net/), which is maintained and distributed by the British Oceanographic Data Centre, Natural Environmental Research Council, and was processed with the Fledermaus software (Version 7).

.

Lowered ventilation ages indicate enhanced deep ventilation or overturning during H1 and the YD in the N Pacific, while stronger stratification seems to have prevailed during the B/A (Ahagon et al., 2003; Ohkushi et al., 2004; Sagawa and Ikehara, 2008; Okazaki et al., 2010), at times when overturning in the Atlantic showed opposite behaviour (McManus et al., 2004). Modeling studies are in agreement with these observations and attribute the enhanced (reduced) Pacific Meridional Overturning Circulation (PMOC) to the weakened (strengthened) Atlantic Meridional Overturning Circulation (AMOC), and predict the potential weakening or disappearance of the halocline during H1 (e.g. Menviel et al., 2012).

Support for increased upper-ocean salinity in the subarctic NW Pacific during H1 comes from the few available Mg/Ca-based reconstructions (Sarnthein et al., 2006; Gebhardt et al., 2008; Sagawa and Ikehara, 2008). Results from Detroit Seamount (Sarnthein et al., 2006; Gebhardt et al., 2008), however, also show maxima in SST during that time, which is contradictory to alkenone-based reconstructions indicating restricted marine productivity and a later deglacial SST rise during the subsequent B/A. Finally, the salinity reconstruction of Sarnthein et al. (2004) might imply that the modern salinity-driven stratification was established in the early Holocene. This might also be connected to the re-opening of the Bering Strait, which occurred between 12–11 ka BP (Keigwin et al., 2006) (Fig. 1.5). Sea-level changes in the Bering Sea and the according opening/closure of the Bering Strait are suggested to have a considerable influence on deep convection in the N Atlantic due to the transport of relatively fresh surface waters to the Arctic Ocean at times when the Bering Strait was open (Hu et al., 2010).

### 1.4.4. Research questions

With respect to the indicated gaps regarding the paleoceanographic development of the subarctic NW Pacific and its marginal seas during the late Pleistocene to Holocene, the consecutive chapters of this thesis adress the following questions:

**Chapter 3 (to be submitted to *Paleoceanography*)**

- How are glacial-interglacial changes in marine productivity and terrigenous matter supply in the Bering Sea characterized? Do they compare with those observed in the Okhotsk Sea and are they related to the opening/closure of the Bering Strait?
- Is enhanced interglacial marine productivity in the Bering Sea controlled by sea-ice formation or by changes in upper-ocean stratification? On the other hand, what are sources and transport mechanisms related with enhanced terrigenous input during glacials?
- Can rapid climate oscillations, alike those recorded in Greenland ice cores be identified and, if so, how are they characterized and how can their occurrence be explained?

**Chapter 4 (submitted to *Paleoceanography*)**

- How is the deglacial SST development in the subarctic NW Pacific coupled to short-term climate oscillations of the N Atlantic?
- Is the long-term SST development of the NW Pacific and N Atlantic marked by opposing SST trends (temperature seesaw) during the past 7,000 years?
- Is there any change in sea-ice extent during millennial-scale fluctuations of the past 15 kyr?

**Chapter 5 (to be submitted to *Paleoceanography*)**

- How do deglacial records of Mg/Ca-derived subsurface temperatures compare with alkenone-derived SST records in the subarctic NW Pacific? In this context, how can potential differences between the temperature signals be explained?
- Was upper-ocean stratification in the subarctic NW Pacific subject to change during the last deglaciation and during the Holocene and, if so, what were the driving forces?
- When has the modern salinity-driven stratification (halocline) been established?

**Chapter 6 (to be submitted to *Nature Geoscience*)**

- Where was/were the source region(s) of better-ventilated intermediate water masses in the subarctic N Pacific during the last deglaciation?
- What happened to the intermediate to deep water ventilation in the N Pacific when the meridional overturning circulation in the N Atlantic ceased?
- Was deep water formed in the subarctic NW Pacific during rapid climate oscillations of the last glacial termination?

# 2. Material and methods

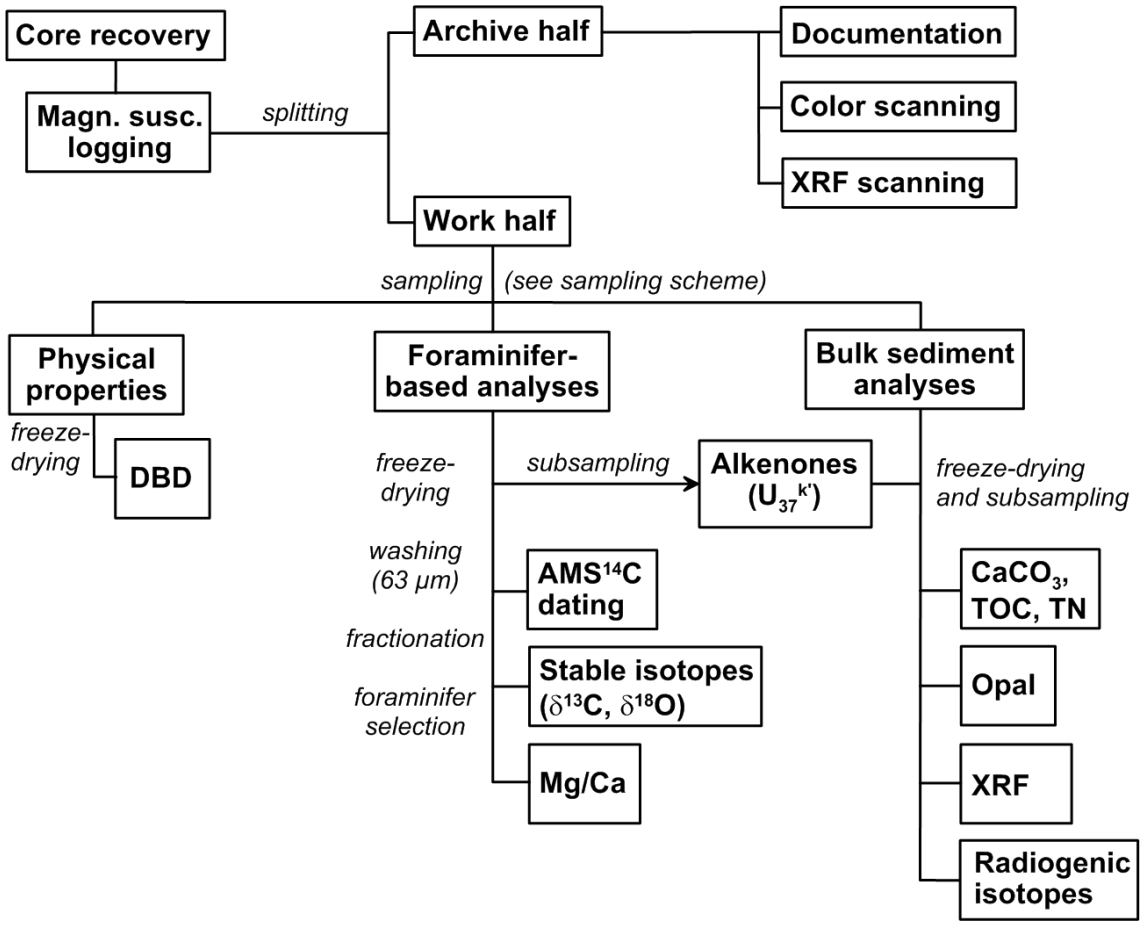


**Figure 2.1.:** Sequence of sample processing performed in the framework of this thesis. In principle, after splitting of core segments, archive halves were subject to documentation and core logging, whereas sediment samples were taken from the work halves.

Sediment cores recovered during SO201-2 used in this thesis were subject to a certain sequence of sample processing (Fig. 2.1). Core segments were split into archive and work halves after magnetic susceptibility was measured. Documentation, i.e. visual description and photography, as well as non-destructive core logging procedures, including color (e.g. color b*) and X-ray fluorescence (XRF) scanning, were performed on the archive halves. Sediment samples were obtained from the work halves following a specific sampling scheme (see Fig. 2.2 on page 15).

## 2.1. Core logging

In this thesis, high-resolution core logging data are used to establish age models (**chapters 3** and **4**), and to assess changes in marine productivity and terrigenous matter supply (**chapter 3**).

### 2.1.1. Magnetic susceptibility

After core recovery, records of magnetic susceptibility were produced aboard R/V Sonne for each unopened core segment. A GEOTEK Multi-Sensor Core Logger in combination with a Bartington MS2C sensor loop was used to perform measurements at a sampling interval of 1 cm. An oscillator circuit within the sensor loop generated a low intensity, non-saturating, alternating magnetic field (H=80 A $m^{-1}$, f=0.565 kHz). Magnetizable material present within the sediments in response to this applied field cause a change in the oscillator frequency, which is detected and converted into magnetic susceptibility values. Terrigenous, siliciclastic sediments usually contain magnetizable minerals. Consequently, magnetic susceptibility was used to approximate changes in the amount of terrigenous material within the sediments. Post-processing of the data included exclusion of outlying data due to core section breaks (Dullo et al., 2009).

### 2.1.2. Color scanning

Color reflectance was determined on the opened archive halves. Sediment surfaces were scrape-cleaned, flattened, and covered with clear plastic film before the measurements. A Minolta CM 508d hand-held spectrophotometer was used each 1 cm to illuminate a pulsed light flash (xenon arc lamp) and to subsequently detect the spectrum of the light reflected from the sediment surface (20 nm increments, $\lambda$ = 400–700 nm). Reflectance data were converted by the Spectramagic software into the CIE (L*, a*, b*) system (CIELAB). The color b*, i.e. the yellow-blue chromaticity (from +60 = yellow to -60 = blue), records provide a pattern of variability that corresponds to contents of biogenic opal. Calibration for white color reflectance and "zero calibration" were carried out prior to measurement of each core segment (Dullo et al., 2009), whereas core breaks and outlying data were eliminated during post-processing.

### 2.1.3. XRF scanning and data processing

Relative downcore changes in the chemical composition of the sediment cores were determined using the Avaatech XRF core scanner at Alfred Wegener Institute for Polar and Marine Research, Bremerhaven (AWI-Bremerhaven). Acquisition of XRF logging data was an integral part of this thesis and the complementary Ph.D thesis of Lars Max (2012) and resulted from extensive collaboration between the KALMAR Subproject 4 Ph.D-students. The scanner was equipped with an Oxford 100 W X-ray source (rhodium anode) and a thermoelectrically cooled two stage Peltier detector with a beryllium window (12 $\mu$m thick). To avoid both, contamination and desiccation, the sediment surfaces of the archive halves were scrape-cleaned, smoothed, and covered with ultrathin film (SPEX CertiPrep 3525 Ultralene foil, 4 $\mu$m thick) before the measurement. Each core segment was scanned three times at constant electric current (1 mA) but at different tube voltages and count times (10 kV, 10 s; 30 kV, 15 s; 50 kV, 30 s) at a sampling resolution of 1 cm. The emitted fluorescence energies of the irradiated sediment surface, which are proportional to element concentrations, are detected and converted into element intensities (counts). This allowed to produce element intensity

records of elements aluminium to barium. However, in general, XRF results are considered semiquantitative due to inhomogeneities within both, the sediment (lithology, physical properties), and the experimental set-up (e.g. uneven sediment surface, air bubbles between sediment and film) (e.g. Richter et al., 2006; Tjallingii et al., 2007).

Post-processing included data quality control, exclusion of recorded core breaks and outlying data, as well as calculation of element count rates and their respective log-ratios. Data quality was controlled by monitoring the "deadtime" and the $\chi^2$ value (cf. Tjallingii, 2006). The "deadtime" is related to the recovering time of the detector crystal, which, at high element intensities, can result in a non-linear input-to-output signal-relationship. It is calculated as the relative fraction between preset (livetime) and actual (realtime) count time and in the scanned sediment cores were lower than the critical value of 40%:

$$deadtime(\%) = 100 - 100 \times \frac{livetime}{realtime} \tag{2.1}$$

The $\chi^2$ value represents the "goodness-of-fit" between the analyzed XRF spectrum and a processing model which converts the XRF spectra into element intensities. XRF results of this study show $\chi^2$ values that lie well below the threshold of 3 given by Tjallingii (2006). Outlying data were identified by comparing records of element intensities of a single element ($I_i$) with normalized records of the same element ($I_{i,norm}$), which were calculated by normalizing the element intensity of one element $i$ to the sum of element intensities recorded for all $i = 1..n$ elements:

$$I_{i,norm} = \frac{I_i}{\sum_{i=1}^{n} I_i} \tag{2.2}$$

Element count rates (reported in counts per second, cps) were calculated by normalizing element intensities to the livetime. XRF results in this thesis are presented as element count rates or as log-ratios (natural logarithm) of element count rates of two elements A and B:

$$(A/B)\ log - ratio = ln\left(\frac{A}{B}\right) \tag{2.3}$$

## 2.2. Sampling and sample preparation

Work halves were completely sampled according to a specific sampling scheme (Fig. 2.2). This sampling scheme, which repeated every 10 cm, allowed to provide various working groups with sample material and to perform different analyses. Samples used in this study (Ti/Nü) were taken as 1 cm-thick slices for foraminifer-based (F) and multi-proxy bulk sediment analyses (M). In addition, plastic syringes (S) with a defined volume of 10 ml were used to determine the dry bulk density (DBD) every 5 cm. Backup samples (B) were eventually used to increase sampling resolution. Okhotsk Sea core LV29-114-3 was re-sampled in 2010. All samples were freeze-dried after sampling prior to subsequent analyses.

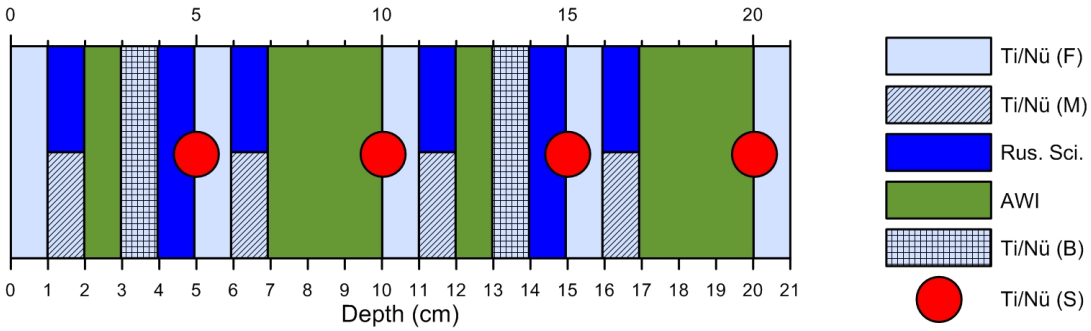


**Figure 2.2.:** Sampling scheme for SO201-2 sediment cores (after Dullo et al., 2009).

## 2.3. Foraminifer-based analyses

Foraminifer-based analyses included radiocarbon dating, stable carbon ($\delta^{13}$C) and oxygen ($\delta^{18}$O) isotope measurements, and Mg/Ca-thermometry. While benthic $\delta^{18}$O and dating results were used to establish the age models (**chapters 3** and **4**), planktonic $\delta^{18}$O and Mg/Ca analyses were used to reconstruct deglacial changes in subsurface temperature and salinity (**chapter 5**). Freeze-dried samples for foraminifer-based analyses also served for alkenone measurements ($U^{k'}_{37}$). Accordingly, subsamples of 5–10 g bulk sediment were taken prior to subsequent preparation steps. The remaining sample material was washed through a 63-$\mu$m mesh to remove clay- and silt-sized material, and then oven-dried at 50°C. Before and after washing the samples were weighed to determine the proportions of coarse (>63 $\mu$m) and fine (<63 $\mu$m) material (in wt.% dry weight). Respective records of coarse material were compared to records of magnetic susceptibility and used to infer changes in terrigenous matter supply (**chapter 3**). After washing, samples were dry-sieved (i.e., fractionated) by hand into six different size fractions: 63–125 $\mu$m, 125–250 $\mu$m, 250–315 $\mu$m, 315–355 $\mu$m, 355–400 $\mu$m, and >400 $\mu$m.

### 2.3.1. AMS radiocarbon dating

Accelerator mass spectrometry (AMS) was used to provide absolute age control for the studied sediment cores via radiocarbon ($^{14}$C) dating. Therefore, monospecific samples of subpolar to polar planktonic foraminifera species *Neogloboquadrina pachyderma* (sin.) (now referred to as *Nps*) were dated at the Leibniz-Laboratory for Radiometric Dating and Isotope Research, Kiel, and at the National Ocean Science Accelerator Mass Spectrometry Facility (NOSAMS) at Woods Hole Oceanographic Institution (WHOI), Woods Hole, MA, USA. Between 1500–2000 (900–1200) calcitic tests were selected from the 125–250 $\mu$m size fraction to account for the required minimum amount of 8 mg $CaCO_3$ (WHOI = 5 mg $CaCO_3$). For one sample (SO201-2-101KL, 445–446 cm) additional planktonic foraminifera species including *Globigerina bulloides* were selected from the same size fraction to compensate for insufficient amounts of *Nps*.

AMS-$^{14}$C ages were converted into 1$\sigma$ calendar age ranges (reported in BP = before present, i.e. before AD 1950) using the Calib Rev 6.1.0 software (Stuiver and Reimer, 1993) and the IntCal09 atmospheric calibration (Reimer et al., 2009). Reservoir ages are assumed to be constant over time but to be different on a regional scale. Hence, for the Okhotsk Sea and NW Pacific (cores LV29-114-3 and SO201-2-12KL) a reservoir age

of 900 years is considered, whereas for the western Bering Sea (cores SO201-2-77KL, -85KL, and -101KL) a lower value of 700 years is assumed. A detailled discussion about these considerations is given in **chapter 4**.

## 2.3.2. Stable carbon and oxygen isotopes

Stable carbon ($\delta^{13}$C) and oxygen ($\delta^{18}$O) isotope ratios, which are given in the common $\delta$-notation ($\delta = (R_{Sample}/R_{Standard} - 1) \times 1000$, where $R$ is the ratio of the heavy to light isotope) were measured on calcitic tests of both, benthic and planktonic foraminifera. Therefore, 2–3 specimens of endobenthic species *U. peregrina* or *U. auberiana* were selected from the 315–355 $\mu$m size fraction. In case of low abundances, size fractions 250–315 $\mu$m and 355–400 $\mu$m were eventually included for selection.

For combined stable isotope and Mg/Ca analyses of planktonic foraminifera ∼100–150 specimens of *Nps* were selected from the 125-250 $\mu$m size fraction to provide a sample amount of ∼500 $\mu$g. To avoid shell size-dependent effects (Elderfield et al., 2002) and potential bias due to different morphotypes (Healy-Williams, 1992) the most abundant, "square-shaped" specimen of *Nps* with four chambers was selected from a single size fraction. Subsequently, planktonic foraminiferal tests were gently crushed, homogenized, divided into two subsamples, and put into acid-leached vials (Eydam safe-lock tubes, RA5615030). Two thirds of total amount were used for Mg/Ca and one third was used for stable isotope analysis. Subsamples for stable isotope analysis were rinsed with ultrapure water and with ethanol, and ultrasonically cleaned in 20 s intervals before the measurements in order to remove clays.

Measurements were conducted at GEOMAR, Kiel, using a Thermo Finnigan MAT 253 mass spectrometer coupled with a Thermo Scientific Kiel IV Carbonate device. The foraminiferal calcite was dissolved at a temperature of 70°C using orthophosphoric acid ($H_3PO_4$) thereby producing $CO_2$ gas which is subsequently analyzed. Manually detrended results are calibrated against the NBS19 standard, and reported relative to the Pee Dee Belemnite scale (PDB). The used internal "Bremen Standard" (Solnhofen limestone) indicates an analytical long-term precision (N >1000 samples) of ±0.03‰ PDB for $\delta^{13}$C and of ±0.06‰ PDB for $\delta^{18}$O. Additional measurements were performed at AWI-Bremerhaven using a Finnigan MAT 251 mass spectrometer coupled with a Kiel II carbonate preparation device. External reproducibility of theses measurements was ±0.04‰ for $\delta^{13}$C and ±0.06‰ for $\delta^{18}$O.

## 2.3.3. Foraminiferal Mg/Ca analysis

Samples were cleaned for Mg/Ca analysis according to the protocol of Barker et al. (2003), including a reductive cleaning step. To initially remove clay particles, samples were rinsed with ultrapure water (3x), ethanol (2x), and ultrapure water (2x), including ultrasonic treatment steps of 20 s. Hydrazine ($N_2H_4$) was used as reducing agent to remove metal oxides. Therefore, 100 $\mu$l of a solution made of 750 $\mu$l hydrazine, 15 ml ammonium hydroxide ($NH_4OH$), and 15 ml ammonium citrate[1] were added to each vial and put in a hot water bath for 30 min. The reaction was accelerated by

1 Ammonium citrate was made from 12.5 g citric acid ($C_6H_8O_7$) and 500 ml of ammonium hydroxide.

two short (10 s) ultrasonic treatment steps. After rinsing with ultrapure water (3x), samples were transferred into new acid-leached vials. Oxidative cleaning in order to remove remaining organic matter followed. It was performed by adding 250 $\mu$l of a solution made from 100 $\mu$l hydrogen peroxide ($H_2O_2$, suprapure) and 30 ml NaOH. Samples were put in a hot water bath for 10 min and briefly (2x 10 s) ultrasonically treated. Gaseous build-up was released several times. After rinsing with ultrapure water (3x), 250 $\mu$l of nitric acid ($HNO_3$, 0.001 M) were added in the final leaching step and samples were subsequently stored until analysis. Immediately before analysis, samples were dissolved using ultrapure $HNO_3$ (0.075 M), including ultrasonic treatment for 25 min. and centrifugation. About 500 $\mu$l of the supernatant were transferred into polypropylene tubes (Eydam, 9400782) and diluted with 1.8 ml $HNO_3$ (0.075 M), which contained 10 ppm of yttrium as internal standard.

Measurements were performed on a simultaneous, axial-viewing Inductively Coupled Plasma–Optical Emission Spectrometer (ICP-OES; VARIAN 720-ES) coupled with a SPS3 sample preparation system at GEOMAR, Kiel. Spectral lines used were 279.553 nm for Mg and 370.602 nm for Ca. Measurement strategy involved analyses of standards and blanks to assure analytical quality control. Software automatically corrected for analytical drift (detrending). Results were manually normalized to the ECRM 752-1 standard (Mg/Ca = 3.761 mmol mol$^{-1}$; Greaves et al., 2008), which was used as internal consistency standard. Analytical precision, determined on behalf of the ECRM 752-1 standard, was 0.1 mmol mol$^{-1}$ ($2\sigma$). Replicate analyses, repeating complete treatment including re-selection of foraminiferal tests, were performed for 11 samples that were considered as outlying data. Results showed discrepancies ranging between 0.1–0.7 mmol mol$^{-1}$. Ratios Mn/Ca, Fe/Ca, and Al/Ca were monitored to detect potential contamination of the samples by detrital material and secondary diagenetic coatings.

Sampling resolution was improved for core LV29-114-3 by including former Mg/Ca measurements which were conducted by Lester Lembke-Jene in 2005 at the University of Kiel. Results are based on 30 specimens of *Nps* for stable isotopes and 50 specimens for Mg/Ca, which were selected from the 150–250 $\mu$m size fraction. Samples were also cleaned according to the protocol of Barker et al. (2003) applying non-reductive cleaning. Analyses were performed on a simultaneous, radially-viewing ICP-OES (Spectro A.I. Ciros CCD SOP) on spectral lines 183 nm for Ca and 270 nm for Mg, respectively. Results from both, reductive and non-reductive measurements, are considered as consistent, since systematical differences were not observed and lie within the error range of the method.

Mg/Ca-based sub sea surface temperatures (subSST$_{Mg/Ca}$) were reconstructed by applying the relationship of Kozdon et al. (2009) for *Nps*:

$$Mg/Ca\ (mmol\ mol^{-1}) = 0.13 \times T\ (^{\circ}C) + 0.35 \tag{2.4}$$

With respect to the slope in Eq. 2.4, analytical precision for Mg/Ca translates into an uncertainty of $\pm 0.8^{\circ}$C for the paleotemperature estimates.

Subsurface salinities (subSSS) were approximated from the calculation of ice-volume corrected seawater $\delta^{18}$O estimates ($\delta^{18}O_{ivc-sw}$). The $\delta^{18}$O-signal of foraminiferal calcite ($\delta^{18}O_{Cc}$) is a function of temperature and of the isotopic composition of seawater ($\delta^{18}O_{sw}$, reported in ‰ SMOW). The latter is influenced by regional variations in

salinity and by global ice-volume (e.g. Schmidt et al., 2004). $\delta^{18}O_{sw}$ was calculated by applying the combined foraminiferal $\delta^{18}O$- and Mg/Ca-results to the relationship of Shackleton (1974):

$$\delta^{18}O_{sw} = \delta^{18}O_{Cc} + 0.27 - \frac{4.38 - \sqrt{4.38^2 - 4 \times 0.1 \times (16.9 - T)}}{2 \times 0.1} \quad (2.5)$$

$\delta^{18}O_{ivc-sw}$ was then calculated by correcting $\delta^{18}O_{sw}$-values for the global ice-volume signal following Waelbroek et al. (2002). This approach cumulates into an uncertainty of about ±0.3‰ SMOW.

Foraminiferal Mg/Ca records are potentially affected by contamination, carbonate dissolution, and diagenetic processes. Hence, it is critical to assess the impact of these processes on the Mg/Ca signal. In this study, a correction of the initial Mg/Ca results was not applied, although all sediment cores were recovered below the modern CSH. The reasons for this as well as the origin of the temperature signal recorded by *Nps* are discussed in **chapter 5**. Notably, samples were identified that have eventually been altered by contamination or by early diagenetic processes, and a respcetive discussion is provided at the end of **chapter 5**. However, only samples from the pre-deglacial phase are affected by these processes.

## 2.4. Bulk sediment analyses

Bulk sediment samples were used to perform CN-analytics ($CaCO_3$, total organic carbon, total nitrogen), opal measurements, quantitative XRF analyses, and to determine radiogenic isotope compositions ($^{143}Nd/^{144}Nd$, $^{87}Sr/^{86}Sr$). Bulk sediment analyses allowed to reconstruct changes in marine productivity and terrigenous matter supply (**chapter 3**). Due to specific restrictions of the respective geochemical proxies, they are used in a multi-proxy approach and shown together with the logging data, which are characterized by similar temporal trends.

### 2.4.1. CN-Analytics and [C/N]a ratios

CN-Analytics included determination of total carbon (TC), total organic carbon (TOC), and total nitrogen (TN) contents. Therefore, 3-4 g of freeze-dried bulk sediment were ground and homogenized for 10 min using a planetary mill. Measurements were performed at GEOMAR, Kiel, using a Carlo Erba CNS Analyzer (model NA-1500). Subsamples of 20 mg were encapsulated into aluminum cups and oxidized at 1050°C based upon "flash combustion". TOC was measured on samples that were previously decalcified using hydrochloric acid (HCl; 0.25 M). The combustion products ($CO_2$, $NO_x$, and $H_2O$) are swept into a reduction reactor (metallic copper) using helium as carrier gas, where they are reduced, subsequently filtered, and gas-chromatographically separated before detection via thermal conductivity. A discription of this procedure can be found in Verardo et al. (1990). Precision ($2\sigma$) was determined on behalf of an internal standard and resulted in a relative standard deviation (RSD) <3% for TC, TOC, and TN. Replicate measurements showed a reproducibility of ±0.03 wt.% for TOC (N = 10)

and of ±0.01 wt.% for TN (N = 19). Contents of calcium carbonate were calculated as:

$$CaCO_3 = 8.333 \times (TC - TOC) \tag{2.6}$$

Additional measurements of TC and TOC were conducted at AWI-Bremerhaven using a LECO CS-125 carbon-sulphur analyzer.

The atomic ratio of organic carbon to organic nitrogen, corrected for inorganic nitrogen ([C/N]a), was used to distinguish between marine and terrigenous sources of TOC. Since TN contents are influenced by an unknown portion of inorganic nitrogen components, usually clay-bound inorganic ammonium (Müller, 1977), a correction was applied to calculate the amount of total organic nitrogen (TON). This correction, which was applied to each core individually, is based on a linear regression between TOC and TN values and produces an intercept-value reflecting the constant amount of inorganic nitrogen (TIN). TON was therefore calculated after the following equation: $TON = TN - TIN$.

### 2.4.2. Opal

Contents of biogenic silica (opal) were measured applying the automated leaching method of Müller and Schneider (1993), which is based on molybdate-blue spectrophotometry. Initially, 3–4 g of freeze-dried bulk sediment were hand-ground using an achat mortar. Silica was extracted from subsamples of 20 mg mixed with 100 ml sodium hydroxide (NaOH; 1 M) in a hot water bath at 85°C for ∼45 min. Five calibration standards were made from silicon tetrachloride ($SiCl_4$) in a NaOH matrix and measured before and after a batch of samples. Results were evaluated after DeMaster (1981). 2–3 replicate measurements were conducted for 75 samples and resulted in an average reproducibility of 1–2 wt.%. For core SO201-2-77KL, additional measurements were conducted at AWI-Bremerhaven following the same approach.

### 2.4.3. Quantitative XRF analysis and $Ba_{excess}$

Concentrations of major (e.g. Al, Ti, Fe, K) and trace elements (e.g. Ba) were determined at the Institute of Geosciences, University of Kiel, using a Philips PW1480 sequential X-ray spectrometer. For preparation, freeze-dried sediment samples (3–4 g) were ground and homogenized using a planetary mill. Measurements were performed on fused glass discs containing a mixture of 0.6 g of sediment and 3.6 g of $Li_2B_4O_7$ ("Spectroflux 100"). Loss on ignition (LOI) was not determined. Weight percentages of major elements were calculated from weight percentages of their respective oxides, whereas trace element concentrations are reported in parts per million (ppm). The BHVO standard showed an analytical precision of <2% RSD ($2\sigma$, N = 15) for the major elements and of ±30 ppm for barium.

Results for Barium ($Ba_{total}$) are the sum of biogenic ($Ba_{excess}$) and nonbiogenic Ba portions. In this study, $Ba_{excess}$ was at first calculated by estimating the aluminosilicate

(i.e. the nonbiogenic) contribution of Ba, and then used to assess new production[2] ($P_{New}$) and annual primary production (PP). The aluminosilicate contribution of Ba was estimated via concentrations of Al (in wt.%) by considering the global average aluminosilicate Ba/Al ratio for pelitic rocks of 6.5 mg $g^{-1}$ (Wedepohl, 1971), which was then used to calculate $Ba_{excess}$ (in ppm):

$$Ba_{excess} = Ba_{total} - Al \times 10^4 \times 0.0065 \tag{2.7}$$

$P_{New}$ (reported in gC $m^{-2}$ $yr^{-1}$) was calculated from $Ba_{excess}$ using the equation of Nürnberg (1995a) considering the flux of biogenic Ba to the sea-floor (F $Ba_{excess}$) and water depth (z, in m):

$$P_{New} = 3.56 \times F\ Ba_{excess}^{1.504} \times z^{-0.0937} \tag{2.8}$$

with

$$F\ Ba_{excess} = AR\ Ba_{excess} \times \frac{1}{0.209 \times log_{10}(AR_{bulk} \times 1000) - 0.213} \tag{2.9}$$

F $Ba_{excess}$ (in $\mu$g $cm^{-2}$ $yr^{-1}$) was calculated after Dymond et al. (1992). The mass accumulation rate ($AR_{Bulk}$) is the product of DBD (in g $cm^{-3}$) and linear sedimentation rate (LSR, in cm $kyr^{-1}$; van Andel et al., 1975), which for the calculation of biogenic Ba accumulation rates (AR $Ba_{excess}$, in mg $cm^{-2}$ $kyr^{-1}$) is multiplied with $Ba_{excess}$:

$$AR\ Ba_{excess} = (Ba_{excess}/1000) \times AR_{Bulk} \tag{2.10}$$

Finally, PP (in gC $m^{-2}$ $yr^{-1}$) was calculated from $P_{New}$ according to Eppley and Peterson (1979):

$$PP = 20 \times \sqrt{P_{New}} \tag{2.11}$$

## 2.4.4. Contents of siliciclastics and terrigenous matter

In this study, bulk sediment is considered to be composed of $CaCO_3$, TOC, TN, opal, and an unknown portion of siliciclastics. Since contents of TN were generally <0.3 wt.%, the relative amount of siliclastics (in wt.%) of a single sample was calculated after the following equation: $\%siliciclastics = 100\% - (CaCO_3 + TOC + Opal)$. In a second approach, relative contents of terrigenous matter were calculated by normalizing quantitative XRF-based results of Al and Ti concentrations (see section 2.4.3) to the average Al and Ti concentration of continental crust ([Al] = 3117 $\mu$mol $g^{-1}$, [Ti] = 112.8 $\mu$mol $g^{-1}$; Taylor and McLennan, 1995). Al-normalized results were on average 4–6% higher than Ti-normalized results and better compared to the records of %siliciclastics.

2 New production refers to marine primary production that results from allochthonous nutrient inputs to the euphotic zone (Eppley and Peterson, 1979).

## 2.5. Radiogenic isotopes

The radiogenic isotope composition for neodymium (Nd), strontium (Sr), and lead (Pb) was extracted from early diagenetic ferromanganese (Fe-Mn) oxyhydroxide coatings for twelve bulk sediment samples from core SO201-2-85KL. The extraction, separation, and purification of Nd, Sr, and Pb, as well as the isotope measurements, were carried out following the methodology described in Gutjahr et al. (2007) in the (clean laboratory) facilities at GEOMAR, Kiel. First, freeze-dried samples of ∼2 g were hand-ground and transferred into acid-cleaned polypropylene tubes. Then, after rinsing with ultrapure water (Milli-Q system) and centrifugation, carbonate was removed using an acetic acid / sodium acetate buffer. The supernatant was removed by centrifugation, decanting, and rinsing with ultrapure water. Subsequently, Fe-Mn oxyhydroxide coatings were dissolved using 15 ml of ultrapure water and 5 ml of a buffered hydroxylamine hydrochloride (0.05 M) / acetic acid (15% suprapure) leaching solution (pH 4). After 60 minutes at room temperature, the supernatant (∼20 ml) was centrifuged and transferred into pre-cleaned teflon vials.

Separation and purification of Nd, Sr, and Pb were performed following standard procedures (as described in Cohen et al., 1988; Galer and O'Nions, 1989; Horwitz et al., 1992). Anion exchange columns were used for purification of Pb (AG1-X8 resin), while cation exchange columns (AG50W-X12 resin) served for separation of alkaline elements. Nd and Sr were purified using Ln Spec resin and Sr Spec resin, respectively. Measurements were conducted on a Nu Plasma MultiCollector-Inductively Coupled Plasma Mass Spectrometer at GEOMAR. Results for Pb are not assessed in the context of this study. Isotope results were normalized to the accepted values of the JNdi-1 standard for Nd ($^{143}$Nd/$^{144}$Nd=0.512115, Tanaka et al., 2000) and of the NIST SRM987 standard for Sr ($^{87}$Sr/$^{86}$Sr=0.710245) to compensate for analytical drift. The Nd isotope ratios are reported in the epsilon notation (Eq. 2.12), which is the corrected $^{143}$Nd/$^{144}$Nd ratio normalized to the Chondrite Uniform Reservoir (CHUR) standard ($^{143}$Nd/$^{144}$Nd=0.512638, Jacobsen and Wasserburg, 1980). External reproducibility was estimated by repeated measurements of an in-house SPEX standard for Nd and the AA standard for Sr, and were ±0.21 for $\varepsilon_{Nd}$ and ±0.00003 for Sr ($2\sigma$). Preliminary results are shown in the perspectives part of this thesis (**section 7.4** on page 150).

$$\varepsilon_{Nd} = \left[ \frac{^{143}Nd/^{144}Nd_{sample}}{^{143}Nd/^{144}Nd_{CHUR}} - 1 \right] \times 10^4 \tag{2.12}$$

## 2.6. Age models

The stratigraphic framework of this thesis is based on several tools including benthic oxygen isotope stratigraphy, magnetostratigraphy, intercore correlations, and absolute age control via AMS-$^{14}$C dating. The establishment of the age models, which is an integral part of this thesis and the complementary Ph.D thesis of Lars Max (2012), resulted from extensive collaboration between the KALMAR Subproject 4 Ph.D-students and members Prof. Dr. Ralf Tiedemann, Prof. Dr. Dirk Nürnberg, Dr. S. Gorbarenko, and Dr. M. Malakhov.

The color b* variability recorded in cores from Shirshov Ridge (SO201-2-77KL, -85KL, and -101KL) strongly corresponds to the Dansgaard-Oeschger climate variability registered in the NGRIP ice core (NGRIP members, 2004). Hence, the chronostratigraphy is primarily based on a graphic correlation between color b* measured in core SO201-2-85KL and the NGRIP $\delta^{18}$O record (GICC05 timescale; Rasmussen et al., 2006), which was verified by AMS-$^{14}$C dating. Further support came from comparison of the produced benthic $\delta^{18}$O records with the widely accepted global benthic reference stack LR04 (Lisiecki and Raymo, 2005), and from paleomagnetic data of core SO201-2-85KL which were compared with the PISO-1500 geomagnetic paleointensity stack (Channell et al., 2009). This approach is illustrated in Fig. 2.3. Paleomagnetic records shown in this study were provided by Dr. Sergey Gorbarenko (Pacific Oceanological Institute, FEB-RAS[3], Vladivostok, Russia) and Dr. Mikhail Malakhov (North Eastern Interdisciplinary Science Research Institute, FEB-RAS, Magadan, Russia) (see **chapter 3**).

Sediment cores from Shirshov Ridge recorded the last glacial-interglacial cycle. Respective age models for the time interval >20 ka BP primarily rely on the stratigraphy of core SO201-2-85KL transferred to cores 77KL and 101KL via intercore correlations using records of color b* and XRF Ca/Ti log-ratios (Fig. 2.4). Additional age control points for core SO201-2-101KL were derived from benthic $\delta^{18}$O results compared with the LR04 stack. Age models for the last glacial-interglacial cycle recorded in Shirhov Ridge cores are discussed in **chapter 3**.

Intercore correlations using color b* and XRF logging data also allowed to transfer AMS-$^{14}$C dates between the sediment records. Dating was mainly performed within the younger parts of the cores (<20 ka BP) on samples showing maxima in $CaCO_3$ content. Two of these maxima (carbonate spikes 1 and 2) correspond to prominent carbonate maxima found in the NW Pacific and indicate consistency with age models from other studies. The age model for the last 20 ka BP is explained in detail in **chapter 4**.

3 Far Eastern Branch, Russian Academy of Sciences

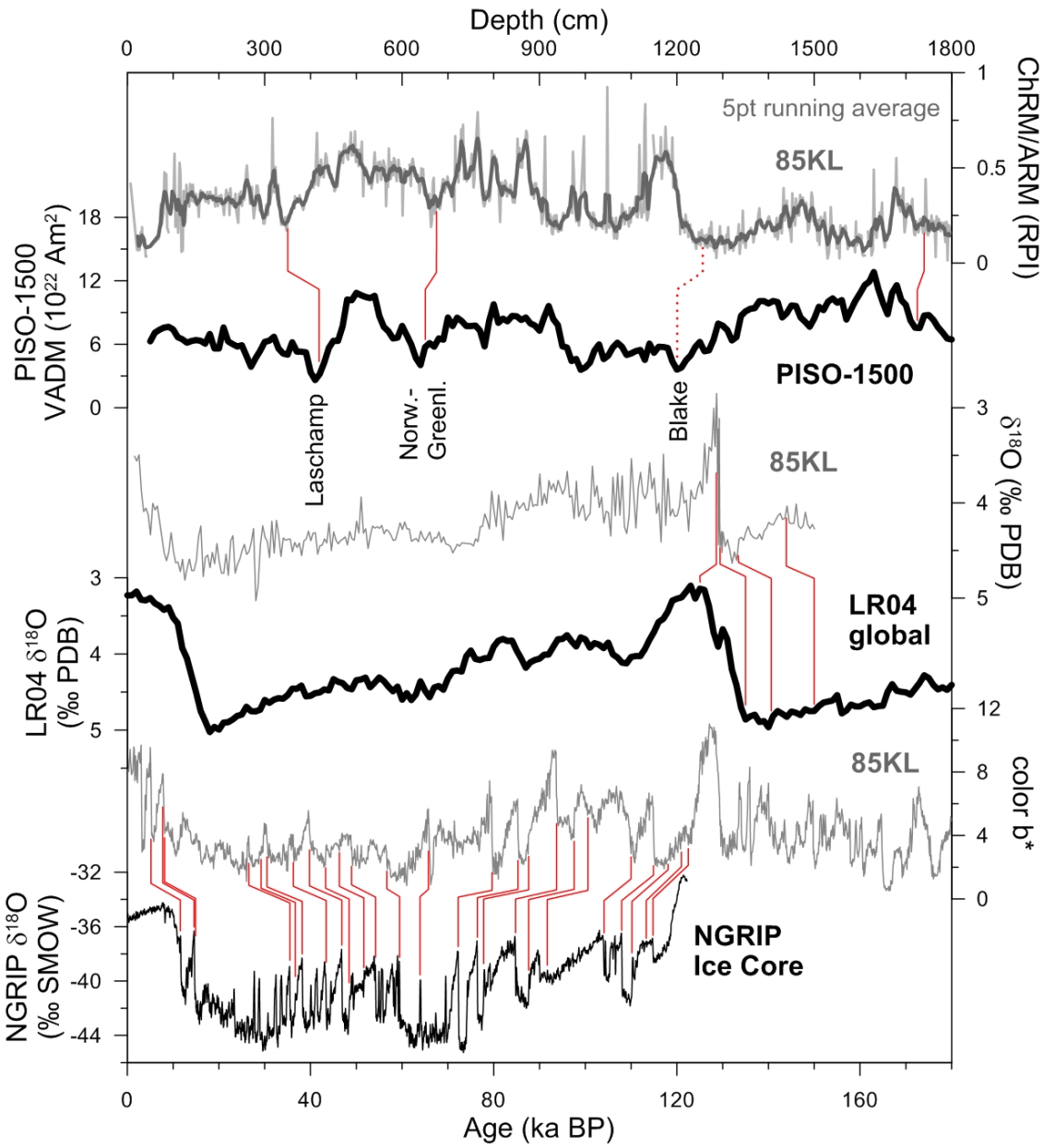


**Figure 2.3.:** The stratigraphy of core SO201-2-85KL is mainly based on graphic correlation between color b* and the NGRIP $\delta^{18}$O record (NGRIP members, 2004; GICC05 timescale, Rasmussen et al., 2006), which is verified by AMS-$^{14}$C age control. Additional age control points were derived from comparison of benthic $\delta^{18}$O with the LR04 reference stack (Lisiecki and Raymo, 2005), and of relative paleointensity (RPI) with the PISO-1500 paleointensity stack (Channell et al., 2009). Red lines indicate age-depth tie lines.

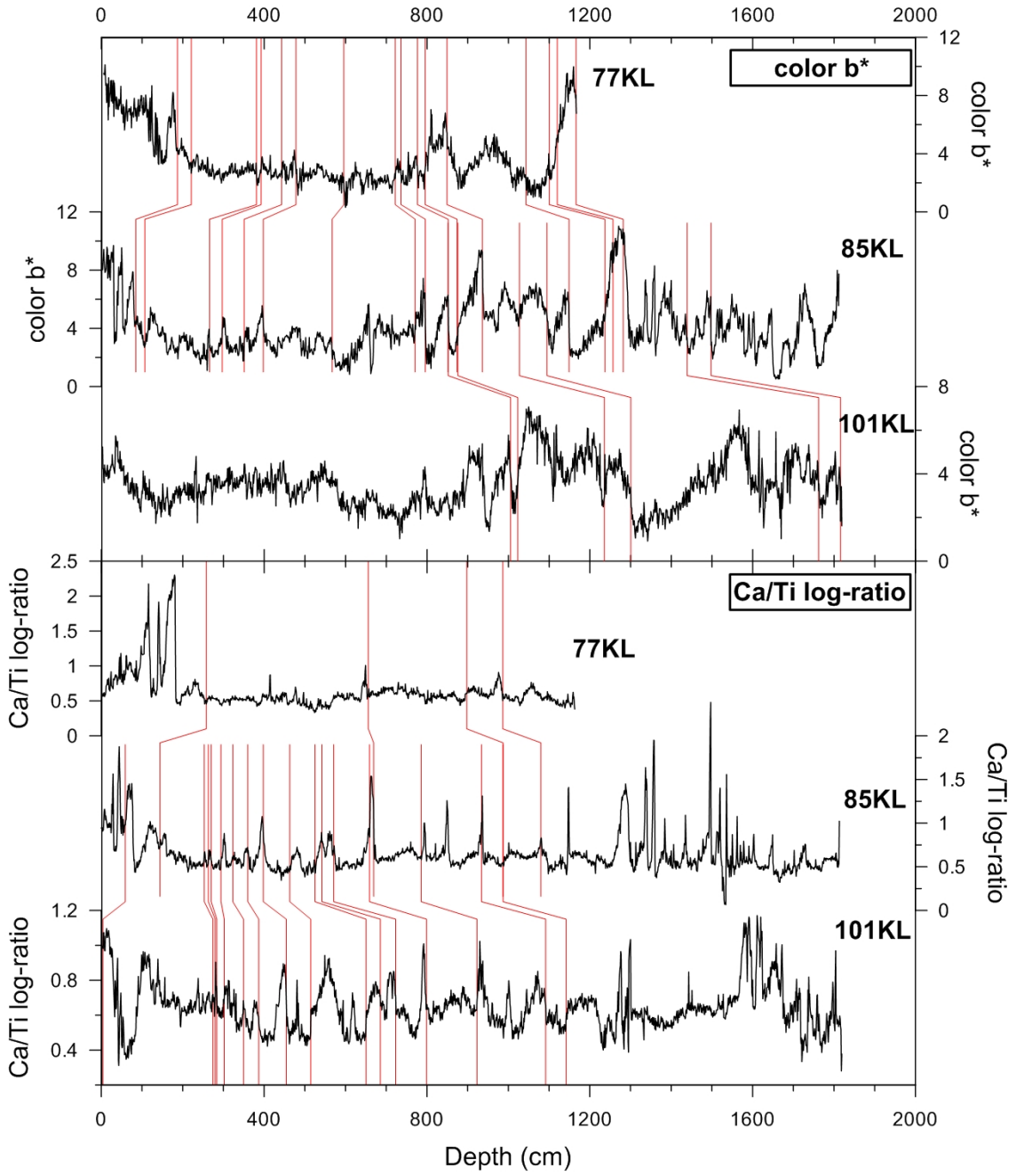


**Figure 2.4.:** Logging data were used for intercore correlations, thereby transferring the stratigraphy of core SO201-2-85KL to the other cores. Shown here are records of color b* (upper hand) and XRF Ca/Ti log-ratios (lower hand) for Shirshov Ridge cores versus core depth. Intercore depth-to-depth correlations are indicated by red lines.

## 2.6.1. Time series analysis

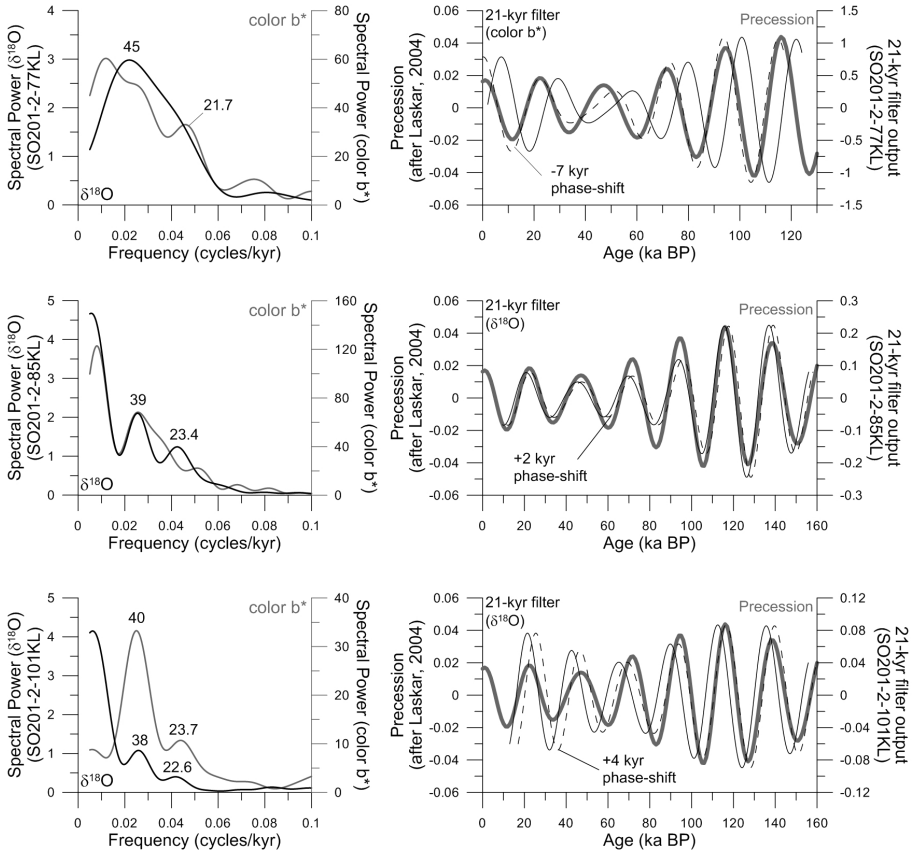


**Figure 2.5.:** Spectral analysis was performed on records of color b* and benthic $\delta^{18}$O for Shirshov Ridge cores. Left-hand figures show the frequency spectra in the time-domain of the respective cores, whereas right-hand figures show a comparison between the 21-kyr filter output and the solution of Laskar et al. (2004) for orbital precession. Cyclicities close to orbital precession (21 kyr) and obliquity (41 kyr) cycles were detected. 21-kyr filter outputs of benthic $\delta^{18}$O for cores 85KL and 101KL agree with the published orbital solution within phase-shifts of +2 to +4 kyr. In core 77KL benthic foraminifera were rather absent below 865 cm core depth (>86 ka BP). Hence, the 21-kyr filter was applied to the color b* record and after applying a phase-shift of -7 kyr also showed good agreement with the published orbital solution.

Age models were tested via spectral analysis in order to detect periodicities within the sediment records that are related to Earth's orbital cycles. Spectral analysis was performed in the time domain of the color b* and benthic $\delta^{18}$O records of cores SO201-2-77KL, -85KL, and -101KL using the AnalySeries software (Version 2.0.4.2; Paillard et al., 1996). Time series were evenly resampled by linear interpolation choosing a sampling step ($\Delta$t) that corresponded to the sampling interval ($\Delta$z) and average sedimentation rate of the respective cores : $\Delta t = \Delta z / LSR$. Accordingly, values for $\Delta$t varied between 0.1–0.5 kyr. The Blackman-Tukey method (Blackman and Tukey, 1958) was then applied using linear trend removement and Welch windowing (Welch, 1967) with a confidence level of 90%. The frequency scale of the output data was resampled from $5\times10^{-3}$ to $2\times10^{-1}$ kyr$^{-1}$ in steps of $10^{-4}$ kyr$^{-1}$. Orbital precession was filtered out using a Gaussian filter (f = 0.047 kyr$^{-1}$, bandwidth = 0.01 kyr$^{-1}$). Spectral analysis resulted in the detection of dominant cyclicities close to orbital precession (21 kyr) and obliquity (41 kyr). 21-kyr filter outputs were in good agreement with the numerical solution of Laskar et al. (2004) for orbital precession (Fig. 2.5).

## 2.6.2. Sedimentation rates and temporal resolution

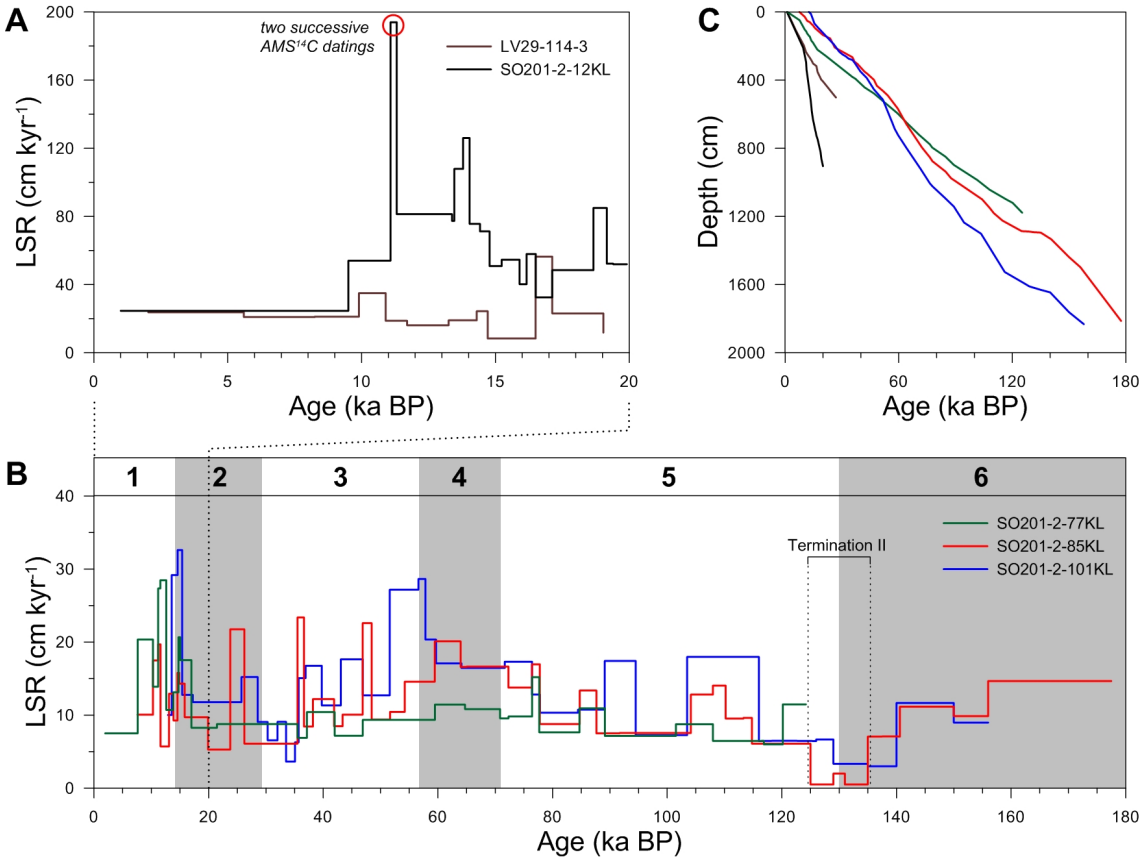


**Figure 2.6.:** Linear sedimentation rates (LSR) for sediment cores LV29-114-3 and SO201-2-12KL during the last 20,000 years (A), and for the last 180,000 years for Shirshov Ridge cores (B), are shown together with the cores' respective depth-age relationships (C). LSR on average vary between 10–15 cm kyr$^{-1}$ on Shirshov Ridge, whereas highest LSR are recorded in core SO201-2-12KL. Sediment records shown in this study therefore allow for paleoceanographic reconstructions in centennial to millennial time-resolution. Black numbers in B indicate Marine Isotope Stages (MIS) 1-6 (boundaries after Lisiecki and Raymo, 2005). Very high LSR in core SO201-2-12KL at ~11.3–11.1 ka BP are the result of two successive AMS-$^{14}$C ages.

Linear sedimentation rates (LSR) were calculated between age control points as the thickness of a sediment interval devided by the time interval of its deposition. In Shirshov Ridge cores average LSR were 10–15 cm kyr$^{-1}$, whereas cores LV29-114-3 and SO201-2-12KL during the last 20,000 years had average LSR values of 25 cm kyr$^{-1}$ and 65 cm kyr$^{-1}$, respectively (Fig. 2.6). Highest values are reached in core SO201-2-12KL. Hence, Shirshov Ridge cores have a potential average time-resolution of 70–100 years with respect to the logging data and of 400–500 years regarding the foraminifer-based and bulk sediment analyses. Core SO201-2-12KL has best average resolution of ~20 years for the logging data and of ~80 years for the geochemical analyses. Cores presented in this study therefore allow to reconstruct environmental changes during the last ca. 180,000 years in centennial to millennial time-resolution.

### 2.6.3. Termination II

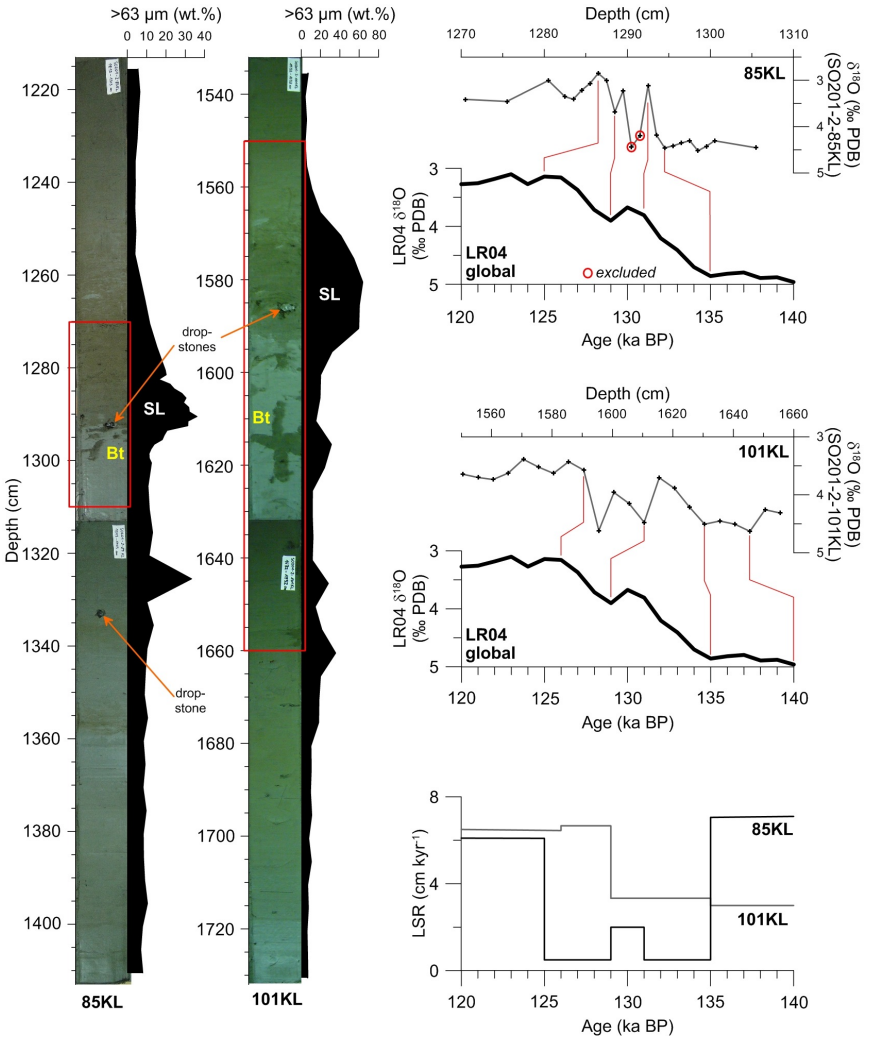


**Figure 2.7.:** This figure shows core photographs of sediment cores 85KL and 101KL, together with relative amounts of coarse material (>63 $\mu$m), and the stratigraphic approach for Termination II. Bioturbation (Bt) and dropstones are indicated in the photographs. Sand layers (SL) at the end of Termination II reflect a change in sedimentary composition. Red boxes denote the position of the benthic $\delta^{18}$O records shown to the right, which are used for comparison with the LR04 stack. Respective age-depth tie lines (red) are indicated. The stratigraphic approach results in reduced LSR during Termination II and indicates a potential hiatus in core 85KL.

Sediment cores SO201-2-85KL and -101KL are subject to bioturbation within core intervals 1288–1300 cm (85KL) and 1590-1632 cm (101KL) thereby showing strong variations in benthic $\delta^{18}$O (Fig. 2.7). These intervals represent Termination II (135–125 ka BP). For core SO201-2-85KL these observations together with a relatively sharp change in sediment composition indicate an erosional contact at ~1290 cm and hence a potential hiatus. The stratigraphy of cores SO201-2-85KL and -101KL during Termination II relies on comparison of benthic $\delta^{18}$O with the LR04 stack. Within the interval of 1280–1301 cm core depth (Termination II), benthic $\delta^{18}$O was determined on *U. peregrina* every 1 cm. Two samples (1290-1291 cm, 1291-1292 cm) were excluded from the stratigraphic approach. Both cores show extremely reduced LSR of <4 cm kyr$^{-1}$ during Termination II, thereby indicating a significant change in sedimentation and/or potential erosion of sediments.

# 3. Millennial-scale variability of marine productivity and terrigenous matter supply in the western Bering Sea during the last glacial-interglacial cycle

**Based on:** *"Millennial-scale variability of marine productivity and terrigenous matter supply in the western Bering Sea during the last glacial-interglacial cycle"* by Jan-Rainer Riethdorf, Dirk Nürnberg, Lars Max, Ralf Tiedemann, Sergey Gorbarenko, and Mikhail Malakhov (to be submitted to *Paleoceanography*).

## Abstract

Piston cores, recovered from intermediate water levels in the western Bering Sea, were used to reconstruct millennial-scale changes in marine productivity and terrigenous matter supply over the past ∼180,000 years. Age models rely on a combination of benthic oxygen isotope stratigraphy, magnetostratigraphy, radiocarbon dating, and intercore correlations via high-resolution core logging data (color b*, XRF scans), which provide a pattern of variability that strongly corresponds to Dansgaard-Oeschger climate variability registered in the NGRIP ice core record. Reconstructions are based on a geochemical multi-proxy approach indicating closely interacting processes that control biological productivity and terrigenous matter supply comparable to the situation in the Okhotsk Sea. During the last glaciation our results point towards higher terrigenous inputs while primary production was low. Minor increases in marine productivity occur during warm stages of MIS5, while maxima are observed during interglacials and the last glacial termination. Anticorrelated records of marine productivity and terrigenous matter supply, fairly constant Al/Ti and Fe/Al ratios, and high [C/N]a ratios suggest that seasonal sea-ice formation is the dominant transport agent for terrigenous material. From our results we propose scenarios for environmental change in the Bering Sea during the last glacial-interglacial cycle. These changes seem to be primarily controlled by insolation and sea-level changes, thereby influencing the strength of atmospheric pressure systems, seasonal contrasts, and sea-ice rafting. Sea-ice dynamics are thought to drive changes in surface productivity, terrigenous inputs, and upper-ocean stratification. We found indications that the opening and closure history of the Bering Strait might have had an additional impact on the observed changes. Abrupt environmental changes recorded during the last glacial period supposedly apply to the deglacial situation and are potentially related to North Atlantic Dansgaard-Oeschger events, supporting an atmospheric coupling mechanism of Northern Hemisphere climates.

## 3.1. Introduction

Late Quaternary glacial-interglacial cycles are characterized by correlated changes in global climate and atmospheric concentrations of carbon dioxide (e.g. Sigman et al., 2010). Although the specific cause of these variations is still not fully understood, the subarctic N Pacific and its marginal seas may hold an important key for its understanding due to the presence of high marine productivity and polar stratification. However, especially for the last glacial period and deglaciation, when strong reorganizations in meridional overturning circulation occurred in the N Atlantic, marine records from the subarctic N Pacific allowing for decadal to millennial-scale paleoceanographic reconstructions are sparse. Existing reconstructions are further constrained by the shallow carbonate lysocline within the N Pacific realm limiting the use of carbonate-based proxies and causing stratigraphic uncertainties.

The subarctic N Pacific is a high-nitrate, low-chlorophyll (HNLC) region (e.g., Kienast et al., 2004; Tyrrell et al., 2005), characterized by salinity-driven stratification (permanent halocline) of the upper water column, which is suggested as a potential control mechanism of glacial-interglacial variations in atmospheric $CO_2$ (Haug et al., 1999; Sigman and Boyle, 2000; Sigman et al., 2004; Haug et al., 2005; Jaccard et al., 2005; Sigman et al., 2010). The halocline prevents the formation of deep water (Warren, 1983; Emile-Geay et al., 2003) and modulates the supply of nutrient-rich deep water into the euphotic zone, thereby influencing the extent of marine productivity and nutrient utilization. Although the halocline also acts as a barrier for atmospheric-oceanic gas exchange, the modern subarctic Pacific is considered a net source of atmospheric $CO_2$ (Takahashi et al., 2002b) despite a very high carbon export efficiency (Honda et al., 2002).

Several studies have reported low marine productivity during glacial times in the subarctic N Pacific (Narita et al., 2002; Kienast et al., 2004; Jaccard et al., 2005; Brunelle et al., 2007; Shigemitsu et al., 2007; Galbraith et al., 2008; Gebhardt et al., 2008; Jaccard et al., 2009, 2010). However, it remains unclear, whether reduced marine productivity and low atmospheric $CO_2$ concentrations during glacial times were caused by increased polar ocean stratification or enhanced sea-ice cover. Both processes would result in a less efficient "biological pump", i.e. the biologically-driven drawdown of organic matter to the deep ocean and its subsequent degradation to $CO_2$ at the sea-floor, and hamper the release of deep-sequestered $CO_2$ to the atmosphere. E.g., Jaccard et al. (2005) for Ocean Drilling Program (ODP) Site 882 argued that maxima in export productivity during interglacials were the result of reduced stratification ruling out sea-ice influence for this site.

In contrast, the influence on past ocean-atmosphere $CO_2$ exchange via the "biological pump" might have been different for the Bering Sea, which today is marked by high marine productivity (e.g. Springer et al., 1996) and seasonal sea-ice formation (e.g. Niebauer et al., 1999). Paleoceanographic reconstructions in the Bering Sea show that surface water productivity was also reduced during the last glacial period, that it increased during the last deglaciation and remained high in the Holocene (Gorbarenko, 1996; Cook et al., 2005; Gorbarenko et al., 2005; Okada et al., 2005; Okazaki et al., 2005a; Brunelle et al., 2007; Itaki et al., 2009; Brunelle et al., 2010; Khim et al., 2010; Kim et al., 2011). This variability has been explained by a complex interplay of changes in sea surface temperatures (SST), sea-ice extent, inflow of Pacific surface

waters, and upper-ocean stratification (e.g. Katsuki and Takahashi, 2005; Brunelle et al., 2007, 2010; Kim et al., 2011). Knowledge of the extent and variability of sea-ice in the Bering Sea mainly comes from diatom and radiolarian assemblages (Cook et al., 2005; Katsuki and Takahashi, 2005; Tanaka and Takahashi, 2005). Although sea-ice formation is considered a key parameter for understanding stratification and water mass formation, and despite supposedly being an important transport mechanism for terrigenous material, geochemical or sedimentological studies assessing past terrigenous matter supply are rather absent for the Bering Sea. Only few studies regarding terrigenous fluxes in sea-ice influenced regions of the Pacific Ocean exist and so far have focused on the Okhotsk Sea (Sato et al., 2002; Nürnberg and Tiedemann, 2004; Nürnberg et al., 2011) and the Southern Ocean (Latimer and Filippelli, 2001). For the Okhotsk Sea Nürnberg and Tiedemann (2004) report nearly synchronous glacial-interglacial changes in biological and terrigenous fluxes arguing for a modulation by sea-ice processes related to changes in the Siberian atmospheric high-pressure cell. Some provenance studies involving sedimentological and geochemical characteristics of surface sediments are available for the northern and western (Lisitzin, 2002), as well as the southern Bering Sea (Gardner et al., 1980). However, downcore records on the compositional variability of terrigenous matter are missing.

Sea-ice formation in the Okhotsk Sea is related to the formation of N Pacific intermediate water masses, which today originate in the Okhotsk Sea (e.g. Yasuda, 1997). Here, sea-ice forms near the northwestern shelf region resulting in an increase in surface water density due to brine formation. It has been speculated that during glacials these water masses were better ventilated and/or subject to intensified formation (e.g. Keigwin and Jones, 1990; Gorbarenko, 1996; Keigwin, 1998). This led to the assumption that the Bering Sea had a stronger impact on glacial intermediate water mass formation, and that its source region shifted to the Okhotsk Sea only after the Last Glacial Maximum (Ohkushi et al., 2003; Tanaka and Takahashi, 2005).

Recent progress has been made in detecting millennial-scale climate variability in Bering Sea sediments (Cook et al., 2005; Gorbarenko et al., 2005; Okazaki et al., 2005a; Brunelle et al., 2010; Khim et al., 2010; Kim et al., 2011). Most of these studies are restricted to the last ∼70 kyr and focus on deglacial changes in the northern, southern, and southeastern Bering Sea. Together with studies from the NE Pacific (e.g. Hendy and Kennett, 2000) they imply that short episodes of increased marine productivity are connected with interstadials recorded in Greenland ice cores.

However, since the Bering Sea is characterized by a shallow-lying calcite saturation horizon (<500 m; Feely et al., 2002), most of the beforementioned studies making use of carbonate-based proxies are restricted to shallow shelf areas or morphological highs located in the northern, southern, and southeastern Bering Sea. Here, we present millennial-scale reconstructions of marine productivity and terrigenous matter supply for three sediment records recovered from Shirshov Ridge in the hitherto only poorly studied western Bering Sea. Results were derived from a suite of geochemical proxies and high-resolution core logging data covering the last ∼180,000 years, thereby extending existing records into Marine Isotope Stage (MIS) 6. From our results we propose scenarios for environmental changes during the last glacial-interglacial cycle.

## 3.2. Regional setting

The Bering Sea links the Pacific Ocean with the Arctic Ocean via the only shallow (∼50 m) Bering Strait. Morphologically, it is devided into the Aleutian Basin, and into a wide and shallow (0–200 m) continental shelf area in the northern and eastern part. The Aleutian Basin is a large and deep (>3500 m) abyssal plain containing two morphological highs, which provide better $CaCO_3$ preservation: the north-south striking Shirshov Ridge in the west, and Bowers Ridge in the south (Fig. 3.1).

Pacific surface waters, transported by the westward flowing Alaskan Stream, enter the Bering Sea through several passes within the Aleutian Island Arc (e.g. Takahashi, 2005). Inside the Bering Sea, a large-scale cyclonic surface circulation pattern develops with the Bering Slope Current (BSC) and the East Kamchatka Current (EKC) acting as eastern and western boundary currents, respectively (Fig. 3.1). Outflow occurs through the Bering Strait into the Arctic Ocean and through the Aleutian passes, mainly Kamchatka Strait, into the N Pacific (Stabeno et al., 1999). Only little is known about deep circulation in the Bering Sea. As it allows for deep water exchange, Stabeno et al. (1999) argue from oceanographic data of Reed et al. (1993) that deep water must flow northward and eastward from Kamchatka Strait with return outflow above 3,000 m water depth.

Oceanographic and climatic conditions in the Bering Sea are characterized by a strong seasonal variability of SST and sea-ice coverage that result from the interaction of the Siberian High and Aleutian Low pressure cells. The Arctic Oscillation (AO), Pacific Decadal Oscillation (PDO), and the Pacific–North American pattern (PNA) are reported to be related with decadal variations of both atmospheric pressure cells (Niebauer, 1988; Mantua et al., 1997; Niebauer, 1998; Overland et al., 1999, 2002). During winter, a strong Siberian High leads to advection of cold Arctic air masses and mainly northerly wind directions (Stabeno et al., 1999). This causes a significant cooling of the sea surface, sea-ice formation, as well as enhanced vertical mixing of the upper water column, thereby returning nutrients from the subsurface. In contrast, during summer, the reduced strength of both atmospheric pressure cells and enhanced insolation lead to a sea surface warming and melting of sea-ice, which results in a stratified mixed layer and an increase in marine productivity. As revealed by sediment trap studies, primary productivity is dominated by siliceous plankton organisms (mainly diatoms) during spring, whereas biological $CaCO_3$ fluxes (coccolithophores, planktonic foraminifera) occur during spring and late summer/early fall (e.g. Takahashi et al., 2002a). Highest annual production rates are associated with shelf areas and vary regionally between >200 and >800 gC $m^{-2}$ (Arzhanova et al., 1995; Springer et al., 1996; Stabeno et al., 1999). Available nutrients are reported to be often fully consumed during seasonal blooms (Niebauer et al., 1995).

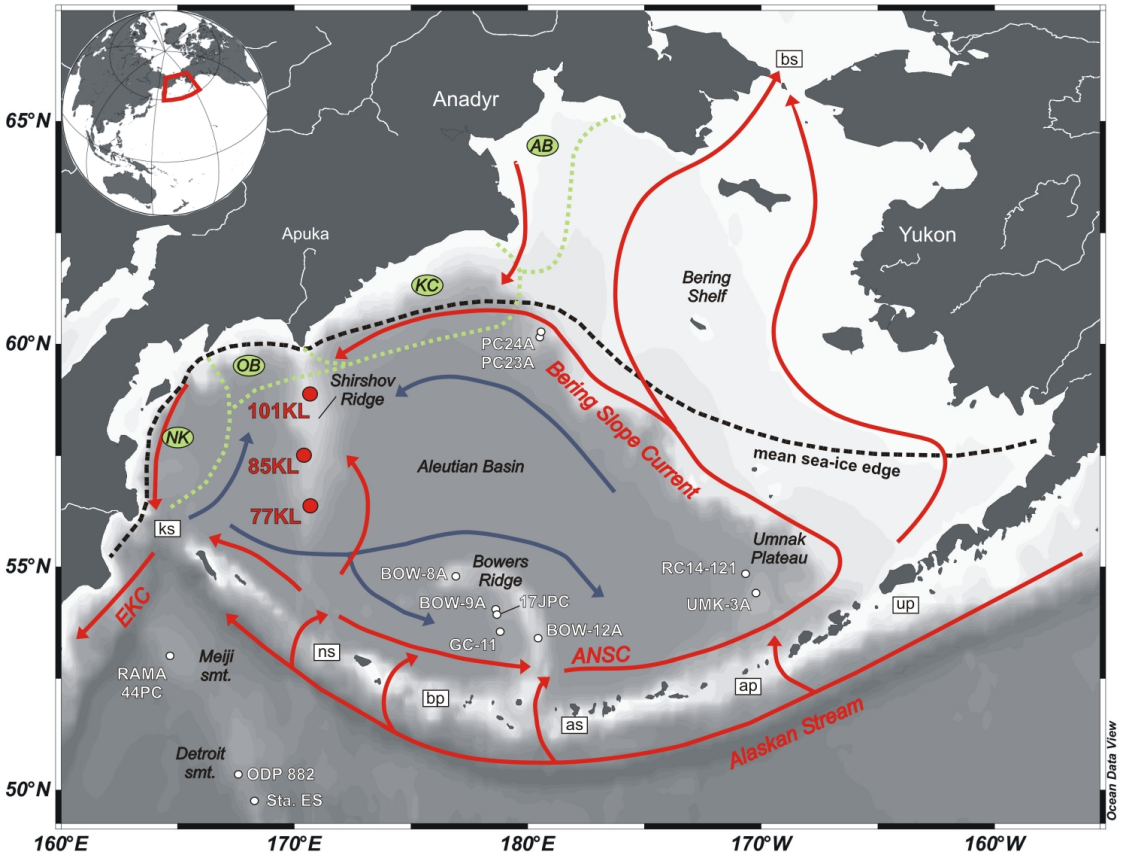


**Figure 3.1.:** Bathymetric map of the study area. Locations of sediment cores SO201-2-77KL, -85KL, and -101KL presented in this study are marked by red dots. Other reference records from the Bering Sea and subarctic NW Pacific referred to in this study are indicated by white dots. Meiji Seamount: RAMA44PC (Keigwin et al., 1992). Detroit Seamount: ODP Site 882 (Jaccard et al., 2005), KH99-3 Sta. ES (Narita et al., 2002). Bowers Ridge: GC-11 (Gorbarenko, 1996; Gorbarenko et al., 2005; Gorbarenko et al., 2010), KH99-3-BOW-8A and -BOW-12A (Katsuki and Takahashi, 2005; Okada et al., 2005; Tanaka and Takahashi, 2005), KH99-3-BOW-9A (Okada et al., 2005; Okazaki et al., 2005a; Tanaka and Takahashi, 2005), HLY02-02-17JPC (Brunelle et al., 2007, 2010). Umnak Plateau: KH99-3-UMK-3A (Okada et al., 2005; Okazaki et al., 2005a; Tanaka and Takahashi, 2005), RC14-121 (Cook et al., 2005). Northern slope: MR06-04-PC23A (Itaki et al., 2009; Khim et al., 2010; Kim et al., 2011), MR06-04-PC24A (Kim et al., 2011). Dashed black line indicates mean extent of sea-ice edge (March 15; 1973-1986; after Niebauer et al., 1999). Dotted greenish line shows mineralogical provinces of coarse silts (after Lisitzin, 2002), while surface and deep circulation patterns (after Stabeno et al., 1999) are indicated by red and dark blue arrows, respectively. Mineralogial provinces: NK = Northern Kamchatka, OB = Olyutorskii Bay, KC = Koryak Coast, AB = Anadyr Bay; Surface currents: ANSC = Aleutian North Slope Current, EKC = East Kamchatka Current; Straits: ks = Kamchatka Strait, ns = Near Strait, bp = Buldir Pass, as = Amchitka Strait, ap = Amukta Pass, up = Unimak Pass, bs = Bering Strait. This map was generated with "Online Map Creation" (https://sfb574.ifm-geomar.de/gmt-maps/) and "Ocean Data View" (Schlitzer, 2011).

Sea-ice formation begins during October/November on the northern Bering Sea continental shelf (Anadyr Bay, Bering Strait), reaching maximum distribution in March/April, subsequently disintegrating until July (Tomczak and Godfrey, 1994; Niebauer et al., 1999; Lisitzin, 2002). It takes place in shallow shelf areas, bays, and coastal areas. As in the Arctic, coastal polynyas play an important role for the build-up of sea-ice, and consequently for water mass ventilation due to brine rejection (Niebauer et al., 1999; Stabeno et al., 1999), which was proven by the presence of anthropogenic chlorofluorocarbons in bottom waters of the Aleutian Basin (Warner and Roden, 1995). Northerly winds blow sea-ice southwards where it melts in warmer waters.

## 3.3. Material and methods

### 3.3.1. Sediment cores

This study focuses on piston cores SO201-2-77KL, -85KL, and -101KL from Shirshov Ridge, western Bering Sea (Fig. 3.1; Tab. 3.1). Cores were recovered along a ∼280 km-long north-south transect from shallow to deep intermediate water levels during R/V Sonne cruise SO201-KALMAR Leg 2 in 2009 after extensive hydroacoustic sea-floor mapping (Dullo et al., 2009). Sediments are characterized as monotonous sequences of mainly clay- and silt-sized siliciclastic material, which are repeatedly interrupted by phases of diatomaceous ooze deposition.

**Table 3.1.:** Site information.

| Core | Latitude | Longitude | Depth (mbsl) | Recovery (m) |
|---|---|---|---|---|
| SO201-2-77KL | 56°19.83'N | 170°41.98'E | 2135 | 11.78 |
| SO201-2-85KL | 57°30.30'N | 170°24.77'E | 968 | 18.13 |
| SO201-2-101KL | 58°52.52'N | 170°41.45'E | 630 | 18.32 |

### 3.3.2. Age models

Age models of all three cores are based on a combination of different tools including high-resolution (non-destructive) core logging procedures (color b*, XRF scanning), benthic oxygen isotope stratigraphy, and magnetostratigraphy. Absolute age control is provided by accelerator mass spectrometry radiocarbon dating (AMS-$^{14}$C) (Fig. 3.2).

#### Core logging

Color reflectance measurements were carried out immediately after opening of the cores on the damp split core surface of the archive halves covered by clear plastic film. Therefore, a Minolta CM 508d hand-held spectrophotometer was used at 1 cm-spaced intervals (Dullo et al., 2009). Reflectance data was automatically converted by Spectramagic software into CIE L*, a* and b* color space (CIELAB).

The Avaatech X-ray fluorescence (XRF) core scanner at Alfred Wegener Institute for Polar and Marine Research, Bremerhaven, was used to record downcore changes in the elemental composition of the sediments. The principle of XRF is discussed in

Jenkins and De Vries (1970), while a technical description of the applied XRF logging system is given in Richter et al. (2006). Core scanning was performed on the scrape-cleaned, flattened split core surface covered with SPEX CertiPrep 3525 Ultralene foil (4 $\mu$m thick) to avoid desiccation and contamination. Each core segment was triple-scanned for analysis of elements aluminium (Al) through barium (Ba) at constant electric current (1 mA), but at different tube voltages and count times (10 kV, 10 s; 30 kV, 15 s; 50 kV, 30 s), using a sampling resolution of 1 cm. Results are considered semiquantitative and to reflect relative downcore variability in elemental composition only (Richter et al., 2006; Tjallingii et al., 2007) and are either given as count rates in counts per second (cps) or as log-ratios (natural logarithm) of element count rates of two different elements.

### Stable oxygen isotopes

For oxygen isotope stratigraphy we used endobenthic foraminifer species *Uvigerina peregrina* and *Uvigerina auberiana*, since *Uvigerina* $\delta^{18}$O values are reported to be in equilibrium with seawater (Shackleton and Hall, 1984). Stable oxygen isotopes were measured every 5 cm on 2–3 specimens of *U. peregrina*, or, if not present, of *U. auberiana*, collected from the 315–355 $\mu$m size fraction of the washed sample. In case of low foraminiferal abundances, this range was extended to 250–400 $\mu$m. Size-effects and inter-species offsets in $\delta^{18}$O were not observed. Measurements were performed at GEOMAR, Kiel, using a Thermo Finnigan MAT253 mass spectrometer coupled with a Thermo Scientific Kiel IV Carbonate device. Results were referenced to the NBS19 standard and calibrated to the VPDB scale. Long-term precision (N >1000 samples) for $\delta^{18}$O of the used internal "Bremen standard" (Solnhofen limestone) was $\pm$0.06‰ PDB. Unfortunately, in core 77KL benthic foraminifera were only preserved until 865 cm core depth.

### Paleomagnetics

For core 85KL, the magnetic minerals responsible for the natural remanent magnetization of sediments (NRM) were determined based on remanent saturation magnetization, the saturation magnetization in magnetic-hysteresis parameters, and differential thermomagnetic analyses using a Faraday magnetic balance and a coercive spectrometer at Kazan University, Russia (Burov and Yasonov, 1979; Yasonov et al., 1998). The natural remanent magnetization module (NRM) and direction were measured with a AGICO JR-5A spinner magnetometer after the stepwise demagnetization of a reference sample. Magnetic cleaning by an alternating magnetic field using an amplitude of 10 mT proved optimal for recognizing the characteristic component of magnetization (ChRM). Anhysteretic remanent magnetization (ARM) was generated in the preliminarily demagnetized samples using a AGICO AMU-1A anhysteretic magnetizer under a constant field of 0.05 mT and a maximum alternating field of 100 mT. Relative paleointensity of the magnetic field (RPI) was then calculated by normalization of ChRM to ARM. In addition, we determined scalar petromagnetic properties (SPP; Enkin et al., 2007; Malakhov et al., 2009).

### AMS radiocarbon dating

Absolute age control was provided by AMS-$^{14}$C dating of planktonic foraminifera in the uppermost core sections. We used monospecific samples of subpolar to polar species *Neogloboquadrina pachyderma* (sin.) collected from the 125–250 $\mu$m size fraction. For one sample, insufficient abundances of this species were compensated by selection of additional tests from planktonic species *Globigerina bulloides* from the same size fraction. Samples were dated at the Leibniz-Laboratory for Radiometric Dating and Isotope Research, Kiel, and at the National Ocean Science Accelerator Mass Spectrometry Facility (NOSAMS) at Woods Hole Oceanographic Institution (WHOI), U.S.A. The Calib Rev 6.1.0 software (Stuiver and Reimer, 1993) was used to convert radiocarbon to calendar ages, applying the IntCal09 calibration (Reimer et al., 2009) and a reservoir correction of 700 years. AMS-$^{14}$C dating results are presented in Max et al. (in review).

### Chronostratigraphic approach

Due to the remarkable correspondence, the chronostratigraphy of core 85KL is primarily based on the graphic correlation between the color b* record and the Dansgaard-Oeschger climate variability registered in the NGRIP $\delta^{18}$O ice core record (NGRIP members, 2004; GICC05 timescale, Rasmussen et al., 2006) (Fig. 3.2). The stratigraphy of core 85KL is then transferred via intercore correlations (color b*, XRF Ca/Ti log-ratios) to cores 77KL and 101KL showing a similar variability and correspondence to the NGRIP record. This approach is verified by AMS-$^{14}$C dating results from all cores. Several studies report two prominent carbonate maxima in records from the NW Pacific (Keigwin et al., 1992; Keigwin, 1998; Gorbarenko et al., 2002a; Gorbarenko et al., 2005; Caissie et al., 2010), corresponding to the Bølling-Allerød warm phase (B/A) and the early Holocene. Our dating results, which were obtained from samples showing maxima in foraminiferal abundance and $CaCO_3$ content, are consistent with age models from these studies. A detailled discussion on the stratigraphic framework of all cores for the last 20 kyr is presented elsewhere (Max et al., in review).

For the time interval >20 ka BP, our chronostratigraphic approach is supported and extended by correlating our benthic $\delta^{18}$O records to the global reference stack LR04 (Lisiecki and Raymo, 2005), which is also used to identify Marine Isotope Stages (MIS) 1–6. Further support comes from paleomagnetic measurements in core 85KL, specifically from comparison of RPI with the PISO-1500 geomagnetic paleointensity stack (Channell et al., 2009) and of SPP (not shown) with MIS-boundaries of the LR04 stack. Core logging data (color b*, XRF Ca/Ti log-ratios) further served for intercore correlations.

Age models of all cores covering the last ∼180 kyr are shown in Fig. 3.2 and age-depth points for cores 77KL, 85KL, and 101KL are given in the supplementary information. For cores 85KL and 101KL, stratigraphic interpretation of benthic $\delta^{18}$O values was difficult during Termination II (135–125 ka BP). Both cores are bioturbated within core intervals 1288–1300 cm (85KL) and 1590–1632 cm (101KL), respectively. In core 85KL, bioturbation occurs together with a relatively sharp change in sediment composition indicating an erosional contact and potential hiatus at ∼1290 cm core depth.

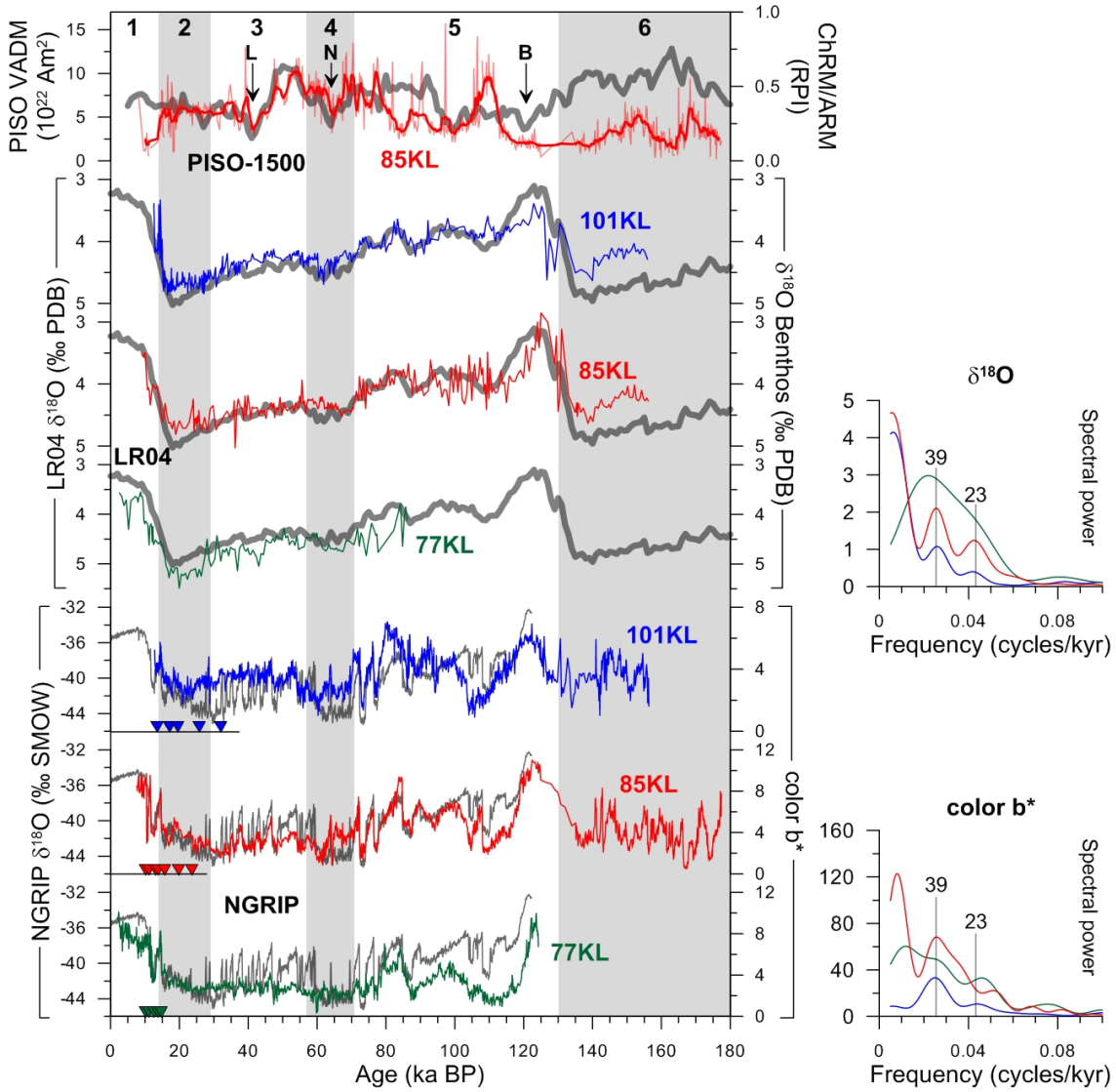


**Figure 3.2.:** Stratigraphy of cores SO201-2-77KL (green lines), -85-KL (red lines), and -101-KL (blue lines). Age models are primarily based on the graphic correlation between records of color b* (coloured lines) and oxygen isotopes from the NGRIP ice core (underlying grey lines; NGRIP members, 2004; GICC05 timescale, Rasmussen et al., 2006). Further age control comes from benthic oxygen isotope stratigraphy ($\delta^{18}$O) of *U. peregrina* and *U. auberiana* (coloured lines) related to the global benthic reference stack LR04 (underlying thick grey lines; Lisiecki and Raymo, 2005). In addition, for core 85KL, a record of relative paleointensity (RPI; red line; a 5-point running average is shown as thick red line to smooth the record) was compared to the paleomagnetic reference record PISO-1500 (underlying thick grey line; Channell et al., 2009). The Laschamp (L), Norwegian-Greenland Sea (N), and Blake (B) paleomagnetic events are indicated. Absolute age control is provided by AMS-$^{14}$C dating (coloured triangles). Intercore correlations were conducted using color b* records and XRF-based records of Ca/Ti log-ratios (not shown). Spectral analysis of benthic $\delta^{18}$O and color b* records (right hand inlets) performed in the time domain, reveal dominant cyclicities at 39 kyr and 23 kyr, close to Earth's orbital cycles of obliquity and precession, respectively.

Since orbital tuning to Earth's orbital parameters turned out inapplicable on the generated timescales, we tested our age models via spectral analysis in the time domain of the color b* and benthic $\delta^{18}$O records to detect orbital frequencies (Fig. 3.2). Spectral analysis was performed using the AnalySeries 2.0 software (Paillard et al., 1996). Despite the shortness of the time span covered by our cores with respect to orbital-scale changes, we found dominant cyclicities of ∼23 and ∼39 kyr, which are close to orbital precession (21 kyr) and obliquity cycles (41 kyr), suggesting that our age models are correct.

### 3.3.3. Sedimentation and accumulation rates

A reliable chronostratigraphy is the basis for accurate calculations of linear sedimentation rates (LSR, in cm kyr$^{-1}$) and bulk accumulation rates (AR$_{Bulk}$, in g cm$^{-2}$ kyr$^{-1}$). LSR were calculated between age control points as the thickness of a sediment interval devided by the time interval of its deposition, while AR$_{Bulk}$ were calculated as the product of LSR and the dry bulk density (DBD, in g cm$^{-3}$) (van Andel et al., 1975), which was determined each 5 cm in all cores:

$$AR_{Bulk} = DBD \times LSR \tag{3.1}$$

Records of LSR and AR$_{Bulk}$ for all cores are shown in Fig. 3.3. All three cores from Shirshov Ridge are characterized by LSR (AR$_{Bulk}$) ranging between ∼1 and 33 cm kyr$^{-1}$ (∼1–30 g cm$^{-2}$ kyr$^{-1}$), with average values of 10–15 cm kyr$^{-1}$ (7–15 g cm$^{-2}$ kyr$^{-1}$) (Tab. 3.2). These values allow a centennial to millennial time-resolution for our reconstructions. Absolute values of LSR (AR$_{Bulk}$) as well as their variability increase from core 77KL in the south towards core 101KL in the north. In general, LSR (AR$_{Bulk}$) are higher during cold stages (MIS4, MIS5b/d, MIS6) than during warm stages (MIS1, MIS3, MIS5a/c/e), but highest during Termination I (20–10 ka BP). In contrast, Termination II, which is only preserved in cores 85KL and 101KL, is characterized by low LSR of <4 cm kyr$^{-1}$. Core 85KL also shows short-lived maxima during MIS2 and MIS3.

**Table 3.2.:** Ranges and variability of linear sedimentation rates (LSR, in cm kyr$^{-1}$) and bulk accumulation rates (AR$_{Bulk}$, in g cm$^{-2}$ kyr$^{-1}$) at the site locations.

| | SO201-2-77KL | | SO201-2-85KL | | SO201-2-101KL | |
|---|---|---|---|---|---|---|
| | LSR | AR$_{Bulk}$ | LSR | AR$_{Bulk}$ | LSR | AR$_{Bulk}$ |
| Average | 10.7 | 7.2 | 12.8 | 11.4 | 15.4 | 14.8 |
| Standard deviation | 4.6 | 3.0 | 4.5 | 4.3 | 6.2 | 5.4 |
| Maximum | 28.5 | 29.1 | 23.4 | 21.0 | 32.6 | 29.8 |
| Minimum | 6.0 | 2.8 | 0.6 | 0.6 | 3.0 | 3.5 |

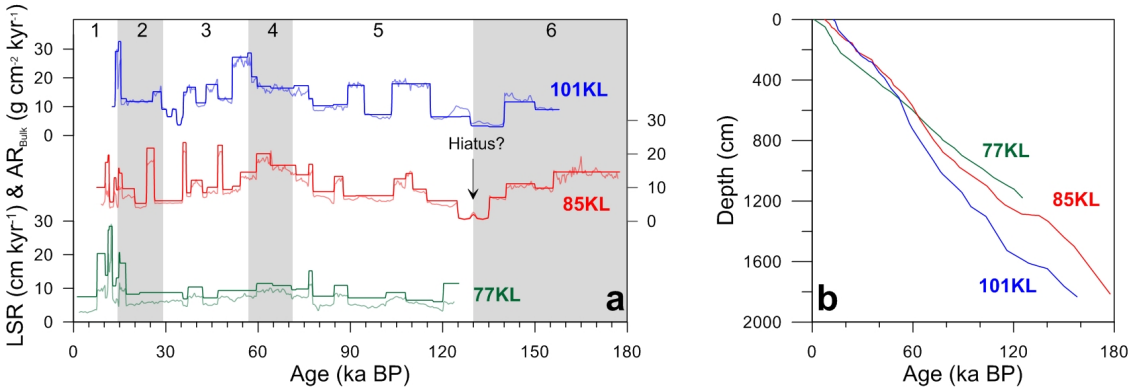


**Figure 3.3.:** (a) Linear sedimentation rates (LSR; coloured lines) and bulk accumulation rates ($AR_{Bulk}$; transparent coloured lines), as well as age-depth-relationships (b) of sediment cores SO201-2-77KL (green), -85KL (red), and -101KL (blue) from Shirshov Ridge. LSR and $AR_{Bulk}$ are plotted on the same scale. Top numbers indicate Marine Isotope Stages (MIS). LSR and $AR_{Bulk}$ increase towards northern core locations and reveal maxima during MIS4, MIS6, as well as during Termination I. Core 85KL also reveals short-termed maxima during MIS3. Average LSR and $AR_{Bulk}$ lie between 10–15 cm $kyr^{-1}$ and 7–15 g $cm^{-2}$ $kyr^{-1}$, respectively, with strongest variability being recorded in core 101KL. Note extremely reduced values during Termination II in cores 85KL and 101KL, potentially indicative of a hiatus in core 85KL.

Top ages of the sediment cores were not validated by absolute age control due to insufficient datable material. Consequently, Holocene sediments are either subject to low LSR (77KL) or missing (85KL, 101KL). We do not consider this to be an artifact of the applied piston coring technique, since piston cores are rather subject to oversampling (stretching) of the sediments (Szeremeta et al., 2004). Moreover, potential sediment loss during coring should have been prevented by the piston. Although, we can not exclude sediment loss during core handling on deck, we favorize the view that the low Holocene LSR are the result of a general change in sedimentation favoring the deposition of highly porous diatomaceous ooze, which is more easily eroded by bottom currents.

### 3.3.4. Assessment of changes in marine productivity

Past changes in marine productivity are approximated from applying a suite of different proxies: total organic carbon (TOC), $CaCO_3$, biogenic opal, biogenic barium ($Ba_{excess}$), and evaluation of various XRF logging data. This multi-proxy approach was necessary due to specific restrictions of the respective proxies. TOC preservation in sediments is highly debated (e.g. Hartnett et al., 1998; Ganeshram et al., 1999; Thunell et al., 2000; Hedges et al., 2001) as it is, amongst others, influenced by oxidation processes in combination with the bottom water ventilation state (De La Rocha, 2007). Moreover, its source can be of marine and terrigenous origin. The preservation of $CaCO_3$ in the subarctic N Pacific is limited by the shallow lysocline. Accordingly, contents of $CaCO_3$ rather reflect changes in the bottom water calcite saturation state than biological $CaCO_3$ fluxes (e.g. Jaccard et al., 2005; Gebhardt et al., 2008). Opal dissolves during settling to the sea-floor due to the ocean's undersaturation with respect to silicic acid, but its preservation is independent from bottom water oxygenation. Biogenic opal is most often used in reconstructions of marine productivity in the N Pacific due

to the observation that opal-rich sediments are linked to biogenic silica production (e.g. Nelson et al., 1995; Ragueneau et al., 2000; Pondaven et al., 2000). Barium, which is present within the sediments as barite ($BaSO_4$) is used in several studies to reconstruct paleoproductivity (e.g. Dymond et al., 1992; Francois et al., 1995; Dymond and Collier, 1996; Gingele et al., 1999), although evidence for direct biogenic barite formation does not exist. Barite particles occur in areas of high new production (Dehairs et al., 1991) and in surface waters are associated with siliceous debris (Bishop, 1988), while in deeper waters they occur as free particles (Dehairs et al., 1990). Moreover, barite precipitation requires microenvironments like decaying organic matter (Chow and Goldberg, 1960) and seems to be coupled to the marine silica cycle.

Accumulation rates (AR) in contrast to proxy concentrations are unaffected by depositional dilution or enrichment. However, if proxy concentrations in marine sediment cores are low or vary only little, AR variability is reported to mainly reflect LSR (Middelburg et al., 1997). This situation applied to our sediment cores. Accordingly, in this study we report proxy concentrations rather than quantified flux rates and treat the respective records as qualitative.

### TOC and $CaCO_3$

Measurement of total carbon (TC), TOC, and total nitrogen (TN) were performed using the Carlo Erba CNS analyzer model NA1500 at GEOMAR, Kiel. Freeze-dried, ground and homogenized bulk sediment samples of 20 mg were used to measure TC and TN, while TOC was measured on previously decalcified samples using 0.25 M hydrochloric acid following procedures described in Verardo et al. (1990). Precision, determined for an internal standard, was <3% relative standard deviation (RSD, $2\sigma$) for TC, TOC and TN, while reproducibility of the TOC- and TN measurements were $\pm$0.03 wt.% and $\pm$0.01 wt.%, respectively. $CaCO_3$ contents were calculated as:

$$CaCO_3 = 8.333 \times (TC - TOC) \tag{3.2}$$

The atomic ratio of TOC to TN, corrected for inorganic nitrogen compounds ([C/N]a), provides a geochemical tool to distinguish between marine and terrigenous sources of TOC. The Redfield ratio (Redfield et al., 1963) translates the [C/N]a ratio of marine organic matter to a value between 6 and 7. Typical terrigenous values lie between 20–200 (Hedges et al., 1986). We applied a correction for inorganic nitrogen, usually clay-bound inorganic ammonium (Müller, 1977), based on a linear relationship between TOC and TN (after Goñi et al., 1998).

### Biogenic opal

Measurements of biogenic opal followed the approach of Müller and Schneider (1993), who established an automated leaching method making use of molybdate-blue spectrophotometry. Silica was extracted from 20 mg of freeze-dried, hand-ground and homogenized bulk sediment samples using 100 ml NaOH (1 M) at 85°C for ~45 min. Working solutions made up of silicon tetrachloride served as calibration standards. Results are evaluated applying the procedure of DeMaster (1981). Replicate measurements showed a reproducibility of 1–2 wt.%.

### Biogenic barium ($Ba_{excess}$)

Concentrations of major (Al, Ti, Fe, K) and trace elements (Ba) were quantitatively measured at the Institute of Geosciences, Kiel University, using a Philips PW1480 XRF spectrometer. Samples were chosen from selected depths based on evaluation of the qualitative XRF logging data. Analyses were performed using 0.6 g of freeze-dried, ground bulk sediment without determination of LOI (loss on ignition) following standard procedures. Analytical precision ($2\sigma$, N = 15) was determined for the BHVO standard, which was <2% RSD for the major elements and ±30 ppm for Ba.

Results for barium ($Ba_{total}$) are the sum of biogenic ($Ba_{excess}$) and nonbiogenic portions of Ba. $Ba_{excess}$ was therefore calculated via concentrations of Al by estimating the aluminosilicate contribution of Ba considering the global average Ba/Al ratio for pelitic rocks ($Ba/Al_{aluminosilicate}$) of 0.0065 g $g^{-1}$ (Wedepohl, 1971):

$$Ba_{excess} = Ba_{total} - Al \times Ba/Al_{aluminosilicate} \tag{3.3}$$

$Ba_{excess}$ was subsequently used to assess new production ($P_{New}$) by applying the relationship of Nürnberg (1995a), as well as annual primary production (PP) using the equation of Eppley and Peterson (1979):

$$PP = 20 \times \sqrt{P_{New}} \tag{3.4}$$

### XRF logging data (Br, Ca/Ti, Si/Al, Ba/Al)

Temporal variability of several logging data were in good qualitative agreement with the bulk geochemical analyses (Tab. 3.3). Count rates of Br compare with contents of TOC. This supports the assumption of Ziegler et al. (2008), who suggested a linear relationship between biophilic halogen bromine in case TOC input is dominated by marine organic matter. Records of XRF Ca/Ti log-ratios show a temporal evolution similar to the $CaCO_3$ records. This is explained by assuming a detrital origin of Ti and Al. Normalization of XRF-derived Ca to Ti and/or Al abundances has been applied before (Jaccard et al., 2005) and is thought to reflect biogenic $CaCO_3$ contents within the sediment. The XRF signals for Al were better than for Ti and were subsequently used for normalization. However, we favored Ca/Ti over Ca/Al log-ratios due to better correlation to $CaCO_3$. Although opal contents were close to analytical precision for most samples from the last glaciation, good correlations to records of XRF Si/Al log-ratios were observed. We found similar relationships between opal and color b* records, but with smaller linear correlation coefficients ($R^2$). These results are in accordance with other observations considering a connection between Si/Al ratios and biogenic opal contents (McDonald et al., 1999). Finally, we found a significant relationship between $Ba_{excess}$ and XRF Ba/Al ratios in core 77KL, consistent with the finding of Jaccard et al. (2005).

**Table 3.3.:** Correlations between geochemical bulk analyses and XRF logging data.

| | SO201-2-77KL | | SO201-2-85KL | | SO201-2-101KL | |
|---|---|---|---|---|---|---|
| | N | $R^2$ | N | $R^2$ | N | $R^2$ |
| TOC (wt.%) vs. Br (cps) | 222 | 0.57 | 267 | 0.74 | 254 | 0.35 |
| $CaCO_3$ (wt.%) vs. Ca/Ti log-ratio | 211 | 0.63 | 251 | 0.65 | 254 | 0.07 |
| Opal (wt.%) vs. Si/Al log-ratio | 172 | 0.73 | 132 | 0.63 | 135 | 0.04 |
| $Ba_{excess}$ (ppm) vs. Ba/Al log-ratio | 35 | 0.74 | 36 | 0.28 | 35 | 0.09 |
| [Al] ($\mu$mol $g^{-1}$) vs. Al (cps) | 35 | 0.50 | 36 | 0.22 | 35 | 0.19 |
| [Fe] ($\mu$mol $g^{-1}$) vs. Fe (cps) | 35 | 0.49 | 36 | 0.56 | 35 | 0.52 |
| [Ti] ($\mu$mol $g^{-1}$) vs. Ti (cps) | 35 | 0.59 | 36 | 0.40 | 35 | 0.51 |

Correlations are considered significant for cores 77KL and 85KL, whereas $R^2$ values calculated for core 101KL were <0.35, indicating absent relationships between the logging data and the quantitative analyses for this core. Since correlations significantly vary between both, the respective sites and the respective proxies, logging data were not used to apply calibration functions in order to enable absolute cm-scale reconstructions, but are shown together with the quantitative analyses.

## 3.3.5. Assessment of changes in terrigenous matter supply

Changes in the supply of terrigenous matter were approximated from a set of sedimentological and geochemical proxies together with XRF and magnetic susceptibility logging data. The report of proxy concentrations instead of flux rates is favored according to the arguments stated earlier.

### Coarse material, magnetic susceptibility, and amount of siliciclastics

The proportions of coarse (>63 $\mu$m) and fine (<63 $\mu$m) material (in wt.% dry weight) were determined every 5 cm by weighing freeze-dried samples before and after wet-sieving through a 63 $\mu$m mesh. Magnetic susceptibility was determined using a GEOTEK Multi-Sensor Core Logger in combination with a Bartington MS2C sensor loop each 1 cm on the unopened core segments directly after recovery (Dullo et al., 2009). In general, sediments from Shirshov Ridge exhibit very low (<15 SI units) magnetic susceptibility values, rather typical for oceanic pelagic environments. Accordingly, we did not find significant linear correlations between magnetic susceptibility data and amounts of coarse material ($R^2$ <0.13), which indicates that magnetizable minerals in sediment cores from Shirshov Ridge are rare and are mainly bound to the fine fractions.

Relative amounts of siliciclastics provide a more accurate way to assess changes in terrigenous matter supply. We calculated percentages of siliciclastic material by considering the bulk sediment to be composed of siliciclastics, $CaCO_3$, TOC, and biogenic opal, and thus by subtracting their relative amounts from a total of 100 wt.%. As contents of TN were generally <0.3 wt.%, TN is not considered in the calculation:

$$\%siliciclastics = 100\% - (CaCO_3 + TOC + Opal) \tag{3.5}$$

In a second approach, relative contents of terrigenous matter were calculated by normalizing bulk sedimentary Al and Ti concentrations to the concentration of these elements in average continental crust ([Al]=3117 $\mu$mol g$^{-1}$, [Ti]=112.8 $\mu$mol g$^{-1}$; Taylor and McLennan, 1995). Both normalizations resulted in similar temporal trends, but Al-normalized results, which were on average 4-6% higher than Ti-normalized results, better compared to the records of %siliciclastics.

#### Lithogenous elements

Metal geochemistry of lithogenous elements serve as proxies for continental input (e.g. Duce and Tindale, 1991; Bareille et al., 1994), dust-supply via grain-size (e.g. Boyle, 1983a; Calvert and Fontugne, 2001), terrestrial runoff (e.g. Schmitz, 1987; Jansen et al., 1998), or mineralogical variations (e.g. Schneider et al., 1997; Yarincik et al., 2000). Accordingly, we used our XRF bulk analyses of elements Al, Ti, Fe, and K and their respective ratios to reconstruct temporal changes in their supply and to identify sources of terrigenous matter. Linear relationships between bulk analyses of lithogenous elements and respective XRF logging data were found (Tab. 3.3). Although being considered insignificant, similar temporal trends clearly exist. Hence, we did not establish calibration functions, but show the XRF logging data for comparison.

## 3.4. Results and discussion

### 3.4.1. Changes in marine productivity

All Shirshov Ridge cores are characterized by a similar variability of the parameters reflecting paleoproductivity, but along the core transect show trends of increasing concentrations towards the southernmost site (77KL). Results for TOC, opal, $CaCO_3$, as well as their approximating logging data are shown in Fig. 3.4. In general, proxy concentrations and their variability remain low during the last glacial period and during MIS6, while increases are recorded during interglacials (MIS1, MIS5e), stages MIS5a and MIS5c, and during Termination I, with maximum amplitudes in core 77KL. Core 101KL exhibits overall lowest proxy concentrations and amplitude variations (Tab. 3.4). At all sites glacial concentrations hardly exceed ∼1 wt.% for TOC, ∼3 wt.% for opal, and ∼2 wt.% for $CaCO_3$. Stages MIS5a and MIS5c, as well as abruptly occurring events recorded during MIS3–6, are characterized by ∼1 to 3-times higher concentrations at most. Changes during MIS5e, Termination I and the Holocene (since 11.7 ka BP) are more pronounced with TOC, opal, and $CaCO_3$ varying up to ∼2 wt.%, ∼50 wt.%, and ∼30 wt.%, respectively. Notably, strongest maxima in opal contents are recorded during MIS5e and the Holocene at Site 77KL, while strongest $CaCO_3$ maxima are reached during the Bølling-Allerød (B/A; 14.7–12.9 ka BP, Blockley et al., 2012) and Preboreal (PB; ∼11.7–11.0 ka BP) phases.

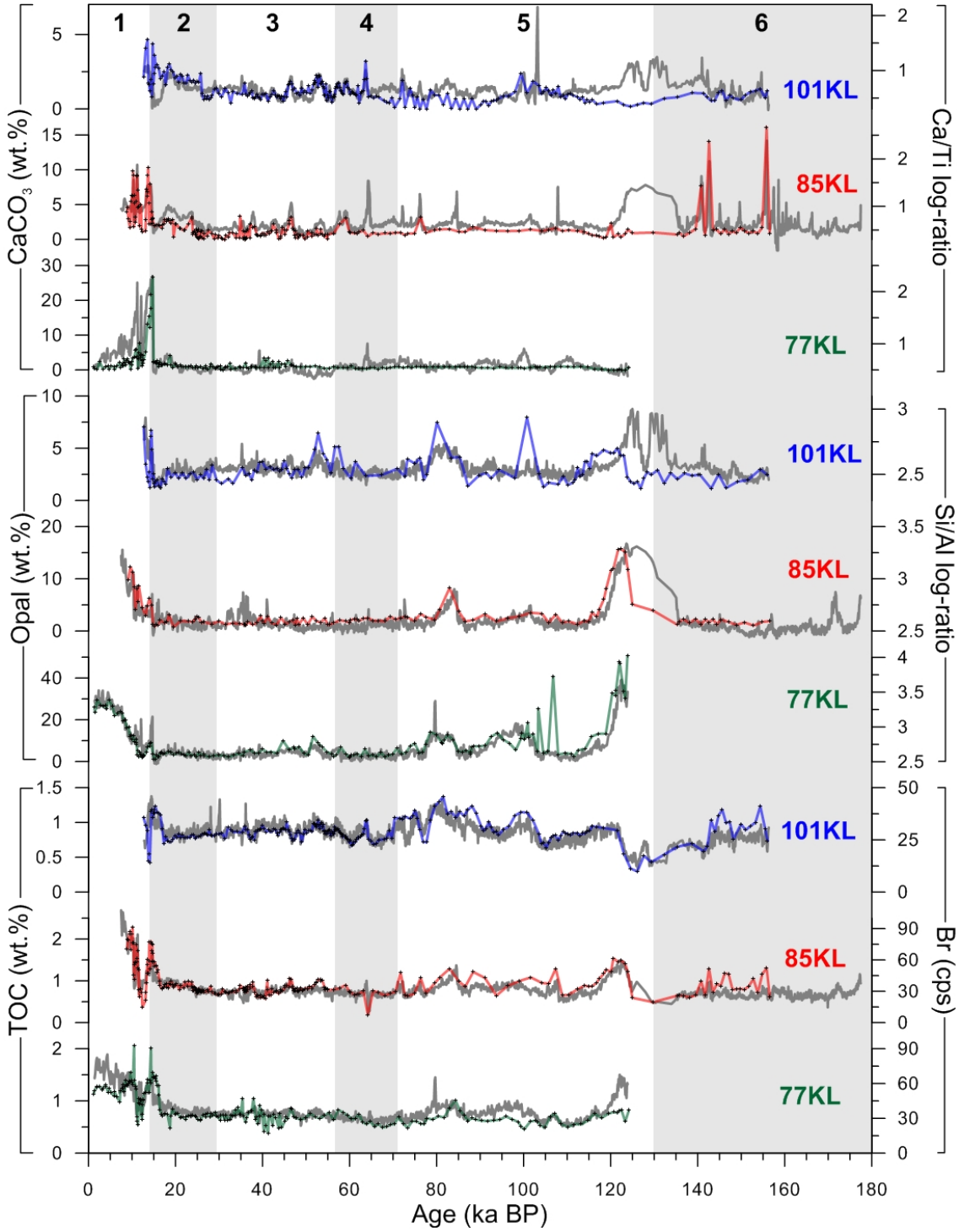


**Figure 3.4.:** Concentrations of TOC, opal, and $CaCO_3$ (coloured lines), in comparison to their XRF-based Br-intensity (in cps), and Si/Al and Ca/Ti log-ratio records (underlying grey lines) for cores SO201-2-77KL (green lines), -85KL (red lines), and -101KL (blue lines) from Shirshov Ridge. Shaded horizontal bars mark Marine Isotope Stages (MIS) 2, 4, and 6. Black numbers on top indicate MIS1-6 (after Lisiecki and Raymo, 2005).

**Table 3.4.:** Statistics of parameters approximating marine productivity.

| | SO201-2-77KL | | SO201-2-85KL | | SO201-2-101KL | |
|---|---|---|---|---|---|---|
| | Avg. | StDev. | Avg. | StDev. | Avg. | StDev. |
| TOC (wt.%) | 0.85 | 0.30 | 0.96 | 0.36 | 0.88 | 0.16 |
| [C/N]a | 13.0 | 2.9 | 11.9 | 1.6 | 12.4 | 1.6 |
| Opal (wt.%) | 9.5 | 9.7 | 3.3 | 3.2 | 2.9 | 1.3 |
| $CaCO_3$ (wt.%) | 1.9 | 3.2 | 1.9 | 2.2 | 1.2 | 0.7 |
| $Ba_{excess}$[(1)] (ppm) | 733 | 330 | 436 | 141 | 260 | 85 |
| $P_{New}$[(2)] (gC $m^{-2}$ $yr^{-1}$) | 50.6 | 47.5 | 35.5 | 21.4 | 29.3 | 21.4 |
| PP[(3)] (gC $m^{-2}$ $yr^{-1}$) | 131.9 | 54.2 | 114.1 | 34.9 | 101.3 | 39.0 |

[(1)]via Al using $Ba/Al_{aluminosilicate} = 0.0065$ g $g^{-1}$ (Wedepohl, 1971)
[(2)]after Nürnberg (1995a)
[(3)]after Eppley and Peterson (1979)

The evolution of productivity changes during Termination I is characterized by synchronous increases in all proxies during the B/A starting at ∼14.7 ka BP, which are preceded by early deglacial minima between ∼18–15 ka BP. This interval is considered to correspond to the Heinrich Stadial 1 (H1) recorded in the N Atlantic (18.0–14.7 ka BP, Sarnthein et al., 2001). During the interval of 12.9–11.7 ka BP, representing the N Atlantic analog of the Younger Dryas cold phase (YD; N Atlantic timing after Blockley et al., 2012), all proxies almost decrease to glacial values. Subsequent to the YD, the PB interval is characterized by synchronous increases in all cores and all proxies, their extent being comparable to those recorded during the B/A. Concentrations of all proxies (except $CaCO_3$) during the following Holocene are higher than during the glacial period. The described deglacial evolution, as well as the range of proxy concentrations during the last glacial-interglacial cycle, resemble that described for the Bering Sea (Gorbarenko, 1996; Cook et al., 2005; Gorbarenko et al., 2005; Okazaki et al., 2005a; Brunelle et al., 2007; Itaki et al., 2009; Brunelle et al., 2010; Caissie et al., 2010; Gorbarenko et al., 2010; Khim et al., 2010; Kim et al., 2011), the Okhotsk Sea (Ternois et al., 2001; Gorbarenko et al., 2002b; Narita et al., 2002; Nürnberg and Tiedemann, 2004), as well as the NW Pacific (Keigwin et al., 1992; Narita et al., 2002) and NE Pacific (McDonald et al., 1999).

TOC contents commonly lie <1 wt.% (Tab. 3.4) and are highest during the B/A and PB where they reach maximum values of ∼2.0 wt.% in core 85KL (Fig. 3.4). Stages MIS5a, MIS5c, and MIS5e are characterized by up to 0.5 wt.% higher-than-glacial values. TOC appears to lead the deglacial increase of the other productivity proxies by ∼2,000 years, starting at ∼17.3 ka BP at Site 101KL and at ∼16.5 ka BP at sites 77KL and 85KL. Similar reports of a deglacial rise in TOC considerably leading that of $CaCO_3$ come from Bowers Ridge core GC-11 (Gorbarenko, 1996) starting at ∼17.5 ka BP, core UMK-3A from Umnak Plateau (Okazaki et al., 2005a) starting ∼16.7 ka BP, and core PC23A from the northern slope of the Aleutian Basin (Kim et al., 2011) starting at ∼18.4 ka BP (core locations are indicated in Fig. 3.1). Although records of TOC and XRF-derived records of Br correspond well in our cores (Fig. 3.3; Tab. 3.3), Br does not follow this deglacial TOC increase, suggesting a changing source of TOC. Corrected atomic [C/N]a ratios in our cores mainly vary between 10 and 15 (Fig. 3.5a), indicating that TOC input contains mainly marine, but considerable amounts of terrestrial matter. Strongest [C/N]a variability is observed at Site 77KL, while indeed all sites record a rise of [C/N]a ratios during the last deglaciation, indicating enhanced supply of terrestrial matter during that time. Lowest [C/N]a variability is recorded in cores 85KL and 101KL during most of the last glacial-interglacial cycle

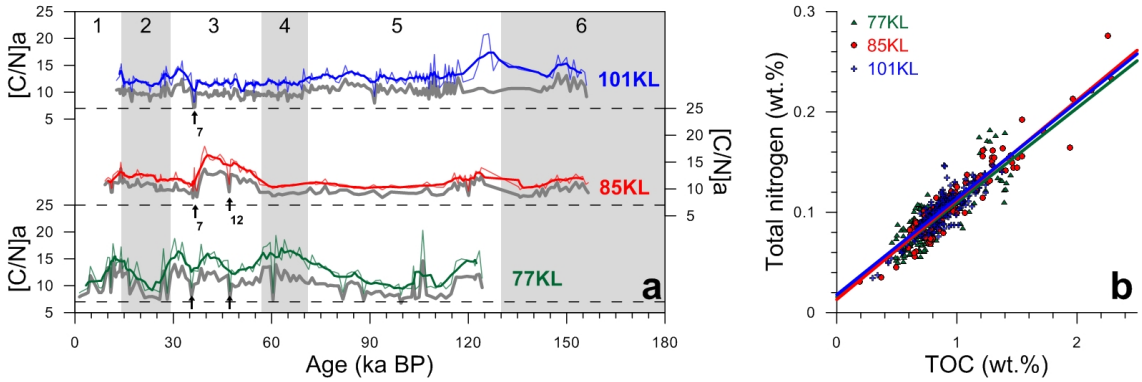


**Figure 3.5.:** (a) Atomic [C/N]a ratios corrected for inorganic nitrogen compounds (coloured lines) as well as uncorrected [C/N]a ratios (underlying grey lines) for cores SO201-2-77KL (green line), -85KL (red line), and -101KL (blue line). Corrected [C/N]a ratios are smoothed by a 5-point-running average. Dashed horizontal lines mark a [C/N]a ratio of 7. Higher values indicate a stronger contribution of terrestrial-derived organic matter. Note occurrence of pronounced minima during MIS3, possibly reflecting D/O-events 7 and 12 (arrows). (b) A linear regression between TOC and TN values was conducted for each core and produced an intercept-value reflecting the (assumed constant) amount of inorganic nitrogen. Subtracting this value from the TN contents resulted in organic nitrogen portions which were then used to calculate [C/N]a ratios. Respective linear correlation equations are summarized in Tab. 3.5.

and MIS6 around a value of ∼12. TN concentrations were corrected for contents of inorganic nitrogen clearly showing linear relationships between TOC and TN (Fig. 3.5b; Tab. 3.5). Values for inorganic nitrogen ranged between 0.013 and 0.018 wt.%. Since average concentrations of TN varied at ∼0.10±0.03 wt.% ($1\sigma$), sediments from Shirshov Ridge contain a considerable amount of inorganic nitrogen compounds. Consequently, corrected [C/N]a ratios are by up to 4 units higher than uncorrected ratios (Fig. 3.5a).

For the eastern and southern part of the Aleutian Basin, Nakatsuka et al. (1995) report lower [C/N] ratios varying between 6 and 9 during the last 40 kyr. Similar values were observed in the southern Okhotsk Sea during the last 30 kyr (Ternois et al., 2001). Our ratios are closer to those reported for cores PC23A from the northern slope of the Aleutian Basin (Khim et al., 2010) and LV28-42-4 from the central Okhotsk Sea (Nürnberg and Tiedemann, 2004). The authors suggested that the sediments are contaminated by terrestrial organic material, which would also apply to Shirshov Ridge sediments. Core 77KL shows high [C/N]a ratios (∼16) during MIS4, not observed at the more northerly sites (Fig. 3.5a). Increased variability and high values (∼16) characterize sites 77KL and 85KL during MIS3. Both cores during MIS3 record two rapid decreases of [C/N]a possibly reflecting Dansgaard-Oeschger interstadial events 7 and 12 (D/O-events; e.g. Schulz, 2002). At the same time XRF logging data for Br, as well as Si/Al and Ca/Ti log-ratios increase in all cores (Fig. 3.4). At Site 77KL, Termination I is characterized by an increase in [C/N]a ratios beginning at ∼17 ka BP, reaching its maximum of ∼15 within the YD. A subsequent decrease into the Holocene is recorded. The same deglacial evolution is observed at the northern slope of the Aleutian Basin (Khim et al., 2010) and in the southern Okhotsk Sea (Ternois et al., 2001; Seki et al., 2003) and was related to the discharge of terrestrial material from the flooded shelf due to sea-level rise. In contrast, cores from the eastern and southern Bering Sea show a gradual decrease of [C/N] ratios since the Last

**Table 3.5.:** Linear correlation equations for calculation of corrected [C/N]a ratios.

| Core | N | [(1)]Slope (a) | [(1)]Intercept (b) | $R^2$ |
|---|---|---|---|---|
| SO201-2-77KL | 126 | 0.094 | 0.016 | 0.64 |
| SO201-2-85KL | 155 | 0.099 | 0.013 | 0.89 |
| SO201-2-101KL | 254 | 0.096 | 0.018 | 0.73 |

[(1)]for the following equation: $TN = b + a \times TOC$

Glacial Maximum (LGM) (Nakatsuka et al., 1995).

Biogenic opal contents in Bering Sea sediments are reported to be high and to be related to the abundance of siliceous plankton organisms (diatoms, radiolorians; e.g. Matul et al., 2002), who today play a major role for biological production as revealed by sediment trap studies (Takahashi et al., 2002a). Takahashi et al. (2002a) showed that in the southern Aleutian Basin two annual periods of biological particle fluxes occurred during spring/summer (siliceous plankton) and fall (calcareous plankton; foraminifera). Furthermore, they found strong correlations between fluxes of opal and diatoms and the dominance of the pennate diatom species *Neodenticula seminae*. In our cores opal matches the TOC records and is characterized by increasing concentrations and variability towards the southern core locations (Fig. 3.4). In contrast to TOC and $CaCO_3$, we observe only minor deglacial increases of opal (up to 8 wt.%) during the B/A and a subsequent gradual increase into the Holocene. These results are comparable to opal records from the northern Aleutian Basin (Itaki et al., 2009; Khim et al., 2010; Kim et al., 2011), whereas other studies from Bowers Ridge (Okada et al., 2005; Okazaki et al., 2005a; Brunelle et al., 2007, 2010), Umnak Plateau (Okada et al., 2005; Okazaki et al., 2005a), and the southern Okhotsk Sea (Gorbarenko, 1996; Gorbarenko et al., 2002a, 2002b; Narita et al., 2002; Brunelle et al., 2010) show a similar temporal evolution during the last glacial-interglacial cycle and last glacial termination, but 1.5 to 3-times higher values. This emphasizes the dominance of diatoms as the main primary producers during warm stages and their increasing abundance towards the south.

$CaCO_3$ contents within our sediments are related to the abundance of planktonic and benthic foraminifera, as well as nannoplanktonic remains (coccoliths). XRF Ca/Ti log-ratios in cores 77KL and 85KL correlate with $CaCO_3$ contents (Tab. 3.3) and are thought to reflect relative changes of biogenic calcareous vs. terrigenous components in the sediment. During most of the last glacial-interglacial cycle, MIS6, and also during MIS5e, $CaCO_3$ contents were low ($<$3 wt.%) showing almost no variability (Fig. 3.4). High Ca/Ti log-ratios during MIS5e in cores 85KL and 101KL originate from low XRF counts of Ti and not from increased Ca counts. In all cores significant increases in $CaCO_3$ content only occur during Termination I, specifically during the B/A and PB, with concentrations of up to ∼30 wt.% at Site 77KL. The more northerly sites 85KL and 101KL during this time are characterized by lower $CaCO_3$ contents of ∼10 wt.% and ∼5 wt.%, respectively. Minor, short-lived increases of up to ∼3 wt.% are recorded during MIS3–6. Low $CaCO_3$ contents in Bering Sea sediments and likewise deglacial changes were reported previously (Cook et al., 2005; Okazaki et al., 2005a; Brunelle et al., 2007; Itaki et al., 2009; Brunelle et al., 2010; Khim et al., 2010; Kim et al., 2011). At ODP Site 882 Jaccard et al. (2005) for the last 450 kyr found interglacial maxima in $CaCO_3$ that are accompanied by maxima in biogenic barium. Since enhanced preservation of $CaCO_3$ in the subarctic N Pacific is explained by a release of deep sequestered $CO_2$ from the deep ocean basin (Broecker and Peng, 1987;

Marchitto et al., 2005), Jaccard et al. (2005) suggested that these $CaCO_3$ maxima are the result of a higher bottom water calcite saturation state due to the weakening of the subarctic N Pacific halocline favoring the release of $CO_2$ to the atmosphere. Deglacial maxima of carbonate contents in Bering Sea sediment cores were also explained by denitrification on continental shelves (Okazaki et al., 2005a), which might have resulted in an increase in alkalinity and, thus, in enhanced carbonate preservation (Chen, 2002). Today, the calcite saturation horizon (CSH; i.e. the approximate top of the lysocline) in the Bering Sea is reported to lie above 500 m water depth (Feely et al., 2002) and in particular at our sites lies <200 m w.d. (Riethdorf et al., in prep.), which is shallower than the coring locations. Accordingly, we consider maxima in $CaCO_3$ contents in our cores to rather reflect a higher bottom water calcite saturation state than higher paleoproductivity.

In this respect it is noteworthy that high-resolution core logging resulted in the detection of short-lived excursions in our color b* and Ca/Ti log-ratio records during MIS3–6. Maxima in color b* and Ca/Ti log-ratios appear synchronous with minima in lithogenous element intensities (Al, Ti, Fe), while the color b* records show a remarkable similarity when compared to the NGRIP $\delta^{18}O$ record (Fig. 3.2). Most Ca/Ti log-ratio peaks are detected at intermediate water sites 85KL and 101KL within which they are characterized by only 1–3 cm sediment thickness corresponding to a duration of ∼100–300 years (Fig. 3.4). The most prominent events that are recorded at all sites correspond to D/O-events 7, 12, 18, and 19. Northernmost cores 85KL and 101KL additionally share the occurrence of D/O-events 14 and 20. Moreover, they recorded eight more events off the Greenland record, occuring at approximately 141, 143, 145, 150, 155, 158, 166, and 171 ka BP. However, due to our stratigraphic approach, which relies on the NGRIP record, and unless further age control is provided, we can neither argue for nor against an in-phase evolution between abrupt climate changes recorded in Greenland ice and western Bering Sea sediment composition during MIS3–6.

### 3.4.2. Estimation of export production via $Ba_{excess}$

Records of biogenic barium ($Ba_{excess}$) are shown in Fig. 3.6 together with XRF Ba/Al log-ratios. Although our $Ba_{excess}$ records are characterized by low temporal resolution, they generally match the TOC and opal records. Variability is strongly reduced during most of the last glacial-interglacial cycle and MIS6, with average concentrations becoming higher from Site 101KL (∼300 ppm), via Site 85KL (∼400 ppm), to Site 77KL (∼500 ppm). Significant increases only occur at Site 77KL during the Holocene and during MIS5e with concentrations of ∼1700 ppm and ∼1000 ppm, respectively. Ranges of $Ba_{excess}$ are considerably lower at sites 85KL (∼300–800 ppm) and 101KL (∼100–500 ppm) (Tab. 3.4). Ba/Al log-ratios covary with Si/Al log-ratios and Br records, thereby also showing minor increases during MIS3, MIS5a, and MIS5c, which are (due to temporal resolution) not reflected in $Ba_{excess}$. At sites 85KL and 101KL Ba/Al log-ratios show higher values during MIS5e, which result from decreased portions of Al. A similar range and variability as found for core 77KL is reported for core 17JPC from Bowers Ridge (Brunelle et al., 2007), as well as cores PS2082-1 and PS1768-8 from the Subantarctic and Antarctic zones of the Southern Ocean, respectively (Nürnberg et al., 1997).

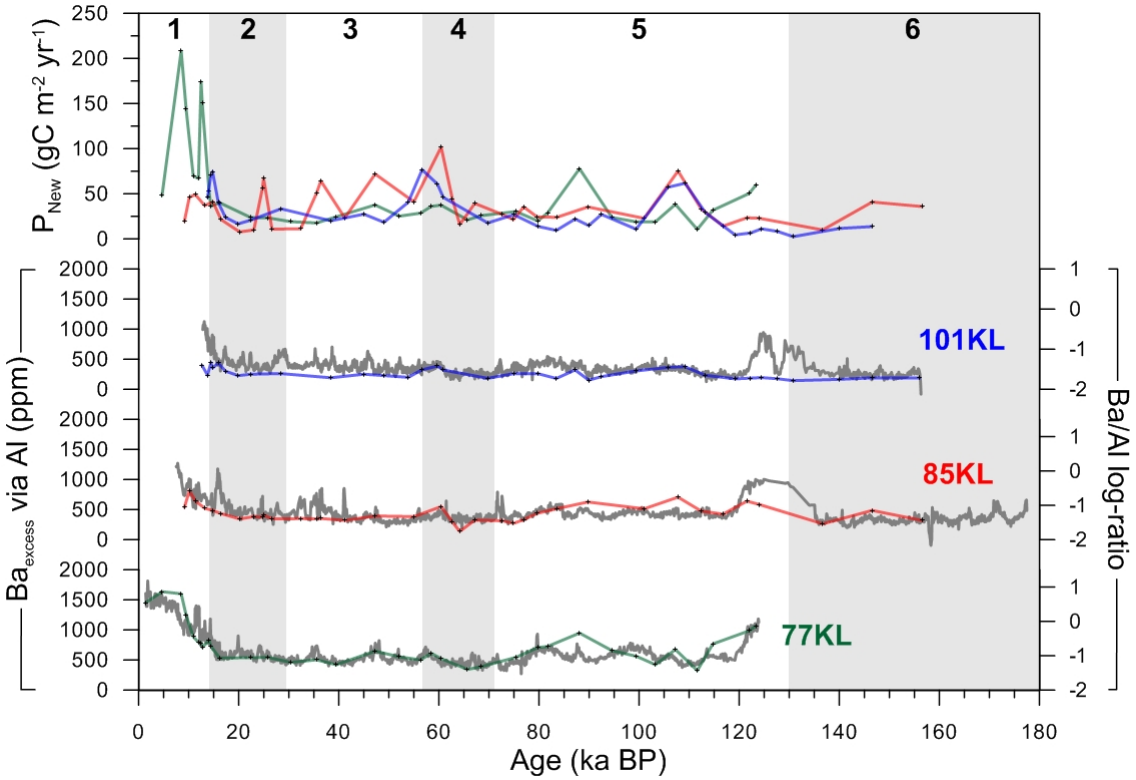


**Figure 3.6.:** Concentrations of biogenic barium ($Ba_{excess}$; coloured lines) and approximating XRF Ba/Al log-ratios (underlying grey lines) for cores SO201-2-77KL (green lines), -85KL (red lines), and -101KL (blue lines), as well as our reconstructions of new production ($P_{New}$), i.e. primary production that results from allochthonous nutrient inputs to the euphotic zone. $P_{New}$ was calculated from $Ba_{excess}$ using the equation of Nürnberg (1995a): $P_{New} = 3.56 \times F\ Ba_{excess}^{1.504} \times z^{-0.0937}$, where $F\ Ba_{excess} = AR\ Ba_{excess}$ / $[0.209 \times \log10(AR_{Bulk} \times 1000) - 0.213]$ (Dymond et al., 1992), and z = water depth (in m). $F\ Ba_{excess}$ is the flux of biogenic Ba to the sea-floor (in $\mu g\ cm^{-2}\ yr^{-1}$), $AR\ Ba_{excess}$ is the accumulation rate of biogenic Ba (in $mg\ cm^{-2}\ kyr^{-1}$). MIS 2, 4, and 6 are highlighted by shaded horizontal bars and top numbers indicate MIS1–6 (after Lisiecki and Raymo, 2005).

Cores from the southern (core GGC27, Brunelle et al., 2010) and central Okhotsk Sea (core PC1, Sato et al., 2002; core LV28-42-4, Nürnberg and Tiedemann, 2004), as well as from the sea-ice influenced Antarctic Zone of the Southern Ocean (core PS1772-8, Nürnberg et al., 1997) exhibit generally lower glacial (∼200–400 ppm) and peak interglacial (∼800–1000 ppm) contents of $Ba_{excess}$, being more comparable to sites 85KL and 101KL. Notably, Sato et al. (2002) and Brunelle et al. (2010) for the Okhtosk Sea report a deglacial lead in the rise of $Ba_{excess}$ prior to that observed for opal contents. From our records of $Ba_{excess}$ and Ba/Al log-ratios we can not verify this lead at our Bering Sea sites.

A potential source of error in the calculation of $Ba_{excess}$ comes from estimating the aluminosilicate contribution of Ba via Al. $Ba/Al_{aluminosilicate}$ ranges between 0.005–0.010 g $g^{-1}$ in crustal rocks (Taylor, 1964; Rösler and Lange, 1972) with a crustal average of 0.0075 g $g^{-1}$ (Dymond et al., 1992). Klump et al. (2000) established a method to estimate regional $Ba/Al_{aluminosilicate}$ values by applying a depth-dependent exponential regression on Ba/Al ratios measured in surface sediments from continental slope transects. Although a different setting, we applied this method to our surface sediment samples from Shirshov Ridge (Riethdorf, unpublished data, 2011) which resulted in

a $Ba/Al_{aluminosilicate}$ value of 0.007 g $g^{-1}$. This value is close to the global average of pelitic rocks of 0.0065 g $g^{-1}$ (Wedepohl, 1971), which was used for the reconstruction of $Ba_{excess}$ in the central Okhotsk Sea (Nürnberg and Tiedemann, 2004). Consequently, we also applied the value of Wedepohl (1971).

Export production ($P_{New}$) was calculated from $Ba_{excess}$ using the approach of Nürnberg (1995a) rather than being assessed from TOC, which at our sites is influenced by terrestrial carbon. Results show that export production during most of the last glacial-interglacial cycle was commonly low (<50 gC $m^{-2}$ $yr^{-1}$) (Fig. 3.6, Tab. 3.4). Only core 77KL is characterized by two significant increases to >150 gC $m^{-2}$ $yr^{-1}$ at ∼12.7–12.5 ka BP (YD) and ∼9.5-8.5 ka BP. Although both maxima correspond to higher concentrations of $Ba_{excess}$, they might be overestimated due to the use of $AR_{Bulk}$ in the calculations, which might as well explain the strong variability of $P_{New}$ observed during MIS2–5. However, the range of our results is comparable to those reported for the central Okhotsk Sea (Nürnberg and Tiedemann, 2004) and the Antarctic continental margin (Gingele et al., 1999), albeit these studies show lower glacial values of <10 gC $m^{-2}$ $yr^{-1}$. Annual primary production (PP) was estimated from $P_{New}$ after Eppley and Peterson (1979) and therefore shows identical temporal changes. Accordingly, PP mainly remains <150 gC $m^{-2}$ $yr^{-1}$ during the last glacial-interglacial cycle and MIS6, whereas the deglacial maxima in core 77KL translate into PP-maxima of ∼250–300 gC $m^{-2}$ $yr^{-1}$ (Tab. 3.4). Modern PP on the eastern Bering Sea shelf edge (the "Green Belt") is reported to lie between 175–275 gC $m^{-2}$ $yr^{-1}$ (Springer et al., 1996). Values of >200 gC $m^{-2}$ $yr^{-1}$ are reached over the southeastern shelf and >800 gC $m^{-2}$ $yr^{-1}$ are reached north of St. Lawrence Island (Stabeno et al., 1999), whereas Arzhanova et al. (1995) found >400 gC $m^{-2}$ $yr^{-1}$ over the western shelf. Consequently, modern PP values might only have been reached at our Site 77KL since the last deglaciation.

### 3.4.3. Changes in terrigenous matter supply

Sediments from Shirshov Ridge are characterized by the dominance of siliciclastic material (sandy/silty clay) over most of the time span covered by the cores, which only declines during phases of diatomaceous ooze deposition. Light microscope observations reveal silt to fine sand-sized angular-shaped quartz grains as major components, supplemented by minor portions of feldspar and mica. Coarse ice-rafted debris (IRD) and dropstones (1–2 cm in diameter) are commonly rare although occurring over the entire length of the cores. Proxy data reflecting changes in terrigenous matter supply at all sites show similar ranges and temporal variations (Fig. 3.7). Along the core transect we observe trends of increasing variability towards the southernmost site and, unlike the productivity proxies, decreasing concentrations. In general, proxy records of marine productivity and terrigenous matter supply are anticorrelated, which becomes most evident when comparing the last glacial termination. As noted earlier, records of magnetic susceptibility and >63 $\mu$m are not correlated in any core. Nevertheless, in core 77KL higher amounts of >63 $\mu$m are reflected by higher contents of $CaCO_3$ (and Ca/Ti log-ratios), indicating that in this core changes in $CaCO_3$ result from higher foraminiferal abundance in the coarse fraction. Covariation definitely exists between Al-normalized records of %terrigenous matter and %siliciclastics, thereby showing almost identical ranges (Fig. 3.7). This might be an important observation since both records were derived independently.

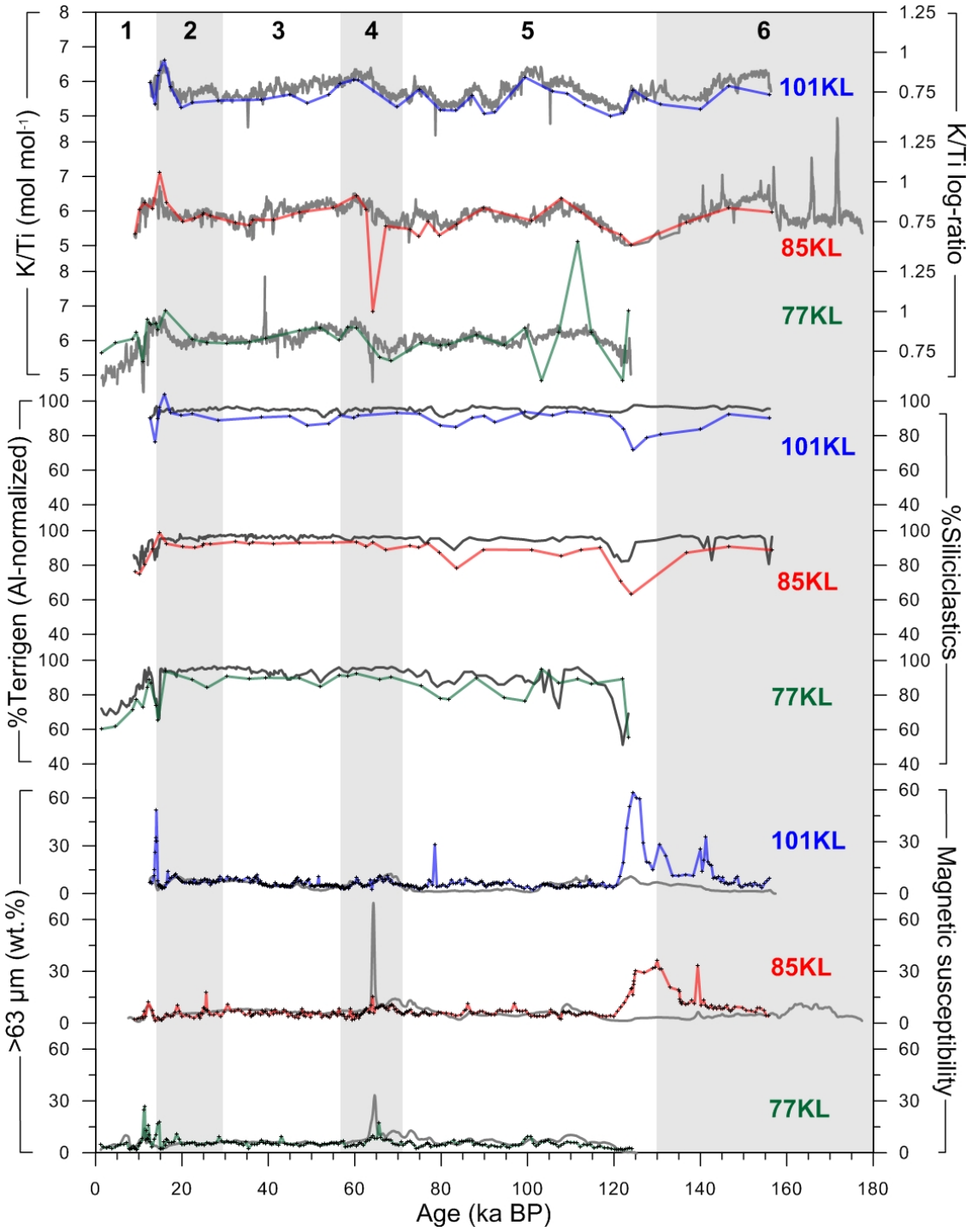


**Figure 3.7.:** Relative contents of coarse material (<63 $\mu$m), terrigenous matter (normalized to Al concentrations of continental crust; Taylor and McLennan, 1995), and the atomic ratio of potassium (K) to titanium (Ti) (coloured lines), in comparison to records of magnetic susceptibility, relative amounts of siliciclastics, and XRF K/Ti log-ratios (underlying grey lines) for cores SO201-2-77KL (green lines), -85KL (red lines), and -101KL (blue lines). MIS were identified using the LR04 stack (Lisiecki and Raymo, 2005) and are marked by black numbers on top. MIS2, 4, and 6 are highlighted by shaded horizontal bars.

**Table 3.6.:** Statistics of parameters approximating terrigenous matter supply.

| | SO201-2-77KL | | SO201-2-85KL | | SO201-2-101KL | |
|---|---|---|---|---|---|---|
| | Avg. | StDev. | Avg. | StDev. | Avg. | StDev. |
| >63 $\mu$m (wt.%) | 5.6 | 3.1 | 7.5 | 5.4 | 7.9 | 7.4 |
| Magn. Susc. (SI) | 6.6 | 3.3 | 6.8 | 5.0 | 4.5 | 2.6 |
| %Siliciclastics | 88.9 | 8.8 | 94.1 | 4.4 | 94.9 | 1.5 |
| %Terrigen (Al-norm.)$^{(1)}$ | 82.7 | 10.2 | 88.2 | 7.3 | 89.3 | 5.9 |
| %Terrigen (Ti-norm.)$^{(2)}$ | 76.6 | 9.6 | 84.4 | 8.4 | 83.8 | 6.2 |
| [Ti] ($\mu$mol g$^{-1}$) | 86.4 | 10.9 | 95.2 | 9.5 | 94.5 | 7.0 |
| [Fe] ($\mu$mol g$^{-1}$) | 762 | 112 | 792 | 96 | 740 | 90 |
| [Al] ($\mu$mol g$^{-1}$) | 2578 | 316 | 2751 | 227 | 2783 | 185 |

$^{(1)}$using [Al] = 3117 $\mu$mol g$^{-1}$ of continental crust (Taylor and McLennan, 1995)
$^{(2)}$using [Ti] = 112.8 $\mu$mol g$^{-1}$ of continental crust (Taylor and McLennan, 1995)

The last glacial-interglacial cycle and MIS6 are represented by sediments containing on average >85% siliciclastics and only <10% coarse material (>63 $\mu$m), indeed tying the terrigenous matter mainly to the fine fractions (Tab. 3.6). Atomic ratios of potassium (K) to titanium (Ti) show a similar range of 5–7 mol mol$^{-1}$ in all cores and correspond to XRF K/Ti log-ratios. We consider changes in this ratio to be indicative of geochemical changes of the terrigenous matter itself. During most of the last glaciation average values of K/Ti lie between ∼5.5 and 6.0 mol mol$^{-1}$. Most significant decreases in %terrigenous matter and %siliclastics are observed during MIS5e and the Holocene with minima of ∼50% siliciclastics at Site 77KL. At sites 85KL and 101KL these minima are at ∼60% and ∼70 respectively. Here, atomic K/Ti ratios decrease to minima of ∼5 mol mol$^{-1}$. During the B/A, %siliciclastics show less pronounced drops by up to ∼25% at Site 77KL, whereas this core shows drops by up to ∼15% during MIS5a and MIS5c. K/Ti records also show reductions by ∼0.5 mol mol$^{-1}$ in all cores during these times, while increases of ∼0.5 mol mol$^{-1}$ are observed at the terminations of MIS4 (∼62–57 ka BP) and during H1. Subsequent to the B/A, during the YD, %terrigenous matter and %siliciclastics return to glacial values, which is followed by a gradual decrease into the Holocene. Records of K/Ti also at first return to glacial values but then continue to decline during the Holocene. Changes in terrigenous matter supply during the PB, as recorded for TOC and $CaCO_3$, are not observed. Notably, the >63 $\mu$m records show strongest variability at Site 101KL, and both northerly sites are characterized by highest amounts of coarse material during Termination II (∼30% at Site 85KL and ∼60% at Site 101KL). During Termination II records of >63 $\mu$m parallel Ca/Ti log-ratio records in both cores, although contents of $CaCO_3$ remain low. At ∼124 ka BP >63 $\mu$m starts to decline, which is reflected by a synchronous increase of TOC and opal contents, which not long after start to decline as well (at ∼122 ka BP). The described proxy ranges and their temporal variability almost compare to those reported for the central Okhotsk Sea (Nürnberg and Tiedemann, 2004), except that respective sediment records showed more pronounced peak interglacial minima in %siliciclastics (∼35%).

### 3.4.4. Sources of terrigenous matter

In all cores we found significant linear correlations between lithogenous elements Al, Fe, and Ti (Tab. 3.7), as well as temporal changes that resemble each other for both, the quantitative $XRF_{Bulk}$ analyses and the semiquantitative XRF intensity records

(Fig. 3.8). This might indicate that these elements originate from the same geochemical source and/or share the same transport mechanism of terrigenous matter. Al concentrations (concentrations are given in angular brackets hereafter) correlate with %siliciclastics in cores 77KL ($R^2 = 0.42$) and 85KL ($R^2 = 0.74$), but not in core 101KL ($R^2 = 0.08$), which might be attributed to the extremely reduced variability of %siliciclastics recorded in that core. Correlation between [Al] and Al intensities is lower than between [Ti] and Ti intensities (Tab. 3.3). Hence, Al in our cores might have been subject to scavenging by organic material and bottom sediment resuspension (Orians and Bruland, 1986; Nameroff et al., 2004). However, especially during interglacials, which in our cores are characterized by high contents of TOC and opal, these processes should have resulted in an increased accumulation of Al in the sediment, which is not the case as reflected by decreased [Al]. Accordingly, we consider an influence of particulate scavenging or biosedimentation variations on [Al] insignificant, which is supported by Al/Ti ratios that are close to crustal values. Records for [Al], [Fe], and [Ti] follow the same temporal evolution described earlier for %siliciclastics and K/Ti with general high values during most of the last glacial-interglacial cycle and MIS6 (∼2600–2800 $\mu$mol $g^{-1}$ for [Al], ∼700–900 $\mu$mol $g^{-1}$ for [Fe], ∼90–100 $\mu$mol $g^{-1}$ for [Ti]) (Tab. 3.6). During MIS5e and the Holocene in all cores [Al], [Fe], and [Ti] decrease by ∼800 $\mu$mol $g^{-1}$, ∼300 $\mu$mol $g^{-1}$, and ∼30 $\mu$mol $g^{-1}$, respectively, while minor decreases are recorded during MIS5c, MIS5a, and the B/A. From MIS3 to MIS1, [Fe] is slightly higher in core 77KL than in the other cores. The YD is characterized by a return of proxy concentrations to glacial values. A gradient regarding concentrations of the other lithogenous elements along the core transect is not observed. Notably, XRF intensity records for Fe and Ti show a temporal evolution that seems to be anticorrelated to XRF log-ratios of Si/Al and Ba/Al. These results at most compare to those of cores PC1 in the central Okhotsk Sea (Sato et al., 2002) and RC13-259 south of the Antarctic Polar Front in the Southern Ocean (Latimer and Filippelli, 2001). However, these cores show glacial [Al] and [Ti] that are by ∼30% lower than those recorded at Shirhov Ridge, while glacial [Fe] are almost the same at Site RC12-259. Moreover, these studies congruently describe interglacial minima (∼100 $\mu$mol $g^{-1}$ for [Al], ∼100 $\mu$mol $g^{-1}$ for [Fe], ∼10–20 $\mu$mol $g^{-1}$ for [Ti]) clearly not found at our sites. This argues for interglacial inputs of terrigenous matter at Shirshov Ridge that have decreased by only 30–40% when compared to the last glaciation and MIS6.

Atomic element ratios of Al/Ti and Fe/Al further helped us to characterize the geochemical signature of the terrigenous matter in our sediments. In general, Al/Ti and Fe/Al ratios remain fairly constant during the last 180 kyr and show similar ranges at all sites (Fig. 3.9). Distinct glacial-interglacial differences in either ratio are not observed, indicating that the source of the terrigenous matter or its underlying transport mechanism did not change. This is an interesting result, since records of %siliciclastics, %terrigenous matter, and lithogenous element concentrations indeed are characterized by significant variations on the glacial-interglacial level. An exception is Termination II, which at all sites is characterized by reduced Fe/Al ratios. Al/Ti ratios, however, do not reflect this pattern.

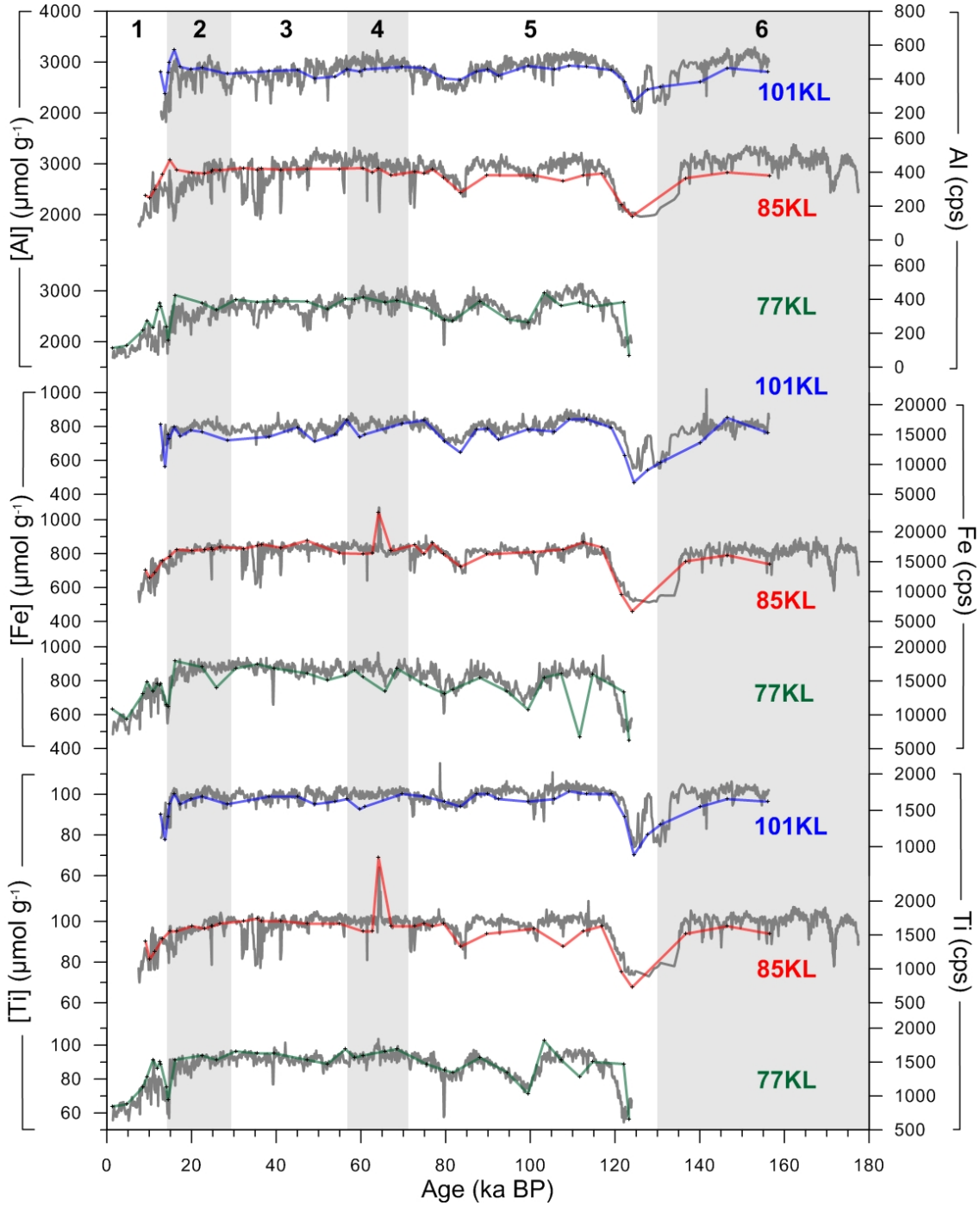


**Figure 3.8.:** Concentrations of lithogenous elements titanium (Ti), iron (Fe), and aluminium (Al) (coloured lines), as well as their respective approximating XRF-based intensity records (in cps; underlying grey lines) for Shirshov Ridge cores SO201-2-77KL (green lines), -85KL (red lines), and -101KL (blue lines). Shaded horizontal bars indicate MIS 2, 4, and 6, whereas black numbers on top mark MIS1-6 (after Lisiecki and Raymo, 2005).

**Table 3.7.:** Linear correlation coefficients ($R^2$) between concentrations of lithogenous elements Al, Fe, and Ti, derived from the same samples.

| Core | N | Ti vs. Al | Ti vs. Fe | Fe vs. Al |
|---|---|---|---|---|
| SO201-2-77KL | 35 | 0.85 | 0.67 | 0.54 |
| SO201-2-85KL | 36 | 0.59 | 0.85 | 0.72 |
| SO201-2-101KL | 35 | 0.70 | 0.78 | 0.74 |

Al/Ti ratios vary between 24–33 (mol $mol^{-1}$), with minor increases (∼3) during Terminations I and II and at the end of MIS4. The maximum during Termination I is followed by a successive return to glacial values during the Holocene. Average Al/Ti values of ∼29.5±3 (2$\sigma$; Tab. 3.8) are almost identical with surface sediment values from Shirshov Ridge (29.4±4, 2$\sigma$) and from the eastern Kamchatka continental margin (32.1±3, 2$\sigma$) (Riethdorf, unpublished data, 2011), indicating that past and modern sources of terrigenous matter are identical. These values compare with Al/Ti ratios reported for Paleozoic (∼29) and Mesozoic/Cenozoic shales (∼32) from the Russian Platform (Ronov and Migdisov, 1971), but also with average values for sediment and continental crust (∼28; McLennan, 1995; Taylor and McLennan, 1995), river particulate and mud (∼30; McLennan, 1995), pelagic clay (∼32; McLennan, 1995), as well as the range reported for loess deposits (∼26–31; Taylor et al., 1983; Pye, 1987; McLennan, 1995). Values are clearly lower than that of the North American shale composite (∼38; Gromet et al., 1984), but higher than Al/Ti ratios of oceanic tholeiitic basalt (∼17; Engel et al., 1965) and surface samples from St. George Basin, SE Bering Sea (∼24; Gardner et al., 1980). Nürnberg and Tiedemann (2004) for sediments from the central Okhotsk Sea report a different range that is extended to higher values (∼24–45).

The overall variability of Fe/Al ratios lies between 0.20–0.34 (mol $mol^{-1}$) (Fig. 3.9). The observed range for Fe/Al is in agreement with results from the central Okhotsk Sea (Nürnberg and Tiedemann, 2004). In contrast to Al/Ti, Fe/Al ratios on our core transect are slightly higher at the southernmost site. Especially during MIS1–3, and MIS5 differences of up to ∼0.06 occur. During Termination I all cores record a decrease of ∼0.04 and a subsequent return to glacial values in the Holocene. A similar range for Fe/Al (0.22–0.39), as well as a latitudinal trend towards higher values in the south is observed in surface sediment samples from Shirshov Ridge (Riethdorf, unpublished data, 2011). Our Fe/Al ratios compare with those reported for the North American shale composite and average mud (∼0.24; Gromet et al., 1984; McLennan, 1995), Mesozoic/Cenozoic (∼0.26) and Paleozoic (∼0.28) Russian Platform shales (Ronov and Migdisov, 1971), average values for river particulate (∼0.25) and sediment (∼0.27; McLennan, 1995). Oceanic tholeiitic basalt (∼0.28; Engel et al., 1965) and surface samples from St. George Basin (∼0.28; Gardner et al., 1980) also apply to the overall range. The value for bulk continental crust is higher (∼0.41; Taylor and McLennan, 1995), while loess deposits show a lower range between ∼0.17–0.25 (Taylor et al., 1983; Pye, 1987; McLennan, 1995). From these results we conclude that sediments from Shirshov Ridge represent a mixture of geochemical signatures from aeolian sediments (loess) and continental sources that are supposedly not influenced by North American shales. Along our core transect, continental and aeolian influences might successively decrease with increasing distance from the coast.

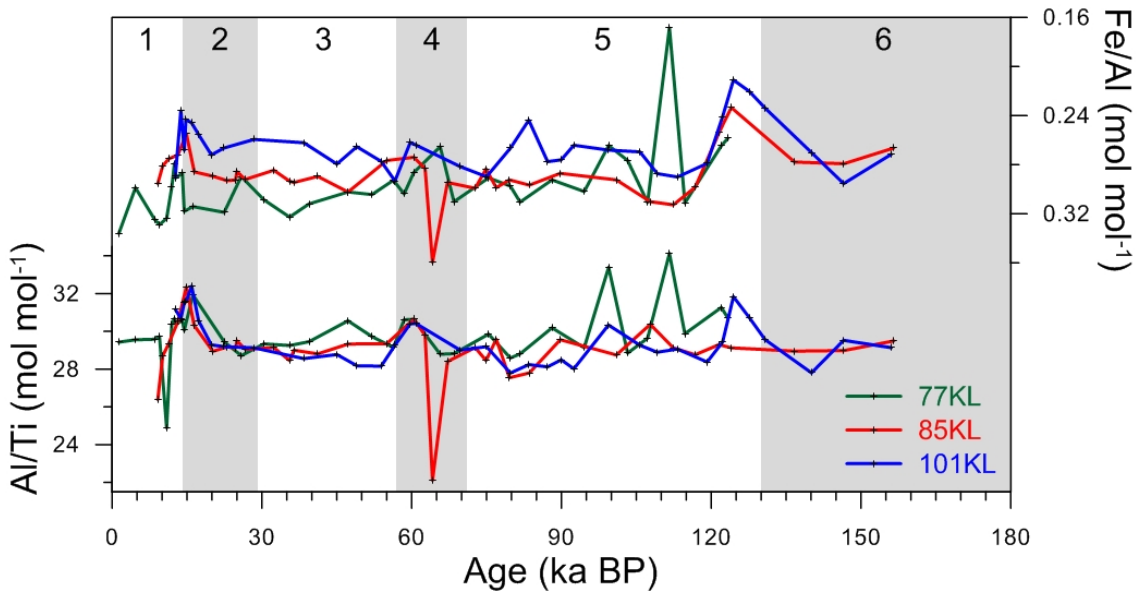


**Figure 3.9.:** Temporal variations of atomic Al/Ti and Fe/Al ratios in cores SO201-2-77KL (green lines), -85KL (red lines), and -101KL (blue lines). Note scale of Fe/Al is inversely plotted. All sites are characterized by overall low variability and similar temporal trends. While Al/Ti ratios are characterized by similar ranges in all cores, Fe/Al ratios become successively higher towards the southernmost site (77KL), especially during MIS2 and MIS3. Note reduced Fe/Al ratios during Termination II. The minimum (maximum) in Al/Ti (Fe/Al) at Site 85KL during MIS4 (∼64 ka BP) corresponds to the respective maximum in the concentration of Ti (Fe) (Fig. 3.8), as well as maxima in coarse material and magnetic susceptibility (Fig. 3.7), and XRF logging data of Ca intensities and Ca/Ti log ratios in that core (Fig. 3.4). MIS are given by black numbers on top (after Lisiecki and Raymo, 2005), and MIS2, 3, and 6 are indicated by shaded horizontal bars.

### 3.4.5. Transport mechanism and source area

Possible mechanisms for the transport of terrigenous matter to Shirshov Ridge encompass fluvial and aeolian supply as well as sea-ice rafting. Major rivers entering the Bering Sea are the Yukon (NW Alaska) and Anadyr (NE Siberia) rivers (Fig. 3.1). As both rivers are situated at rather long distances from Shirshov Ridge, ca. 1300 km in case of Yukon, and given that further minor river systems in the surrounding of the Bering Sea (like Apuka river) are rare, we consider particulate material transport by rivers as insignificant for Shirshov Ridge sedimentation. Wind transported aerosols present in N Pacific sediments are restricted to the source areas of the transported material. Sources of wind-transported material in the vicinity of our study area are most likely situated in NE Siberia. Model results of global desert dust deposition compared with sediment trap data show fluxes of 500–1000 mg $m^{-2}$ $yr^{-1}$ for the Bering Sea (Mahowald et al., 2005), indicating that today aeolian input is negligible. This, however, might have been different during MIS2–3 as indicated by the higher Fe/Al ratios in core 77KL. The higher Fe/Al ratios towards southern Shirshov Ridge sites might as well be the result of dust deposits relatively enriched in Fe.

**Table 3.8.:** Range, average and variability of atomic elemental ratios in cores -77-KL, -85KL, and -101KL.

| | SO201-2-77KL | | SO201-2-85KL | | SO201-2-101KL | |
|---|---|---|---|---|---|---|
| | Al/Ti | Fe/Al | Al/Ti | Fe/Al | Al/Ti | Fe/Al |
| Average | 29.9 | 0.30 | 29.0 | 0.29 | 29.5 | 0.26 |
| Standard deviation | 1.5 | 0.03 | 1.5 | 0.02 | 1.2 | 0.02 |
| Maximum | 34.1 | 0.34 | 32.3 | 0.36 | 32.4 | 0.30 |
| Minimum | 24.9 | 0.17 | 22.1 | 0.23 | 27.8 | 0.21 |

Accordingly, we suggest that sea-ice rafting is and has been the prevailing transport agent of terrigenous matter at our sites, which lie in the glacial drift ice area that was suggested by Katsuki and Takahashi (2005). Processes entraining sediment into newly formed ice involve tidal sea-level oscillations, wind mixing, resuspension of sediments from the sea-floor (suspension freezing), beach-ice formation, nearshore anchor ice formation, seabed freezing, as well as aeolian deposition on top of the ice (e.g. Nürnberg et al., 1994; Stein, 2008, and references therein; Nürnberg et al., 2011, and references therein). Especially during fall and winter, storms affect reworking and resuspension processes by sea-ice crushing, mixing of the water column, and detachment of the sediment-laden ice from the coast. The sediment freight is released by sea-ice melting, especially during spring/summer, and then contributes to (hemi-) pelagic sedimentation. For the Arctic, Nürnberg et al. (1994) reported on sediments entrained in sea-ice to be generally fine grained (clayey silts, silty clays) and mainly composed of quartz, clay minerals and diatom flora. Sediments from the central Okhotsk Sea, which are also assumed to originate from sea-ice rafting are described as mainly clay and silt-sized siliciclastics (>65% siliciclastics) featuring dropstones (3–5 cm), and various lithogenic components (mainly quartz, rock fragments, mica, and dark minerals), with regionally different IRD composition (Nürnberg and Tiedemann, 2004; Nürnberg et al., 2011). The described overall composition is comparable to that of our sediment cores, although validation via IRD component analysis should be a future task.

We favor sea-ice over iceberg transport due to the dominance of silt- and clay-sized terrigenous material in our cores, the absence of large dropstones, and the fact, that today no marine-terminating glaciers exist around the Bering Sea realm. Moreover, the presence of the Beringian Ice Sheet during the LGM (e.g. Grosswald and Hughes, 2002) seems to be disproved (e.g. Brigham-Grette et al., 2001; Karhu et al., 2001; Brigham-Grette et al., 2003). From geochronological investigations, Kaufman et al. (1996) suggested that in Bristol Bay, southwestern Alaska, the most recent major ice advance occurred between ∼75–90 ka BP. For MIS3, Bigg et al. (2008) proposed the existence of a large Kamchatka-Koryak Ice Sheet with marine-terminating ice margins and iceberg discharge at ∼40 ka BP, which was disproved by Nürnberg et al. (2011). Our cores are lacking evidence for such an event not supporting the iceberg migration paths suggested by Bigg et al. (2008), although icebergs calved from marine-terminating glaciers might have reached Bowers Ridge. Furthermore, a recent study by Barr and Clark (2011) indicates that at least during the LGM Kamchatkan climate was too arid for the development of large continental ice sheets. As our records of coarse material show a similar variability during most of the last glacial-interglacial cycle (including the LGM), we do not affirm the influence of iceberg-related IRD from Kamchatkan marine-terminating glaciers at our sites. The variability seen in amounts of coarse material is rather caused by temporal changes in the intensity of sea-ice rafting. Since dropstones are a rather uncommon feature in our cores, which, if present, appear as

well rounded pebbles, we favor a beach deposit origin and tidal pumping, suspension freezing and beach-ice formation to be responsible for the entrainment of terrigenous matter into newly formed sea-ice.

Only shallow shelf areas provide favorable conditions for sea-ice formation. A large continental shelf characterizes the eastern Bering Sea, while relatively small shelf areas exist in its northern and northeastern parts. From mineralogical and petrographical studies, Lisitzin (2002) identified seven mineralogical provinces for western Bering Sea surface sediments together with their possible migration paths. He found that both, coarse silt material and the larger grain-size fractions (pebbles, gravel, boulder) are controlled by sea-ice and share the same provinces and transport pathways. Regarding these results the Koryak Coast, Olyutorskii Bay, and northern Kamchatka provinces can be considered as source areas for the ice-rafted material in Shirshov Ridge sediments (Fig. 3.1). Modern seasonal sea-ice formation begins during October/November in Anadyr Bay, which might as well be taken into consideration as potential source area. In this respect, the K/Ti ratio might be helpful, since it is linked to acidic (more K) and basaltic (more Ti) source rocks (Richter et al., 2006), and thus can be used to track temporal changes in sediment sources weathered from these rocks. We observed relatively increased K/Ti ratios at times when terrigenous matter supply is thought to be enhanced and marine productivity is supposedly reduced. Considering sea-ice rafting to mainly drive the observed changes marine productivity and terrigenous matter supply, hence would characterize the geochemical source of terrigenous matter (and consequently the ice-rafted material) as being relatively increased in K. Both, Koryak Coast and Olyutorskii Bay are characterized by basaltic index rocks (Lisitzin, 2002). Unfortunately, geochemical data do not exist to clearly exclude these areas as potential source areas. The northern Kamchatka province instead is described as a mixed terrigenous-volcanogenic sediment source (Lisitzin, 2002). Shirshov Ridge cores feature marker tephra layers of which most have a homogeneous rhyolitic (acidic) composition and most probably originate from Kamchatkan volcanoes (Derkachev et al., 2011). Furthermore, surface sediment samples from northern Kamchatka and Shirshov Ridge show K/Ti ratios similar to our sediment records ($5.27 \pm 1.04$, $2\sigma$, Riethdorf, unpublished data, 2011), which at first glance would imply that sediments from these areas share the same geochemical source. However, predominantly northwesterly wind directions or southeastward flowing surface currents would be required to transport newly formed sea-ice from northern Kamchatka to Shirshov Ridge where it can release the entrained sediment.

In a modelling study, Zhang et al. (2010) quantified the sea-ice response to changes in atmospheric and oceanic forcing in the modern Bering Sea and found that interannual variability in Bering Sea ice cover is controlled by wind-driven ice mass advection. However, mean ice mass advection in this model clearly is southeastward leaving Anadyr Bay as the remaining potential source area. Indeed, bottom sediment provinces of Anadyr Bay contain acidic index rocks (granite, quartz porphyry, granophyre; Lisitzin, 2002), which might provide the ice-rafted material. Nevertheless, further geochemical investigations are definitely needed to verify this assumption.

## 3.4.6. Environmental changes in the Bering Sea during the last 180 kyr

### Glacial situation

Most of the last glacial-interglacial cycle, specifically MIS2–4, MIS5b/d, and MIS6, are characterized by extremely low contents of TOC, opal, $CaCO_3$, $Ba_{excess}$ and their approximating XRF logging data, indicating strongly reduced, but maintained, primary productivity. Although regionally different, low glacial export production characterizes the whole subarctic N Pacific during the last 800 kyr (for a review see Kienast et al., 2004). In contrast, amounts of coarse material and siliciclastics, contents of lithogenous elements, as well as LSR show high values during these stages, indicating high input of terrigenous matter at our sites. This is in agreement with proposed glacial situations for the Okhotsk Sea (Nürnberg and Tiedemann, 2004; Nürnberg et al., 2011).

From an increase in IRD accumulation rates and a change in IRD composition, Nürnberg et al. (2011) argued for extreme glacial ice conditions in the Okhotsk Sea during MIS6 with a potentially perennial ice coverage. From our results, we can not infer that at Shirshov Ridge conditions during MIS6 were significantly different from those during later glacial stages. Glacial conditions in the Okhotsk Sea are supposed to be similar to the modern winter situation of a strong Siberian High and a weak Aleutian Low, thereby resulting in strong offshore, northerly winds (Nürnberg and Tiedemann, 2004; Nürnberg et al., 2011). This situation might as well apply to the adjacent Bering Sea and might have resulted in enhanced sea-ice formation under a generally colder climate, thereby explaining the higher LSR and terrigenous inputs. Lowered subsurface temperatures at least during MIS2 and MIS3 are supported by low numbers of planktonic foraminifera (dominated by polar species *N. pachyderma* (sin.) and reduced/absent numbers of *Globigerina bulloides*) at Bowers Ridge (Gorbarenko et al., 2005). The notion of a spatially extended sea-ice coverage fostered by a shortened summer season as a result of lower insolation, can hamper light and nutrient availability in the surface ocean. Since primary production is limited by the availability of light and nutrients, which are transported to the euphotic zone by upwelling or vertical winter mixing, a prolonged sea-ice season would consequently lead to the reduction in marine productivity observed at our sites. An extended sea-ice coverage might also have resulted in less wind-induced winter mixing by directly decoupling the wind from the sea surface, which should be reflected by stronger nutrient utilization. Indeed, bulk sediment and diatom-bound nitrogen isotope ratios ($\delta^{15}N$) measured in core 17JPC from Bowers Ridge (Brunelle et al., 2007) show higher glacial than interglacial values (Fig. 3.10), thereby supporting enhanced glacial nitrate utilization and confirming earlier assumptions of suppressed vertical mixing in the glacial Bering Sea (Nakatsuka et al., 1995).

It has been speculated, that the net-inflow of Alaskan Stream waters (Fig. 3.1) into the Bering Sea was reduced at times when the Bering Strait and/or other Aleutian passes, like Unimak Pass (70 m deep), were closed due to lower glacial sea-level, thereby affecting Beringian climate (Pushkar et al., 1999; Tanaka and Takahashi, 2005). In consequence, nutrient supply to the Bering Sea should have been further limited and nitrate utilization should have been even more amplified at times of reduced inflow of Pacific waters. Considering an approximate sill depth of 50 m for the Bering Strait, the global relative sea-level (RSL) reconstruction of Waelbroek et al. (2002), based on

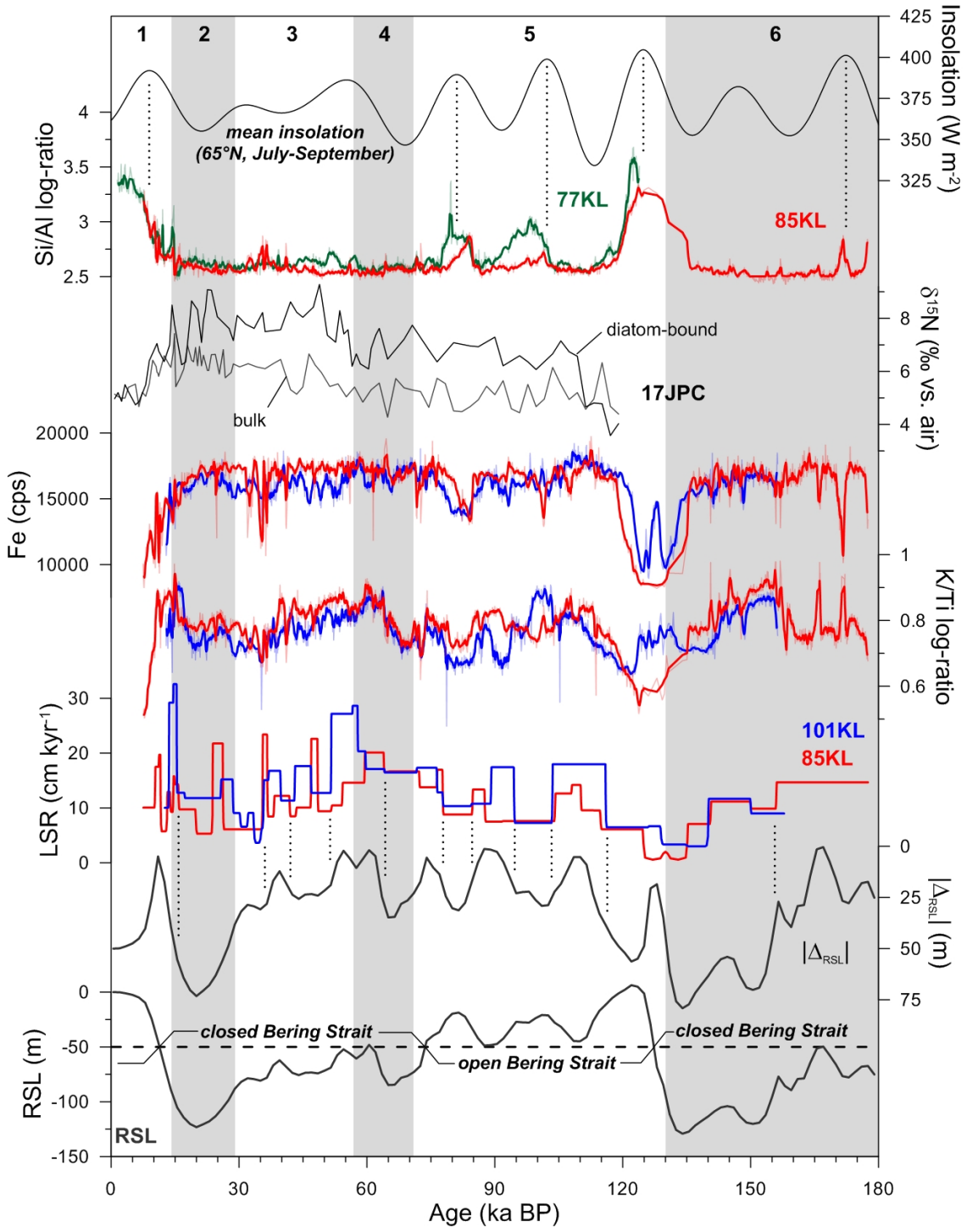


**Figure 3.10.:** Records of linear sedimentation rates (LSR), XRF-based Si/Al log-ratios reflecting changes in marine productivity, as well as K/Ti log-ratios and Fe intensities reflecting changes in terrigenous matter supply at sites SO201-2-77KL (green lines), -85KL (red lines), and -101KL (blue lines) for the last 180 kyr. Logging data are smoothed by 5-point running averages. Relative sea-level (RSL) is after Waelbroek et al. (2002). The dashed horizontal line indicates RSL of -50 m, reflecting the approximate sill depth of the Bering Strait. $|\Delta_{RSL}|$ reflects the absolute difference between the RSL record and the Bering Strait sill depth. Summer insolation at 65°N (July–August) was calculated after Laskar et al. (2004). For comparison, records of diatom-bound and bulk nitrogen isotope ratios ($\delta^{15}$N) for core HLY02-02-17JPC from Bowers Ridge are shown indicating changes in nitrate utilization (data from Brunelle et al., 2007). MIS were identified using the LR04 stack (Lisiecki and Raymo, 2005) and are marked by black numbers on top. MIS2, 4, and 6 are highlighted by shaded horizontal bars.

cores from the N Atlantic and the equatorial Pacific, implies sea-level lowstand and a closed Bering Strait during MIS6, as well as in between MIS2 and MIS4 until the PB (Fig. 3.10). Keigwin et al. (2006) suggested the last major opening of Bering Strait between 12–11 ka BP. RSL changes in the Bering Strait are reported to be predominantly controlled by eustatic changes and to considerably influence deep convection in the N Atlantic (Hu et al., 2010). $\delta^{15}$N values in Bowers Ridge core 17JPC are highest during MIS2 and MIS3 (Fig. 3.10), supporting the influence of RSL on stratification and, hence, nitrate utilization in the Bering Sea. Moreover, we observe increasing LSR at times when RSL approaches the approximate sill depth of the Bering Strait. At the same time maxima in the K/Ti ratio are recorded (Fig. 3.10). Accordingly, from our interpretation of K/Ti ratios we suggest that the intensity of sea-ice rafting is most enhanced at times when sea level changes cause the opening/closure of the Bering Strait, thereby resulting in stronger erosional processes on the flooded/exposed shelf areas.

Today, primary production in HNLC regions is limited by the availability of Fe (Fe-fertilization). During glacials increasing primary production was observed in the HNLC region of the equatorial Pacific, implying a link to Fe delivery (Murray et al., 2012). Notably, although the western deep basin of the Bering Sea is considered as HNLC (Tyrrell et al., 2005), we found high glacial concentrations of Fe despite low marine productivity. Accordingly, we favor sea-ice influence over Fe-fertilization as the limiting factor of primary production on glacial-interglacial timescales in the western Bering Sea. Evidence for seasonal sea-ice formation in the Bering Sea during glacial periods comes from diatom and radiolarian assemblages (Katsuki and Takahashi, 2005; Tanaka and Takahashi, 2005) and is supported by our study. Gorbarenko et al. (2005) argued that during MIS2 a strengthened Subarctic Front led to a reduced flow of (warmer) surface waters from the Pacific to the Bering Sea via the Aleutian passes, which is supported by results from Katsuki and Takahashi (2005) and which, although driven by another mechanism also supports our assumptions.

Finally, the overall low $CaCO_3$ concentrations point towards the presence of corrosive bottom waters as a consequence of organic matter degradation under oxic bottom water conditions rather than the complete absence of calcifiying plankton organisms, a mechanism only recently suggested for the Bering Sea by Kim et al. (2011). If correct, this implies, that either dissolved oxygen is transported to the sea-floor by the formation of intermediate water within the Bering Sea itself, or due to an inflow of $O_2$-rich water masses from the Pacific side. Sea-ice formation in the Bering Sea due to brine rejection results in denser, $O_2$-rich surface waters (e.g. Niebauer et al., 1999), and thus might have maintained the production and ventilation of intermediate water. However, as the modern origin of North Pacific Intermediate Water (NPIW) lies in the Okhotsk Sea (Yasuda, 1997; Cook et al., 2005) and during glacial stages a closed Bering Strait prevented inflow of surface waters from the Arctic Ocean into the Bering Sea (Takahashi, 1998, 1999), inflow of water masses from the N Pacific can not be ruled out.

### Interglacial situation

Compared to the glacial situation, interglacials, as well as MIS5a and MIS5c, show increased marine productivity and decreased terrigenous matter supply, which is opposite to the glacial situation. Strongest variability is recorded at Site 77KL, implying

slight meridional differences along the core transect. Especially during MIS5e and the Holocene, variability and concentration ranges of marine productivity proxies at Site 77KL better compare to those reported for Bowers Ridge, whereas sites 85KL and 101KL resemble records from the northern slope of the Aleutian Basin and the central Okhotsk Sea. $CaCO_3$ contents remain at or close to glacial values implying a similar bottom water calcite saturation state. Increased marine productivity most probably resulted from reduced sea-ice formation during an insolation-induced prolonged summer season. The reduced strength of the atmospheric pressure systems might have further contributed to less intense sea-ice formation. Decreased K/Ti ratios and LSR are congruent with this interpretation. However, the observed concentrations of Al, Fe, and Ti, only imply a reduction of ∼30–40% in terrigenous matter supply. Changes in XRF-based Si/Al log-ratios are in good agreement with mean insolation calculated after Laskar et al. (2004) for boreal summer (July–September) at 65°N (Fig. 3.10), and alkenone-derived SST-records for our sites verify higher values for the Holocene (Max et al., in review). High Si/Al log-ratios (and opal contents) are also reached during MIS5a and MIS5c when summer insolation is high as well. The less extended sea-ice coverage or its later build-up allows for sufficient light availability during the productive seasons and for more intense winter mixing, thereby returning nutrients to the surface layer. The enhanced melting of sea-ice during spring/summer would further have strengthened the halocline. At Bowers Ridge Site 17JPC, $\delta^{15}N$ values are lowest during interglacials (Brunelle et al., 2007, 2010) and they remain also low during most of MIS5 (Fig. 3.10), implying reduced nitrate utilization as a consequence of enhanced vertical mixing. Better availability of nutrients and a reduced sea-ice coverage might have been fostered by an open Bering Strait and Unimak Pass, allowing for enhanced inflow of water masses from the Alaskan Stream. Other studies consider a strengthening of the Alaskan Stream and consequently the BSC in turn reducing sea-ice formation and enhancing nutrient supply and vertical mixing (Gorbarenko et al., 2005; Okazaki et al., 2005a; Kim et al., 2011). This situation might also be responsible for the observed gradient along our core transect with considerably more sea-ice influence and hence higher terrigenous input towards Site 101KL and conditions becoming more favorable for marine productivity towards Site 77KL. At this site the opal concentrations are highest and can be explained as open-water spring blooms (Niebauer et al., 1995) at times of ice-free conditions and enhanced seasonal stratification. Since opal concentrations were higher during MIS5e than during the Holocene, this situation might have been amplified during the last interglacial by more reduced sea-ice influence.

### Deglacial situation

At sites 85KL and 101KL, the situation during Termination II does not resemble that of Termination I. Remarkably, our proxy records resemble the deglacial evolution in the N Atlantic, supporting quasi-synchronity with the deglacial climate evolution in the N Atlantic (Max et al., in review). The most notable feature of Termination II is the extremely high amount of coarse material, not observed previously or later at any site (Fig. 3.7). It is accompanied by minima in all productivity proxies, minima in concentrations of [Al], [Fe], and [Ti], but %siliciclastics that remain on the glacial level. Only Site 101KL is subject to a minor decrease in Al-normalized amounts of terrigenous matter. However, cores 85KL and 101KL show a decrease in Fe/Al ratios during that time, which might indicate a different source. When compared to

the RSL record (Waelbroek et al., 2002), specifically, its absolute difference to the approximate sill depth of Bering Strait ($|\Delta_{RSL}|$=|RSL+50 m|), LSR records show almost synchronous extrema during the last 180 kyr (Fig. 3.10). The most pronounced maxima in >63 $\mu$m during both terminations mirror the respective minima in $|\Delta_{RSL}|$, which reflect the times of most pronounced sea-level rise, when most of the Bering Shelf was overflown/drained. Accordingly, we consider sediments covering Termination II at sites 85KL and 101KL to be affected by erosional processes as a consequence of strong deglacial sea-level rise.

During Termination I high marine productivity but low terrigenous input is observed during the B/A and PB warm phases, which are preceded by the H1 and YD cold phases, respectively. In contrast, H1 and the YD are characterized by reduced marine productivity and enhanced terrigenous matter supply. The early deglacial phase starts with continuously rising [C/N]a ratios just after the LGM at ∼17 ka BP. At the same time LSR and TOC show increasing values, while XRF count rates of Br remain constant. This is explained by higher input of terrestrial organic matter derived from flooded shelf areas in the course of sea-level rise and was previously suggested for the Okhotsk Sea (Ternois et al., 2001; Seki et al., 2003) and the Bering Sea (Khim et al., 2010). Notably, Khim et al. (2010) for the northern slope of the Aleutian Basin report increasing C/N ratios, TOC and Al contents already at ∼19 ka BP, which is ∼2,000 years earlier than at our sites. This timelag for increased terrigenous carbon input suggests that both locations are supplied from different sources. Accordingly, terrestrial runoff from Yukon River denitrifying the eastern Bering Sea continental shelf might have had a stronger influence on the northern slope area. As, e.g., the northern Kamchatka continental shelf was considerably less extended and shallower, shelf denitrification due to sea-level rise in this region might indeed have started later.

Due to increasing LSR and K/Ti ratios at our sites, as well as high %siliciclastics, we propose enhanced sea-ice rafting during H1, thereby also explaining low contents of opal and $Ba_{excess}$. Evidence for stronger sea-ice rafting comes from the significant increase in the abundance of sea-ice-related diatom genus *Nitzschia* at Umnak Plateau (Cook et al., 2005). Like during glacial stages, primary production might have been restricted by reduced availability of light and nutrients and a shortened summer season. However, Bering Sea cores are marked by a sudden decrease of bulk sedimentary and diatom-bound $\delta^{15}$N (Fig. 3.10), pointing to decreased nitrate utilization due to increased nutrient supply by enhanced vertical mixing (Brunelle et al., 2007, 2010; Kim et al., 2011). Support for intensified mixing and/or overturning during H1 comes from reduced ventilation ages in the subarctic N Pacific realm (Ohkushi et al., 2004; Sarnthein et al., 2007; Sagawa and Ikehara, 2008; Okazaki et al., 2010) as well as modeling studies (e.g. Okazaki et al., 2010; Chikamoto et al., 2012; Menviel et al., 2012), and was related to the disappearance of the halocline (Menviel et al., 2012). The low $\delta^{15}$N values then might be explained by restricted marine productivity during a still shortened but successively extending summer season, despite sufficient nutrient availability caused by enhanced winter mixing. Enhanced winter mixing, however, requires a less extended sea-ice coverage or its later build-up, thereby implying that rising temperatures might have led to more dynamic ice conditions and northward propagating ice margins. Indeed, rising SST and beginning coccolithophorid production are inferred from first detectable concentrations of alkenones during H1 (Caissie et al., 2010; Max et al., in review). Increasing insolation and sea level rise might have further amplified the surface ocean warming via inflow of Pacific waters. During the YD cold phase, our

records also indicate reduced marine productivity and enhanced terrigenous matter supply with proxy values that almost compare to those recorded during H1 and other cold stages of the last glacial-interglacial cycle. This is confirmed by other studies from the Bering Sea (Cook et al., 2005; Gorbarenko et al., 2005; Brunelle et al., 2010) and indicates similar environmental conditions.

The onset of the B/A, and to a lesser degree also the PB phase, is characterized by a sharp increase or at least higher-than-glacial values of all productivity proxies, while LSR, as well as amounts of coarse material, %siliciclastics, and concentrations of lithogenous elements significantly decline. Similar observations regarding changes in marine productivity have previously been reported for the Bering Sea (Gorbarenko, 1996; Cook et al., 2005; Gorbarenko et al., 2005; Okazaki et al., 2005a; Khim et al., 2010) and other parts of the subarctic N Pacific (Keigwin and Jones, 1990; Keigwin et al., 1992; Gorbarenko, 1996; Keigwin, 1998; Crusius et al., 2004; McKay et al., 2004; Gebhardt et al., 2008). In contrast to $CaCO_3$, contents of opal, suggested to originate from spring blooms of siliceous plankton, remain low. Accordingly, we suggest further reduced sea-ice rafting and coverage, now developing into a more dynamic transport agent for terrigenous matter, which is supported by lowered K/Ti ratios. In consequence, a prolonged sea-ice free summer season was established favouring calcareous plankton blooms. Decreasing contents of $CaCO_3$ (and opal) along the core transect towards Site 101KL might indicate stronger sea-ice influence there. The suggested summer situation relies on increased SST, which for our and other Bering Sea sites is confirmed by alkenone-based reconstructions (Caissie et al., 2010; Max et al., in review) and according concurrent changes in foraminiferal assemblages (Gorbarenko et al., 2005). Since increased SST during summer would amplify sea-ice melting, we would expect the establishment or strengthening of a seasonal halocline, thereby resulting in enhanced upper-ocean stratification. The according surface water freshening is supported by higher abundances of radiolarian species *Rhizoplegma boreale* (Kim et al., 2011), as well as brackish diatom species *Paralia sulcata* (Gorbarenko et al., 2005). Further evidence for enhanced stratification during the B/A comes from higher subarctic N Pacific ventilation ages (Adkins and Boyle, 1997; Ahagon et al., 2003; Ohkushi et al., 2004; Sagawa and Ikehara, 2008; Okazaki et al., 2010) and from an increase in $\delta^{15}N$ values (bulk and diatom-bound; Fig. 3.10) implying increased nitrate utilization or even denitrification of seawater nitrate (Brunelle et al., 2007, 2010; Khim et al., 2010). Obviously, winter mixing was insufficient to compensate this high nitrate utilization or was reduced as well.

It might further be speculated, that high marine productivity associated with reduced sea-ice formation might have resulted in organic matter supply exceeding its degradation by available concentrations of dissolved $O_2$. As a consequence, bottom water conditions might have become dysoxic or anoxic, impeding benthonic life and favouring laminae formation. Indeed, formation of dysoxic or laminated sediment formation is observed at oxygen minimum zone (OMZ) depths in the entire N Pacific and Bering Sea (van Geen et al., 2003; Cook, 2006, and references therein) and most probably was related to an intensification of the OMZ (Zheng et al., 2000). Accordingly, a subsequent rise in alkalinity and a deepening of the CCD might have been responsible for the observed enhanced carbonate preservation at our and other Bering Sea sites during the B/A and PB.

### Millennial-scale changes (interstadial situation)

Our cores from Shirshov Ridge recorded changes in sediment composition that might be related to D/O-events (interstadials) registered in the NGRIP ice core during the last 123 kyr. These compositional changes, which are also recorded during MIS6, are characterized by short-lived maxima in color b* and Ca/Ti log-ratios appearing synchronous with minima in XRF intensities of Al, Fe, and Ti. We consider these short-lived events as brief intervals of enhanced marine productivity, decreased terrigenous matter supply, and a higher bottom water calcite saturation state. Intermittently recorded minima in [C/N]a reflect higher portions of marine-derived organic carbon.

Millennial-scale climate changes, connected to N Atlantic D/O-events, are reported to have occurred during the last 70 kyr, especially during MIS3, at Bowers Ridge (Gorbarenko et al., 2005), the northern slope of the Aleutian Basin (Kim et al., 2011), as well as in the Santa Barbara Basin, NE Pacific (Behl and Kennett, 1996; Hendy and Kennett, 2000; Ortiz et al., 2004). They were also detected in stalagmites from China (Wang et al., 2001) which implies a Northern Hemisphere-wide, fast-acting teleconnection. Kennett and Ingram (1995) proposed a tight atmospheric coupling mechanism operating between the N Atlantic and N Pacific directly affecting the ventilation of NPIW. This explanation has also been applied to interstadial conditions of the last glacial period pointing towards weak ventilation of NPIW during interstadials combined with increased biological productivity (Behl and Kennett, 1996; Hendy and Kennett, 2000; Kim et al., 2011). Atmospheric rather than oceanic teleconnections are consistent with the observed $\delta^{18}$O variability in the Chinese stalagmite records. Accordingly, temperature changes in Greenland were related to the intensity of the East Asian Monsoon (Wang et al., 2001). Results from Gorbarenko et al. (2005) also suggest warmer interstadial SSTs from high abundances of thermophilic diatom and planktonic foraminiferal species. Recently, Kim et al. (2011) found brief episodes of high bulk $\delta^{15}$N values at the northern Bering Sea slope that were related to D/O-events, which would indicate increased nitrate utilization and/or denitrification. At our sites, interstadial maxima in Ca/Ti log-ratios imply enhanced carbonate preservation, a result verified by other studies (Gorbarenko et al., 2005; Kim et al., 2011). Hence, we speculate that short-lived changes in sediment composition recorded at our sites might be related to D/O-events and reflect conditions similar to those recorded during the B/A. We can, however, neither argue for nor against an in-phase evolution between interstadials recorded in the N Pacific and in the N Atlantic.

## 3.5. Summary and conclusions

During the last 180 kyr, the Bering Sea paleoenvironment was characterized by the close coupling of insolation and sea-level changes controlling atmospheric circulation patterns, sea-ice dynamics and upper-ocean stratification. These processes, in turn, are responsible for the recorded variability in marine productivity and terrigenous matter supply. We used sediment cores from Shirshov Ridge, western Bering Sea, recovered along a north-south transect from intermediate water depths, to reconstruct these changes by means of geochemical and sedimentological analyses, as well as high-resolution core logging procedures, conducted in a multi-proxy approach. The underlying stratigraphy was generated by a combined approach using core logging data, oxygen isotope stratigraphy, magnetostratigraphy, and AMS-$^{14}$C dating.

Our sediment records allow for centennial to millennial-scale reconstructions. Marine productivity, dominated by siliceous plankton, remained low during most of the last glacial-interglacial cycle and MIS6, when the Bering Strait was closed and summer insolation was weak. Significant increases occured during interglacials, as well as during MIS5a and MIS5c, at times when insolation was high and the Bering Strait was open. Sediment composition is dominated by terrigenous, siliciclastic material mainly bound to the silt and clay-size fraction. Terrigenous matter supply is generally high during the last 180 kyr and reductions of ∼30–40% mainly occur during interglacials, but also during MIS5a and MIS5c. Changes in terrigenous matter supply and marine productivity occur synchronously and show anticorrelated proxy behaviour. Differences are found along our core transect, suggesting stronger sea-ice influence towards the northern Shirshov Ridge sites, and, hence, higher marine productivity towards the southernmost site. Sea-ice rafting is considered as the predominant transport agent for terrigenous material and to limit marine productivity during cold stages. Geochemical signatures of surface and core sediments are a mixture of aeolian and continental sources, indicating that Shirshov Ridge sediments most likely originate from Anadyr Bay which were widely distributed after having formed in coastal areas.

From our results we propose scenarios for environmental change in the Bering Sea during glacial, interglacial, and deglacial times. During the last glacial termination, our sites were subject to distinct environmental changes resembling the deglacial evolution in the N Atlantic, which supports the idea of Northern Hemisphere-wide acting atmospheric teleconnections. The situation during the H1 and YD cold phases compared to that of glacial times with enhanced sea-ice rafting limiting marine productivity during a shortened summer season. Vertical mixing, however, seems to have been stronger. In contrast, the B/A and PB warm phases were characterized by enhanced marine productivity as a result of a prolonged summer season and reduced sea-ice rafting. Along with enhanced upper-ocean stratification these observations are in accordance with higher nitrate utilization or denitrification of seawater nitrate and better $CaCO_3$ preservation. Moreover, we found evidence for abrupt environmental changes that might be related to interstadials recorded in the N Atlantic, thereby reflecting the situation proposed for the B/A.

## Acknowledgements

This study resulted from the German-Russian joint research project "KALMAR–Kurile-Kamchatka and Aleutean Marginal Sea-Island Arc Systems: Geodynamic and Climate Interaction in Space and Time". It was funded by the German Ministry of Education and Research (BMBF), grant nos. 03G0672A and B. We thank master and crew of R/V Sonne cruise SO201 Leg 2 for their professional support in recovering high-quality cores. Technical support and laboratory assistance came from B. Domeyer, N. Gehre, L. Haxhiaj, P. Appel, and J. Heinze and is gratefully acknowledged. E. Maier (AWI-Bremerhaven) conducted additional opal measurements for core 77KL. A. Matul (Shirshov Institute of Oceanology, Moscow) provided additional benthic foraminiferal tests to improve oxygen isotope stratigraphy for cores 85KL and 101KL.

# 3.6. Supplementary information

## 3.6.1. Age models

Age models for cores SO201-2-77KL, -85KL, and -101KL are given in Tables 3.9, 3.10, and 3.11, respectively.

**Table 3.9.:** Age-depth points for core SO201-2-77KL. AMS-$^{14}$C ages have been derived from Max et al. (in review) and are given with 1$\sigma$-ranges (in cal. ka BP).

| Core | Depth (cm) | Cal. Age (ka BP) | Approach |
|---|---|---|---|
| SO201-2-77KL | 6 | 2.0[(1)] | color b* vs. color b* (SO201-2-12KL) |
| SO201-2-77KL | 49 | 7.6[(1)] | color b* vs. color b* (SO201-2-12KL) |
| SO201-2-77KL | 103 | 10.3 | Carbonate spike 1 |
| SO201-2-77KL | 105.5 | / | AMS-$^{14}$C dating (10.05-10.15)[(2)] |
| SO201-2-77KL | 115.5 | / | AMS-$^{14}$C dating (11.17-11.22)[(3)] |
| SO201-2-77KL | 116 | 11.2 | Carbonate spike 2 |
| SO201-2-77KL | 126 | 11.6 | color b* vs. NGRIP |
| SO201-2-77KL | 155.5 | 12.62 | AMS-$^{14}$C dating (12.61-12.73) |
| SO201-2-77KL | 168.5 | 13.83 | AMS-$^{14}$C dating (13.82-13.97) |
| SO201-2-77KL | 180.5 | 14.75 | AMS-$^{14}$C dating (14.50-14.95) |
| SO201-2-77KL | 187 | 15.1 | color b* vs. color b* (85KL) |
| SO201-2-77KL | 221 | 17.0 | color b* vs. color b* (85KL) |
| SO201-2-77KL | 258 | 21.5 | Ca/Ti vs. Ca/Ti (85KL) |
| SO201-2-77KL | 381 | 35.5 | color b* vs. color b* (85KL) |
| SO201-2-77KL | 393 | 37.2 | color b* vs. color b* (85KL) |
| SO201-2-77KL | 443 | 42.0 | color b* vs. color b* (85KL) |
| SO201-2-77KL | 478 | 46.9 | color b* vs. color b* (85KL) |
| SO201-2-77KL | 596 | 59.5 | color b* vs. color b* (85KL) |
| SO201-2-77KL | 656 | 64.7 | Ca/Ti vs. Ca/Ti (85KL) |
| SO201-2-77KL | 722 | 70.8 | color b* vs. color b* (85KL) |
| SO201-2-77KL | 736 | 72.3 | color b* vs. color b* (85KL) |
| SO201-2-77KL | 777 | 76.4 | color b* vs. color b* (85KL) |
| SO201-2-77KL | 796 | 77.7 | color b* vs. color b* (85KL) |
| SO201-2-77KL | 849 | 84.7 | color b* vs. color b* (85KL) |
| SO201-2-77KL | 898 | 89.1 | Ca/Ti vs. Ca/Ti (85KL) |
| SO201-2-77KL | 986 | 101.5 | Ca/Ti vs. Ca/Ti (85KL) |
| SO201-2-77KL | 1043 | 108.0 | color b* vs. color b* (85KL) |
| SO201-2-77KL | 1100 | 116.9 | color b* vs. color b* (85KL) |
| SO201-2-77KL | 1120 | 120.2 | color b* vs. color b* (85KL) |
| SO201-2-77KL | 1166 | 124.2 | color b* vs. color b* (85KL) |

[(1)]uncertain age; [(2)]used to define carbonate spike 1; [(3)]used to define carbonate spike 2

**Table 3.10.:** Age-depth points for core SO201-2-85KL. AMS-$^{14}$C ages have been derived from Max et al. (in review) and are given with 1$\sigma$-ranges (in cal. ka BP).

| Core | Depth (cm) | Cal. Age (ka BP) | Approach |
|---|---|---|---|
| SO201-2-85KL | 1 | 7.6[(1)] | color b* vs. color b* (SO201-2-12KL) |
| SO201-2-85KL | 26.5 | / | AMS-$^{14}$C dating (10.38-10.51)[(2)] |
| SO201-2-85KL | 28 | 10.3 | Carbonate spike 1 |
| SO201-2-85KL | 44 | 11.2 | Carbonate spike 2 |
| SO201-2-85KL | 45.5 | / | AMS-$^{14}$C dating (10.79-10.97)[(3)] |
| SO201-2-85KL | 52 | 11.6 | color b* vs. NGRIP |
| SO201-2-85KL | 60.5 | 13.10 | AMS-$^{14}$C dating (13.10-13.22) |
| SO201-2-85KL | 70.5 | 13.87 | AMS-$^{14}$C dating (13.67-13.89) |
| SO201-2-85KL | 77 | 14.6 | color b* vs. NGRIP |
| SO201-2-85KL | 82 | 14.9 | color b* vs. NGRIP |
| SO201-2-85KL | 95.5 | 15.84 | AMS-$^{14}$C dating (15.80-15.82) |
| SO201-2-85KL | 135.5 | 19.90 | AMS-$^{14}$C dating (19.58-19.90) |
| SO201-2-85KL | 155.5 | 23.78 | AMS-$^{14}$C dating (23.71-24.19) |
| SO201-2-85KL | 209 | 26.2 | transfer of AMS-$^{14}$C age from core (101KL) |
| SO201-2-85KL | 266 | 35.5 | color b* vs. NGRIP |
| SO201-2-85KL | 292 | 36.6 | color b* vs. NGRIP |
| SO201-2-85KL | 305 | 38.2 | color b* vs. NGRIP |
| SO201-2-85KL | 350 | 41.9 | RPI vs. PISO-1500 (Laschamp) |
| SO201-2-85KL | 363 | 43.4 | color b* vs. NGRIP |
| SO201-2-85KL | 398 | 46.9 | color b* vs. NGRIP |
| SO201-2-85KL | 433 | 48.4 | color b* vs. NGRIP |
| SO201-2-85KL | 463 | 51.7 | color b* vs. NGRIP |
| SO201-2-85KL | 490 | 54.2 | color b* vs. NGRIP |
| SO201-2-85KL | 567 | 59.5 | color b* vs. NGRIP |
| SO201-2-85KL | 657 | 64.0 | color b* vs. NGRIP |
| SO201-2-85KL | 675 | 65.0 | RPI vs. PISO-1500 (Norwegian-Greenland Sea) |
| SO201-2-85KL | 796 | 72.3 | color b* vs. NGRIP |
| SO201-2-85KL | 853 | 76.4 | color b* vs. NGRIP |
| SO201-2-85KL | 876 | 77.8 | color b* vs. NGRIP |
| SO201-2-85KL | 937 | 84.7 | color b* vs. NGRIP |
| SO201-2-85KL | 976 | 87.7 | color b* vs. NGRIP |
| SO201-2-85KL | 1006 | 91.7 | color b* vs. NGRIP |
| SO201-2-85KL | 1100 | 104.1 | color b* vs. NGRIP |
| SO201-2-85KL | 1149 | 108.0 | color b* vs. NGRIP |
| SO201-2-85KL | 1180 | 110.2 | color b* vs. NGRIP |
| SO201-2-85KL | 1210 | 113.3 | color b* vs. NGRIP |
| SO201-2-85KL | 1224 | 114.8 | color b* vs. NGRIP |
| SO201-2-85KL | 1287 | 125.0 | $\delta^{18}$O vs. LR04 |
| SO201-2-85KL | 1289 | 129.0 | $\delta^{18}$O vs. LR04 |
| SO201-2-85KL | 1293 | 131.0 | $\delta^{18}$O vs. LR04 |
| SO201-2-85KL | 1295 | 135.0 | $\delta^{18}$O vs. LR04 |
| SO201-2-85KL | 1334 | 140.6 | $\delta^{18}$O vs. LR04 |
| SO201-2-85KL | 1439 | 150.0 | color b* vs. color b* (101KL) |
| SO201-2-85KL | 1498 | 156.0 | color b* vs. color b* (101KL) |
| SO201-2-85KL | 1740 | 172.5[(4)] | SMP vs. LR04 (min MIS6) |
| SO201-2-85KL | 1813 | 177.5[(5)] | Extrapolation |

[(1)]uncertain age; [(2)]used to define carbonate spike 1; [(3)]used to define carbonate spike 2;
[(4)]scalar magnetic properties (SMP) correlated with MIS boundaries of LR04;
[(5)]by extrapolation using linear sedimentation rate (LSR)

**Table 3.11.:** Age-depth points for core SO201-2-101KL. AMS-$^{14}$C ages have been derived from Max et al. (in review) and are given with 1$\sigma$-ranges (in cal. ka BP).

| Core | Depth (cm) | Cal. Age (ka BP) | Approach |
|---|---|---|---|
| SO201-2-101KL | 4 | 12.9 | Ca/Ti vs. Ca/Ti (85KL) |
| SO201-2-101KL | 10.5 | 13.56 | AMS-$^{14}$C dating (13.69-13.84) |
| SO201-2-101KL | 41 | 14.6 | color b* vs. NGRIP |
| SO201-2-101KL | 67 | 15.4 | color b* vs. NGRIP |
| SO201-2-101KL | 90.5 | 17.25 | AMS-$^{14}$C dating (17.17-17.51) |
| SO201-2-101KL | 110.5 | / | AMS-$^{14}$C dating (19.54-19.92)$^{(1)}$ |
| SO201-2-101KL | 190.5 | 25.74 | AMS-$^{14}$C dating (25.88-26.35) |
| SO201-2-101KL | 234 | 28.6 | color b* vs. NGRIP |
| SO201-2-101KL | 249 | 30.3 | color b* vs. NGRIP |
| SO201-2-101KL | 260.5 | 32.0 | AMS-$^{14}$C dating (32.12-33.54) |
| SO201-2-101KL | 274 | 33.5 | Ca/Ti vs. Ca/Ti (85KL) |
| SO201-2-101KL | 280 | 35.1 | Ca/Ti vs. Ca/Ti (85KL) |
| SO201-2-101KL | 284 | 35.7 | Ca/Ti vs. Ca/Ti (85KL) |
| SO201-2-101KL | 302 | 36.9 | Ca/Ti vs. Ca/Ti (85KL) |
| SO201-2-101KL | 349 | 39.7 | Ca/Ti vs. Ca/Ti (85KL) |
| SO201-2-101KL | 387 | 43.1 | Ca/Ti vs. Ca/Ti (85KL) |
| SO201-2-101KL | 454 | 46.9 | Ca/Ti vs. Ca/Ti (85KL) |
| SO201-2-101KL | 514 | 51.6 | Ca/Ti vs. Ca/Ti (85KL) |
| SO201-2-101KL | 650 | 56.6 | Ca/Ti vs. Ca/Ti (85KL) |
| SO201-2-101KL | 685 | 57.8 | Ca/Ti vs. Ca/Ti (85KL) |
| SO201-2-101KL | 723 | 59.7 | Ca/Ti vs. Ca/Ti (85KL) |
| SO201-2-101KL | 799 | 64.1 | Ca/Ti vs. Ca/Ti (85KL) |
| SO201-2-101KL | 923 | 71.7 | Ca/Ti vs. Ca/Ti (85KL) |
| SO201-2-101KL | 1004 | 76.4 | color b* vs. color b* (85KL) |
| SO201-2-101KL | 1023 | 77.8 | color b* vs. color b* (85KL) |
| SO201-2-101KL | 1092 | 84.4 | Ca/Ti vs. Ca/Ti (85KL) |
| SO201-2-101KL | 1142 | 89.1 | Ca/Ti vs. Ca/Ti (85KL) |
| SO201-2-101KL | 1236 | 94.5 | color b* vs. color b* (85KL) |
| SO201-2-101KL | 1301 | 103.5 | color b* vs. color b* (85KL) |
| SO201-2-101KL | 1526 | 116.0 | $\delta^{18}$O vs. LR04 |
| SO201-2-101KL | 1591 | 126.0 | $\delta^{18}$O vs. LR04 |
| SO201-2-101KL | 1611 | 129.0 | $\delta^{18}$O vs. LR04 |
| SO201-2-101KL | 1631 | 135.0 | $\delta^{18}$O vs. LR04 |
| SO201-2-101KL | 1646 | 140.0 | $\delta^{18}$O vs. LR04 |
| SO201-2-101KL | 1762 | 150.0 | $\delta^{18}$O vs. LR04 |
| SO201-2-101KL | 1816 | 156.0 | $\delta^{18}$O vs. LR04 |

$^{(1)}$not used

# 4. Sea surface temperature variability and sea-ice extent in the subarctic northwest Pacific during the past 15,000 years

**Based on:** *"Sea surface temperature variability and sea-ice extent in the subarctic northwest Pacific during the past 15,000 years"* by Lars Max, Jan-Rainer Riethdorf, Ralf Tiedemann, Maria Smirnova, Lester Lembke-Jene, Kirsten Fahl, Dirk Nürnberg, Alexander Matul, and Gesine Mollenhauer (submitted to *Paleoceanography*).

## Abstract

Past changes in North Pacific sea surface temperatures and sea-ice conditions are proposed to play a crucial role in deglacial climate development and ocean circulation but are less well known than from the North Atlantic. Here we present new alkenone-based sea surface temperature records from the subarctic northwest Pacific and its marginal seas (Bering Sea and Sea of Okhotsk) for the time interval of the last 15 kyr, indicating millennial-scale sea surface temperature fluctuations similar to short-term deglacial climate oscillations known from Greenland ice-core records. Past changes in sea-ice distribution are derived from relative percentage of specific diatom groups and qualitative assessment of the $IP_{25}$ biomarker related to sea-ice diatoms. The deglacial variability in sea-ice extent matches the sea surface temperature fluctuations. These fluctuations suggest a linkage to deglacial variations in Atlantic meridional overturning circulation and a close atmospheric coupling between the North Pacific and North Atlantic. During the Holocene the subarctic North Pacific is marked by a complex sea surface temperature pattern, which does not support the hypothesis of a Holocene seesaw trend in temperature development between the North Atlantic and the North Pacific.

## 4.1. Introduction

Knowledge of the deglacial SST development and variability in sea-ice extent in the subarctic Pacific provide important climate boundary conditions to understand oceanic / atmospheric teleconnections between the Atlantic and the Pacific and evaluating most recent hypotheses related to deepwater formation in the North Pacific (N-Pacific). The pattern of sea surface temperature (SST) variability in the subarctic N-Pacific realm as well as the timing of SST changes during the last glacial termination and the Holocene have remained elusive. In general, the spatial and temporal development of SSTs in the N-Pacific on centennial-millennial timescales is not well conceived for several reasons: (1) SST reconstructions from the N-Pacific are sparse (Figure 4.1);

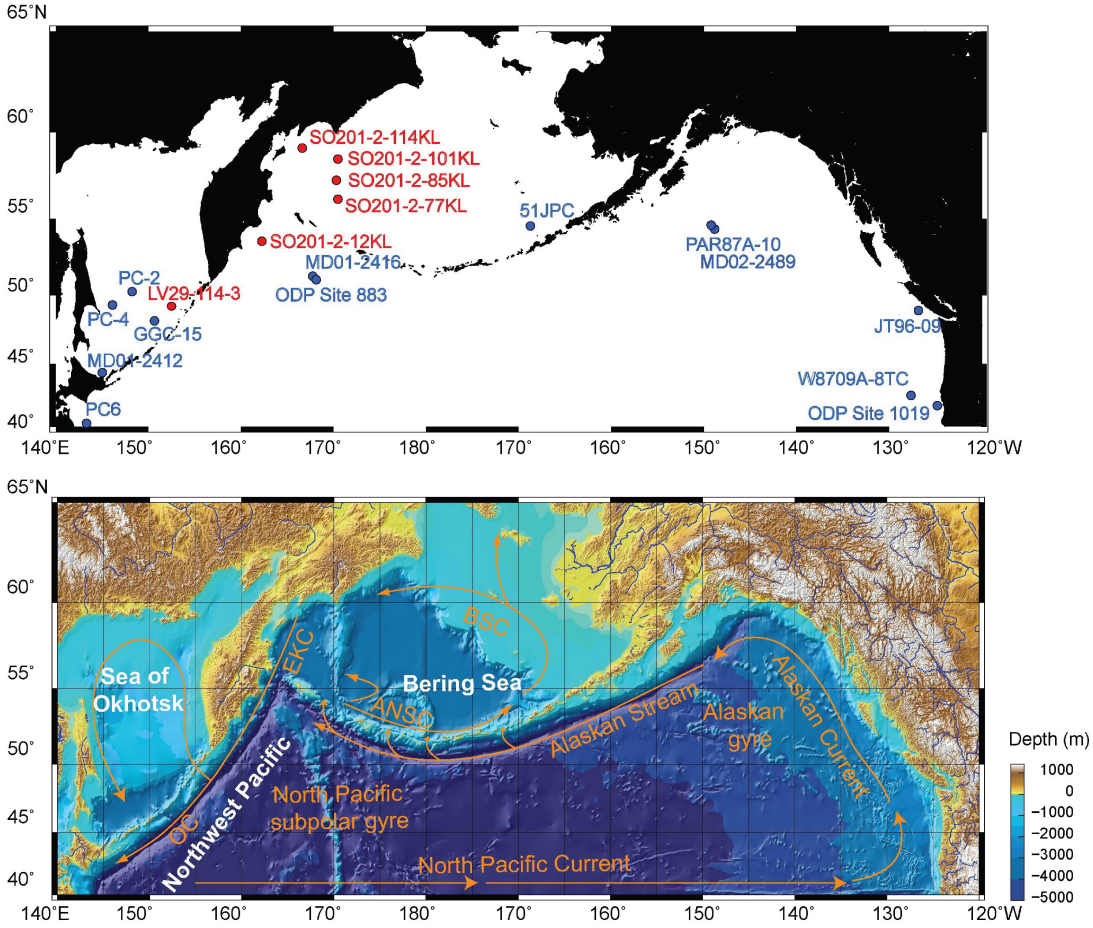


**Figure 4.1.:** (upper hand): Core sites in the subarctic Pacific from this study (in red), together with published sediment records (in blue) in the Sea of Okhotsk (PC-2 and PC-4, Seki et al., 2004a; GGC-15, Ternois et al., 2000; MD01-2412, Harada et al., 2006b) the Bering Sea (51JPC, Caissie et al., 2010) and the N-Pacific (PC6, Minoshima et al., 2007a; ODP Site 883, Kiefer et al., 2001; MD01-2416, Sarnthein et al., 2004; PAR87A-10, Pisias et al., 2001; MD02-2489, Gebhardt et al., 2008; JT96-09, Kienast and McKay, 2001; W8709A-8TC, Pisias et al., 2001; ODP Site 1019, Barron et al., 2003). (lower hand): Bathymetric chart of the subarctic N-Pacific with the general surface circulation pattern indicated by orange arrows (modified after Stabeno et al., 1999). OC = Oyashio Current; EKC = East Kamchatka Current; ANSC = Aleutian North Slope Current; BSC = Bering Slope Current.

(2) The available SST reconstructions are based on a variety of different temperature proxies, which may lead to inconsistent temperature signals as the recording of each proxy can be afflicted with a seasonal bias and/or is related to a different water depth; (3) The availability of carbonate-bearing sediment records with high sedimentation rates is restricted to shallow water depths due to the shallow position of the calcite compensation depth in the N-Pacific (<3000 m); (4) The absence of carbonate for major parts in N-Pacific sediments excludes the application of carbonate-based proxies and $^{14}$C-datings on planktonic foraminifers, thus limiting detailed climate reconstructions; (5) Changes in paleo-$^{14}$C reservoir ages are not well defined and may lead to imprecise age models in the N-Pacific (Sarnthein et al., 2004).

As a consequence, model simulations and proxy-based interpretations led to partly contradictory results concerning the deglacial and Holocene SST variability in the N-Pacific and its underlying mechanisms during the past 15 kyr. Studies with general

circulation models (GCMs) suggest both, an in-phase behavior of deglacial SST pattern (∼15–10 ka BP) between the North Atlantic (N-Atlantic), and the N-Pacific (Mikolajewicz et al., 1997; Vellinga and Wood, 2002; Okumura et al., 2009; Chikamoto et al., 2012) as well as an out-of-phase response (Saenko et al., 2004; Schmittner et al., 2007; Okazaki et al., 2010). The in-phase behavior has been related to rapid atmospheric teleconnections, acting on years to decades. The out-of-phase response has been attributed to oceanic readjustments of the Atlantic Meridional Overturning Circulation (AMOC). More specifically, the simulated reduction of the AMOC as a consequence of enhanced sea surface freshening in the N-Atlantic (like during Heinrich 1 and the Younger Dryas) resulted in a strengthening of the Pacific meridional overturning circulation (PMOC) and an associated warming in the N-Pacific. The warming resulted from an enhanced poleward heat transport from the subtropics to the N-Pacific. Accordingly, the proposed seesaw between AMOC reduction and PMOC intensification suggests a N-Pacific warming during Heinrich 1 (H1) and the Younger Dryas (YD). In turn, the reestablishment of the AMOC (shutdown of PMOC) leads to a surface cooling in the N-Pacific during the Bølling/Allerød (B/A) and the early Holocene. Consequently, the interplay between the two meridional overturning cells is expected to provide millennial-scale out-of-phase fluctuations in SST between the N-Atlantic and the N-Pacific (Saenko et al., 2004).

The few available deglacial SST proxy records from the N-Pacific and its adjacent seas also provide a quite inconsistent picture. They support both an in-phase and out-of-phase relationship with regard to the N-Atlantic SST development or show a pattern of continuously cold SSTs from the last glacial to the onset of the Holocene (no warming event during the B/A). For example, a remarkable similarity between the Greenland/N-Atlantic temperature pattern and changes in subarctic N-Pacific SST, based on alkenone paleothermometry, radiolarian assemblages and dinocyst studies, was found in sediment records from the subarctic northeast Pacific (NE-Pacific) (Kienast and McKay, 2001; Pisias et al., 2001; Seki et al., 2002; Barron et al., 2003), the Bering Sea (Caissie et al., 2010) and the Sea of Okhotsk (Ternois et al., 2000). These records rather argue for an in-phase relationship of temperature fluctuations between the N-Pacific and N-Atlantic. On the other hand N-Pacific SST records from pelagic core MD01-2416 and MD02-2489, derived from planktonic Mg/Ca ratios and from census counts of planktonic foraminifera using the SIMMAX transfer function, indicate a different SST development. These records suggest temperature maxima during H1 and the YD and thus millennial-scale fluctuations out-of-phase with the Greenland/N-Atlantic temperature pattern (Sarnthein et al., 2004; Kiefer and Kienast, 2005; Sarnthein et al., 2006; Gebhardt et al., 2008). The timing of temperature changes is possibly best constrained in sediment record MD01-2416 from the pelagic NW-Pacific. Unfortunately, this record allowed no direct comparison between Mg/Ca- and alkenone-derived SSTs. Other records provide inconsistent pattern of deglacial SST variability. For example, records from the Sea of Okhotsk and the Pacific continental margin of Japan show no SST maximum during the B/A and the deglacial temperature rise does not appear before the end of the YD (Seki et al., 2004a; Minoshima et al., 2007a).

For the Holocene, Kim et al. (2004) summarized alkenone-based SST reconstructions from the N-Pacific and the N-Atlantic and used a coupled atmosphere-ocean general circulation model to assess the inter-oceanic teleconnected climate variability. Their investigations led to the hypothesis of a long-term temperature seesaw between the N-Atlantic and the N-Pacific. Their model-supported proxy-interpretation suggests a

warming trend in the N-Pacific and a cooling trend in the N-Atlantic for the time period of the last 7 kyr. The inverse SST trends between the N-Atlantic and the N-Pacific have been attributed to an atmospheric interaction of the positive Pacific North American (PNA) and the negative North Atlantic Oscillation (NAO) phase. However, the derived warming trend in the N-Pacific relies on one proxy record from the NW-Pacific only (Ternois et al., 2000), which is marked by low alkenone concentrations (close to the detection limit) within the time interval spanning the last 8 kyr BP.

Apart from the differences in Holocene and deglacial Pacific SST pattern, an exact chronostratigraphic correlation between Greenland ice-core records and $^{14}$C-dated deglacial marine climate records is limited to assumptions about the $^{14}$C reservoir age of the surface water, the habitat in which planktonic foraminifera incorporate the $^{14}$C signal into their carbonate shells. Knowledge of the $^{14}$C reservoir age is a necessary precondition for converting radiocarbon ages into calendar years in order to balance for the $^{14}$C disequilibrium between the upper ocean and the atmosphere. Since the variability of past reservoir ages is largely unknown, most studies assume a constant reservoir effect over time, thereby taking an uncertainty of several hundred years into account. Such uncertainties may increase to more than thousand years within time intervals associated with prominent atmospheric $^{14}$C-plateaus (i.e. intervals of very low $^{14}$C change with calendar age). Such plateaus especially mark the period of the last deglaciation. Accordingly, the lead and lag of different proxies indicative of rapid climate change in the subarctic Pacific are difficult to constrain in comparison to the Greenland climate signal.

Here we present the first alkenone-derived high-resolution SST estimates from the subarctic NW-Pacific continental margin and the western Bering Sea as well as a new record from the southeastern Sea of Okhotsk. Our study provides a stratigraphic framework for the NW-Pacific realm, which is based on detailed core-to-core correlations and 37 AMS-$^{14}$C datings. This framework is best developed between 20 to ∼6 ka BP and can be used via X-ray Fluorescence (XRF) core scanner data (e.g. Ca intensities) to transfer ages to other available and future sediment records. The relatively high sedimentation rates enable us to investigate past SST changes on multicentennial to millennial timescales in comparison to rapid climate oscillations known from other parts of the N-Pacific and the N-Atlantic for the last 15 kyr. Additionally, relative percentages of specific diatom groups in combination with qualitative measurements of the $C_{25}$ monounsaturated hydrocarbon ($IP_{25}$) are used to assess past changes in the sea-ice extent (Belt et al., 2007; Müller et al., 2009) with regard to short-term warm/cold fluctuations. Our data suggest that the subarctic NW-Pacific region is characterized by a deglacial pattern of SST fluctuations, which shows a strong similarity to the Greenland/N-Atlantic SST pattern. The sea-ice distribution is closely coupled to the pattern of SST development. The SST records from the NW-Pacific realm presented here close a spatial gap in the N-Pacific and provide new insights into the spatio-temporal pattern of millennial-scale SST variability during the deglacial period from ∼15–10 ka BP and the Holocene. Our results shed new light onto the discussion of whether the deglacial temperature development in the NW-Pacific supports an in-phase or an out-of-phase behavior with respect to the N-Atlantic SST development and the related seesaw between AMOC and PMOC. With respect to the Holocene the SST reconstructions are also used to reconsider the hypothesis of a seesaw mechanism that led to a contrasting long-term temperature trend between the N-Atlantic and the N-Pacific (temperature seesaw) during the past 7 kyr.

## 4.2. Regional setting

The subarctic Pacific regions are characterized by a large, seasonal variability in SST and sea-ice distribution, tightly coupled to atmospheric pressure cells, which in turn are influenced by large-scale interannual-decadal variability associated with the Pacific–North American Oscillation (PNA) and the Pacific Decadal Oscillation (PDO) (Niebauer, 1988; Mantua et al., 1997; Niebauer, 1998; Overland et al., 2002). During winter, the contrast between the Siberian High and Aleutian Low-Pressure System (ALPS) brings cold air masses from the Arctic to the subarctic Pacific, which results in strong sea surface cooling and mixing of nutrient-rich subsurface waters and favors the expansion of sea-ice in the Bering Sea and Sea of Okhotsk. During summer, both increased insolation and weakening of the ALPS lead to warm SSTs, ice-free conditions and strong upper ocean stratification (Ohtani et al., 1972). This leads to strong, seasonal temperature differences between winter (0–2°C) and summer (8–10°C) SSTs in the subarctic NW-Pacific and its marginal seas. Maxima in biogenic productivity occur during spring (dominated by diatoms) and late summer (dominated by coccolithophorids).

The structure of the upper water column is characterized by the presence of a strong halocline, which is a permanent feature of the subarctic Pacific. It forms a barrier for the heat and gas exchange between the deep ocean and the atmosphere as well as for the supply of nutrients into the photic zone. This leads to the highest carbon export efficiency in the world oceans and a net sink of atmospheric $CO_2$ today (Honda et al., 2002).

The surface circulation of the subarctic NW-Pacific follows a large-scale cyclonic pattern of surface currents, which regulate the exchange of heat and nutrients between different ocean regions. The superior large-scale circulation pattern in the subpolar N–Pacific consists of the Kuroshio–North Pacific Current system in the south and two counterclockwise circulating systems: the Alaskan gyre in the east and the western North Pacific subpolar gyre (Fig. 4.1). The North Pacific Current (the Kuroshio extension) transports relatively warm water masses eastward into the Alaskan gyre. The Alaskan Stream forms the northern boundary current and transports water masses from the Alaskan gyre along the Aleutian Islands into the western subpolar gyre, thereby entering the Bering Sea through several passages between the Aleutian Islands. This inflow drives a large-scale counterclockwise surface circulation in the Bering Sea. The surface waters leave the Bering Sea via the Bering Strait into the Arctic Ocean but mainly through the Kamchatka Strait back into the N-Pacific via the East Kamchatka Current (EKC). The EKC delivers nutrient-rich waters from the Bering Sea into the NW-Pacific (Stabeno et al., 1999) and represents the western branch of the North Pacific subpolar gyre. On its path to the south, a part of the EKC enters the Sea of Okhotsk through the Kurile Island Arc, thereby influencing the water mass signature of the Okhotsk gyre. During winter, the intrusion of the relatively warm EKC promotes ice-free conditions around the southern tip of Kamchatka (Seki et al., 2004b) (Fig. 4.1).

# 4.3. Material and methods

We investigated six piston cores from the western Bering Sea, the continental slope of east Kamchatka and the southeastern Sea of Okhotsk (Fig. 4.1). Sediment records were obtained during cruises LV29 KOMEX Leg 2 with RV Akademik Lavrentyev in 2002 and RV Sonne during SO201 KALMAR Leg 2 in 2009. Core site selection was done by intensive sediment echo-sounding studies onboard to detect high-resolution sediment deposits, which are located well above the shallow calcite compensation depth (CCD). Our sediment records provide sufficient amounts of carbonate-bearing material for detailed paleoceanographic reconstructions (Tab. 4.1) except the younger part of the Holocene. During the last 6 kyr, when the productivity of calcareous plankton was generally low in the NW-Pacific, the productivity of diatoms was high. The high amounts of silicious diatom tests further diluted the quantity of planktonic carbonate shells within the sediments (Gorbarenko et al., 2002a).

**Table 4.1.:** Core locations in the subarctic NW-Pacific, Sea of Okhotsk and western Bering Sea as well as the performed proxy studies.

| Sediment core | Latitude (°N) | Longitude (°E) | Depth (mbsl) | Study Area | Performed proxy* studies |
|---|---|---|---|---|---|
| LV29-114-3 | 49°22.54' | 152°53.23' | 1765 | Sea of Okhotsk | $U^{k'}_{37}$, $IP_{25}$, $CaCO_3$, CL, $^{14}C$ |
| SO201-2-12KL | 53°59.47' | 162°22.51' | 2170 | NW-Pacific | $U^{k'}_{37}$, $IP_{25}$, Opal, DS, CL, $^{14}C$ |
| SO201-2-77KL | 56°19.83' | 170°41.98' | 2163 | w. Bering Sea | $U^{k'}_{37}$, $IP_{25}$, CL, $^{14}C$ |
| SO201-2-85KL | 57°30.30' | 170°24.77' | 967 | w. Bering Sea | $U^{k'}_{37}$, $IP_{25}$, CL, $^{14}C$ |
| SO201-2-101KL | 58°52.52' | 170°41.45' | 630 | w. Bering Sea | $U^{k'}_{37}$, $IP_{25}$, CL, $^{14}C$ |
| SO201-2-114KL | 59°13.87' | 166°59.32' | 1394 | w. Bering Sea | $U^{k'}_{37}$, $IP_{25}$, CL, $^{14}C$ |

*$U^{k'}_{37}$ - alkenone paleothermometry; $IP_{25}$ - sea-ice diatoms biomarker; Opal - wt.% biogenic opal; $CaCO_3$ - wt.% $CaCO_3$; CL - Core logging; $^{14}C$ - AMS-$^{14}C$ datings; DS - Diatom studies

## 4.3.1. Stratigraphic approach

### AMS-$^{14}$C-dating

AMS-$^{14}$C ages were measured on monospecific samples of the planktonic foraminifera *Neogloboquadrina pachyderma* sinistral (*N. pachyderma* sin.) from 125–250 $\mu$m fraction. The radiocarbon dating has been performed by the National Ocean Science Accelerator Mass Spectrometry Facility (NOSAMS) at Woods Hole Oceanographic Institute (WHOI) and Leibniz-Laboratory for Radiometric Dating and Isotope Research at Kiel University. Radiocarbon ages have been reported according to the convention outlined by Stuiver and Polach (1977) and Stuiver (1980). All radiocarbon ages were converted into calibrated 1-sigma calendar age ranges using the calibration tool Calib Rev 6.0 (Stuiver and Reimer, 1993) with the IntCal09 atmospheric calibration curve (Reimer et al., 2009) and considering a constant reservoir age throughout the time period covered by the sediment records (see Tab. 4.2 on page 95).

### Biogenic opal and $CaCO_3$

Biogenic opal and $CaCO_3$ were measured at GEOMAR, Kiel. Biogenic opal concentrations were determined from bulk sediment, using the automated leaching method

according to Müller and Schneider (1993) by molybdate-blue spectrophotometry. Results are given with respect to the mineral correction of DeMaster (1981).

Total carbon contents (TC) were determined with a CARLO ERBA Model NA 1500 CNS analyzer. TC was measured on bulk sediments, total organic carbon was derived from decalcified samples. The inorganic carbon ($CaCO_3$) content was calculated as the difference between TC and TOC as follows:

$$CaCO_3 = (TC - TOC) \times 8.333 \tag{4.1}$$

### Core logging data

Relative sedimentary elemental composition was measured using the Avaatech X-ray Fluorescence (XRF) core scanner at the Alfred Wegener Institute for Polar and Marine Research, Bremerhaven. Each core segment was triple-scanned for element analysis at 1 mA and tube voltages of 10 kV (Al, Si, S, K, Ca, Ti, Fe), 30 kV (Cu, Zn, Br, Rb, Zr, Sr, Mo) and 50 kV (Ag, Cd, Sn, Te, Ba), using a sampling resolution of 1 cm and 30 s count time.

Color and light reflectance properties of the sediment cores have been measured with a Minolta CM 508d hand-held spectrophotometer directly after core splitting onboard (Dullo et al., 2009). Measurements were conducted at 1 cm interval. Reflectance data was converted into L*, a* and b* color space with the software Spectramagic.

## 4.3.2. Alkenone analysis and sea surface temperatures ($U^{k'}_{37}$)

Discrete samples (5–10 g) were taken from bulk sediment, freeze-dried and stored frozen until further analysis. Samples were extracted with an accelerated solvent extractor (ASE-200, Dionex) at 100°C and 1000 psi for 15 minutes by using dichlormethane (DCM) as a solvent. Remaining extracts were separated by silica gel column chromatography into three sub-fractions with the following mixture of solvents: fraction 1, 5 ml Hexane; fraction 2, a mixture of 5 ml DCM/Hexane (1:1); fraction 3, 5 ml DCM. Alkenones were eluted in the third fraction and prepared in 100 $\mu$l Hexane. The third fraction was measured at the Alfred Wegener Institute for Polar and Marine Research (AWI), Bremerhaven, using a HP 6890 gas chromatograph, equipped with a cold injection system, a DB-1MS fused silica capillary column (60 × 0.32 mm inner diameter, film thickness of 0.25 $\mu$m) and a flame ionization detector. Individual alkenone (C37:3, C37:2) identification was based on the retention time and the comparison with an external standard, which were also used for controlling the instrument stability. The alkenone unsaturation index ($U^{k'}_{37}$) as proxy for SST (Brassell et al., 1986; Prahl and Wakeham, 1987) was calculated following the relationship between $U^{k'}_{37}$ and temperature as proposed by Müller et al. (1998), which is based on a global core-top calibration (60°N–60°S):

$$U^{k'}_{37} = 0.033 \times T(°C) + 0.044 \tag{4.2}$$

The standard error of this calibration is reported as ±0.050 $U^{k'}_{37}$-units or ±1.5°C. However, it has to be mentioned that for the lower end of the used temperature calibration

a larger error is reported, but still keeps its significance in conjunction to other results from this study. It is also known that in the subpolar N-Pacific, alkenone producers are limited to specific seasons and represent more likely the late summer/early fall SST (Harada et al., 2003; Harada et al., 2006a; Seki et al., 2007). Nevertheless, for a direct comparison to other studies, we decided to use the calibration after Müller et al. (1998) mentioned above, which is widely used in the N-Pacific and other regions rather than the polar temperature function of the Southern Ocean as proposed by Sikes et al. (1997).

### 4.3.3. Qualitative assessment of sea-ice distribution ($IP_{25}$) and microfossil studies (diatoms)

Recently, it has been recognized that when detected in marine sediments, the $C_{25}$ isoprenoid lipid ($IP_{25}$) biosynthesized by Arctic sea-ice diatoms acts as a proxy for previous spring sea-ice occurrence and subsequent melt (Belt et al., 2007). We performed qualitative $IP_{25}$ analysis on selected samples, based on significant changes in our proxy records and reflecting different climate intervals according to our age model. For this purpose the polar fraction (fraction 1, see above) of selected samples were measured with an Agilent 6850 GC (30 m HP-5MS column, 0.25 mm i.d., 0.25 $\mu$m film thickness) coupled to an Agilent 5975 C VL mass selective detector. The GC oven was heated from 60°C to 150°C at 15°C $min^{-1}$, and then at 10°C $min^{-1}$ to 320°C (held 15 min.). Operating conditions for the mass spectrometer were 70 eV and 230°C (ion source). Helium was used as carrier gas. Identification of $IP_{25}$ is based on comparison of its retention time and mass spectra with published data (Belt et al., 2007). The measurements were carried out using SIM (selected ion monitoring) mode (for further details see Müller et al., 2011; Fahl and Stein, in review), the Kovats index is 2085.

Diatom analysis was carried out on discrete samples (approximately every 10 cm) for NW-Pacific core SO201-2-12KL. Observations using a compound light-microscope were made at 1000× magnification; at least 300–500 valves were counted per sample. The number of diatom valves per gram of sediments was estimated. Results are given as relative percentage of diatom species *Fragilariopsis oceanica* (Cleve) Hasle (*F. oceanica*) as sea-ice indicator, and *Neodenticula seminae* (Simonsen & Kanaya) Akiba & Yanagisawa (*N. seminae*) related to open-water conditions.

## 4.4. Results

### 4.4.1. Age model

The color and XRF records have been used to correlate prominent and similar structures between sediment records. This approach also enabled a transfer of conventional $^{14}C$ ages from one core to another (Fig. 4.2; Tab. 4.2 on page 95). We preferentially dated carbonate maxima (maxima in planktonic foraminifer abundance), which are indicated by maxima in Ca intensities (XRF), to avoid age artifacts due to bioturbation effects. Fig. 4.2 shows the Ca intensity records and a detailed core-to-core correlation of our studied core sites. The pattern is marked by two intervals with high Ca intensities.

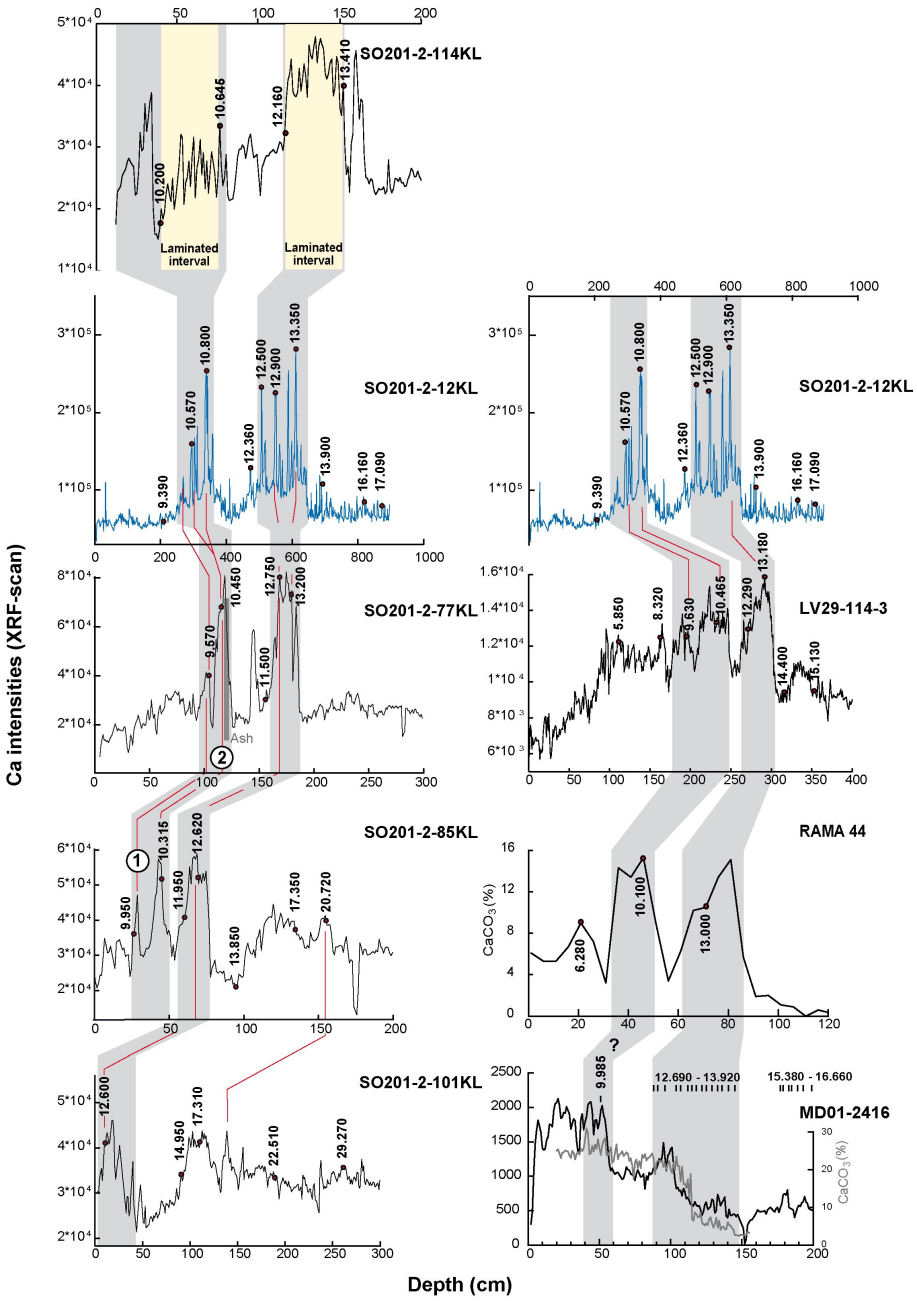


**Figure 4.2.:** (left panel): Stratigraphic framework of sediment records from the western Bering Sea and correlation with high-resolution record SO201-2-12KL record (blue curve) from the subarctic NW-Pacific. The stratigraphy is based on Ca intensity studies, derived from core logging data (XRF), together with raw AMS-$^{14}$C datings (red spots with vertical numbers). Grey shaded areas mark prominent carbonate maxima. Defined carbonate spikes (spike 1 = 9,760 $^{14}$C years; spike 2 = 10,383 $^{14}$C years) are numbered and red lines indicate correlation points between the sediment records. (right panel): Comparison of Ca intensity data from high-resolution record SO201-2-12KL from the NW-Pacific (in blue) and LV29-114-3 from the Sea of Okhotsk to already published records from the open NW-Pacific (RAMA 44, Keigwin, 1998, and MD01-2416, Gebhardt et al., 2008) Ca intensity and $CaCO_3$ (%) data. Red spots (vertical numbers) mark raw AMS-$^{14}$C datings and grey shaded areas indicate carbonate maxima in the sediment records. Sediment record MD01-2416 provides best age control based on $^{14}$C-plateau tuning. However, no correlation was done to the records of this study due to discrepancies between the carbonate records of MD01-2416 and our sediment records.

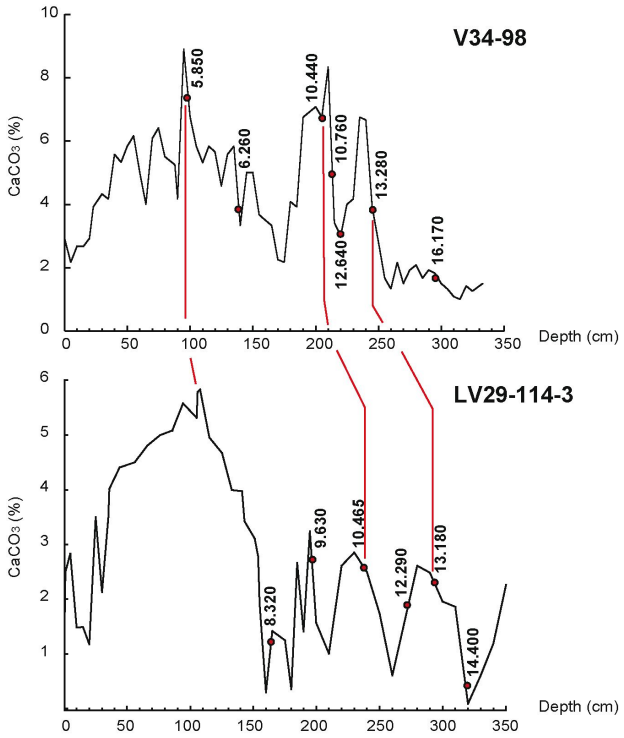


**Figure 4.3.:** Correlation of sediment record LV29-114-3 with core V34-98 (Gorbarenko et al., 2002a) based on $CaCO_3$ (%) data. Numbers with red spots indicate raw $^{14}C$ ages and red lines give correlation points. However, only the raw $^{14}C$ age of 5,850 years was transferred to sediment record LV29-114-3 to improve stratigraphic control in the upper part of this sediment core.

These pronounced carbonate maxima are well known in the NW-Pacific realm and mark the B/A and the interval of the early Holocene (Keigwin et al., 1992; Keigwin, 1998; Gorbarenko et al., 2002a; Gorbarenko et al., 2005; Caissie et al., 2010). The prominent carbonate maxima range from ca. 13,410 (SO201-2-114KL) to 11,950 $^{14}C$ years (SO201-2-85KL) and from ca. 10,800 (SO201-2-12KL) to 9,570 $^{14}C$ years (SO201-2-77KL). The structure of these carbonate maxima is best resolved in NW-Pacific sediment record SO201-2-12KL, which provides sedimentation rates of up to 80 cm $kyr^{-1}$ for these intervals. However, this record suggests that the maxima consist of a sequence of carbonate spikes, which are not fully resolved in the other cores. At Shirshov Ridge, the interplay of lower sedimentation rates and bioturbation effects may have led to stratigraphic uncertainties in the early Holocene. In Shirshov cores SO201-2-77KL and SO201-2-85KL, the match between carbonate spikes 1 and 2 (Fig. 4.2) and their corresponding $^{14}C$ ages provide an uncertainty of up to a few hundred years. In this case, we calculated and used an average $^{14}C$ age for each carbonate spike (spike 1 = 9,760 $^{14}C$ years; spike 2 = 10,383 $^{14}C$ years). At high-resolution core SO201-2-114KL from the northwestern continental margin of the Bering Sea, laminated sediment deposits characterize the intervals of both carbonate maxima (Fig. 4.2).

The mid to late Holocene time interval is marked by low carbonate contents in the NW-Pacific realm. Accordingly, the low abundance or complete absence of foraminifers prevented planktonic $^{14}C$-dating of our records. However, for core LV29-114-3 from the Sea of Okhotsk, we improved the age control via correlation to the well-dated neighbor core V34-98 (Gorbarenko et al., 2002a) and assigned one additional $^{14}C$ age to core LV29-114-3 (5,850 years) as given in Fig. 4.3.

In addition, we also correlated the Ca intensity pattern of NW-Pacific core SO201-2-12KL and Sea of Okhotsk core LV29-114-3 to the pattern of NW-Pacific cores RAMA 44PC (Keigwin et al., 1992) and MD01-2416 (Sarnthein et al., 2004; Gebhardt et al., 2008). This correlation provides a good match with the RAMA 44PC carbonate record. Sediment record MD01-2416 has an excellent age model, including 15 planktonic $^{14}$C-datings, which covers the interval of the first pronounced carbonate maximum between H1 and the B/A. However, the carbonate maximum is less clearly developed in comparison to all other records presented here (Fig. 4.2). A clear correlation is only possible by considering the $^{14}$C ages. Furthermore, the Ca and $CaCO_3$ structure at 9,985 $^{14}$C years in core MD01-2416, which possibly marks the first Ca-spike of the second carbonate maximum in the early Holocene, appears to be several hundred years too young in comparison to the age assignments of our Ca-records from the NW-Pacific, the Bering Sea and the Sea of Okhotsk (Fig. 4.2). Hence, we transferred no $^{14}$C ages from core MD01-2416 to our records.

In general, the sequence of $^{14}$C data and their assignment to prominent carbonate structures is consistent between cores (within a range of a few hundred years) and can be traced from the Bering Sea to the NW-Pacific (except for core MD01-2416) and even into the Sea of Okhotsk. Hence, the registered temporal pattern of the carbonate maxima seems not to be significantly biased by water depth-dependent differences in carbonate dissolution at our investigated records, which range from 630 to 2200 m water depth. However, the $^{14}$C ages of the carbonate maxima at our sediment records from the western Bering Sea (630 to 2200 m water depth) are about 200 years younger than in the NW-Pacific (2170 m water depth) and the Sea of Okhotsk (1765 m water depth). Since the Shirshov Ridge records cover the full range of water depth (630 to 2200 m), we ascribe the temporal offset to regionally different $^{14}$C surface ocean reservoir effects rather than to changes in carbonate dissolution.

The conversion of radiocarbon ages in calendar years requires a correction for the surface ocean reservoir age to balance for the $^{14}$C effect of disequilibrium between the atmosphere and the upper ocean and the input of deep waters into the mixed layer. In the N-Pacific, the surface ocean reservoir age has been reported to range from 600 to 1,000 years (Southon et al., 1990; Kuzmin et al., 2001; McNeely et al., 2006; Yoneda et al., 2007). There is increasing evidence that the reservoir age also varied over the course of the last 20 kyr, which has been attributed to global thermohaline reorganizations as well as to changes in the upper ocean stratification. For the N-Pacific, Sarnthein et al. (2006) and Gebhardt et al. (2008) suggest variable $^{14}$C reservoir ages for the last 20 kyr, which have been derived by $^{14}$C-plateau tuning. For the $^{14}$C-plateaus at 12.3 kyr, 12.8–13.4 kyr and 14.9–15.3 kyr (raw $^{14}$C ages), reservoir ages of 450, 300 and 1350 years have been suggested (Sarnthein et al., 2007), respectively. In contrast, a more recent study claims that the surface ocean reservoir age was close to 730 years and varied by less than ±200 years during the last deglaciation in the NE-Pacific (Lund et al., 2011). Since our $^{14}$C datings are not dense enough to identify the age-calibrated $^{14}$C-plateaus, we were not able to assess the variability of paleo-reservoir ages. Instead, we used constant reservoir ages over time with 700 years for the western Bering Sea cores and 900 years for the NW-Pacific and the Sea of Okhotsk records, which are within the range of NW-Pacific modern surface ocean reservoir ages. After converting the $^{14}$C ages into calendar years, the difference in regional reservoir ages provides the best chronostratigraphic match between our high-resolution core-logging records (color b* and XRF Ca/Ti ratios). This assumes that the pattern of XRF

Ca/Ti ratios and color b* occurred synchronously in the NW-Pacific realm. Trends in the color b* generally correlate with those of biogenic opal (Fig. 4.4). Color b* is reported to provide a good proxy for variations in biogenic opal and total organic matter content of anoxic sediments (Debret et al., 2006). The Sea of Okhotsk is marked by an increase in $CaCO_3$ content rather than an increase of diatom production during the deglaciation (Seki et al., 2009). Thus, we used the pattern of Ca/Ti ratios in the Sea of Okhotsk record, which reflects changes in carbonate contents versus terrigenous siliciclastic input. Our age-depth control points within each record have been moved within the 1-sigma calendar age ranges to improve the fit between records. This also results in a good correlation to the Greenland temperature record (NGRIP) (Rasmussen et al., 2006) shown in Fig. 4.4.

### 4.4.2. SST reconstructions

Calculated alkenone SSTs spanning the time period of the last 15 kyr BP are given in Fig. 4.5. As expected, the SST records reflect successively increasing temperatures from north to south. At the southernmost site (core LV29-114-3), the SSTs are about 3°C warmer than at the northernmost site (core SO201-2-114KL). A general feature of all records is the consistent pattern of temperature variability during the last glacial termination from 15 ka BP to 10 ka BP. This temperature pattern is very similar to that reconstructed from Greenland ice-core records, which mark the temperature rise from H1 into the B/A, the subsequent cold spell of the YD and the following warming into the early Holocene (Fig. 4.5). The early warming step into the B/A does not capture the full amplitude of the SST increase, since all of our records are characterized by alkenone contents below the detection limit prior to 15 ka BP. Hence, the amplitudes of the early temperature increase represent minimum ranges between 3 and 5°C at our studied sites, with lowest SSTs of 2–5.5°C at 15 ka BP and highest values ranging between 6 and 8°C during the B/A. The following temperature decrease into the YD is marked by amplitudes of 1.5–5°C with lowest amplitudes in Sea of Okhotsk core LV29-114-3. At each site, the following temperature increase of up to 5°C consistently culminates in an early Holocene SST maximum between 11 and 9 ka. All records display a maximum with SSTs of 9–10°C except for the northernmost core SO201-2-114KL from the Bering Sea, where the SST maximum remains approx. 3°C cooler. The temperature development during the Holocene is only preserved in Bering Sea core SO201-2-77KL, northwest Pacific core SO201-2-12KL and Sea of Okhotsk core LV29-114-3. These records point to a smooth and gradual SST decrease over the past 9 kyr. However, in Sea of Okhotsk core LV29-114-3, this temperature trend is interrupted by a cold spell between 9–7 ka BP. This pronounced SST minimum displays temperatures as cold as those found during the YD. Nevertheless, the SST trend in this record also suggests a gradual cooling in SST (2°C), which is best developed since 6 ka BP. Another subtle difference is observed for the time interval of the last 3.5 kyr. While the Bering Sea record suggests a slight warming, the records from the NW Pacific and the Sea of Okhotsk indicate a further decline in SST.

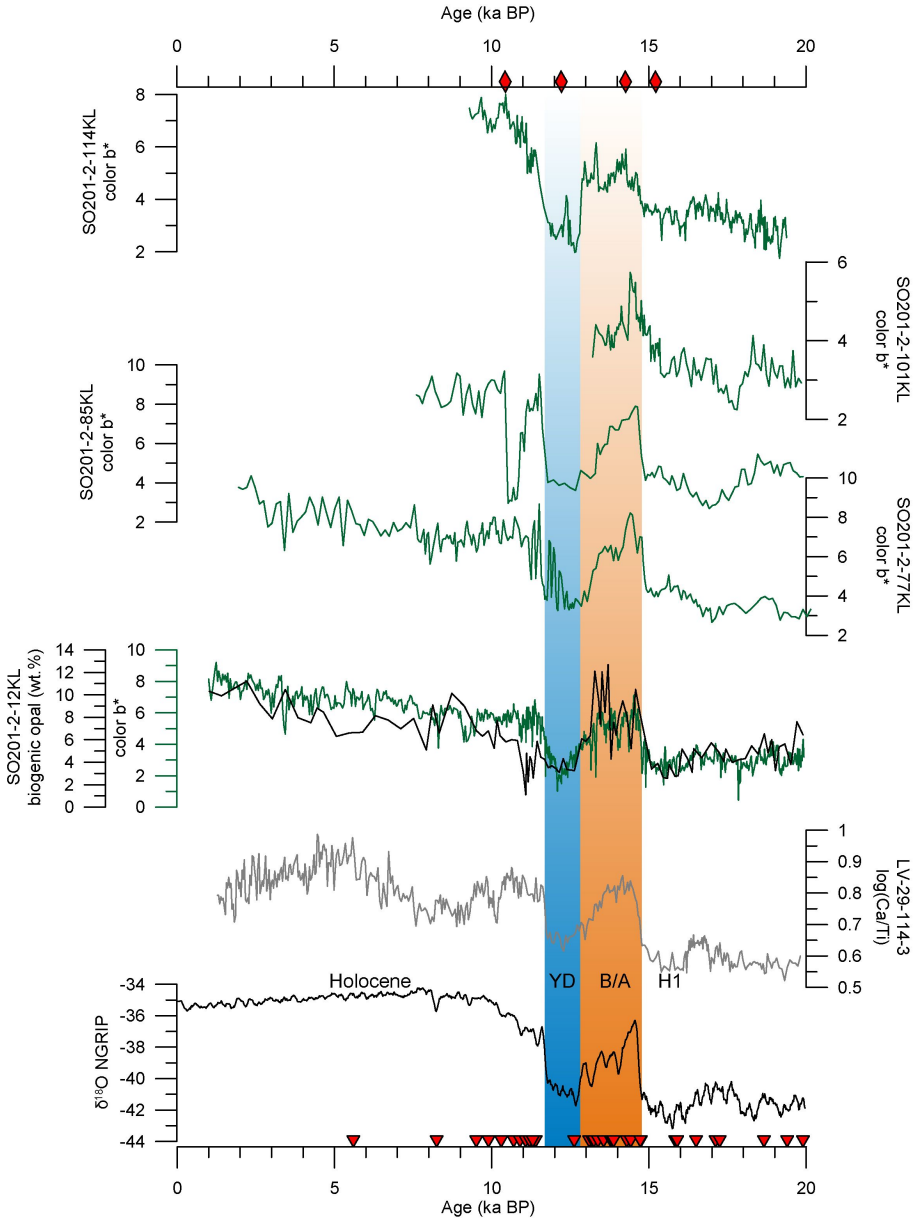


**Figure 4.4.:** Spectrophotometric measurements (color b*, green curves) from sediment records of the western Bering Sea, together with SO201-2-12KL from the NW-Pacific and Ca/Ti log-ratio (XRF element intensities) of LV29-114-3 from the Sea of Okhotsk (in gray) against the NGRIP isotope record (in black) for the last 20 kyr BP. Additionally, biogenic opal (%) (thin black line) is given for SO201-2-12KL. Red triangles at the bottom mark $^{14}$C age control points used in this study. Note the excellent correlation of all studied sediment records with the Greenland isotope record during the last 15 kyr BP. Prominent climate stages as the B/A (shaded in red), the YD (shaded in blue) as well as the onset of the early Holocene are mimicked in the color b* proxy records. Red diamonds on top (representative of all sediment records) mark time slices used for the qualitative assessment of the $IP_{25}$ sea-ice proxy. $IP_{25}$ measurements were conducted on individual sediment records from samples according to the selected time slice.

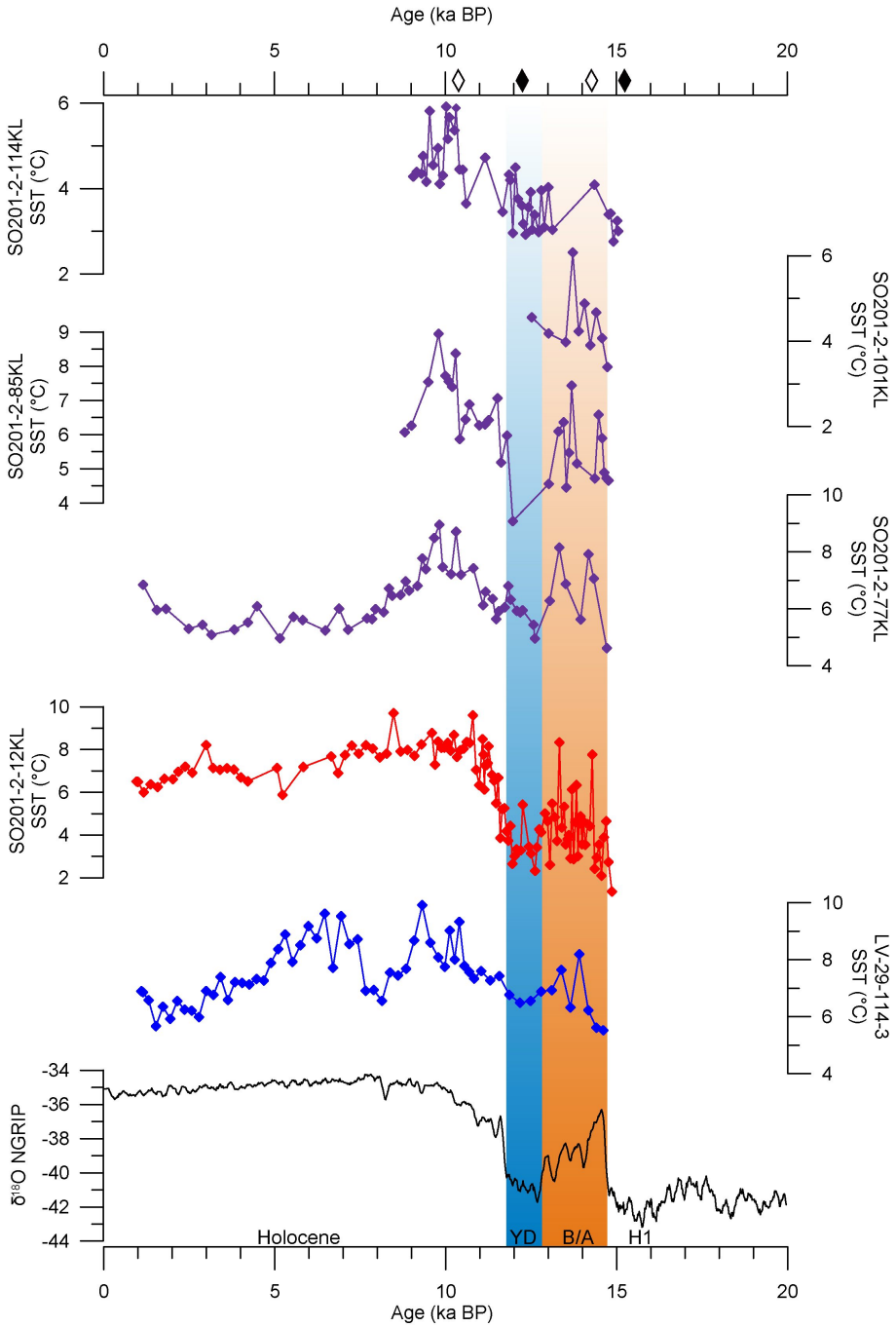


**Figure 4.5.:** Results of the SST reconstructions from the western Bering Sea (in purple), the NW-Pacific (in red) and Sea of Okhotsk (blue curve) compared with the Greenland ice-core record for the last 15 kyr BP. Red shaded area marks the B/A and blue shaded bar indicate the YD cold spell in the records. Diamonds on top mark time slices used for the qualitative assessment of the $IP_{25}$ sea-ice proxy (representative of all sediment records). Black diamonds on top mark time slices (H1 and YD), where the $IP_{25}$ biomarker was found at all core sites and thus the presence of sea-ice inferred. In turn, white diamonds indicate time slices (B/A and early Holocene) where $IP_{25}$ biomarker was absent at all core sites and no sea-ice cover inferred.

### 4.4.3. Sea-ice distribution

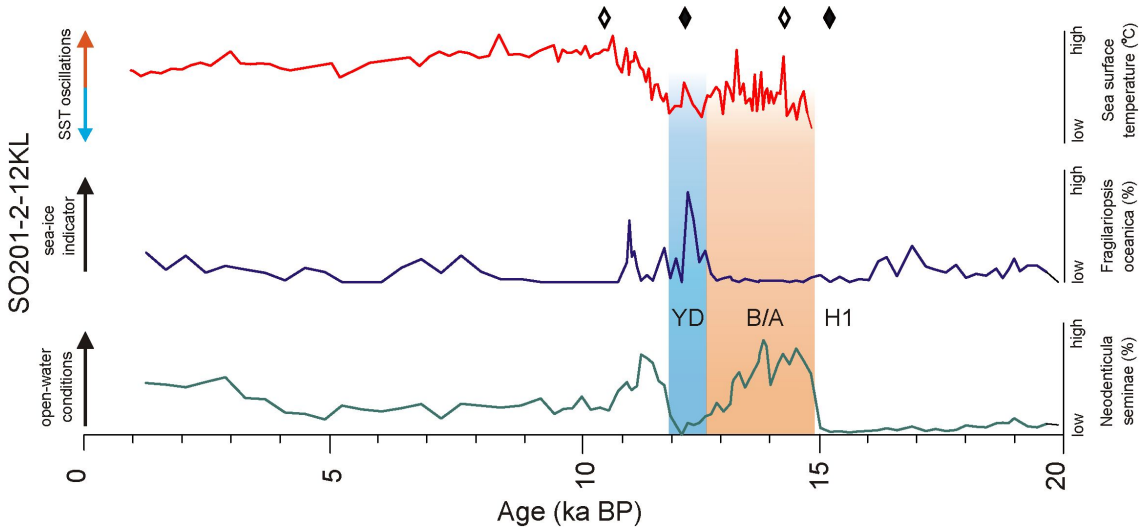


**Figure 4.6.:** Results of the SST reconstructions from sediment record SO201-2-12KL (NW-Pacific) in red together with relative percentage of diatom *Fragilariopsis oceanica* (in blue) and *Neodenticula seminae* (in green). Red shaded area marks the B/A and blue shaded bar indicate the YD cold spell in the sediment records. Diamonds on top mark time slices used for the qualitative assessment of the $IP_{25}$ sea-ice proxy (representative of all sediment records). Black diamonds on top mark time slices (H1 and YD), where the $IP_{25}$ biomarker was found at all core sites and therefore the presence of sea-ice inferred. In turn, white diamonds indicate time slices (B/A and early Holocene) where no $IP_{25}$ biomarker was found at all core sites and thus no sea-ice cover inferred.

To assess past variations in sea-ice extent, we compared relative percentages of diatom species *F. oceanica* (indicative of sea-ice presence) and *N. seminae* (indicative of open water conditions) from sediment record SO201-2-12KL with qualitative measurements of the $IP_{25}$ proxy (indicative of sea-ice presence), derived from specific time slices in all sediment records. The percentages of the diatom species (*F. oceanica* and *N. seminae*) provide a temporal pattern of millennial-scale variability in sea-ice presence, which is consistent with the SST development during the last 15 kyr (Fig. 4.6). Moderate amounts of *F. oceanica* mark the last glacial. Extremely low contents are typical for the B/A. Highest percentages characterize the YD and the subsequent warming phase at the end of Termination I. The SST maximum between approx. 10.5–9.0 ka BP is marked by the absence of *F. oceanica*. The last 9 kyr are marked by a slight increase in *F. oceanica*. *N. seminae* provides an opposite pattern, which is best developed between 15.0–10.5 ka BP, suggesting open water conditions with reduced sea-ice presence during the B/A and the Holocene SST maximum between 10.5–9.0 ka BP. Moderate contents of both *F. oceanica* and *N. seminae* are observed during the past 9 kyr and may indicate temporal variations in sea-ice cover, allowing for both open water conditions as well as sea-ice presence.

As mentioned above, we further applied the $IP_{25}$ proxy indicative of past variations in sea-ice extent. In all records (LV29-114-3, SO201-2-12KL, SO201-2-77KL, SO201-2-85KL, SO201-2-101KL, SO201-2-114KL) we measured $IP_{25}$ at selected time slices (15.1 ka BP, 14.3 ka BP, 12.2 ka BP and 10.5 ka BP), which are representative for distinct climate extremes (H1, B/A, YD, early Holocene SST maximum) recognized in our SST records (Fig. 4.5). As shown for NW-Pacific core SO201-2-12KL, by direct comparison

between *F. oceanica* content and the occurrence of the $IP_{25}$ biomarker, a consistent pattern of sea-ice variability is documented and supports the applicability of the $IP_{25}$ biomarker as sea-ice proxy in the subarctic NW-Pacific (Fig. 4.6). The $IP_{25}$ time slice reconstructions suggest that sea-ice was present during phases of H1 and the YD at each core location in the study area. Conversely, no $IP_{25}$ was found in all sediment samples from the B/A and the early Holocene SST maximum. Accordingly, ice-free conditions mark the positions of all cores during these intervals.

## 4.5. Discussion

### 4.5.1. Deglacial SST development in the subarctic NW-Pacific

The deglacial SST development in the subarctic NW-Pacific realm is reminiscent of the temporal pattern associated with millennial-scale climate variations as revealed by temperature records from Greenland and the N-Atlantic (e.g. Bard et al., 2000). The alkenone temperature records obtained from the subarctic NW-Pacific, the Sea of Okhotsk and the Bering Sea suggest a two-step type of deglacial warming, with a first warming at the onset of the B/A (14.7–12.9 ka BP), subsequently interrupted by a cooling associated with the YD cold phase (12.8–11.8 ka BP) and continued by a second and more pronounced warming step into the early Holocene. Hence, this SST development matches the millennial-scale temperature fluctuations recognized in Greenland ice-core records and N-Atlantic SST records. It has also been reported in previous studies, which established alkenone-derived SST records from other parts of the N-Pacific realm as the NE-Pacific (Kienast and McKay, 2001; Barron et al., 2003), the eastern Bering Sea (Caissie et al., 2010), the Sea of Okhotsk (Ternois et al., 2000; Harada et al., 2006b; Seki et al., 2009; Harada et al., 2012) and off Japan (Harada et al., 2012). These records show remarkable similarities to both the temporal structure and timing of SST changes presented here (Fig. 4.7). On the basis of our age models, the deglacial pattern of SST variability in the NW-Pacific realm seems to be rather in-phase than out-of-phase with the temperature changes in the N-Atlantic. This would suggest a quasi-synchronicity between the N-Atlantic and N-Pacific SST development during the last glacial termination and argues for a strong atmospheric coupling between the N-Pacific and the N-Atlantic.

The majority of model results also favors this interpretation and provides insights into the mechanisms linking the development of SST between the N-Atlantic and the N-Pacific. Numerous studies with coupled General Circulation Models (GCMs) examined whether and how the millennial-scale climate oscillations in the N-Atlantic would impact the N-Pacific SST development via atmospheric and oceanic teleconnections during the last glacial termination. All models propose a close linkage to deglacial variations in AMOC. The temperature changes in the N-Atlantic region are closely coupled to a change in the strength of the AMOC, which is strongly modulated by freshwater forcing due to the instability of the northern hemisphere ice-sheets and melting icebergs (Rahmstorf, 1995; McManus et al., 2004; Yin and Stouffer, 2007).

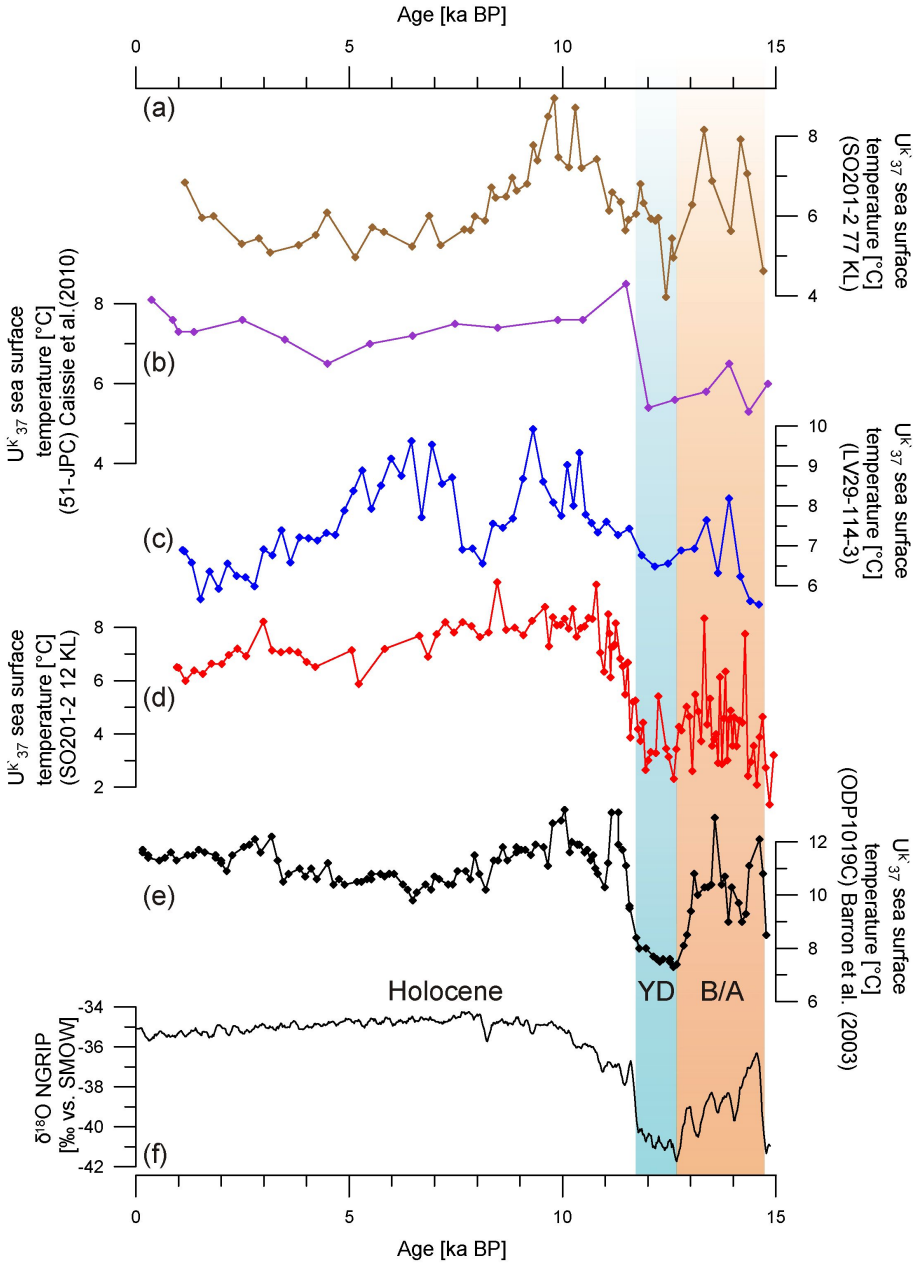


**Figure 4.7.:** Alkenone-based SST reconstructions for the subarctic N-Pacific, including detailed comparison of (a) western Bering Sea (b) eastern Bering Sea (c) Sea of Okhotsk (d) NW-Pacific (e) NE-Pacific compared with (f) NGRIP isotope record for the past 15 kyr. Red shaded area marks the B/A and blue shaded bar indicate the YD cold spell in the records.

The freshwater input into the N-Atlantic led to a reduced thermohaline overturning, which also resulted in a reduced northward advection of saline and warm subtropical surface waters into the N-Atlantic (Manabe and Stouffer, 1988). Manabe and Stouffer (1988) was among the first who demonstrated that the climatic impact of an AMOC shutdown is of global significance. Subsequent freshwater perturbation experiments also suggest, beyond the Atlantic basin, a robust response over the N-Pacific (e.g., Mikolajewicz et al., 1997; Vellinga and Wood, 2002; Okumura et al., 2009; Timmermann et al., 2010). When the AMOC is substantially weakened (e.g. during H1 and the YD), N-Pacific summer and winter SSTs are suggested to have cooled by up to 3–6°C. Most studies attribute the cooling to enhanced thermal advection of cold air masses

from the N-Atlantic via westerly winds (Manabe and Stouffer, 1988). As a result, the deepening of the Aleutian low, the intensification in ocean-to-atmosphere heat flux and southward Ekman transport in combination with the southward shift of the oceanic frontal system would further cool the N-Pacific. More recently, model experiments also provide hints for another atmospheric bridge between the N-Pacific and the subtropical Pacific/Atlantic that may have the potential to influence the strength of the Aleutian low. Tropical SST anomalies in both the Atlantic and Pacific are found to be important for the barotropic response of the Aleutian low (Okumura et al., 2009). These mechanisms represent AMOC-induced fast-acting atmospheric teleconnections on decadal timescales and suggest a similar temperature development between the N-Atlantic and the N-Pacific.

In contrast, Kiefer and Kienast (2005) and Gebhardt et al. (2008) found an inversed millennial-scale pattern of SST oscillations with SST maxima at H1 and the YD in the NW-Pacific (core MD01-2416 and ODP883) as indicated by Mg/Ca-derived and planktonic foraminiferal SIMMAX-based SSTs. This temporal pattern of NW-Pacific SST development is in harmony with model results from Huang et al. (2000) and Okazaki et al. (2010). According to Huang et al. (2000), a slowdown of the Meridional Overturning Circulation in the N-Atlantic (like during H1 and YD) may result in N-Pacific warming due to a reduction of upwelling of cold and nutrient-rich Pacific Deep Water in the N-Pacific subpolar gyre. However, the model experiments of Huang et al. (2000) do not consider the environmental background conditions associated with expanded northern hemisphere ice-sheets during H1 and YD. The study of Okazaki et al. (2010) also suggests a warming in the N-Pacific during times of AMOC slowdown but due to the establishment of the PMOC. Enhanced meridional overturning would result in strengthened northeastward upper-ocean heat transport via the North Pacific Current, thereby warming the N-Pacific, in particular in the Pacific Northeast. Recently, Chikamoto et al. (2012) simulated an AMOC shutdown using glacial boundary conditions (also considering a closed Bering) and examined the impact on N-Pacific climate history by using two different models. Their results indicate that the spatial temperature pattern in the N-Pacific is strongly coupled to the strength of the PMOC. This model experiments suggest cooler SSTs in the NW-Pacific for both cases, a strong and a weak PMOC. However, in case of a strong PMOC the NE-Pacific experienced surface warming due to an enhanced poleward transport of heat and salt from the subtropics to the extratropics via the Kuroshio–North Pacific Current system. Hence, the PMOC associated impact on SSTs seems to be too weak to compensate for the SST cooling in the NW-Pacific during times of expanded northern hemisphere ice-sheets. These results favor AMOC-induced atmospheric teleconnections as the main driver for the SST development in the subarctic N-Pacific and are in accordance with our SST reconstructions from the NW-Pacific.

However, the inconsistent deglacial pattern in the subarctic N-Pacific between alkenone-derived SSTs (this study) and Mg/Ca-derived and planktonic foraminiferal SIMMAX-based SSTs (Kiefer and Kienast, 2005; Gebhardt et al., 2008) raise the question of whether the differences can be explained by stratigraphic uncertainties, by the use of different SST proxies and/or regional oceanographic deviations. The stratigraphic differences are mainly based on the application of different paleo-reservoir $^{14}C$ ages (section 4.4). Compared to our age model, their radiocarbon-based age constraints rely on variable reservoir ages (Sarnthein et al., 2006, 2007). If we apply this variable reservoir correction to our age model (not shown), it would slightly and comparably

affect the stratigraphic position of the B/A temperature maximum in all our records. The temperature increase at the transition from the glacial into the B/A would lag, relative to our age model, by 100–200 years. The end of this temperature maximum would lead that of our age model by up to 350 years. As a result, the temperature maximum remains within the interval of the B/A and will not result in an anti-phased SST pattern between the N-Pacific and the N-Atlantic in our records. The different appearance of the temperature maxima between our and other records (core MD01-2416, ODP-Site 883) cannot easily be ascribed to age model discrepancies. Assuming that the original planktonic $^{14}$C ages (uncorrected) within the NW-Pacific region are marked by similar reservoir ages over time, the SST maxima and minima would occur at different time intervals anyway. For example, the most pronounced temperature maximum at core MD01-2416 occurs between 14,430–13,820 $^{14}$C years (original) and has been assigned to the beginning of a $^{14}$C-plateau that ranges between 16,700–15,300 calendar years BP. The most pronounced temperature maximum in our SST records occurs between 13,350–12,500 $^{14}$C years (original). These ages would correspond to another $^{14}$C-plateau, which marks the beginning of the B/A from 14,900–14,200 calendar years BP (Gebhardt et al., 2008). However, core MD01-2416 provides no SST maximum at this stratigraphic position.

Hence, we speculate that the different SST proxies are afflicted with diverse temperature signals due to seasonal bias and formation of the proxy signal at different water depths. The modern alkenone signal has been shown to reflect the late summer/autumn SST (0–30 m) in the NW-Pacific (Harada et al., 2003; Harada et al., 2006a; Seki et al., 2007). The Mg/Ca-based temperatures are derived from the planktonic foraminifer *N. pachyderma* sin., which is believed to calcify within the upper 200 m of the water column close to the thermocline (Bauch et al., 2002). From this it seems reasonable to assume that the proxy-related differences in the temperature signals rather reflect variations in upper ocean stratification than local differences in oceanography.

### 4.5.2. Holocene SST pattern of the N-Pacific and its marginal seas

Alkenone-derived SST reconstructions from the NW-Pacific region are characterized by a pronounced temperature maximum during the early Holocene between 11 and 9 ka BP (Figs. 4.5 and 4.8). This temperature maximum coincides with the maximum in northern hemisphere summer insolation (June–August) (Laskar et al., 2004). In addition, recent model experiments suggest the reopening of the Bering Strait as another forcing mechanism that has the potential to influence the SST development in the Bering Sea and the NW-Pacific (Hu et al., 2010; Okumura et al., 2009). The reopening of the Bering Strait due to deglacial sea-level rise has been dated to ca. 11 ka BP (Elias et al., 1996; Elias et al., 1997). According to the model results, a reopening of the Bering Strait would increase the freshwater flux from the N-Pacific to the N-Atlantic. This would result in a weakening of the AMOC and a cooling in the N-Atlantic. The N-Pacific would become slightly warmer due to an increased meridional heat transport from the tropics to the extratropics. In addition to the insolation forcing, the gateway-related oceanic forcing may have contributed to extra warming in the NW-Pacific region during the early Holocene. The gateway-induced forcing may have been active for a restricted time interval, which may represent the phase of progressive marine inundation of the Bering Strait during rapid early Holocene sea level

rise (11–8 ka BP) (Fleming et al., 1998). Whether the SST maximum in the Bering Sea (11–9 ka BP) is related to the opening of the Bering Strait gateway remains elusive since the maximum also coincides with the maximum in northern hemisphere summer insolation.

Our SST records in combination with existing SST records from the N-Pacific are further used to reassess the hypothesis of the long-term inverse temperature development between the N-Atlantic and N-Pacific from the middle to late Holocene (Kim et al., 2004). According to Kim et al. (2004), SST trends resemble a basin-scale, long-term N-Pacific warming while the N-Atlantic cools (IOW225514 and IOW225517, Emeis and Dawson, 2003; MD952015 and MD952011, Calvo et al., 2002, Marchal et al., 2002) during the last 7 kyr. However, the interpretation of Kim et al. (2004) is based solely on one record from the subarctic NW-Pacific (GGC-15, Ternois et al., 2000), located in the Sea of Okhotsk. Our more comprehensive compilation of alkenone-based SST records from the N-Pacific and its marginal seas reveal no basin-scale, long-term warming trend over the past 7 kyr in the N-Pacific. The compilation of SST records from the N-Pacific realm hints to complex regional differences in temperature development during the middle to late Holocene (Fig. 4.8).

In the Sea of Okhotsk, the middle to late Holocene SST development is characterized by different trends with relatively large temperature fluctuations (Fig. 4.8). Core LV29-114-3 from the southeastern Sea of Okhotsk shows a clear cooling trend (-2.5°C) during the last 7 kyr. In contrast, at neighbor core GGC-15, which was the only NW-Pacific record included in the study of Kim et al. (2004), shows increased temperatures during this interval (Ternois et al., 2000). However, this SST record is possibly biased by low alkenone contents in the middle to late Holocene interval (Ternois et al., 2000). Three SST records from the central Sea of Okhotsk (XP98-PC 2 and -PC4, Seki et al., 2004a) and the southwestern Sea of Okhotsk (MD01-2412, Harada et al., 2006b) are marked by a pronounced temperature minimum between 6–3 ka BP. Only core MD01-2412 shows a clear SST trend, which points to a warming during the late Holocene (Fig. 4.8). Altogether, we partly ascribe the differences in SST development to a variable inflow of surface water masses from the N-Pacific and the Japan Sea. Core LV29-114-3 is located at the main entrance of Pacific water masses delivered by the EKC (via Krusenstern Strait), which transports relatively cold water-masses to the Sea of Okhotsk. The Holocene cooling trend at core LV29-114-3 thus might be related to temperature changes in the source region of the EKC. On the other hand core MD01-2412 is influenced by the inflow of warm water masses from the Japan Sea via the Soya Strait. The warming trend may indicate a strengthened influence of the Japan Sea.

In the Bering Sea, the middle to late Holocene SST development is derived from two sediment records only, one from the eastern (HLY0202-51JPC, Caissie et al., 2010) and one from the western part (SO201-2-77KL, this study). Both temperature records reveal a consistent pattern of SST development with a net warming indicated by the linear regression trend (Fig. 4.8). This trend seems to be related to a SST rise around the mid- to late Holocene transition (ca. 3.5 ka BP).

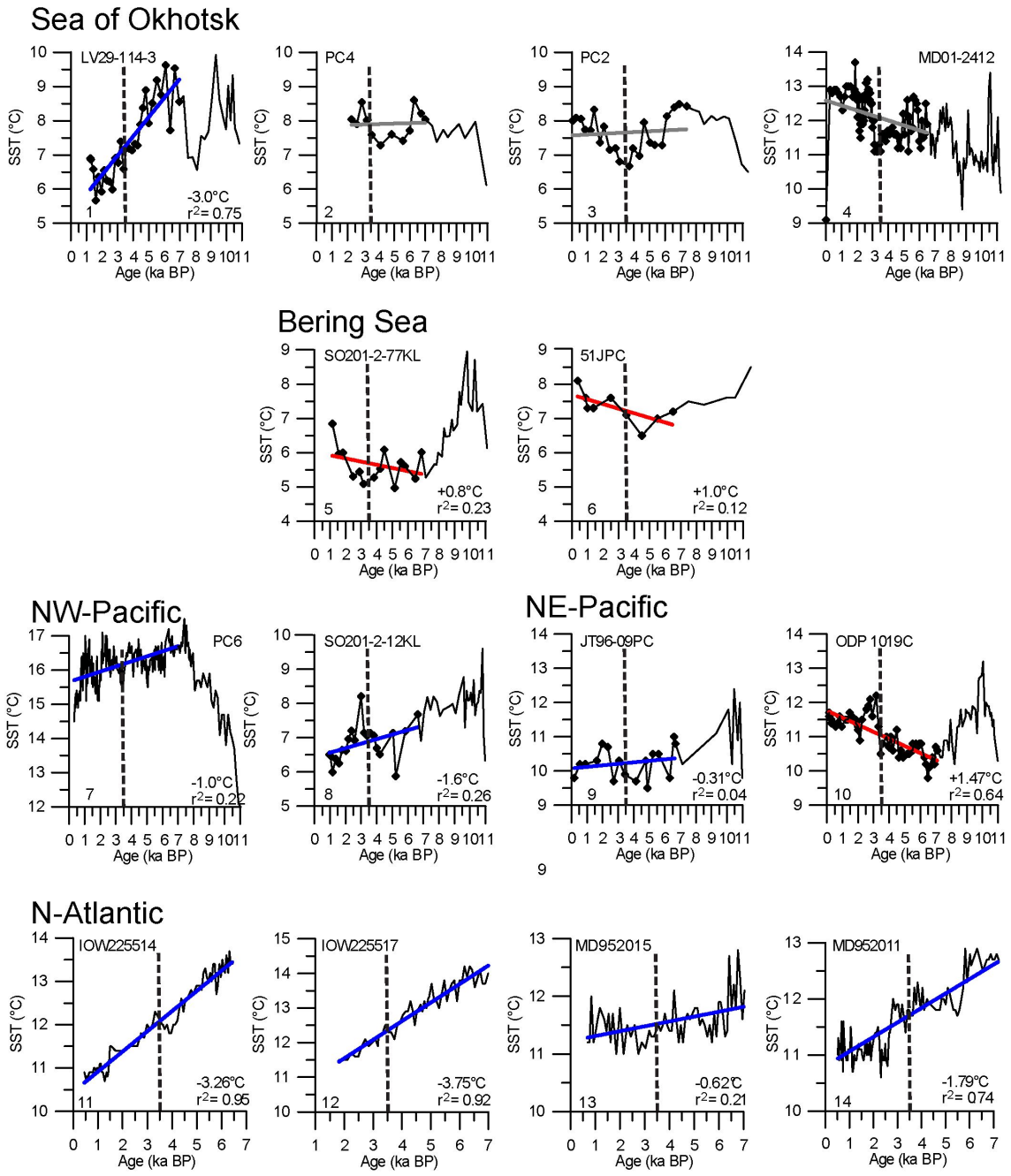


**Figure 4.8.:** Holocene compilation of alkenone-based SST reconstructions for the Sea of Okhotsk (1-4) Bering Sea (5-6) subarctic NW-Pacific (7-8), subarctic NE-Pacific (9-10) compared with subarctic N-Atlantic alkenone-derived SSTs (11-12, Emeis and Dawson, 2003; 13-14, Marchal et al., 2002; 14, Calvo et al., 2002) from the middle to late Holocene. The stippled vertical lines indicate the middle to late Holocene boundary in every record. Linear regression trends are given for all records (blue, red and gray thick lines) for the last 7 kyr BP. Correlation coefficients $r^2$ are shown in the lower right corners, respectively.

The subarctic NW-Pacific SST records reveal a cooling trend from the middle to late Holocene (PC6, Minoshima et al., 2007a; SO201-2-12KL, this study; Fig. 4.8). Available temperature records from the subarctic NE-Pacific margin show no consistent picture of SST development during the last 7 kyr BP (JT96-09PC, Kienast and McKay, 2001; ODP 1019C, Barron et al., 2003; Fig. 4.8). As the SST record from core JT96-09PC indicates weak cooling over the last 7 kyr, SSTs at ODP site 1019 are marked by a clear warming trend.

In summary, the compilation of alkenone-derived SST records from the N-Pacific and its marginal seas show no consistent SST trends and thus do not corroborate the basin-scale, long-term warming from the middle to late Holocene in the N-Pacific (Kim et al., 2004). Regionally consistent pattern in SST development are distinguished for the Bering Sea and the subarctic NW-Pacific, however with opposing trends during the last 7 kyr. The Bering Sea is marked by a warming trend and the subarctic NW-Pacific is characterized by a cooling trend from the middle to late Holocene. The SST development within the Sea of Okhotsk is rather diverse. If the Holocene SST development in the NW-Pacific has been directly affected by variations in local insolation (external forcing), one would expect a consistent response. A direct response to the long-term weakening in northern hemisphere summer insolation (June–July) would call for a decrease in SSTs from the middle to late Holocene. Accordingly, the cooling trend in the NW-Pacific could be partly attributed to the decrease in summer insolation. On the other hand the opposing SST development in the Bering Sea as well as the diverse SST pattern in the Sea of Okhotsk also call for a strong imprint of other processes (internal forcing), involving atmosphere–ocean interactions. AMOC-induced changes, which apparently played a key role for the SST development in the NW-Pacific during the last deglacial period, seems to be of minor importance since the thermohaline circulation has been reported to be relatively stable during the middle to late Holocene (e.g. McManus et al., 2004). Regardless of the underlying forcing mechanism, changes in upper-ocean circulation have to be considered for understanding the complex Holocene SST variability in the NW-Pacific.

### 4.5.3. Changes in sea-ice extent during short climate oscillations of the last glacial termination

The variability in sea-ice distribution during the last glacial termination is closely coupled to the general SST development in the subarctic Pacific realm, although the alkenone-derived SSTs most likely reflect summer-autumn temperature variations and are not associated with the seasonal maximum in sea-ice extent. The qualitative assessment of sea-ice extent ($IP_{25}$) in the subarctic NW-Pacific suggests a highly dynamic sea-ice cover (Fig. 4.9), which at least oscillated over several hundred miles during the last deglaciation. The advancement of sea-ice reached all core sites in the study area during phases of H1 and the YD cold stages and is accompanied by coldest temperatures, derived from our SST records in the NW-Pacific (Fig. 4.5). Due to the limited spatial coverage of sediment cores, the maximum expansion in seasonal sea-ice cover may have been much larger during these intervals. Conversely, the absence of the $IP_{25}$ suggests ice-free conditions at all our core locations during phases of the B/A and the early Holocene warm intervals, which is also in accordance with warmest intervals, derived from our SST records (Fig. 4.5). During the early Holocene the maximum in sea-ice extent was even more limited compared to today (Zhang et al., 2010) (Fig. 4.9). This is suggested by the absence of $IP_{25}$ at the northernmost core site SO201-2-114KL, which today is influenced by sea-ice advances during winter. These findings are underpinned by pronounced millennial-scale shifts in diatom assemblages at core SO201-2-12KL, indicative for changes in seasonal sea-ice cover during the past 15 kyr (Fig. 4.6). High percentages of *F. oceanica* are indicative of the presence of sea-ice during the YD. High percentages of *N. seminae* reflect open water conditions during the B/A and the early Holocene.

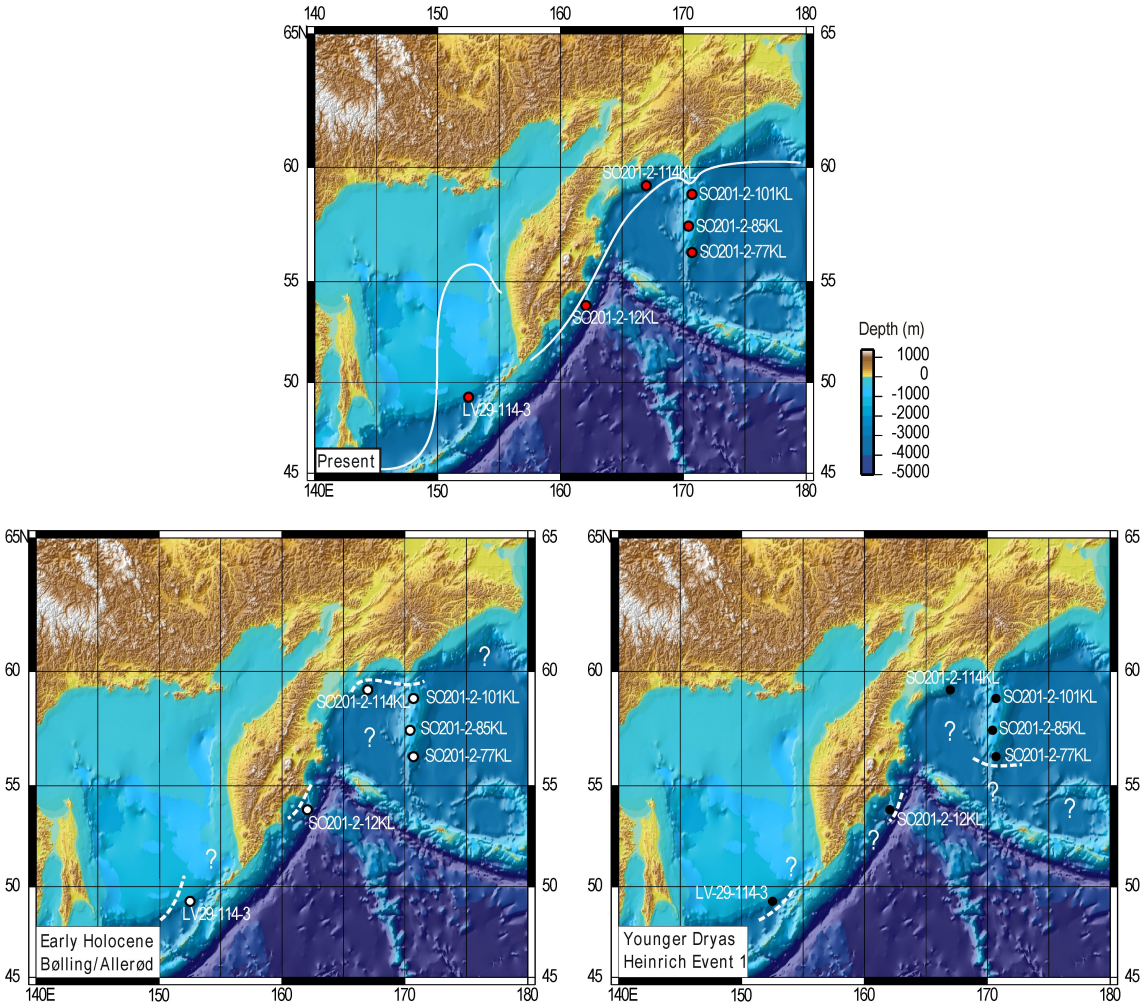


**Figure 4.9.:** Sea-ice extent (dashed lines) derived from occurrence/absence of $IP_{25}$ sea-ice diatoms biomarker measured on a set of six sediment records during time slices of the Bølling/Allerød and Early Holocene (lower left panel), the Younger Dryas and Heinrich Event 1 (lower right panel) compared with the modern sea-ice distribution (redrawn after Zhang et al., 2010) in the subarctic NW-Pacific today (upper panel). Question marks indicate regions where no information of the past sea-ice coverage is available. White circles indicate no $IP_{25}$ was found and black circles mark samples where $IP_{25}$ was detected in the sediment records according to the time slice. Note the strong expansion of sea-ice in the subarctic NW-Pacific during times of H1 and YD, where $IP_{25}$ was detected in every sediment record and thus the maximum sea-ice boundary was shifted several hundred miles to the South (especially in the western Bering Sea) compared to today. During phases of the B/A and early Holocene $IP_{25}$ was absent in all sediment records and thus no sea-ice presence inferred at the core sites.

Combining the information of both proxies ($IP_{25}$ and diatom assemblages) also enables to identify different stages of sea-ice conditions, e.g. permanent sea-ice coverage versus seasonal or no sea-ice presence. With respect to the position of core SO201-2-12KL high amounts of *F. oceanica* during the YD and relatively low amounts during the last glacial provide not necessarily a discrepancy. Since *N. seminae* is marked by extremely low values during both intervals, we infer that the glacial position of the sea-ice margin was in comparison to the YD further offshore of core SO201-2-12KL. At the core site, perennial sea ice cover prevailed during the glacial and the retreat of the summer sea-ice boundary may have reached the core location only occasionally. This interpretation is also supported by low total diatom abundance during the last glacial, as resulted from

enhanced sea ice coverage, which further limits phytoplankton growth. After ∼15 ka BP (beginning of the B/A) total diatom abundance is by an order of magnitude higher (not shown). Our results are also in harmony with previous sea-ice reconstructions based on diatom assemblages and paleo-productivity studies (Sancetta, 1983; Sancetta and Robinson, 1983; Sancetta, 1992; Cook et al., 2005; Katsuki and Takahashi, 2005; Okazaki et al., 2005b; Sakamoto et al., 2006; Katsuki et al., 2009; Caissie et al., 2010). The conclusive variability between SST and the $IP_{25}$-proxy highlights the potential of this relative new sea-ice proxy for more detailed spatial time slice reconstructions in the N-Pacific realm to assess the climate dynamics and feedback mechanisms during millennial-scale climate fluctuations of the last deglaciation.

## 4.6. Conclusions

1. Alkenone-temperatures derived from high-resolution sediment records in the subarctic NW-Pacific, the Sea of Okhotsk and the western Bering Sea show a deglacial temperature pattern similar to the NE-Pacific and even to the N-Atlantic and Greenland temperature variability. From this we suggest a close linkage to deglacial variations in AMOC associated with rapid atmospheric teleconnections, which resulted in a quasi-synchronous SST development between the N-Atlantic and the N-Pacific during the last glacial termination. Although the SST pattern between the N-Atlantic and N-Pacific show striking temporal similarities, uncertainties in age control related to a lack of knowledge in $^{14}C$ reservoir ages of N-Pacific surface waters may bias the timing of SST changes by up to several hundred years.

2. During the middle to late Holocene, the subarctic N-Pacific reveals a complex SST pattern, suggesting strong regional overprints. The compilation of alkenone-derived SST records from the NW-Pacific, the Bering Sea and the Sea of Okhotsk does not support the hypothesis of a long-term Holocene temperature seesaw between the N-Atlantic and N-Pacific associated with a basin-scale warming trend in the N-Pacific during the last 7 kyr. Only the Bering Sea records reveal a tendency towards warmer temperatures compared to a slight cooling in the NW-Pacific. The records from the Sea of Okhotsk exhibit both cooling and warming trends as well as large fluctuations during the middle to late Holocene.

3. Past sea-ice expansion were reconstructed from a set of six sediment records by qualitative assessment of the $IP_{25}$ biomarker for cold (H1 and YD) and warm (B/A and early Holocene) stages and compared to diatom studies during the last glacial termination in the NW-Pacific. Our results suggest a strong variability of sea-ice extent and a close coupling to SST fluctuations in the N-Pacific. The sea-ice advanced at least by several hundred miles during phases of H1 and YD. During the phases of B/A and the early Holocene the maximum in sea-ice cover seems to have been even more reduced compared to today.

## Acknowledgements

This study resulted from the German-Russian multidisciplinary research project "KALMAR–Kurile-Kamchatka and Aleutean Marginal Sea-Island Arc Systems: Geodynamic and Climate Interaction in Space and Time". We gratefully acknowledge the Master and crew of R/V Sonne cruise SO201-2 and thank for their professional support onboard. We also would like to thank the three anonymous reviewers, which helped to improve the quality of this manuscript. This study was funded by the German Federal Ministry of Education and Research (BMBF) grant no. 03G0672B and 03G0672A.

**Table 4.2.:** AMS-$^{14}$C ages of the sediment records with calibrated calendar age $\pm 1\sigma$ (years) and applied reservoir age correction used in this study.

| Lab. No. | Sediment core | Core depth (cm) | Radiocarbon age (years) | Calendar age $\pm 1\sigma$ (years) | Reservoir age (years) |
|---|---|---|---|---|---|
| transferred age | LV29-114-3 | 108 | 5850±60[1] | 5607-5730 | 900 |
| OS-88042 | | 162 | 8320±40 | 8236-8310 | 900 |
| KIA30864 | | 197 | 9630±50 | 9764-10067 | 900 |
| KIA30863 | | 232 | 10465±50 | 10808-11080 | 900 |
| KIA30867 | | 272 | 12290±55 | 13164-13308 | 900 |
| KIA30865 | | 292 | 13180±60 | 13960-14457 | 900 |
| KIA30868 | | 317 | 14400±80 | 16538-16827 | 900 |
| KIA30866 | | 352 | 15130±80 | 17117-17497 | 900 |
| OS-85655 | SO201-2-12KL | 210 | 9390±40 | 9484-9527 | 900 |
| KIA44680 | | 295 | 10570±50 | 11080-11191 | 900 |
| OS-87895 | | 340 | 10800±65 | 11231-11368 | 900 |
| OS-92047 | | 508 | 12500±50 | 13340-13498 | 900 |
| OS-87891 | | 550 | 12900±50 | 13782-13918 | 900 |
| OS-87902 | | 610 | 13350±65 | 14219-14752 | 900 |
| OS-92150 | | 695 | 13900±55 | 15227-15872 | 900 |
| KIA44682 | | 820 | 16160±80 | 18491-18666 | 900 |
| KIA44683 | | 875 | 17090±90 | 19254-19457 | 900 |
| OS-85671 | SO201-2-77KL | 105 | 9570±45[2] | 10051-10152 | 700 |
| OS-85658 | | 115 | 10450±40[3] | 11174-11222 | 700 |
| OS-90700 | | 155 | 11500±50 | 12608-12727 | 700 |
| OS-85657 | | 167-170 | 12750±50 | 13823-13967 | 700 |
| OS-85664 | | 180 | 13200±45 | 14501-14945 | 700 |
| OS-85665 | SO201-2-85KL | 26 | 9950±40[2] | 10378-10507 | 700 |
| KIA42231 | | 45 | 10315±65[3] | 10791-10966 | 700 |
| OS-85669 | | 60 | 11950±45 | 13104-13217 | 700 |
| KIA42232 | | 70 | 12620±90 | 13665-13887 | 700 |
| OS-87896 | | 95 | 13850±55 | 15822-15803 | 700 |
| OS-87890 | | 135 | 17350±65 | 19575-19895 | 700 |
| KIA42233 | | 155 | 20720±160 | 23706-24194 | 700 |
| OS-87887 | SO201-2-101KL | 10 | 12600±55 | 13686-13838 | 700 |
| OS-88041 | | 90 | 14950±60 | 17165-17506 | 700 |
| KIA42229 | | 110 | 17310±120 | 19541-19919 | 700 |
| transferred age | | 140 | 20720±160[4] | 23706-24194 | 700 |
| KIA42230 | | 190 | 22510±190 | 25876-26351 | 700 |
| KIA42506 | | 260 | 29270±440 | 32121-33539 | 700 |
| KIA42235 | SO201-2-114KL | 39 | 10200±70 | 10660-10805 | 700 |
| KIA42236 | | 76-78 | 10645±50 | 11249-11404 | 700 |
| KIA42237 | | 114 | 12160±80 | 13249-13403 | 700 |
| KIA42238 | | 153 | 13410±100 | 14727-15237 | 700 |

[1] - $^{14}$C age transferred from sediment core V34-98 (Gorbarenko et al., 2002a)
[2] - $^{14}$C ages used to define the carbonate spike 1
[3] - $^{14}$C ages used to define the carbonate spike 2
[4] - $^{14}$C age transferred from sediment core SO201-2-85KL

# 5. Deglacial history of (sub) sea surface temperatures and salinity in the subarctic NW Pacific: Implications for upper-ocean stratification

**Based on:** *"Deglacial history of (sub) sea surface temperatures and salinity in the subarctic NW Pacific: Implications for upper-ocean stratification"* by Jan-Rainer Riethdorf, Lars Max, Dirk Nürnberg, Lester Lembke-Jene, and Ralf Tiedemann (to be submitted to *Paleoceanography*).

## Abstract

Based on models and proxy data it has been proposed that in the subarctic North Pacific salinity-driven stratification weakened during the last deglaciation, which might have contributed to the deglacial rise in $CO_2$. Here, we present high-resolution sub sea surface temperature ($subSST_{Mg/Ca}$) and sub sea surface salinity-approximating ($\delta^{18}O_{ivc-sw}$) records across the last 20,000 years from the subarctic North Pacific and its marginal seas, derived from combined stable oxygen isotopes and Mg/Ca ratios of the planktonic foraminiferal species *Neogloboquadrina pachyderma* (sin.). Our results indicate regionally differing changes of subsurface conditions. In general, during the Heinrich Stadial 1 and the Younger Dryas cold phases our sites were subject to reduced thermal stratification and increased advection of low-salinity water from the Alaskan Stream and East Kamchatka Current (EKC). The warm phase of the Bølling-Allerød instead, was characterized by strengthened thermal stratification and high-salinity surface water due to less dilution from the Alaskan Stream and EKC. From direct comparison with alkenone-based $SST_{Uk'37}$ estimates, we suggest that the deglacial thermocline changes were closely related to changes in seasonality and upper-ocean stratification. The modern upper-ocean conditions seem to have developed only since the early Holocene.

## 5.1. Introduction

### 5.1.1. State of knowledge

No deep water is formed in the modern subarctic N Pacific. Here, a relatively steep salinity-gradient (halocline) prevents surface water from becoming dense enough to sink, thereby isolating it from the underlying nutrient-rich deep water (Haug et al., 1999). Upper-ocean stratification most likely developed around 2.7 million years ago

(Haug et al., 1999; Sigman et al., 2004) and is maintained by several processes (Warren, 1983; Emile-Geay et al., 2003; Kiefer, 2010): (i) a restricted meridional exchange between subpolar and subtropical waters, (ii) atmospheric low-latitude moisture transport from the Atlantic to the Pacific, and (iii) northward moisture flux by the Asian monsoon. As a consequence of salinity-driven stratification, the exchange of gas, heat, and nutrients between deep and surface water is limited in the N Pacific. In contrast, the modern Southern Ocean releases carbon dioxide to the atmosphere, which is stored in deep waters. This led to the assumption that high-latitude ocean stratification drives changes in atmospheric $CO_2$-concentrations during recent glacial cycles (Haug et al., 1999; Sigman and Boyle, 2000; Sigman and Haug, 2003; Sigman et al., 2004; Jaccard et al., 2005; Sigman et al., 2010). However, growing paleoceanographic evidence (e.g. Okazaki et al., 2010) suggests that during the last deglaciation deep water was formed in the N Pacific and that the halocline had not been a permanent feature. Hence, the N Pacific might have played a more active role in the deglacial rise of atmospheric $CO_2$ than previously thought.

High-resolution records depicting the deglacial paleoceanographic evolution in the subarctic N Pacific are sparse due to a shallow lysocline and corrosive bottom waters limiting $CaCO_3$ preservation. This restricts most carbonate-bearing records to shallow depths, and for cores from intermediate and deep levels results in stratigraphic uncertainties and limited applicability of carbonate-based proxies. Moreover, regional reservoir ages of surface waters are only little known and potentially subject to strong variation (e.g. Sarnthein et al., 2007).

Nevertheless, available reconstructions of sea surface temperature (SST) and salinity (SSS) indicate strong oceanographic changes and climate oscillations in the subarctic N Pacific during the last deglaciation (20–10 ka BP) similar to those recorded in Greenland ice (Grootes et al., 1993; NGRIP members, 2004), namely the cold periods of the Heinrich Stadial 1 (referred to as H1 in this study) and the Younger Dryas (YD), and the warm phases of the Bølling-Allerød (B/A) and the Preboreal (PB). Recent studies found evidence for enhanced deep water ventilation in the NW Pacific during H1 and the YD (Ahagon et al., 2003; Ohkushi et al., 2004; Sagawa and Ikehara, 2008; Okazaki et al., 2010), while at the same time the Atlantic Meridional Overturning Circulation (AMOC) collapsed or declined (McManus et al., 2004). In contrast, higher ventilation ages were found in the western N Pacific during the B/A, which might indicate reduced ventilation of intermediate waters (Okazaki et al., 2010).

In agreement with this observation, General Circulation Models (GCM) predict a strengthening of the Pacific Meridional Overturning Circulation (PMOC) results from a rise in SSS in the N Pacific due to a weakened AMOC (e.g. Menviel et al., 2012). These studies controversially argue either for an atmosphere-controlled in-phase (Mikolajewicz et al., 1997; Krebs and Timmermann, 2007; Okumura et al., 2009), or for an ocean-controlled anti-phase (Schmittner et al., 2003, 2007; Saenko et al., 2004) relationship between the thermal evolution of the N Atlantic and the N Pacific.

Support for increased SSS during H1 and thus, for a potential disappearance of the halocline comes from Mg/Ca- and $\delta^{18}O$-based reconstructions derived from planktonic foraminifera in NW Pacific sediment cores MD01-2416 (Sarnthein et al., 2006; Gebhardt et al., 2008), and GH02-1030 (Sagawa and Ikehara, 2008). Results from core MD01-2416 suggest that during H1 maxima in SSS were accompanied by maxima in SST,

hence supporting an anti-phase relationship with the N Atlantic (Sarnthein et al., 2006; Gebhardt et al., 2008).

This, however, is in conflict with alkenone-based SST reconstructions, which indicate restricted marine productivity during H1 and a maximum in SST during the B/A in the NE Pacific (Kienast and McKay, 2001; Barron et al., 2003), the Bering Sea (Caissie et al., 2010; Max et al., in review), and the Okhotsk Sea (Ternois et al., 2000; Harada et al., 2006b; Seki et al., 2009). Mg/Ca-based results from core GH02-1030 also show a rise in SST during the B/A (Sagawa and Ikehara, 2008), which may point to a regionally differing development of the thermocline. Nevertheless, core MD01-2416 was recovered from Detroit Seamount and core GH02-1030 is affected by warm and salty Kuroshio waters. Both sites might provide quite different settings when compared to the N Pacific marginal seas.

Consequently, additional reconstructions of SST and SSS, which allow for a direct comparison between alkenone- and Mg/Ca-based results, are essential to elucidate changes in upper-ocean stratification and SST development in the subarctic N Pacific. Especially for the Okhotsk and Bering seas, which are key areas for the formation of North Pacific Intermediate Water (NPIW), salinity reconstructions are rare.

Here, we report combined stable oxygen isotope and Mg/Ca-based reconstructions of sub sea surface temperatures (subSST$_{Mg/Ca}$) and $\delta^{18}O_{ivc-sw}$ (approximating sub sea surface salinity, subSSS) for the last 20 ka BP from sediment cores recovered in the southern Okhotsk Sea, the NW Pacific off Kamchatka, and the western Bering Sea. Our results, which are compared to alkenone-based SST estimates (SST$_{Uk'37}$) derived from the same samples (Max et al., in review), show strong deglacial variations in the thermal structure of the upper water column. Moreover, we present supporting evidence that salinity-driven stratification in the N Pacific was subject to deglacial changes and that the modern halocline is a relatively recent feature as suggested by Sarnthein et al. (2004).

## 5.1.2. Regional setting

The subarctic N Pacific is characterized by a large-scale cyclonic surface circulation pattern (Fig. 5.1). At ∼40°N the North Pacific Current, an extension of the subtropical Kuroshio Current, flows eastward and brings relatively warm water (∼10°C) into the Alaskan gyre in the NE Pacific. From here the Alaskan Current, fed by freshwater discharge from the North American continent (Kowalik et al., 1994; Weingartner et al., 2005), transports surface water to the north. Subsequently, the Alaskan Stream flows westward along the Aleutian Island Arc, thereby causing surface water to flow into the Bering Sea through several passes. Within the Bering Sea, a cyclonic surface circulation develops with the East Kamchatka Current (EKC) and the Bering Slope Current (BSC) acting as western and eastern boundary currents, respectively. Cold and nutrient-rich surface waters leave the Bering Sea through the Bering Strait into the Arctic Ocean, but main outflow occurs back into the NW Pacific via Kamchatka Strait (e.g. Stabeno et al., 1999). The northern straits of the Kurile Islands provide inflow of Pacific water from the EKC into the Okhotsk Sea (e.g. Katsumata and Yasuda, 2010). In the Okhotsk Sea, brine rejection due to sea-ice formation leads to the production of Okhotsk Sea Intermediate Water (OSIW), a major component of NPIW. OSMW flows out through the Kurile Straits thereby mixing with Pacific water and forming

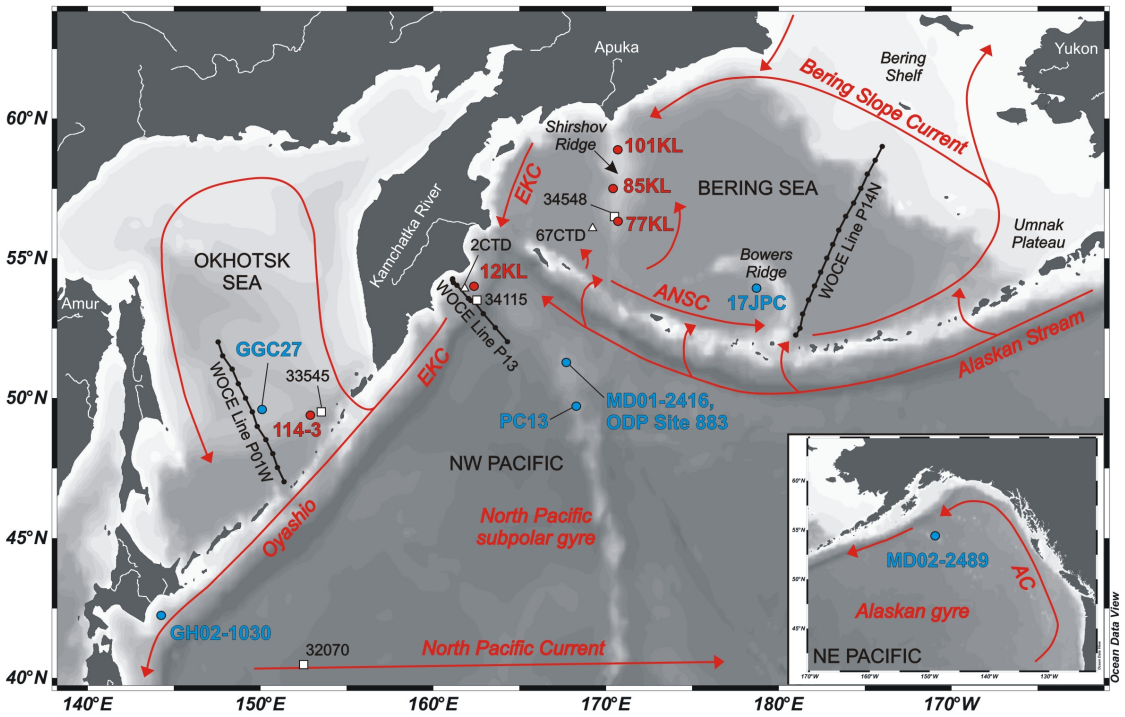


**Figure 5.1.:** Bathymetric map of the subarctic NW Pacific, Okhotsk Sea, Bering Sea, and NE Pacific (inlet). Red dots indicate sediment cores studied here, blue dots denote published reference records: MD01-2416 and ODP Site 883 (Sarnthein et al., 2004, 2006; Gebhardt et al., 2008), and PC13 (Brunelle et al., 2010) from the NW Pacific, MD02-2489 from the NE Pacific (Gebhardt et al., 2008), GH02-1030 off Japan (Sagawa and Ikehara, 2008), GGC27 from the Okhotsk Sea (Brunelle et al., 2010), and HLY-02-02-17JPC from Bowers Ridge (Brunelle et al., 2007, 2010). CTD stations from R/V Sonne expedition SO201-2 (white triangles; Dullo et al., 2009), stations from the World Ocean Atlas 2009 (white squares; Locarnini et al., 2010), and stations from the World Ocean Circulation Experiment (WOCE; black dots) referred to in the text are included. The general surface circulation pattern (after Tomczak and Godfrey, 1994; Stabeno et al., 1999) is indicated by red arrows. AC = Alaskan Current, EKC = East Kamchatka Current, ANSC = Aleutian North Slope Current. This map was generated with "Ocean Data View" (Schlitzer, 2011).

Oyashio Current water (Yasuda, 1997; You, 2003). The Oyashio Current transports this relatively cold (∼4°C), low-salinity (∼33 psu) water along the Kurile Islands to the east of Japan, where it meets with warmer and saltier water (∼34–35 psu) from the Kuroshio. Both, the EKC and the Oyashio, are western boundary currents of the N Pacific subpolar gyre.

### 5.1.3. Modern hydrography and carbonate dissolution

Characteristic oceanographic features of the subarctic NW Pacific are a strong seasonal variability of SST and SSS (Fig. 5.2), as well as a marked upper-ocean stratification. Both are linked to the seasonal interplay between the atmospheric pressure systems of the Siberian High and the Aleutian Low, which in the Okhotsk and the Bering seas leads to intense winter mixing and sea-ice formation (e.g. Niebauer et al., 1999). Stratification during summer arises from increased insolation and melting sea-ice, while a temperature minimum layer (dichothermal layer) remains at ∼100 m water depth. Waters from this layer are supposed to be formed during winter mixing in the Bering

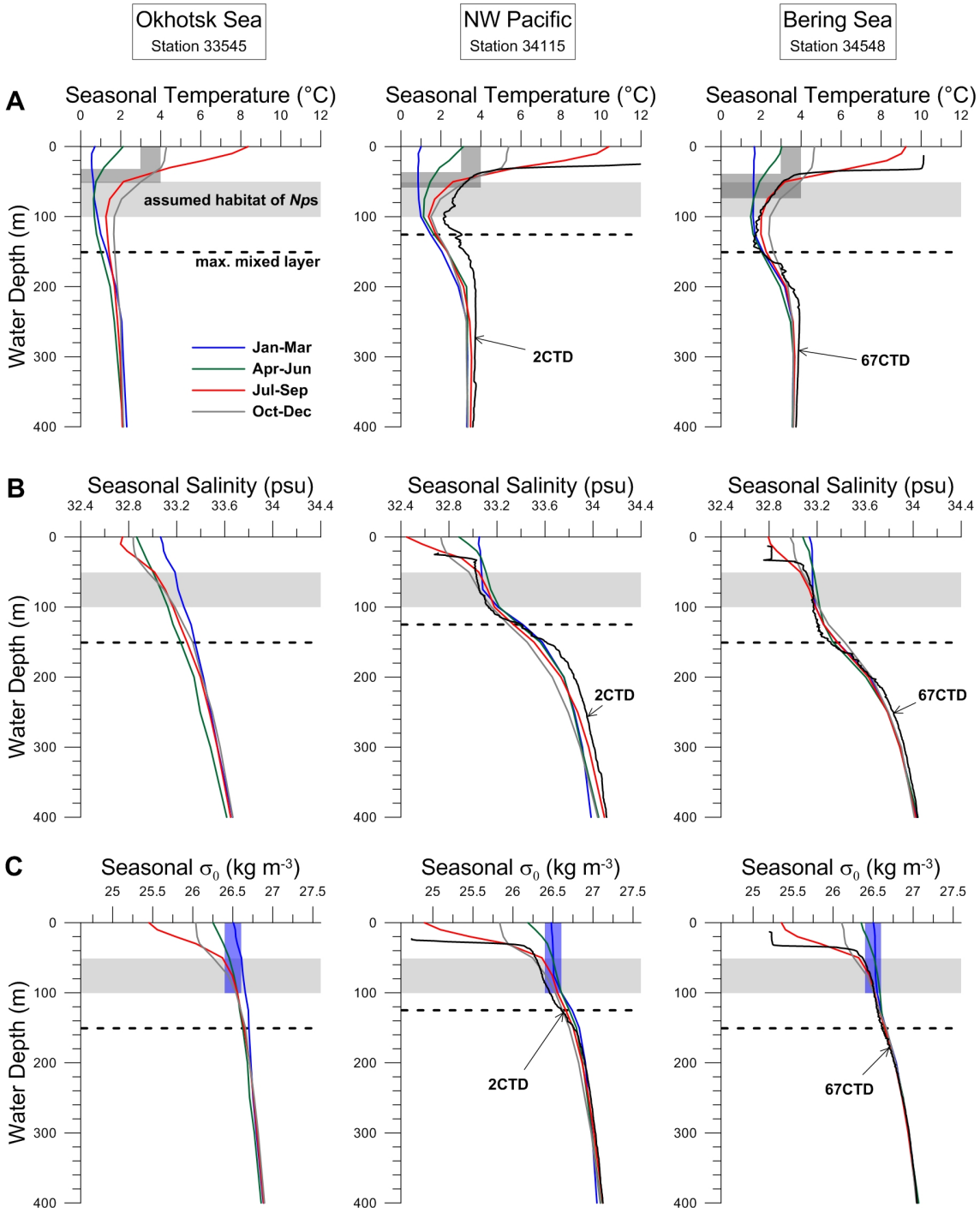


**Figure 5.2.:** Modern seasonal profiles of *in situ* temperature (A), salinity (B), and potential density ($\sigma_0$; C) for the southern Okhotsk Sea, the subarctic NW Pacific, and the western Bering Sea. Stations lying in the vicinity of our core locations were chosen from the World Ocean Atlas 2009 (WOA; stations 33545, 34115, 34548; Locarnini et al., 2010) and are shown together with CTD-measurements conducted during R/V Sonne expedition SO201-2 in September 2009 (stations SO201-2-2CTD, -67CTD; Dullo et al., 2009) (Fig. 5.1). The habitat of the planktonic foraminifer *N. pachyderma* (sin.) is assumed to lie in 50–100 m water depth (light grey-shaded bars) and to be associated with an isopycnal layer of ~26.4–26.6 kg $m^{-3}$ (blue-shaded bars in C). Depths of the maximum mixed layer (dashed line) are inferred from Miura et al. (2002) and fit WOA- and CTD-data. Note that the Mg/Ca-based average Holocene temperatures of 3–4°C (dark grey-shaded bars) only correspond to water temperatures recorded during modern summer (July–September; red line) and fall (October–December; grey line) in the assumed habitat.

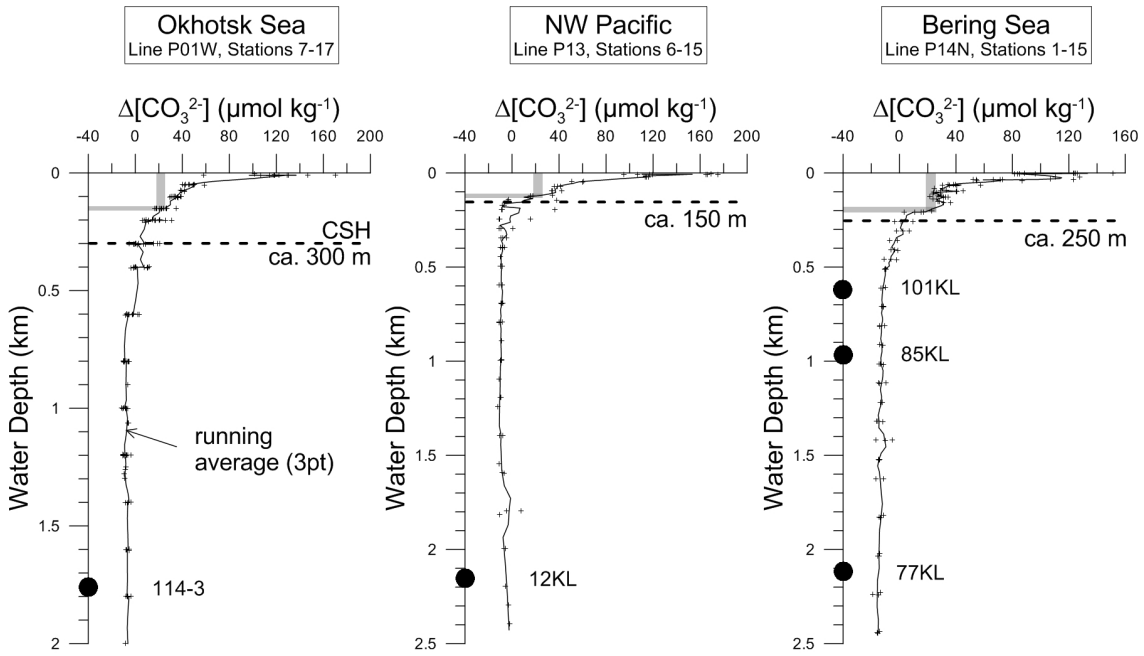


**Figure 5.3.:** Profiles of $\Delta[CO_3^{2-}]$, defined as the difference between the *in situ* carbonate ion concentration ($[CO_3^{2-}]_{insitu}$) (calculated using the CO2SYS macro for MS Excel; Pierrot et al., 2006) and $[CO_3^{2-}]$ at saturation (calculated after Jansen et al., 2002) for the Okhotsk Sea, subarctic NW Pacific, and Bering Sea. Total alkalinity and total $CO_2$ data were obtained from WOCE lines P01W (stations 7-17), P13 (stations 6-15), and P14N (stations 1-15) (available at http://cchdo.ucsd.edu/) (Fig. 5.1). Dashed horizontal lines mark the depth of the calcite saturation horizon (CSH), which represents the approximate top of the lysocline. Grey bars mark the critical $\Delta[CO_3^{2-}]$ threshold of ∼18–26 $\mu$mol kg$^{-1}$, at which $Mg^{2+}$ removal from foraminiferal tests is assumed to start (Regenberg et al., 2006). Black dots mark water depths of core locations, lying clearly below the critical $\Delta[CO_3^{2-}]$ threshold.

and Okhotsk seas and to be subsequently exported to the NW Pacific (Ohtani et al., 1972; Miura et al., 2002). As a consequence of this variability, the modern seasonal thermo- and pycnoclines mainly lie within the upper ∼30–70 m water depth at our study sites.

The subarctic N Pacific is characterized by a shallow-lying lysocline. Data obtained from the World Ocean Circulation Experiment (WOCE), used to estimate the calcite saturation state for seawater ($\Delta[CO_3^{2-}]$), reveal that the calcite saturation horizon (CSH) in the subarctic NW Pacific is between 150–300 m water depth (Fig. 5.3). Critical values of ∼18–26 $\mu$mol kg$^{-1}$ for $\Delta[CO_3^{2-}]$, below which selective removal of $Mg^{2+}$ ions from calcitic foraminiferal tests during calcite dissolution is assumed to start (Regenberg et al., 2006), are already reached at shallower depths (∼120–200 m). As all sediment cores investigated in this study were recovered below the modern CSH (Fig. 5.3), foraminiferal tests must have been affected by calcite dissolution.

# 5.2. Material and methods

## 5.2.1. Sedimentology

**Table 5.1.:** Site information.

| Core | Latitude | Longitude | Depth (mbsl) | Recovery (m) |
|---|---|---|---|---|
| LV29-114-3 | 49°22.54'N | 152°53.23'E | 1765 | 9.64 |
| SO201-2-12KL | 53°59.47'N | 162°22.52'E | 2145 | 9.05 |
| SO201-2-77KL | 56°19.83'N | 170°41.98'E | 2135 | 11.78 |
| SO201-2-85KL | 57°30.30'N | 170°24.77'E | 968 | 18.13 |
| SO201-2-101KL | 58°52.52'N | 170°41.45'E | 630 | 18.32 |

This study is based on piston cores SO201-2-12KL, -77KL, -85KL, and -101KL recovered in 2009 during R/V Sonne cruise SO201-KALMAR Leg 2 in the subarctic NW Pacific and western Bering Sea (Dullo et al., 2009). Cores 77KL, 85KL, and 101KL lie on a 280 km-long north-south transect on Shirshov Ridge in the western Bering Sea in shallow to deep intermediate water levels (630–2135 m; Tab. 5.1). Core 12KL was recovered from the continental slope off eastern Kamchatka close to Kronotsky Peninsula (2145 m) and is lying in the path of the EKC. The sedimentology of cores 77KL, 85KL, and 101KL is characterized by monotonous sequences of siliciclastic material of mainly clay and silt size. Relatively thin layers of diatomaceous ooze/silt are intercalated. Sediments of core 12KL are characterized by monotonous siliciclastic sandy/clayey silt series that are overlain by a diatomaceous sequence.

Additional samples were obtained from core LV29-114-3 (Tab. 5.1) retrieved from the southern Okhotsk Sea in 2002 during LV29-KOMEX Leg 2 cruise with R/V Akademik Lavrentyev (Biebow et al., 2003). Core 114-3 in the eastern Kurile Basin is influenced by the EKC entering the Okhotsk Sea. The sedimentary succession shows a 175 cm thick layer of diatomaceous sediment that is followed by terrigenous sediments with high magnetic susceptibility values. All cores contain only low contents of $CaCO_3$ (<5 wt.%). However, all cores show increased contents during the B/A, reaching maximum values of up to 30 wt.% in cores 12KL and 77KL.

## 5.2.2. Age model

The stratigraphic framework of all cores is in detail presented in Max et al. (in review). For the last 20,000 years, the age models are based on a combined chronostratigraphic approach including color and X-ray fluorescence (XRF) core logging data for intercore correlations, as well as AMS-$^{14}$C dating of the planktonic foraminiferal species *Neogloboquadrina pachyderma* (sin.) (Fig. 5.4). Planktonic AMS-$^{14}$C-ages were converted to calendar ages using the IntCal09 calibration (Reimer et al., 2009) assuming spatially different reservoir age corrections for the Bering and Okhotsk seas. For the last deglaciation the investigated sediment records provide sedimentation rates between 5 and 30 cm kyr$^{-1}$, for core 12KL even up to 125 cm kyr$^{-1}$, hence allowing for a centennial to millennial-scale time resolution in our reconstructions.

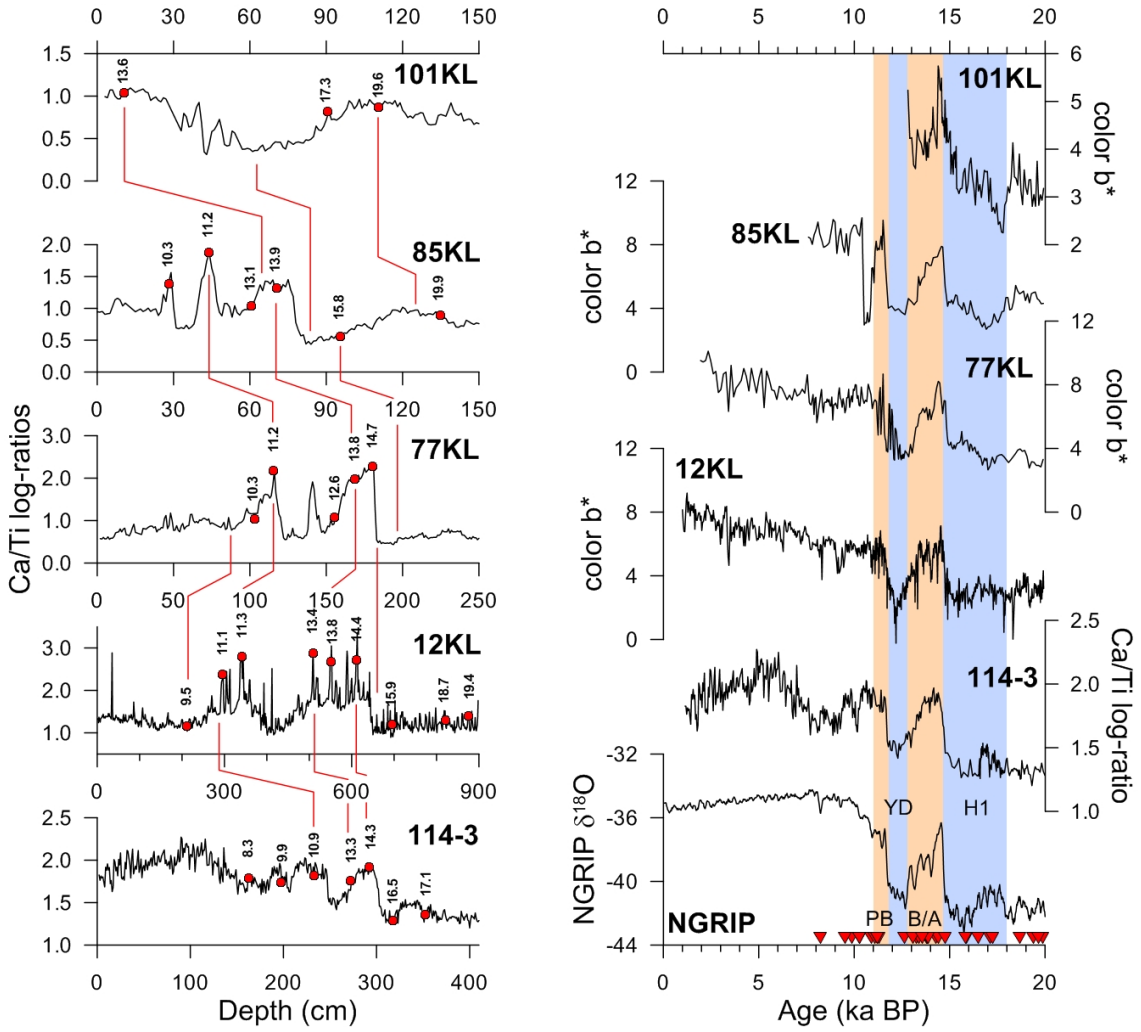


**Figure 5.4.:** Stratigraphy for cores used in this study. Left hand: XRF Ca/Ti log-ratios (shown vs. depth) are used for intercore correlations. Red dots mark AMS-$^{14}$C datings (vertical numbers indicate calendar ages). Right hand: Records of color b* and XRF Ca/Ti log-ratios (shown vs. time) provide a pattern of variability similar to that registered in the NGRIP ice core from Greenland (NGRIP members, 2004; GICC05 timescale, Rasmussen et al., 2006). Red triangels indicate age control points.

## 5.2.3. Stable isotopes and Mg/Ca analyses

Combined stable isotope and Mg/Ca analyses were performed on ∼100–150 specimens (∼500 $\mu$g) of the polar to subpolar shallow-dwelling planktonic foraminifer *Neogloboquadrina pachyderma* (sin.) (referred to as *Nps* hereafter), which were selected from the 125–250 $\mu$m size fraction. We focused on the most abundant four-chambered specimen of *Nps* from a relatively narrow size fraction to avoid potential bias due to shell size (Elderfield et al., 2002) or different morphotypes (Healy-Williams, 1992). Abundance of foraminifera was sufficient in all investigated sediment cores, except for core 12KL, which did not contain enough foraminiferal tests from 0 to 125 cm core depth (<1 wt.% $CaCO_3$).

Foraminiferal tests were gently crushed between two glass plates to open chambers and mixed with a brush for homogenization. Material was divided into two subsamples with

two thirds used for Mg/Ca and one third for stable isotope analyses, and then transferred into acid-cleaned vials. Prior to stable isotope measurements, subsamples were rinsed three times with ultrapure water and twice with ethanol including ultrasonic treatment steps of 20 seconds in order to remove clays. Dried samples were measured on a Thermo Finnigan MAT253 mass spectrometer coupled with a Thermo Scientific Kiel IV Carbonate device at GEOMAR, Kiel. Results were calibrated to the VPDB scale and referenced to the NBS19 standard. Analytical long-term precision ($N > 1000$ samples) of the used in-house Bremen carbonate standard (Solnhofen limestone) was $\pm 0.03‰$ for $\delta^{13}C$ and $\pm 0.06‰$ for $\delta^{18}O$.

Cleaning of planktonic foraminifera for Mg/Ca analyses followed the protocol of Barker et al. (2003) and included a reductive cleaning step using hydrazine ($N_2H_4$) as reducing agent to remove metal oxides. The oxidation step using hydrogen peroxide ($H_2O_2$) to remove the remaining organic matter was applied after a sample transfer to new acid-leached vials. Final leaching was performed using 0.001 M nitric acid ($HNO_3$). Samples were dissolved immediately before analysis with ultra-pure 0.075 M $HNO_3$ including 25 min of ultrasonic treatment and subsequent centrifugation. About 500 $\mu$l of supernatant was then transferred into polypropylene tubes and diluted with 1.8 ml of 0.075 M $HNO_3$ containing 10 ppm of yttrium as an internal standard.

Samples were measured on an axial viewing ICP-OES (VARIAN 720-ES coupled with SPS3 Sample Preparation System). We used spectral lines 279.553 nm for Mg and 370.602 nm for Ca. Post-processing included automatic correction for analytical drift and normalization to the ECRM 752-1 standard, which is used as internal consistency standard applying a reported Mg/Ca ratio of 3.761 mmol mol$^{-1}$ (Greaves et al., 2008). For Mg/Ca measurement the analytical long-term precision of the ECRM752-1 standard, which was measured after each batch of 10 samples including 1 blank, was 0.1 mmol mol$^{-1}$ ($2\sigma$). Due to very low carbonate contents of the sediments and hence, general low abundance of foraminifera, full sample treatment was only repeated for 11 samples that were considered as outliers. These replicate analyses provided discrepancies between 0.1–0.7 mmol mol$^{-1}$ for Mg/Ca that may indicate a contamination of the samples. Benthic and planktonic $\delta^{18}O$, as well as foraminiferal element ratios (Mg/Ca, Mn/Ca, Fe/Ca, Al/Ca) are shown in the supplementary information.

To detect possible contamination by detrital material and secondary diagenetic coatings, which might affect foraminiferal Mg/Ca ratios (e.g. Boyle, 1983b; Barker et al., 2003; Rosenthal et al., 2000), ratios of foraminiferal Mn/Ca, Fe/Ca, and Al/Ca were monitored simultaneously with Mg/Ca. Our cores featured relatively high average Fe/Ca, Mn/Ca, and Al/Ca ratios ranging between 0.21–1.84 mmol mol$^{-1}$, 0.02–0.06 mmol mol$^{-1}$, and 0.08–0.20 mmol mol$^{-1}$, respectively. In particular Fe/Ca ratios were higher than the 0.1 mmol mol$^{-1}$ suggested by Barker et al. (2003) for uncontaminated foraminiferal tests. Each core was individually tested for linear relationships between Mg/Ca and the other ratios, which is explained in the supplementary information. In case of linear correlation coefficients ($R^2$) higher than 0.6, we considered our Mg/Ca analyses possibly affected by contamination and defined core-specific thresholds for Fe/Ca, Mn/Ca, and Al/Ca. No samples from the last 20 ka BP were excluded according to this approach and hence are supposedly not contaminated. Two samples were rejected due to very high Mg/Ca ratios (2.2 and 2.4 mmol mol$^{-1}$) as indicated in the supplementary information.

To improve sampling resolution for core 114-3, Mg/Ca-results based on former mea-

surements of 30 specimens for stable isotopes and 50 specimens for Mg/Ca selected from the 150–250 $\mu$m size fraction were included in our dataset. These samples were also cleaned according to the protocol of Barker et al. (2003) but without a reductive cleaning step and analyzed using a radially viewing ICP-OES (Ciros CCD SOP, Spectro A.I.) at the Institute of Geosciences, University of Kiel, on spectral lines 183 nm for Ca and 270 nm for Mg. Samples cleaned with the reductive step show either similar or relatively increased Mg/Ca ratios, albeit without any systematical differences with respect to non-reductively cleaned samples. We consider the results of both datasets as consistent as the mean offset between both datasets is not constant and lies within the error range of the measurements ($\sim$0.1 mmol mol$^{-1}$), in agreement with studies comparing both cleaning methods (e.g. Rosenthal et al., 2004; Groeneveld et al., 2008).

### 5.2.4. Mg/Ca temperature signal

As there is no locally established Mg/Ca-temperature calibration for *Nps* in the subarctic N Pacific, we used the linear equation of Kozdon et al. (2009) to calculate sub sea surface temperatures from Mg/Ca ratios of *Nps* (subSST$_{Mg/Ca}$):

$$Mg/Ca\ (mmol\ mol^{-1}) = 0.13 \times T(^{\circ}C) + 0.35 \tag{5.1}$$

Considering the slope in Eq. 5.1, the long-term analytical precision of our Mg/Ca measurements translates into an error of $\pm$0.8°C. This temperature calibration is based on Holocene core-top samples from high-latitude Nordic Seas used in a cross-calibration approach between Mg/Ca and independent $\delta^{44/40}$Ca measurements. In contrast, most other temperature calibrations for *Nps* are of exponential character and assume constant calcification depths.

We used this specific relationship because we consider the depth habitat of *Nps* most likely to be related to the seasonal thermo- and pycnocline, similar to the Nordic Seas and the Arctic Ocean. Studies conducted in these areas show that shell calcification of *Nps* mostly occurs at or close to the depth of the main thermocline between 50 and 200 m (Kohfeld et al., 1996; Bauch et al., 1997; Simstich et al., 2003). Based on these studies Sarnthein et al. (2004, 2006) assume a depth range of 30–100 m in the NW Pacific. Bauch et al. (2002) for the Okhotsk Sea calculated $\delta^{18}$O-based average calcification depths lying within the upper 50–200 m, which was in accord with maximum abundances of *Nps*. From their results, Bauch et al. (2002) concluded that *Nps* lives at the bottom of the thermocline. Comparison with temperatures inferred from $\delta^{18}$O and hydrographic data indicate variable calcification depths of *Nps* that are associated with an isopycnal layer (Kozdon et al., 2009). Kuroyanagi and Kawahata (2004) from tow samples from the western N Pacific and Japan Sea report a depth habitat of *Nps* lying below the pycnocline (>20 m w.d.) supporting this indication.

WOA data show that at our study sites during boreal summer (July–September) the average depth of the pycnocline lies at $\sim$30 m w.d., and that the thermocline extends to $\sim$70 m with a temperature minimum of 1–2°C in $\sim$100 m (Fig. 5.2). At all sites an isopycnal layer with a potential density ($\sigma_0$) of 26.4–26.6 kg m$^{-3}$ is present within almost the same depth interval (50–100 m). If *Nps* occupies a habitat that lies below the pycnocline and is related to an isopycnal layer covering depths down to the bottom of

the thermocline, then the depth habitat of *Nps* must lie between 50–100 m at our sites. The assumption that *Nps* records a summer signal is supported by our reconstructed average Holocene (<8 ka BP) subSST$_{Mg/Ca}$-estimates, which range between 3–4°C and therefore only correspond to summer and fall (October–December) temperatures in the suggested depth habitat. In contrast modern boreal winter (January–March) and spring (April–June) temperatures lie below 3°C (Fig. 5.2), which also lie below our reconstructed temperatures. Accordingly, we assume *Nps* Mg/Ca data to reflect temperatures recorded during late summer and early fall in 50–100 m water depth.

Sarnthein et al. (2006) and Gebhardt et al. (2008) assumed that the temperature signal recorded by *Nps* at Site MD01-2416 is characteristic for late spring and late summer/early fall. Indeed, in the southern Aleutian Basin, Takahashi et al. (2002a) observed two maxima of biological $CaCO_3$ fluxes during spring/summer and fall that are caused by enhanced foraminiferal abundances. However, in contrast to our core locations, their sediment trap study sites as well as Site MD01-2416 are located in regions not dominantly influenced by seasonal sea-ice inhibiting marine productivity during spring. Furthermore, the southern Bering Sea primary $CaCO_3$ maximum occurred during October to November (Takahashi et al., 2002a), which was also observed along the Subarctic Front in the NW Pacific (Mohiuddin et al., 2005). These observations indicate that at our more northerly located study sites the main temperature signal of *Nps* might indeed rather represent late summer/early fall.

Application of the multispecies calibration of Elderfield and Ganssen (2000) and the relationship of Nürnberg et al. (1996) (specific for *G. sacculifer* and *Nps*) to our Mg/Ca data would produce a larger temperature variability and would result in subSST$_{Mg/Ca}$ that were on average warmer by about +1°C and +3°C, respectively. Consequently, mean Holocene temperature estimates would not fit modern instrumental data within the assumed habitat of *Nps* when using the equation of Nürnberg et al. (1996), whereas the difference to the calibration of Elderfield and Ganssen (2000) lies within the error range of our method. We thereby consider our subSST$_{Mg/Ca}$ results as reliable and the choice of the temperature calibration as justified.

Mg/Ca-based paleotemperature estimations are constrained by the influence of calcite dissolution of the foraminiferal tests in conjunction with selective removal of $Mg^{2+}$ ions (e.g. Regenberg et al., 2006, and references therein). Since all sediment cores investigated in this study were recovered below the modern CSH (Fig. 5.3), foraminiferal tests might have been affected by dissolution. Accordingly, we employed strict quality control and assessed the applicability of correction efforts. Although we admit, that our Mg/Ca ratios are to an unknown degree influenced by dissolution effects, we are confident in our results and refrained from correcting the initial Mg/Ca values. A detailed discussion on the impact of applying procedures to correct planktonic foraminiferal Mg/Ca for dissolution effects is provided in the supplementary information.

### 5.2.5. Alkenone temperature signal

We compared our subSST$_{Mg/Ca}$ records with the alkenone-based sea surface temperature (SST$_{Uk'37}$) records of Max et al. (in review), which were derived from the same samples. SST$_{Uk'37}$ estimates are calculated according to the global (60°N-60°S) core-top calibration of Müller et al. (1998), which is widely used in N Pacific temperature reconstructions:

$$U_{37}^{k'} = 0.033 \times T(^{\circ}C) + 0.044 \tag{5.2}$$

The standard error of this calibration is given as ±1.5°C (Müller et al., 1998). A core-top calibration in the eastern Bering Sea suggests that most alkenones are synthesized during September (Harada et al., 2003). Harada et al. (2006a) showed that *Emiliania huxleyi* is the most abundant alkenone producer in the NW Pacific, which is present within the upper 50 m w.d. and shows maximum export fluxes between July and November. For the western Okhotsk Sea, definitely influenced by seasonal sea-ice, maximum alkenone export fluxes were reported during September and October (Seki et al., 2007). Mean insolation calculated after Laskar et al. (2004) for July–September at 65°N is in good agreement with the $SST_{Uk'37}$ records (Fig. 5.5) supporting a restriction to late summer/early fall. Other calibrations, e.g. that of Prahl et al. (1988) and Sikes et al. (1997), in our cores produce temperatures that are higher by up to 0.1°C and 3°C, respectively. However, our reconstructed mean Holocene alkenone- and Mg/Ca-based temperature estimates almost compare with the modern instrumental range.

Differences between alkenone- and Mg/Ca-paleotemperatures can be the result of seasonal bias (e.g. Leduc et al., 2010). Due to the influence of seasonal sea-ice formation at our sites, we consider a restriction of both, alkenone producers and planktonic foraminifera, to the sea-ice-free late summer/early fall season to be more likely. Nevertheless, we consider seasonal bias possible in case of a disappearing sea-ice influence. Regarding depth habitats, in this study the alkenone signal is thought to represent temperatures from the photic zone (0–30 m w.d.), while Mg/Ca results represent temperatures from the colder subsurface (50–100 m w.d.).

## 5.2.6. Salinity estimation

Past changes in subSSS are approximated from seawater $\delta^{18}O$ estimates. The oxygen isotope signal recorded in foraminiferal calcite ($\delta^{18}O_{Cc}$) is a combination of the local seawater isotopic composition ($\delta^{18}O_{sw}$; reported in ‰ vs. SMOW) and temperature. Local $\delta^{18}O_{sw}$ is influenced by changes in global ice-volume and regional variations of salinity that are mainly controlled by local changes of the evaporation–precipitation budget (e.g. Schmidt et al., 2004). In this study, $\delta^{18}O_{sw}$ is calculated by applying the relationship of Shackleton (1974) that includes our foraminiferal values ($\delta^{18}O_{Cc}$) in combination with the corresponding Mg/Ca-based paleotemperature estimates:

$$\delta^{18}O_{sw} = \delta^{18}O_{Cc} + 0.27 - \frac{4.38 - \sqrt{4.38^2 - 4 \times 0.1 \times (16.9 - T)}}{2 \times 0.1} \tag{5.3}$$

This equation extends the results of an inorganic precipitation study (O'Neil et al., 1969) to the endobenthic foraminifera *Uvigerina peregrina*, assumed to calcify in isotopic equilibrium with seawater. Mulitza et al. (2003) found that the T–$\delta^{18}O$-relationships of *N. pachyderma* and epibenthic foraminifera species *Cibicides* are nearly identical and that *N. pachyderma* shows a mean sensitivity of 0.28‰ per °C, which is in agreement with that of *U. peregrina* within -2° to +13°C. We therefore decided to use the equation of Shackleton (1974) based on *U. peregrina*. The factor of 0.27‰ in Eq. 5.3 is due to

the conversion of $\delta^{18}O_{sw}$ from the PDB to the SMOW scale (Hut, 1987). Finally, we corrected for the global ice-volume signal following Waelbroek et al. (2002) based on a $\delta^{18}O_{sw}$ change of 1.1‰ per 130 m relative sea-level change (Yokoyama et al., 2000) to produce ice-volume corrected seawater estimates ($\delta^{18}O_{ivc-sw}$).

The absolute estimation of salinity from $\delta^{18}O_{sw}$ relies on regional calibrations and hence from actual measurements of water samples, as variations in the ratio of evaporation to precipitation can cause different $\delta^{18}O_{sw}$–salinity relationships. Such calibrations exist for the Okhotsk Sea and western subarctic Pacific (Yamamoto et al., 2001, 2002). However, the uncertainty of the $\delta^{18}O_{sw}$-approach already cumulates to ∼0.3‰ which would translate into a salinity error of about ±0.8 psu applying the calibration of Yamamoto et al. (2001). Since our study sites are characterized by a modern seasonal salinity range of ∼32.4–33.6 psu within the upper 150 m (Fig. 5.2), we consider this error as too large and did not apply a conversion into absolute salinity estimates. We rather interprete regional hydrological changes from relative changes of our $\delta^{18}O_{ivc-sw}$ results in such that heavier (more positive) $\delta^{18}O_{ivc-sw}$ values are equivalent to a rise in local subSSS, while a drop in subSSS is indicated by lighter (more negative) $\delta^{18}O_{ivc-sw}$ values.

### 5.2.7. Biogenic opal

Biogenic opal was measured via molybdate-blue spectrophotometry applying the automated leaching method of Müller and Schneider (1993). We used 20 mg of freeze-dried bulk sediment samples mixed with 100 ml of sodium hydroxide (1 M) in a water bath at 85°C for 45 min. The procedure of DeMaster (1981) was used to calculate weight percentages of biogenic opal. Reproducibility of the measurements was 1–2 weight.%.

## 5.3. Results

### 5.3.1. Temperature reconstructions

Fig. 5.5 shows our temperature reconstructions for the last 20 kyr together with the alkenone-based $SST_{Uk'37}$ records from Max et al. (in review). Reconstructed $subSST_{Mg/Ca}$ show a similar range in all cores of about 2° to 6°C, except for core 12KL, which extends this range to a maximum of ∼9°C. Also, this core records the most pronounced amplitude variations, whereas the temperature variability of the cores from both Pacific marginal seas is low. We found similar $subSST_{Mg/Ca}$ in the Bering and Okhotsk seas during the last deglaciation as reflected by reconstructions from the northernmost site (101KL) and the southernmost site (114-3).

In contrast, alkenones, which prior to 15 ka BP are characterized by concentrations below detection limit, point to increasing $SST_{Uk'37}$ of ∼3°C from the north to the south (Max et al., in review). Relative temperature changes of both proxy records (Fig. 5.5) are consistent amongst each other in all records during the last glacial termination and their overall evolution almost parallels the thermal evolution registered in the NGRIP ice core from Greenland until the onset of the early Holocene. However, in part, $subSST_{Mg/Ca}$ and $SST_{Uk'37}$ records show different trends which result in temperature

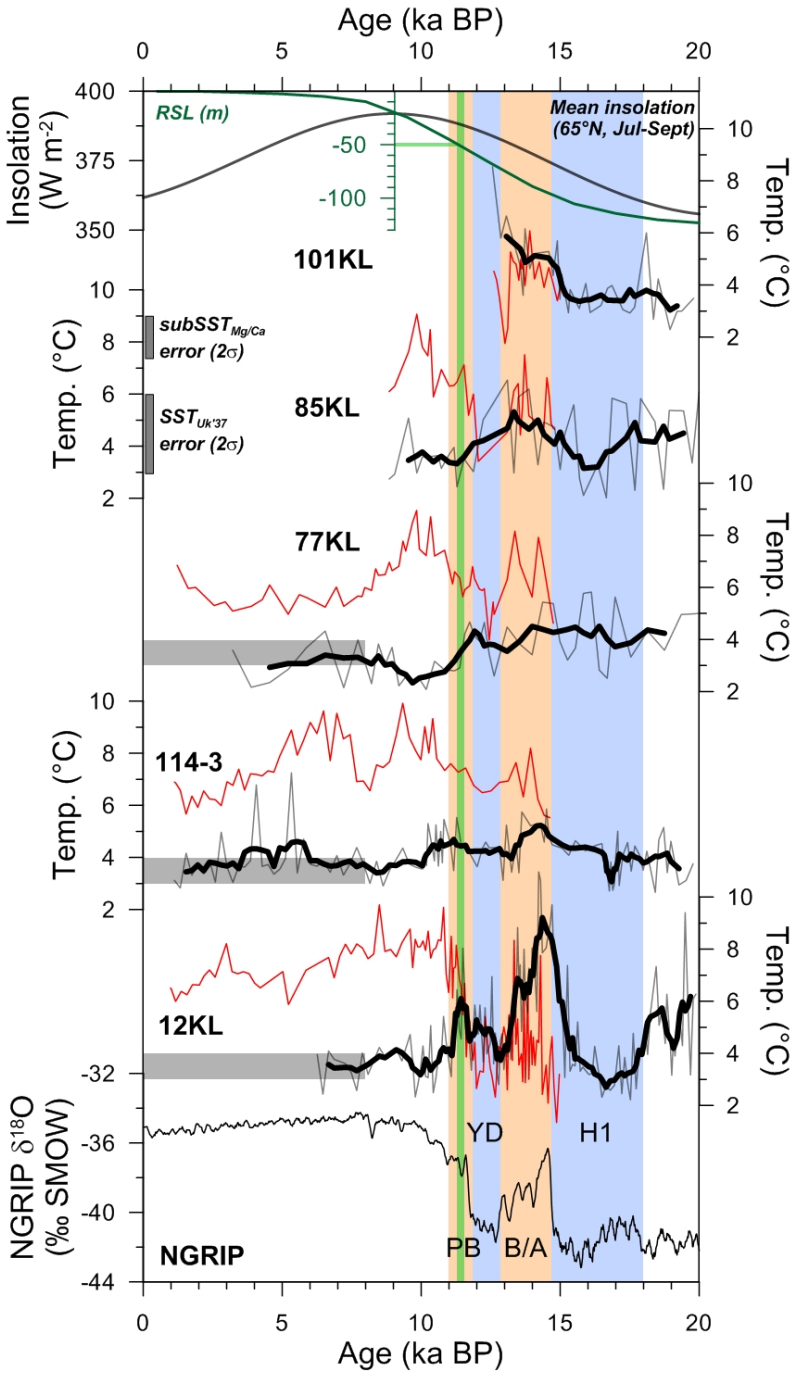


**Figure 5.5.:** Temperature reconstructions over the last 20 kyrs from the Bering Sea (SO201-2-101KL, -85KL, -77KL), the subarctic NW-Pacific off Kamchatka (SO201-2-12KL), and the southern Okhotsk Sea (LV29-114-3). The NGRIP ice core oxygen isotope record (NGRIP members, 2004; GICC05 timescale, Rasmussen et al., 2006) is for reference. Our subSST$_{Mg/Ca}$ records (light grey lines) are shown together with alkenone-based SST$_{Uk'37}$ records (thin red lines) from Max et al. (in review) on the same scale. Running 5-point-averages of subSST$_{Mg/Ca}$ (thick black lines) are given to smooth the records. The calculated error of our temperature estimates is given. Average middle to late Holocene (<8 ka BP) temperature estimates of 3-4°C are highlighted (grey vertical bars). Relative sea-level (RSL, green line) is from (Waelbroek et al., 2002), and a green vertical bar marks the interval when RSL reached the approximate sill depth of the Bering Strait (∼50 m). Mean insolation calculated for boreal summer (July–September) at 65°N (grey line) was calculated after Laskar et al. (2004). Pale orange and pale blue shadings represent the B/A and PB, and H1 and YD, respectively.

differences between the surface and subsurface (ΔT). All cores show low subSST$_{Mg/Ca}$ between 18–16 ka BP and values of ca. ∼3-4°C, supposedly reflecting the H1 stadial in the N Atlantic (18.0–14.7 ka BP, Sarnthein et al., 2001). This mimimum is most pronounced in NW Pacific core 12KL and only short-lived in core 114-3 from the Okhotsk Sea. Due to the lower temporal resolution it is not well resolved in Bering Sea cores 77KL and 85KL. Moreover, in core 85KL the Mg/Ca variability during 20–17 ka BP is very large.

At the end of H1 a warming is recorded at the transition into the following B/A. Within a period of 1,000 to 2,000 years subSST$_{Mg/Ca}$ increase by 2–4°C to maxima of ∼5–6°C at sites 114-3, 77KL, 85KL, and 101KL, and to ∼9°C at Site 12KL. SST$_{Uk'37}$ show increases from 2–6°C at 15 ka BP to 6–8°C during the B/A (Max et al., in review). While Bering Sea cores 85KL and 101KL record almost similar subSST$_{Mg/Ca}$ and SST$_{Uk'37}$ until the PB, cores 114-3 and 77KL show ΔT of ∼2–3°C during the B/A. In contrast to the other records, core 12KL shows a two-step subSST$_{Mg/Ca}$ cooling during the B/A and, most notably, negative ΔT values of up to -6°C. ΔT is minimal at the onset of the B/A and subsequently increasing, until temperatures from both proxies converge at the end of the B/A at a value of ∼4°C.

Cores 114-3, 12KL and 77KL record a cooling of subSST$_{Mg/Ca}$ following the early B/A maximum. Subsequently, subSST$_{Mg/Ca}$ minima of 3–4°C are recorded at either the end of the B/A (114-3) or at the beginning of the YD (12KL, 77KL). In contrast, core 85KL shows the temperature maximum at the end of the B/A and decreasing values since. During the YD cores 114-3 and 77KL record almost stable subSST$_{Mg/Ca}$ (∼4°C), while core 12KL is characterized by a slight warming. SST$_{Uk'37}$ show a decrease of 2–5°C into the YD (Max et al., in review). ΔT is reduced to about +2°C at sites 114-3 and 77KL, to 0°C at Site 85KL, and again becomes negative (-2°C) at Site 12KL.

Core 12KL records a pronounced and short-lived subSST$_{Mg/Ca}$ maximum of ∼6°C during the PB (∼11.5 ka BP), whereas Okhotsk Sea core 114-3 is characterized by a stronger variability between 4° and 5°C during ∼11.5–10.0 ka BP. Bering Sea cores 77KL and 85KL show decreasing and minimum subSST$_{Mg/Ca}$ of ∼3°C, respectively, during the PB. At all sites the PB is either subject to a cooling to subSST$_{Mg/Ca}$ of ∼3–4°C or followed by a respective cooling during the early Holocene. The timing for this is different at the respective sites. At Site 77KL it starts at the onset of the PB, while sites 12KL and 114-3 experience a later cooling at ∼11 ka BP and ∼10 ka BP, respectively. SST$_{Uk'37}$ increase by up to 5°C subsequent to the YD and culminate in maximum values of 9–10°C between 11–9 ka BP (Max et al., in review). Consequently, in all cores both proxies start to significantly diverge in the PB until ∼10 ka BP, with ΔT-maxima of up to 6°C. The Holocene SST$_{Uk'37}$ maximum occurs simultaneous with the insolation maximum calculated after (Laskar et al., 2004) for boreal summer (July–September) at 65°N (Fig. 5.5). Notably, SST$_{Uk'37}$ estimates from core 12KL became higher than subSST$_{Mg/Ca}$ only since the PB.

The later Holocene subSST$_{Mg/Ca}$ development is characterized by almost constant values that are ∼1°C warmer in cores 114-3 and 12KL than in Bering Sea core 77KL. In core 85KL, for which sediments are not preserved after 9 ka BP, subSST$_{Mg/Ca}$ remain at ∼3°C. Holocene subSST$_{Mg/Ca}$ estimates are lower than those of the B/A and YD but compare with those recorded during H1. For the last 9 kyr, SST$_{Uk'37}$ records from cores 114-3, 12KL, and 77KL point to a gradual ∼2°C decrease in SST$_{Uk'37}$, which in core 114-3 is interrupted between 9–7 ka BP by a cooling to YD levels (Max et al.,

in review). Hence, the temporal evolution of ΔT during the middle to late Holocene follows the $SST_{Uk'37}$ signal and records a ΔT-minimum between 9–7 ka BP in core 114-3.

### 5.3.2. Reconstruction of $\delta^{18}O_{ivc-sw}$

Reconstructed $\delta^{18}O_{ivc-sw}$ values approximating subSSS on average range between -1‰ vs. SMOW (fresher) to +1‰ vs. SMOW (more saline) during the last 20,000 years and are shown in Fig. 5.6. The most prominent variability is recorded in NW Pacific core 12KL, while our northernmost Bering Sea cores 85KL and 101KL show less amplitude variations in a narrower range of about -0.3 to +0.3‰. Notably, core 85KL shows a distinct variability around a value of 0‰. Okhotsk Sea core 114-3 records almost only negative values between -0.4‰ and 0‰, showing a variability not significantly higher than the error estimate for $\delta^{18}O_{ivc-sw}$. In general, relative changes of $\delta^{18}O_{ivc-sw}$ are regionally different, but at each site a general covariation between $\delta^{18}O_{ivc-sw}$ and $subSST_{Mg/Ca}$ is observed.

During 20–18 ka BP cores 12KL, 77KL, and 85KL show positive average values (0 to 0.4‰), whereas $\delta^{18}O_{ivc-sw}$ is negative at sites 114-3 and 101KL (-0.3‰ to 0‰). The interval 18–16 ka BP in core 12KL is marked by a $\delta^{18}O_{ivc-sw}$ decrease of about -0.6‰ until ∼17 ka BP. Bering Sea cores are characterized by low temporal resolution in combination with high variability of $\delta^{18}O_{ivc-sw}$ results during 20–16 ka BP, and, hence, do not show consistent and significant changes within that interval. Core 77KL at the end of H1 features positive values of about +0.3‰. Although in Okhotsk Sea core 114-3 a restricted negative H1-excursion of about -0.2‰ occurs at ∼16.8 ka BP, $\delta^{18}O_{ivc-sw}$ variability during H1 is very low.

At the end of H1, data from cores 114-3 and 77KL show decreasing $\delta^{18}O_{ivc-sw}$. In contrast, $\delta^{18}O_{ivc-sw}$ recorded in cores 12KL and 101KL is increasing during that time. Results from core 85KL still vary around an almost constant level, with slightly higher $\delta^{18}O_{ivc-sw}$ during the B/A. During the B/A cores 114-3 and 77KL show generally lower values than during H1 of about -0.2‰, whereas the other cores have positive values, which are maximal in core 12KL with $\delta^{18}O_{ivc-sw}$ of up to +1‰. This core is characterized by a 2-step decrease in $\delta^{18}O_{ivc-sw}$ until a minimum of -0.2‰ is reached at the end of the B/A. Here, a minimum is also recorded in core 114-3. Core 77KL shows decreasing $\delta^{18}O_{ivc-sw}$ already after ∼16 ka BP until the onset of the YD.

The YD is characterized by rising $\delta^{18}O_{ivc-sw}$ in core 12KL to +0.3‰ at 12.0 ka BP, whereas cores 114-3, 77KL, and 85KL only show insignificant changes around -0.2‰. Further, core 12KL shows a short-lived drop to ∼0‰ during the YD–PB transition ∼11.7 ka BP, before a second pronounced maximum (ca. +0.5‰) is reached in the PB near ∼11.5 ka BP. This PB maximum is only found in core 12KL, where it is followed by a sharp subsequent decrease until 10 ka BP. In core 114-3 the $\delta^{18}O_{ivc-sw}$ record, like the $subSST_{Mg/Ca}$ record, is characterized by a stronger variability around ca. -0.1‰ between 11.5 and 10.0 ka BP. Only Bering Sea core 77KL shows decreasing $\delta^{18}O_{ivc-sw}$ values since the PB until a minimum of -0.7‰ between 9 and 10 ka BP, whereas $\delta^{18}O_{ivc-sw}$ in core 85KL continues to vary around ∼0‰.

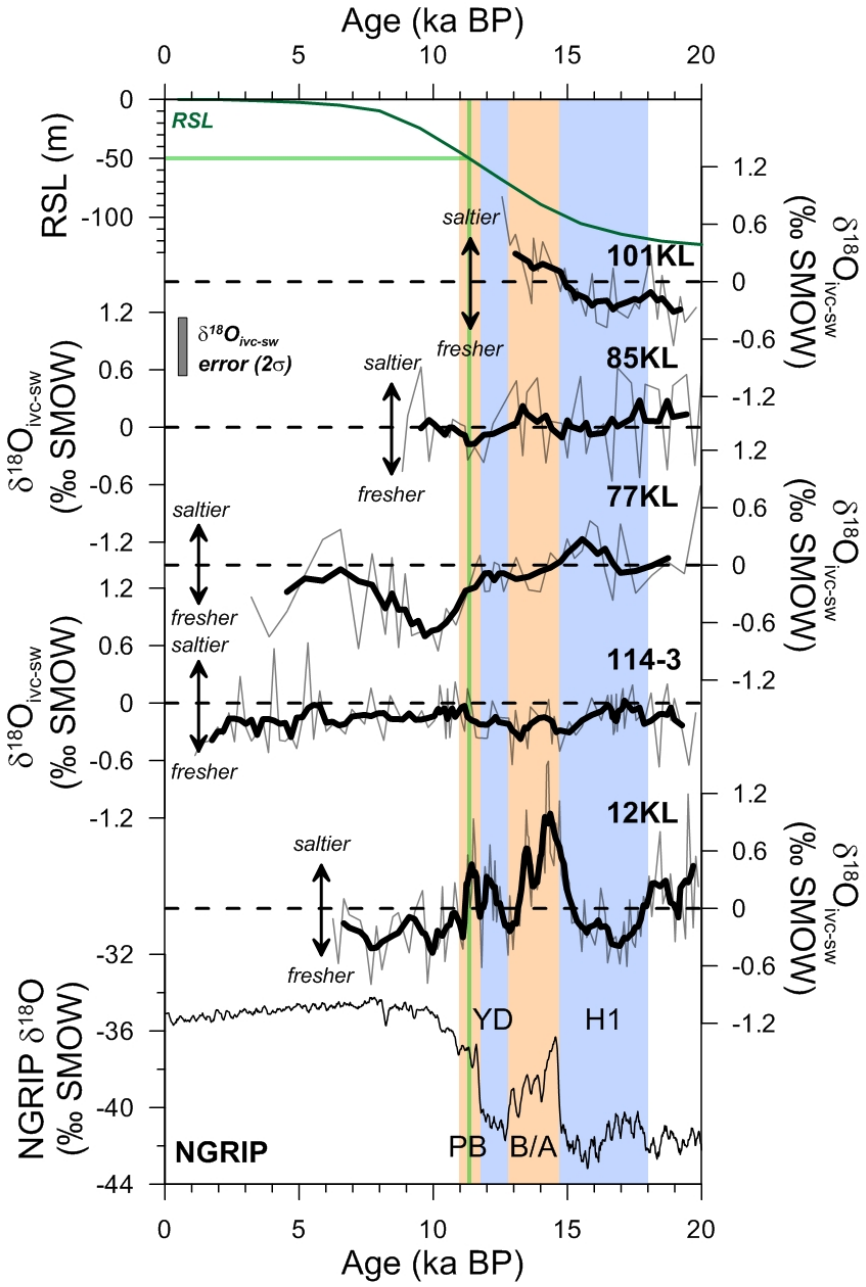


**Figure 5.6.:** Ice-volume corrected $\delta^{18}$O-estimates of seawater ($\delta^{18}O_{ivc-sw}$) from the Bering Sea (SO201-2-101KL, -85KL, -77KL), the subarctic NW Pacific off Kamchatka (SO201-2-12KL), and the southern Okhotsk Sea (LV29-114-3) during the last 20 kyrs, together with the NGRIP $\delta^{18}$O record (NGRIP members, 2004; GICC05 timescale, Rasmussen et al., 2006). Records are smoothed by running 5-point averages (thick black lines). Trends towards heavier (lighter) $\delta^{18}O_{ivc-sw}$-signatures are equivalent to increasing (decreasing) local subsurface salinity. Dashed lines indicate $\delta^{18}O_{ivc-sw}$ = 0‰ SMOW. Pale orange and pale blue shadings represent the B/A and PB, and the H1 and YD, respectively. During the Holocene, after relative sea-level (RSL; green line, after Waelbroek et al., 2002) has risen above the sill depth of Bering Strait (-50 m), all cores are characterized by negative average $\delta^{18}O_{ivc-sw}$ values.

During the Holocene $\delta^{18}O_{ivc-sw}$ values are negative at all sites. At Site 12KL these vary between -0.1‰ and -0.5‰ with a local minimum at ∼8 ka BP. Core 114-3 shows small variations between -0.1‰ and -0.4‰ and gradually fresher values until the late Holocene. Bering Sea core 77KL from 9 ka BP until ∼6 ka BP shows increasing $\delta^{18}O_{ivc-sw}$ to about -0.1‰ and is characterized by a strong variability. Fresher conditions are subsequently preserved until ∼4 ka BP.

## 5.4. Discussion

### 5.4.1. Deglacial variability of temperature and salinity

Our Mg/Ca-based reconstructions from the southern Okhotsk Sea, the NW Pacific off Kamchatka, and the western Bering Sea indicate synchronous changes in $subSST_{Mg/Ca}$ and $\delta^{18}O_{ivc-sw}$ during the last glacial termination with most pronounced amplitude variations recorded at Site 12KL. These changes reflect variations between warm/more saline and cold/fresher subsurface waters. Regional differences are found regarding the deglacial subSSS development, with more saline subsurface conditions during the B/A and PB in the NW Pacific (Site 12KL), while the Bering Sea cores are characterized by opposing trends during the B/A. At the same time, sites 114-3 and 77KL in the southern Okhotsk and Bering seas, respectively, show fresher subSSS. However, all cores indicate fresher subsurface waters during H1, and since the early Holocene. The deglacial $SST_{Uk'37}$ evolution is different from $subSST_{Mg/Ca}$ and characterized by two warmings that occured during the B/A (∼14.7–12.9 ka BP, Blockley et al., 2012) and the PB (∼11.7–11.0 ka BP), respectively. They are preceded and interrupted by two cold phases associated with H1 and the YD (∼12.9–11.7 ka BP, Blockley et al., 2012), and followed by a cooling step during the early Holocene and stable temperatures since. The temporal variations of $SST_{Uk'37}$, hence, are quasi-synchronous with the deglacial N Atlantic climate evolution (Max et al., in review).

#### Heinrich Stadial 1

Our cores show a decrease in $subSST_{Mg/Ca}$ while $\delta^{18}O_{ivc-sw}$ indicates fresh subsurface conditions between 18–16 ka BP (Figs. 5.5 and 5.6). This is most evident for Site 12KL. We consider this to be caused by increased advection of cold, low-salinity waters from the Alaskan Current via the Alaskan Stream at times when the Bering Strait was closed. Today, the Alaskan Stream as a continuation of the Alaskan Current provides relatively fresh surface waters (Stabeno et al., 1999). Given that land masses surrounding the subarctic NW Pacific do not contribute to major fluvial runoff and that there was supposedly no Beringian Ice Sheet during the LGM (e.g. Brigham-Grette et al., 2001; Karhu et al., 2001; Brigham-Grette et al., 2003) is in agreement with Gebhardt et al. (2008) who related drops in salinity during H1 to North American river and meltwater discharge and their subsequent transport via the Alaskan Current and Alaskan Stream to the NW Pacific.

South of the Aleutian Island Arc, at ODP Site 883D and core MD01-2416 from Detroit Seamount (Sarnthein et al., 2006; Gebhardt et al., 2008; Fig. 5.1), SSTs during H1 were clearly higher and characterized by three sharp increases of ∼4–6°C, most likely

excluding sea-ice formation. As these SST-pulses are accompanied by locally increased salinity, they were explained by either short-term incursions of warm and salty Kuroshio waters (Sarnthein et al., 2006) or by northward expansions of the N Pacific gyre filled with Kuroshio waters (Gebhardt et al., 2008). Alkenone-based reconstructions off central Japan showed that SSTs of Kuroshio waters ranged between 20–24°C during the last deglaciation (Sawada and Handa, 1998) and, hence, were considerably warmer than in the far NW Pacific (Fig. 5.5). NE Pacific core MD02-2489 does not show significantly enhanced SSTs during H1 (Gebhardt et al., 2008). Also, Sagawa and Ikehara (2008) reported only a minor increase in subSST$_{Mg/Ca,G.bulloides}$ of ∼1°C at ∼15.5 ka BP off Hokkaido (GH02-1030; Fig. 5.1), followed by a sharp 2°C drop. Their salinity reconstruction implied that relatively saline conditions prevailed at least since the LGM, with a maximum at 15.5 ka BP and a subsequent decrease.

Gebhardt et al. (2008) argued for short phases of pronounced seasonal sea-ice formation in the subpolar N Pacific that induced vertical mixing during H1. Evidence for increased vertical mixing and/or intensified overturning during H1 and the YD comes from reduced reservoir ages of surface waters (Gebhardt et al., 2008), and reduced ventilation ages (Ohkushi et al., 2004; Sarnthein et al., 2007; Sagawa and Ikehara, 2008; Okazaki et al., 2010), and is supported by climate modeling studies (e.g. Okazaki et al., 2010; Chikamoto et al., 2012; Menviel et al., 2012). Increased ventilation and the potential disappearance of the halocline (Menviel et al., 2012) in the N Pacific during H1 and the YD would require an increased salinity, which is consistent with the reconstructions of Sarnthein et al. (2006) and Sagawa and Ikehara (2008), but not supported by our study.

SST$_{Uk'37}$ is of no help in this respect. Indeed, prior to ∼15 ka BP alkenone concentrations were non-determinable in our sediments or insufficient for any reliable paleotemperature calculation. This indicates either limited alkenone-preservation or restricted alkenone-production by coccolithophorids. The restriction in alkenone-production, in particular during H1, is most likely attributed to insufficient availability of light and nutrients, which at our sites might have been caused by enhanced sea-ice coverage during a prolonged winter season.

### Bølling-Allerød

Our subSST$_{Mg/Ca}$ results indicate a maximum at the onset (∼14.7 ka BP) or during the B/A and a subsequent cooling until the YD, most prominent at Site 12KL, and less pronounced at sites 85KL and 101KL (Fig. 5.5). More positive $\delta^{18}O_{ivc-sw}$ values until ∼14.0 ka BP and the subsequent decrease imply more saline conditions at sites 12KL, 85KL, and 101KL (Fig. 5.6). This subSST pattern is congruent with Mg/Ca-based results from NE Pacific core MD02-2489 (Gebhardt et al., 2008) and NW Pacific core GH02-1030 (Sagawa and Ikehara, 2008), and supported by alkenone-based SST reconstructions from the NE Pacific (Kienast and McKay, 2001; Barron et al., 2003), the Bering Sea (Caissie et al., 2010; Max et al., in review), and the Okhotsk Sea (Ternois et al., 2000; Harada et al., 2006b; Seki et al., 2009). The presence of warmer and more saline subsurface waters at most of our core locations during the B/A is best explained by the reduced contribution of cold and fresh Alaskan Stream and EKC waters in combination with less vertical mixing and hence, stronger stratification of the upper water column. Enhanced stratification during the B/A is supported by

increased ventilation ages found in the N Pacific (Adkins and Boyle, 1997; Ahagon et al., 2003; Ohkushi et al., 2004; Sagawa and Ikehara, 2008; Okazaki et al., 2010). Thermal stratification at the northernmost Shirshov Ridge cores 85KL and 101KL might have been less developed than at the other sites by the still extended sea-ice season and the low seasonal constrast at these locations as indicated by $\Delta$T-values of 0–1°C. It might further be speculated that at times when the Bering Strait was still closed, the net-inflow of Alaskan Stream waters into the Bering Sea was reduced. Hence, the Alaskan Stream might still have influenced Site 77KL but not necessarily have reached sites 85KL and 101KL further to the north.

At the southernmost Shirshov Ridge core location (77KL) and in the southern Okhotsk Sea (114-3), fresher subsurface conditions characterize the B/A (Fig. 5.6), with surface freshening off Japan from 14.6 ka BP to 13.6 ka BP (Sagawa and Ikehara, 2008). Freshening during the B/A has previously been suggested for the southern Okhotsk Sea (Gorbarenko et al., 2004; Seki et al., 2004b), and for Bowers Ridge in the southern Bering Sea (Gorbarenko et al., 2005) from the observation of negative shifts in planktonic $\delta^{18}$O and increasing abundances of the diatom species *Paralia sulcata*. The freshening at these sites may be attributed to invigorated melting of sea-ice close to the ice margin during the warm season, accelerated by the presence of the EKC and hence, potentially favoring a seasonal halocline. In both cores, the B/A subSST$_{Mg/Ca}$ are similar to those of the northernmost sites 85KL and 101 KL, whereas SST$_{Uk'37}$ estimates are higher by 2–3°C (Fig. 5). Consequently, at sites 114-3 and 77KL an enhanced seasonal contrast with respect to H1 might have resulted in stronger thermal stratification during summer.

A possible explanation for warmer subSST$_{Mg/Ca}$ than SST$_{Uk'37}$ in core 12KL during the B/A involves the formation of a strongly developed thermocline and warm SST$_{Uk'37}$ that reduce the sea-ice season. In that case seasonal bias of proxy signal formation arises and the colder SST$_{Uk'37}$ most likely represent early spring conditions, while the subSST$_{Mg/Ca}$ signal still formed during late summer/early fall. If this notion is correct, the seasonal bias was limited to the subarctic NW Pacific (Site 12KL) and did not occur in the marginal seas' sites. Unfortunately, alkenone-based temperature reconstructions are not available for core MD01-2416 from Detroit Seamount to verify this assumption, and the cause of the high subSST$_{Mg/Ca}$ amplitude at Site 12KL remains elusive. Evidence for a modern subarctic N Pacific coccolithophorid bloom occurring in spring comes from the sediment trap study of Takahashi et al. (2002a). Seki et al. (2004a) for the Okhotsk Sea already suggested a seasonal bias to explain alkenone-based temperatures that during the LGM were as high as during the Holocene.

### The Younger Dryas to Preboreal transition

During the YD our records show minima in subSST$_{Mg/Ca}$, SST$_{Uk'37}$, and $\delta^{18}O_{ivc-sw}$ with conditions that were comparable to those of H1. The YD is followed by an abrupt surface warming in the PB as indicated by SST$_{Uk'37}$, while the subsurface temperatures gradually decline (Fig. 5.5). Only core 12KL exhibits a short excursion towards higher subsurface temperatures during the PB, accompanied by a $\delta^{18}O_{ivc-sw}$ maximum (Fig. 5.6). The subSST$_{Mg/Ca}$ and $\delta^{18}O_{ivc-sw}$ evolution observed at sites 114-3, 12KL, and 77KL broadly matches that from further to the south in the NW Pacific (Sarnthein

et al., 2004, 2006; Gebhardt et al., 2008; Sagawa and Ikehara, 2008) which just have higher $\delta^{18}O_{ivc-sw}$ values.

$SST_{Uk'37}$ indicate also low surface temperatures during the YD (Fig. 5.5). Kienast and McKay (2001) from a core off Vancouver Island suggest that low $SST_{Uk'37}$ during the YD were caused by the southeastward expansion of the W Pacific Subarctic Gyre and the Bering Sea Gyre. The modeling study of Mikolajewicz et al. (1997) predicted that the Aleutian Low was stronger and expanded eastwards during the YD, which initiated better ventilation of thermocline waters. The well-mixed upper-ocean during the YD is supported by resembling $subSST_{Mg/Ca}$ and $SST_{Uk'37}$ and is in agreement with reduced ventilation ages in the N Pacific. Our proxy records, however, suggest regionally different developments with weak thermal stratification at sites 12KL, 77KL, and 114-3 due to reduced $\Delta T$ values ($\sim 2°C$), and a more homogenized upper water column at Site 85KL ($\Delta T = 0°C$) similar to conditions valid for H1. Subsequently during the PB, $subSST_{Mg/Ca}$ and related $\delta^{18}O_{ivc-sw}$ values imply subsurface cooling and freshening (77KL, 85KL) and/or conditions comparable to the YD (114-3). Possible explanations for this observation include reduced thermal stratification and/or enhanced advection of Arctic surface waters in the course of the major opening of the Bering Strait between 12–11 ka BP (Keigwin et al., 2006). Core 12KL is an exception in this respect. The distinct and short-term subsurface warming with the onset of the PB (Fig. 5.5) is most probably due to the invigorated stratification of the upper water column alike during the B/A.

### Holocene

Most notably for all our cores are the differently developing $subSST_{Mg/Ca}$ and $SST_{Uk'37}$ since the YD (Fig. 5.5), best explained by insolation changes affecting the surface ocean, increasing seasonal contrasts, and oceanographic changes at the subsurface level that control the shape and position of the thermocline. Holocene $subSST_{Mg/Ca}$ remain either equal or stay lower than those recorded during H1 (Fig. 5.5). Our $subSST_{Mg/Ca}$ well reflect modern conditions, which is consistent with other studies (Sarnthein et al., 2004, 2006; Gebhardt et al., 2008; Sagawa and Ikehara, 2008). With respect to our salinity reconstruction, the Holocene $\delta^{18}O_{ivc-sw}$ values are generally negative indicating relatively fresh conditions at all sites similar to conditions during H1, arguing for a deglacial evolution of the halocline. Sarnthein et al. (2004) reported on the long-term decrease in subsurface salinity at Detroit Seamount, characterized by three steps of distinct salinity decline during the early to middle Holocene. From the magnitude of change, which is comparable to our results, they speculated that the modern salinity-driven stratification developed only since the Holocene. However, due to the low time-resolution of our proxy records we can not confirm the stepwise nature of the subSSS decline.

The low Holocene $subSST_{Mg/Ca}$ at our study sites being considerably cooler than the $SST_{Uk'37}$ in line with relatively fresh subsurface conditions indicates a strengthened temperature contrast between the surface and subsurface during summer. Dominant control of the subarctic NW Pacific $SST_{Uk'37}$ evolution during the Holocene is attributed to Northern Hemisphere summer insolation (Okumura et al., 2009; Hu et al., 2010; Max et al., in review), being additionally influenced by the opening of the Bering Strait. In consequence, stronger seasonal contrasts might have developed in the early

Holocene as the result of a prolonged summer season, enhanced sea-ice melting during summer, and stronger winter mixing, thereby leading to the formation of the dichothermal layer. Our high $\Delta$T values of ~5–6°C are then explained by higher $SST_{Uk'37}$ with respect to the deglacial situation, and by *Nps* recording gradually cooler subsurface temperatures due to the presence of the dichothermal layer. Accordingly, thermal stratification during summer was consolidated and fresher subsurface conditions were the result of a stronger summer halocline. The largest difference between $subSST_{Mg/Ca}$ and $SST_{Uk'37}$ at ~10 ka BP coincides with the early Holocene thermal maximum recorded in the western Arctic, which in Alaska and northwest Canada occurred between 11–9 ka BP (Kaufman et al., 2004), supporting this interpretation. Additionally, enhanced precipitation driven by the Westerlies, and strengthened advection of cold/fresh waters from the Alaskan Stream might have contributed to the N Pacific cooling and freshening (Sarnthein et al., 2004).

### 5.4.2. Scenarios for deglacial water mass changes

Our reconstructions of $subSST_{Mg/Ca}$ and $\delta^{18}O_{ivc-sw}$ depend on the calcification depth of *Nps*. Following Kozdon et al. (2009) we assume that today *Nps* occupies a habitat that is bound to the isopycnal layer ($\sigma_0$ of ~26.4–26.6 kg $m^{-3}$) at the bottom of the summer thermocline in 50–100 m water depth. Accordingly, if the thermocline and hence the pycnocline deepens (shoals), the habitat depth of *Nps* will expand to deeper (shallower) depths as well, thereby eventually counterbalancing absolute temperature variations (Kozdon et al., 2009). Since there is no way to assess the extent of past habitat changes, we assume that the maximum habitat depth of *Nps* is at the base of the pycnocline, which today at our study sites is located at a maximum water depth of ~150 m (Fig. 5.2). Based on this assumption, we use TS-diagrams to illustrate deglacial changes in water mass characteristics in the subarctic NW Pacific (Fig. 5.7). Due to both the error in the $\delta^{18}O_{sw}$-reconstruction and the lack of according salinity calibrations for the Bering Sea, we refrained from converting $\delta^{18}O_{sw}$ into salinity. Instead, salinity was estimated by projecting the average $subSST_{Mg/Ca}$ estimates onto the isopycnal layer of ~26.4–26.6 kg $m^{-3}$ (Fig. 5.7).

Today, the difference in temperature, salinity, and potential density in the southern Bering Sea (WOA station 34548) is depicted in Fig. 5.7a and is the expression of the strong seasonality within the upper water column. For the H1 stadial we assume TS-conditions relatively similar to the modern winter situation with homogenous T, S, and $\sigma_0$ conditions down to ~150 m and the absence of the dichothermal layer (Fig. 5.7b). As the reconstructed $subSST_{Mg/Ca}$ lies between 3°C and 4°C at all sites implying that subsurface waters were slightly warmer and saltier than the modern winter conditions we argue that the thermal stratification was strongly reduced. The homogenization of the upper water column must have been even more pronounced and deeper than during the modern winter situation. The most likely cause for the less stratified water column might have been the intensified and expanded sea-ice formation during winter and the shortened summer season. The invigorated sea-ice formation might have enhanced salinity in comparison to today due to brine-rejection and, by light limitation, might have restricted primary productivity. Indeed, during H1 alkenones were absent or below detection limit. The expanded sea-ice coverage during the extended winter season might have also reduced winter mixing, thereby preventing the formation of the dichothermal layer as a seasonal feature, which would explain the slightly

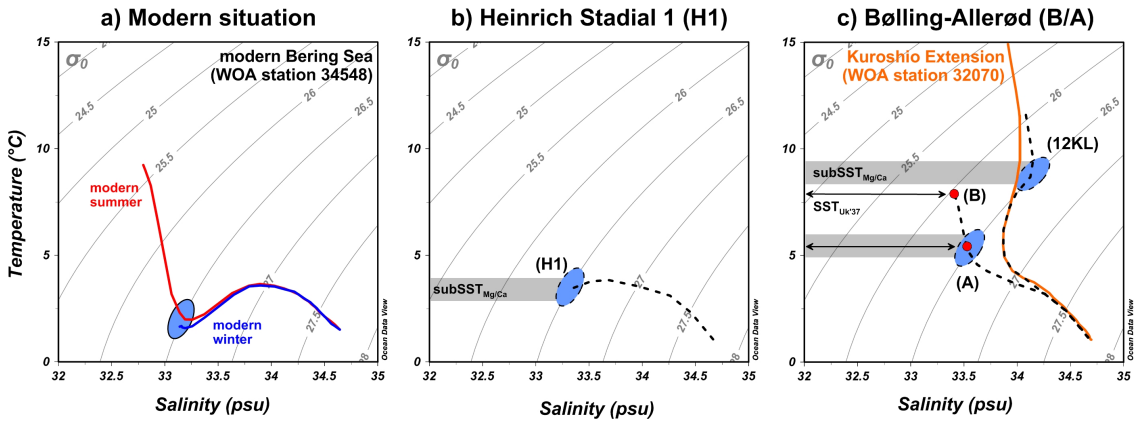


**Figure 5.7.:** TS-diagrams showing temperature, salinity, and potential density of modern and past water masses in the subarctic NW Pacific realm (based on WOA data; Locarnini et al., 2010). a) Water masses during modern summer (red line) and winter (blue line) in the southern Bering Sea (WOA station 34548). The blue ellipse denotes temperature and salinity conditions within the depth habitat of *N. pachyderma* (sin.), which is assumed to lie in an isopycnal layer of ~26.4–26.6 kg $m^{-3}$ in 50–100 m water depth. b) Scenario for H1. The reconstructed average $subSST_{Mg/Ca}$ of 3-4°C (grey bar) at all sites is projected onto the isopycnal layer of ~26.4–26.6 kg $m^{-3}$ and indicates subsurface conditions that were saltier than today. c) Scenario for the B/A at Bering Sea sites SO201-2-85KL and -101KL (A), Bering Sea Site SO201-2-77KL and Okhotsk Sea Site LV29-114-3 (B), and NW Pacific Site SO201-2-12KL (12KL), in comparison with the modern TS-conditions in the Kuroshio Extension area (orange line; WOA station 32070: 40°30'N, 152°30'E). Red dots mark average $SST_{Uk'37}$ temperatures and grey bars mark average $subSST_{Mg/Ca}$ temperatures at the respective sites.

higher (1–2°C) $subSST_{Mg/Ca}$ during H1 when compared to today. The reduced thermal stratification, in consequence, could have resulted in the shallowing of the habitat of *Nps*. This notion is supported by low biogenic opal and light diatom-bound nitrogen isotope ratios ($\delta^{15}N_{db}$) in the Okhotsk Sea, Bering Sea, and the subarctic Pacific during H1 (Brunelle et al., 2007, 2010) (Fig. 5.8), indicative of the decrease in nitrate utilization in response to both the less-established stratification and the light-limited phytoplankton growth.

During the B/A warm phase, the oceanographic setting became different at the respective sites (Fig. 5.7c). At Bering Sea sites 85KL and 101KL, similar mean $SST_{Uk'37}$ and $subSST_{Mg/Ca}$ of 5–6°C point to a weak thermal stratification with higher subsurface temperature and salinity compared to today and to H1 (Fig. 5.7c, A). The low gradient between $SST_{Uk'37}$ and $subSST_{Mg/Ca}$ implies that seasonal changes in thermocline depth remained small, probably a little more pronounced than during H1 as preserved alkenones suggest phytoplankton growth during the ice-free season. Nevertheless, marine productivity remained low (biogenic opal <5 wt.%), most likely caused by a still expanded sea-ice season. The heavy $\delta^{15}N_{db}$ from nearby Bowers Ridge (Brunelle et al., 2010) at a first glance implies enhanced nitrate utilization, but the data set rather reflects conditions not quite comparable to the northern part of Shirshov Ridge.

NW Pacific Site 12KL shows much higher $subSST_{Mg/Ca}$ of ~9°C and a further increase in subsurface salinity during the B/A (Fig. 5.7c, 12KL) compared to the northern Shirshov Ridge sites 85KL and 101KL. Further, the $subSST_{Mg/Ca}$ are consistently higher than the $SST_{Uk'37}$, suggesting that seasonal differences were pronounced at Site 12KL. The prominent seasonality in signal formation implies both an extended

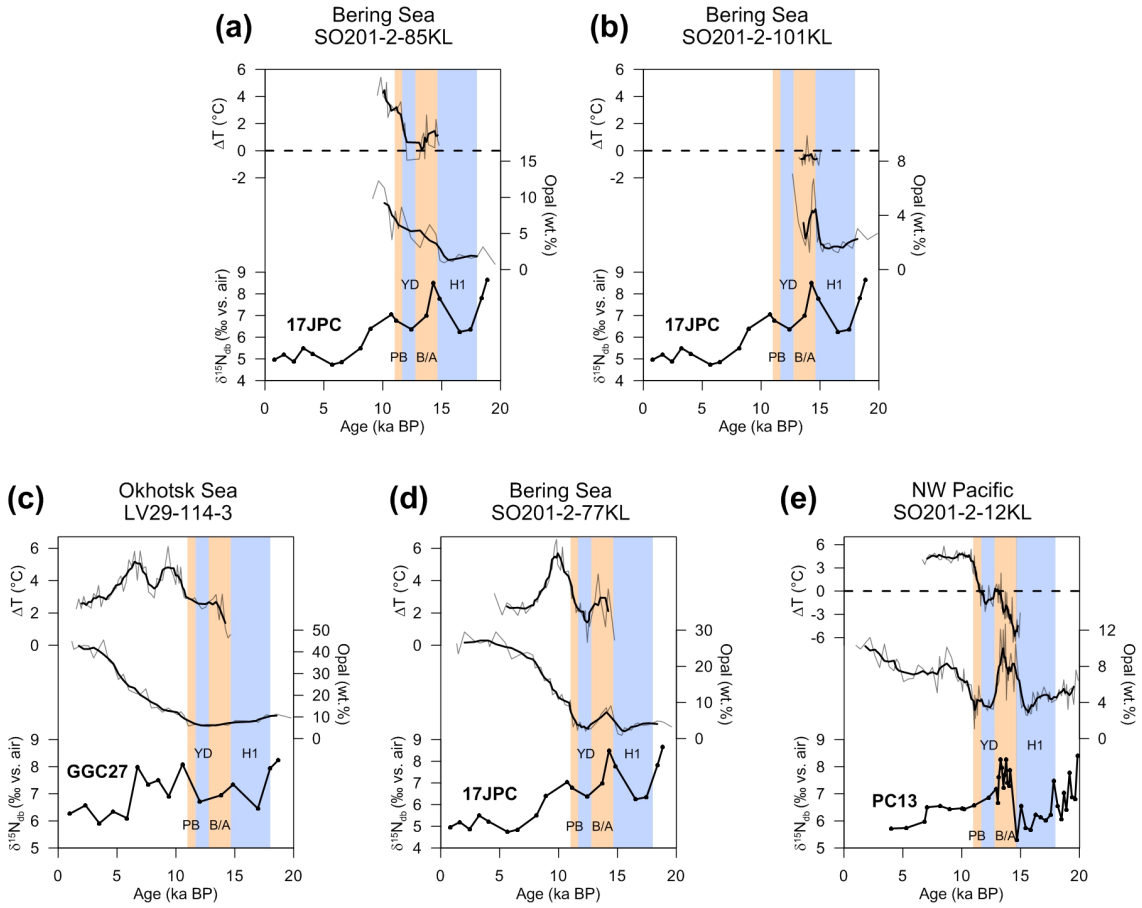


**Figure 5.8.:** Temperature gradients ($\Delta$T) between $SST_{Uk'37}$ and $subSST_{Mg/Ca}$, and concentrations of biogenic opal for cores from the Bering Sea (SO201-2-77KL, -85KL, -101KL), the NW Pacific off Kamchatka (SO201-2-12KL), and the southern Okhotsk Sea (LV29-114-3). Data are smoothed by running 5-point-averages (black lines). Dashed lines indicate $\Delta T = 0°C$. For comparison, records of $\delta^{15}N_{db}$ from southern Okhotsk Sea core GGC27 (49°36.07'N, 150°10.78'E, 995 m), southern Bering Sea core HLY02-02-17JPC (53°55.98'N, 178°41.93'E, 2209 m), and open subarctic Pacific core PC13 (49°43.09'N, 168°18.11'E, 2393 m) are shown (data from Brunelle et al., 2007, 2010). Pale orange and pale blue shadings represent the B/A and PB, and the H1 and YD, respectively.

ice-free summer season and a strong thermal stratification. Biogenic opal concentrations of up to ~12% comparable to the Holocene values suggest enhanced marine productivity during the prolonged summer season (Fig. 5.8), fostered by a better nitrate utilization or denitrification leading to heavy $\delta^{15}N_{db}$ values. The B/A subsurface temperature and salinity conditions at Site 12KL were close to conditions, which today prevail in the Kuroshio Extension area (40°30'N, 152°30'E, WOA station 32070; Locarnini et al., 2010) much further to the south of the core location (Fig. 5.7c). The higher subsurface salinities reconstructed for the B/A might be caused by a northward expansion of the N Pacific gyre filled with Kuroshio waters as suggested by Gebhardt et al. (2008).

Site 114-3 in the southern Okhotsk Sea and Site 77KL from the southernmost part of Shirshov Ridge record conditions in between these extremes (Fig. 5.7c, B). We speculate that both temperature signals were generated at the same season, since contents of biogenic opal remain low (<10 wt.%, Fig. 5.8), suggesting a still shortened ice-free summer season. In consequence, thermal stratification at these sites and hence, sea-

sonality, must have been stronger than during H1 and more pronounced than at sites 85KL and 101KL.

According to the gradual increase in subSST$_{Mg/Ca}$ and subSSS during the B/A, we would expect stronger seasonal contrast as well as enhanced thermal stratification of the upper water columns from sites 85KL and 101KL, via sites 114-3 and 77KL, towards site 12KL. Moreover, we suggest that during the B/A increased thermal stratification at Site 12KL was accompanied by higher subSSS, thereby resulting in a weakened (or shallowed) halocline. The cause of this increase in subSSS remains elusive, but due to the recorded (warm) temperatures we can exclude upwelling of cold/saline subsurface waters. This, together with the observed subSSS reduction during the Holocene, emphasizes that the halocline as a main oceanographic feature of the subarctic N Pacific was subject to deglacial changes and that modern conditions could be the result of only recent environmental change as suggested by Sarnthein et al. (2004).

### 5.4.3. What caused deglacial changes in stratification and ventilation?

The deglacial to early Holocene subsurface and surface temperature and salinity evolution in the subarctic NW Pacific appears to be related to, and in-phase with, the thermal evolution that is recorded in Greenland ice and in N Atlantic sediments, suggesting atmospheric and/or oceanic coupling between the N Atlantic and the N Pacific during the last deglaciation (e.g. Max et al., in review). Several modelling studies investigated the sensitivity of the PMOC in response to perturbations of the AMOC on millennial timescales during the last deglaciation. All models predicted an enhanced PMOC at times of a weakened AMOC, whose strength during the last deglaciation was modulated by freshwater input into the Atlantic or by freshwater extraction from the Pacific.

According to model conceptions, the weakened AMOC during H1 and the YD (e.g. McManus et al., 2004) which is assumed to have resulted from freshwater input into the Atlantic, leads to the southward shift of the Intertropical Convergence Zone (ITCZ) and weakened Indian and Asian summer monsoons (Zhang and Delworth, 2005). Today, the salinity gradient between the Atlantic and Pacific is maintained by atmospheric moisture transport across Central America and the east Asian monsoon (Emile-Geay et al., 2003), which are modulated by changes in AMOC (Okazaki et al., 2010). Consequently, a weakening of the AMOC results in a warming and salinity-increase in the N Pacific and thus to the establishment of a PMOC (Haug et al., 2005; Chikamoto et al., 2012; Menviel et al., 2012). In contrast, the in-phase models (e.g. Mikolajewicz et al., 1997) suggest an atmospheric forcing, which causes better ventilation of thermocline waters by atmospheric cooling. The cooling is attributed to the strengthened Aleutian Low, which increases surface heat loss and southward Ekman transport, but atmospheric bridges between the tropical N Atlantic, eastern tropical Pacific, and N Pacific are considered to play an important role as well (Okumura et al., 2009). Ventilation is supposed to be amplified by the oceanic propagation of AMOC weakening (Mikolajewicz et al., 1997). Both, in-phase and anti-phase hypotheses, are supported by low ventilation ages in the N Pacific during H1 and the YD.

The study of Menviel et al. (2012) predicts that the PMOC was established during H1 together with the removal of the subarctic N Pacific halocline. This notion is supported

by the high $\delta^{18}O_{ivc-sw}$ values recorded in NW Pacific cores MD01-2416 (Sarnthein et al., 2006; Gebhardt et al., 2008) and GH02-1030 (Sagawa and Ikehara, 2008). In contrast, our results for core 12KL as well as alkenone-based SST reconstructions form the subarctic N Pacific show a significant drop in $subSST_{Mg/Ca}$ and $SST_{Uk'37}$, while $\delta^{18}O_{ivc-sw}$ values indicate fresh subsurface conditions during H1. Although we admit, that the records of Site 12KL might not be representative, this pattern is rather indicative of an atmospheric-controlled in-phase evolution of the N Atlantic and the subarctic N Pacific. High $subSST_{Mg/Ca}$ and low $\delta^{18}O_{ivc-sw}$ in the Okhotsk and Bering seas during the B/A and PB are then explained by stronger stratification of the subarctic N Pacific due to the reduced PMOC in response to the AMOC intensification. Subsequent to the PB, the subarctic NW Pacific is subject to enhanced thermal summer stratification, which for the Bering Sea sites is possibly related to the opening of Bering Strait resulting in stronger inflow of N Pacific surface waters into the Bering Sea. Moreover, increased surface freshening during the Holocene results from sea-ice melting during summer, enhanced precipitation from the Westerlies and/or increased advection of cold-fresh waters from the Alaskan Stream.

## 5.5. Conclusions

1. Our results point to synchronous changes in $subSST_{Mg/Ca}$ and subSSS in the subarctic NW Pacific, which are different on a regional scale. During H1 and the YD our sites are characterized by the presence of cold subsurface waters, which is related to reduced upper-ocean stratification due to enhanced sea-ice formation and a shortened summer season, and increased advection of waters from the Alaskan Stream and EKC. In contrast, warm subsurface waters prevail during the B/A with increased subsurface salinity in the NW Pacific (Site 12KL) and Bering Sea (sites 85KL and 101KL), but fresher conditions in the southern Okhotsk and Bering seas (sites 114-3 and 77KL). This is explained by enhanced stratification of the upper water column, reduced dilution from the Alaskan Stream and EKC, and regionally different sea-ice influence. A long-term decrease in $subSST_{Mg/Ca}$ and subSSS during the early Holocene argues for oceanographic changes at the subsurface level related to the opening of the Bering Strait and for an only recent establishment of modern, salinity-driven stratification since the early Holocene.

2. Differences in alkenone- and Mg/Ca-based SST-reconstructions indicate deglacial oceanographic changes in the mixed layer, which are most likely related to changes in Northern Hemisphere summer insolation and atmospheric pressure systems, thereby driving changes in seasonality, sea-ice formation, and upper-ocean stratification. From our results we propose scenarios for deglacial water mass changes, which suggest that seasonality and hence thermal summer stratification, although being regionally different, was reduced during H1 and the YD, but strong during the B/A.

## Acknowledgements

This study was funded by the German Ministry of Education and Research (BMBF), grant nos. 03G0672A and B, and resulted from the German-Russian joint research project "KALMAR–Kurile-Kamchatka and Aleutean Marginal Sea-Island Arc Systems: Geodynamic and Climate Interaction in Space and Time". Master and crew of R/V Sonne cruise SO201 Leg 2 are gratefully acknowledged for their professional support. E. Maier (AWI-Bremerhaven) conducted additional opal measurements for core 77KL. We thank N. Gehre, L. Haxhiaj, and D. Poggemann for laboratory assistance and technical support, and N. Khelifi for discussions.

# 5.6. Supplementary information

## 5.6.1. Assessment of potential contamination of foraminiferal tests

Our records of foraminiferal element ratios (Mg/Ca, Mn/Ca, Fe/Ca, Al/Ca) are shown in Fig. 5.9 together with results for benthic and planktonic $\delta^{18}$O. Significant linear relationships ($0.62 < R^2 < 0.85$) were found for cores 77KL, 85KL, and 101KL between foraminiferal Mn/Ca and Mg/Ca ratios indicating general covariation (Fig. 5.10). Core-specific thresholds reflecting potentially contaminated samples were defined as ratios that were more than $2\sigma$ higher than the average of all samples measured in the respective core. For Mn/Ca, thresholds ranged between 0.08–0.17 mmol mol$^{-1}$. Linear correlation coefficients between Fe/Ca and Mg/Ca ratios were $R^2 \leq 0.26$, except for core 77KL ($R^2 = 0.61$), which is in accord with a strong correlation between Mn/Ca and Mg/Ca ($R^2 = 0.66$) in that core. Here, a Fe/Ca threshold of 0.85 mmol mol$^{-1}$ was applied. Correlations between Al/Ca and Mg/Ca are insignificant ($R^2 \leq 0.18$). In general this approach shows that (i) neither Fe/Ca nor Al/Ca ratios have a significant influence on the Mg/Ca signal and that main contamination should come from Mn-bearing minerals and coatings, and (ii) that only samples from core sections older than 20 ka BP are subject to contamination. Respective samples are not relevant for our paleoceanographic discussion, which focuses on the last 20 ka BP.

In case of diagenetic overprinting by Mn-bearing minerals and coatings, the reconstructed subSST$_{Mg/Ca}$ could be too warm due to the diagenetically-induced addition of Mg. Average Mn/Ca ranged between 0.02–0.06 mmol mol$^{-1}$, while core-specific thresholds for Mn/Ca all were <0.2 mmol mol$^{-1}$. Mn-Mg carbonates have Mg/Mn ratios of ∼0.1 mol mol$^{-1}$ (Barker et al., 2003). Thus, a maximum increase in Mn/Ca of 0.2 mmol mol$^{-1}$ would lead to a Mg/Ca increase of only 0.02 mmol mol$^{-1}$, translating into a subSST$_{Mg/Ca}$-increase of +0.15°C. Considering an unrealistic Mg/Mn ratio of 1 mol mol$^{-1}$, a correction for Mn/Ca generates therefore results that per core are on average by 0.02–0.06 mmol mol$^{-1}$ lower in Mg/Ca (-0.2 to -0.5°C), ultimately showing the same temporal trends. Accordingly, we refrained from correcting for Mn/Ca.

## 5.6.2. Evaluation of correction for carbonate dissolution

Procedures to correct planktonic foraminiferal Mg/Ca for dissolution effects primarily focus on water depth-dependency (Lea et al., 2000; Dekens et al., 2002) and the influence of the seawater carbonate ion concentration ($[CO_3^{2-}]$) with respect to calcite saturation (Regenberg et al., 2006). To estimate the dissolution effect on Mg/Ca we followed the approach of Regenberg et al. (2006) who proposed species-specific saturation correction routines for seven planktonic species. Therefore, for our calculations, we adopted a critical calcite saturation state for seawater ($\Delta[CO_3^{2-}]_{critical}$) of 20 $\mu$mol kg$^{-1}$ lying within the range of 18–26 $\mu$mol kg$^{-1}$ suggested by Regenberg et al. (2006).

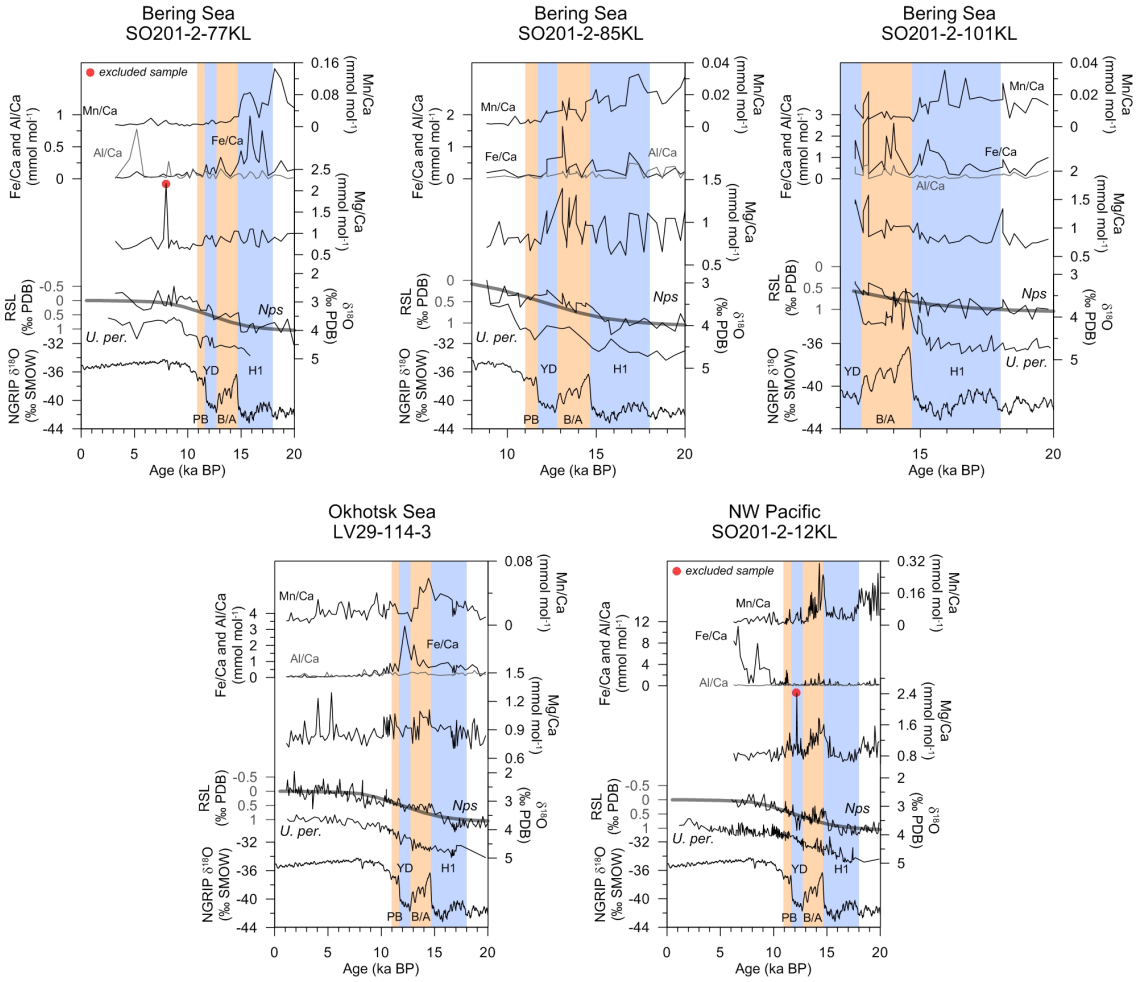


**Figure 5.9.:** Raw data of benthic and planktonic $\delta^{18}O$ in comparison with planktonic foraminiferal ratios of Mg/Ca, Mn/Ca, Fe/Ca, and Al/Ca. The NGRIP record (NGRIP members, 2004; GICC05 timescale, Rasmussen et al., 2006) is shown for comparison. Two samples were excluded due to very high Mg/Ca values and are indicated by red dots. Thick grey line marks the relative sea level record of Waelbroek et al. (2002) which is used for ice-volume correction of planktonic $\delta^{18}O$. The B/A and PB are indicated by pale orange shadings, whereas pale blue shadings represent H1 and the YD.

$\Delta[CO_3^{2-}]_{critical}$ is defined as the difference between the *in situ* carbonate ion concentration ($[CO_3^{2-}]_{insitu}$) and the carbonate ion concentration at calcite saturation ($[CO_3^{2-}]_{sat}$), below which $Mg^{2+}$ removal due to dissolution is assumed to start. $[CO_3^{2-}]_{sat}$ was calculated after Jansen et al. (2002), while $[CO_3^{2-}]_{insitu}$ was calculated using the CO2SYS Macro for MS Excel (Pierrot et al., 2006) applying dissociation and equilibrium constants from Dickson (1990) and Roy et al. (1993). Necessary input data were obtained from the World Ocean Circulation Experiment (WOCE) available at the CCHDO | CLIVAR & Carbon Hydrographic Data Office (http://cchdo.ucsd.edu/). For the southern Okhotsk Sea we used WOCE line P01W (stations 7–17), while lines P13 (stations 6–15) and P14N (stations 1–15) were used for the NW Pacific and the Bering Sea, respectively. This allowed for the calculation $\Delta[CO_3^{2-}]$ and to determine critical water depths for the respective regions, where $\Delta[CO_3^{2-}]$ equals 20 $\mu$mol kg$^{-1}$. Critical water depths ranged between 120 and 200 m.

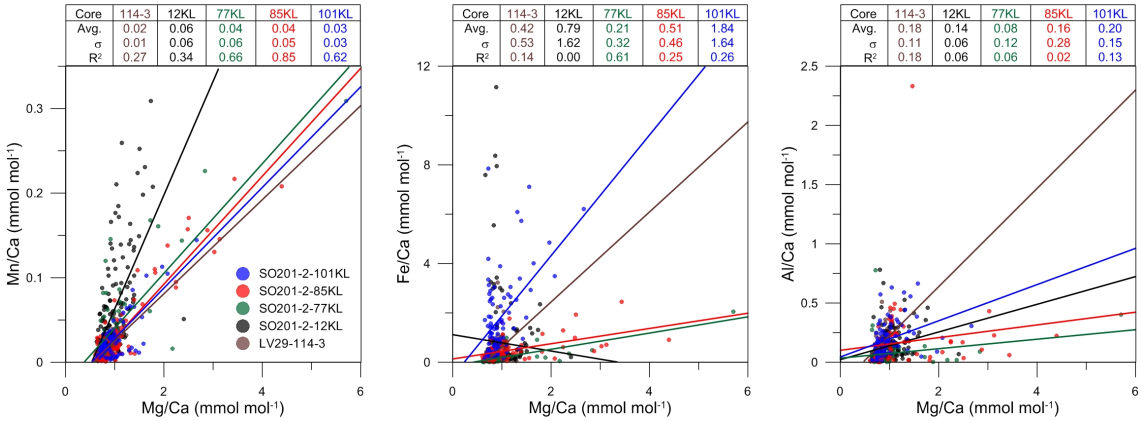


**Figure 5.10.:** Comparison of foraminiferal Mg/Ca with foraminiferal Mn/Ca, Fe/Ca, and Al/Ca. Significant linear correlations ($R^2 > 0.6$) are found between element ratios Mg/Ca and Mn/Ca for cores 77KL, 85KL, and 101KL. Core 77KL also shows a correlation between Mg/Ca and Fe/Ca. In general, linear correlation coefficients ($R^2$) between Mg/Ca and Fe/Ca (Al/Ca) are low and indicate that main contamination and influence on Mg/Ca comes from Mn-bearing minerals and coatings. However, only samples older than 20 ka BP, which are not used for interpretation, seem affected by contamination.

Regenberg et al. (2006) introduced species-specific linear correction equations for critical water depth correction (referred to as d-correction hereafter) and for critical calcite saturation state correction (referred to as Δ-correction hereafter). To calculate Mg/Ca correction factors (ΔMg/Ca) we applied sensitivities for the respective corrections that were derived from the averages of the slopes of regression lines from all species-specific correction relationships presented in Regenberg et al. (2006). For d-correction we used an average sensitivity of 1600 m per mmol mol$^{-1}$ Mg/Ca, and for Δ-correction we used an average sensitivity of 16 $\mu$mol kg$^{-1}$ per mmol mol$^{-1}$ Mg/Ca.

Depending on the core location, d-correction resulted in a Mg/Ca gain between +0.3 and +1.3 mmol mol$^{-1}$ (+2°C to +10°C applying the sensitivity given in the equation of Kozdon et al., 2009), similar to the approach of Lea et al. (2000). This result is intriguing as all cores show a similar Holocene (<8 ka BP) subSST$_{Mg/Ca}$ range of 3–4°C which is only little higher (1–2°C) than the modern instrumental record at 50–100 m w.d.. We rather attribute this small difference to the potentially less developed dichothermal layer with respect to modern conditions. In contrast, the depth-corrections that were established for planktonic warm-water species *Globigerinoides ruber* and *Globigerinoides sacculifer* (Dekens et al., 2002) result in constantly warmer subSST$_{Mg/Ca}$ of 2 to 3°C. However, Dekens et al. (2002) modified existing Mg/Ca-T-relationships for these two species by introducing depth-dependent correction factors into the exponential part of the equations, which produces an artificial phase-shift to higher temperatures. These equations do not compare with those that are associated with *Nps* (Nürnberg, 1995b; Nürnberg et al., 1996; Elderfield and Ganssen, 2000) or other cold-water species like *Globigerina bulloides* (e.g. Mashiotta et al., 1999).

Δ-correction produced even higher values compensating for an unlikely loss of Mg/Ca between -1.6 and -2.1 mmol mol$^{-1}$. Consequently, subSST$_{Mg/Ca}$ estimates would be higher by +13°C to +16°C applying the temperature sensitivity given by Kozdon et al. (2009), which is far off the modern annual temperature range of the subarctic NW Pacific. On the other hand applying a correction considering a sensitivity of about 0.009 mmol mol$^{-1}$ Mg/Ca per $\mu$mol kg$^{-1}$ Δ[$CO_3^{2-}$], as found for epibenthic foraminifera *Cibicidoides wuellerstorfi* (Elderfield et al., 2006; Yu and Elderfield, 2008), would result in

ca. 0.23–0.31 mmol mol$^{-1}$ higher Mg/Ca (+2°C) for all cores. Although this correction produces reasonable results off the combined error range of the measurement uncertainty and the applied paleotemperature relationship, it is not verified for planktonic species and applying it would not have any influence on temporal trends.

It needs to be mentioned, also, that established dissolution corrections only account for modern dissolution effects and do not consider possible temporal changes in calcite preservation and their influence on Mg/Ca (e.g. Farrell and Prell, 1989; Le and Shackleton, 1992). Our cores feature deglacial maxima of carbonate contents indicating better $CaCO_3$ preservation during the Bølling-Allerød (B/A) and Preboreal (PB). Hence, increased Mg/Ca during the B/A and PB might be related to increased carbonate preservation.

Based on all considerations discussed above, we refrained from correcting the initial Mg/Ca values for potential dissolution effects although we admit that the Mg/Ca ratios are to an unknown degree affected by dissolution. Any correction would lead to increased subSST$_{Mg/Ca}$ that are either significantly different for all studied subarctic Pacific regions, or off the modern annual instrumental record, or, despite being reasonable, based on procedures previously not applied to *Nps*. Moreover, applying any correction would not alter temporal trends in our records. Additional validation of our Mg/Ca-based paleotemperature reconstructions comes from a general covariation between subSST$_{Mg/Ca}$ and ice-volume corrected oxygen isotope values determined on the same biotic carrier. Furthermore, the range of our subSST$_{Mg/Ca}$ reconstructions is almost consistent with other deglacial Mg/Ca-derived records from the subarctic NW Pacific using *Nps* (Sarnthein et al., 2004, 2006; Gebhardt et al., 2008). However, due to the application of the temperature calibration of Elderfield and Ganssen (2000), these studies show a slightly higher temperature range by 1–2°C.

***The following subsection will not be part of the submitted manuscript. It presents results derived from samples not used in the context of the deglacial temperature and salinity reconstructions. These results are shown to emphasize the need for future work.***

## 5.6.3. Potential diagenetic effects

In SO201-2 cores 12KL, 77KL, and 85KL, we found linear relationships between paired measurements of $\delta^{13}$C and Mg/Ca on *Nps* ($0.34 < R^2 < 0.41$). Bering Sea cores are characterized by short intervals during 37–23 ka BP with planktonic $\delta^{13}$C values that decrease to -1.2‰ PDB and that appear together with both, elevated Mg/Ca ratios, and increased Mn/Ca ratios (Fig. 5.11). Mg/Ca is as high as 5.7 mmol mol$^{-1}$ which would translate into unrealistic subSST$_{Mg/Ca}$ estimates of up to 41°C. Scanning electron microscope (SEM) analyses (CamScan Serie 2 CS 44EDX, Univ. Kiel) on uncleaned tests of *Nps* with unusually high Mg/Ca (>2 mmol mol$^{-1}$) from that interval show that outer and inner surfaces are covered with crystalline overgrowths of single tetrahedra-shaped crystals with a maximum size of 2–3 $\mu$m (Fig. 5.12). This might indicate a potential diagenetic overprint on sediments from Shirshov Ridge older than 23 ka BP.

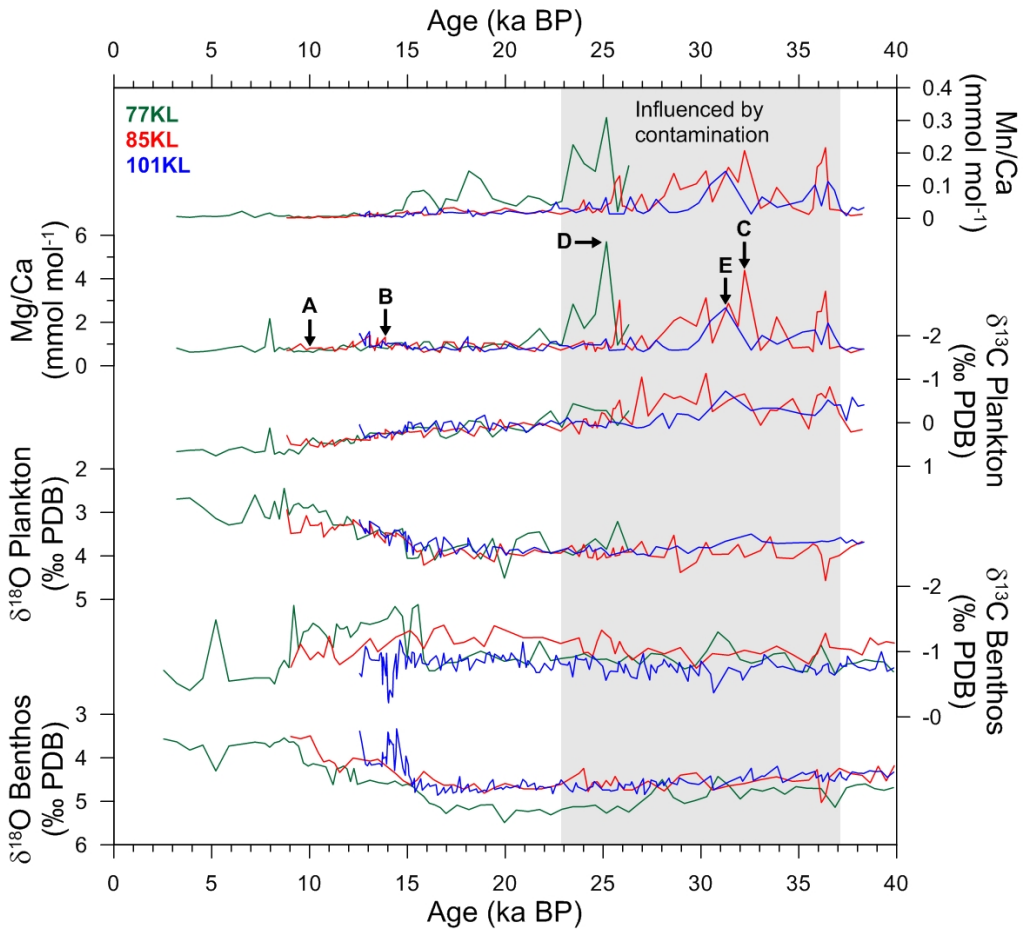


**Figure 5.11.:** Stable carbon ($\delta^{13}$C) isotopes, stable oxygen ($\delta^{18}$O) isotopes, as well as Mg/Ca and Mn/Ca ratios of the planktonic foraminiferal species *N. pachyderma* (sin.) and of the endobenthic foraminifer *U. peregrina* for Bering Sea cores SO201-2-77KL (green lines), -85KL (red lines), and -101KL (blue lines) for the last 40 kyrs. Short intervals with relatively high (>2 mmol mol$^{-1}$) planktonic Mg/Ca ratios are accompanied by high Mn/Ca ratios in the time interval 37-23 ka BP (grey-shaded area). Note that, except for the excursion around 36 ka BP in core 85KL, benthic and planktonic records do not show similar oscillations in $\delta^{13}$C and $\delta^{18}$O. Black arrows labeled A-E mark positions of SEM images shown in Fig. 5.12.

Negative $\delta^{13}$C values related to diagenetic overgrowths of authigenic carbonate were found in Umnak Plateau sediments (southern Bering Sea), but are reported to have extreme benthic (-6.8‰) and planktonic (-13‰) amplitudes (Cook, 2006). Cook (2006) speculated that due to mobilization of methane in line with the anaerobic methane oxidation, and its subsequent transport to the sediment-water interface, authigenic carbonate minerals may form due to supersaturation of pore waters with respect to carbonate. Although a different setting, similar coherencies are reported from Greenland Sea sediments low in $CaCO_3$, which contain benthic and planktonic foraminifera with also extremely negative $\delta^{13}$C values (up to -6‰) during MIS3 and authigenic calcite overgrowths (Millo et al., 2005a, 2005b). The authors suggested that post-depositional clathrate instability led to the supersaturation of $^{13}$C-depleted bicarbonate in pore waters from which authigenic calcite precipitated as crystalline overgrowths. Coincident large negative benthic (-5‰) and planktonic (-3‰) excursions of $\delta^{13}$C were also observed in MIS3 in sediments from Santa Barbara Basin (E Pacific), which were related to methane release in accord with temperature changes (Kennett et al., 2000).

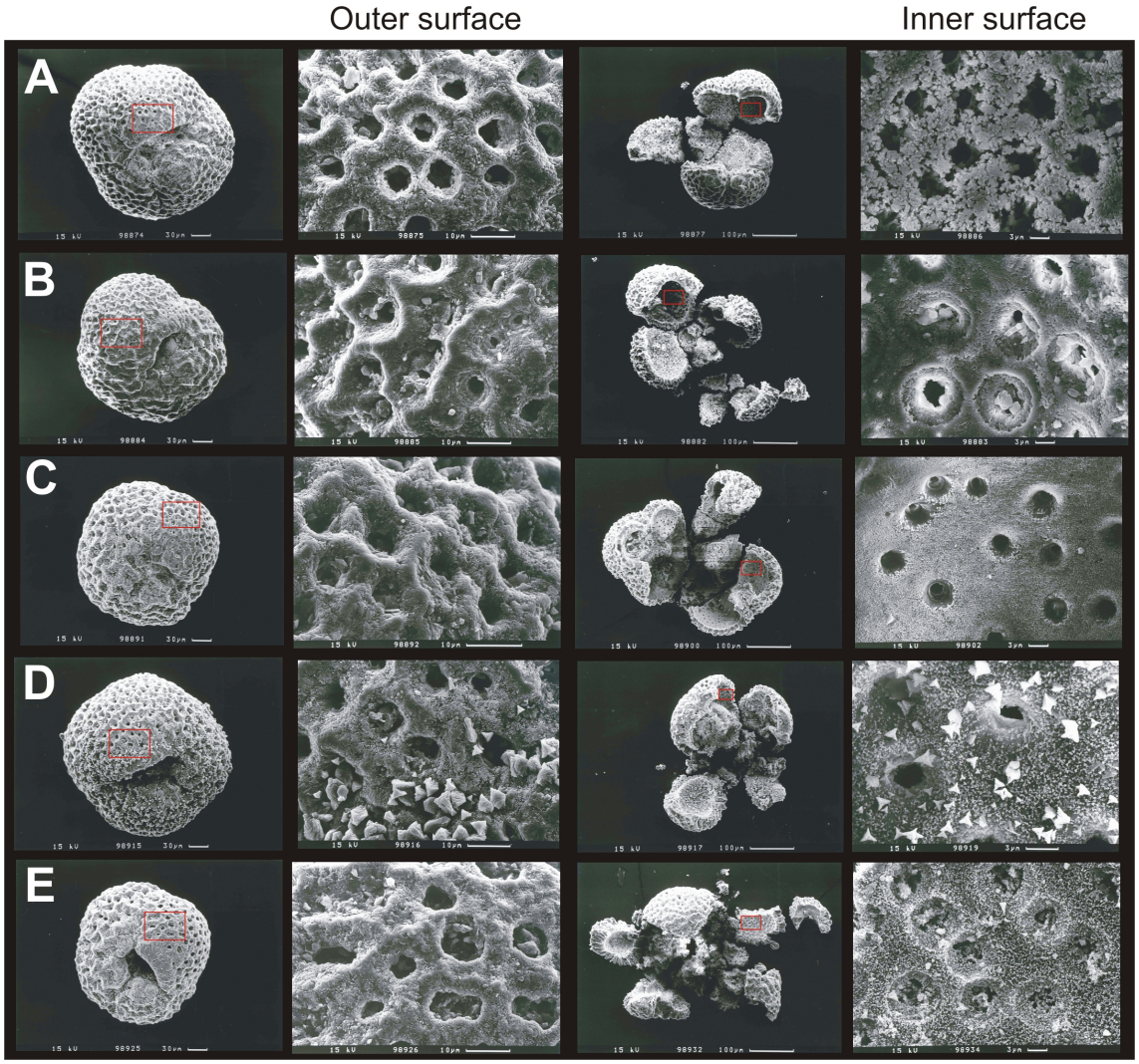


**Figure 5.12.:** Scanning electron microscope images (SEM) (CamScan Serie 2 CS 44/EDX, Univ. Kiel, Germany) of uncleaned tests of *N. pachyderma* (sin.) from Bering Sea sites. Pairs of images show an overview of opened/unopened tests and the according enlargements of the outer/inner test surfaces. The site scale is about the same for all images. Tests shown in A and B look unaltered, whereas tests in C-E show an overgrowth of tetrahedra-shaped crystals. A: SO201-2-85KL (25–26 cm, 10.0 ka BP), B: SO201-2-85KL (70–71 cm, 13.9 ka BP), C: SO201-2-85KL (245–246 cm, 32.2 ka BP), D: SO201-2-77KL (290–291 cm, 25.2 ka BP), E: SO201-2-101KL (255–256 cm, 31.3 ka BP).

If our foraminiferal tests actually were subject to methane-induced diagenetic overgrowth of authigenic carbonates precipitated from pore waters, tests of benthic foraminifera should be similarly affected. We therefore performed additional measurements of stable carbon and oxygen isotopes on endobenthic foraminifera *U. peregrina* (2–3 specimens, 315–355 $\mu$m size fraction). Neither *Nps* nor *U. peregrina* featured $\delta^{13}$C variations of the magnitude described by the beforementioned studies (Fig. 5.11). Both species also did not show a covariation of $\delta^{13}$C-oscillations, which argues against a methane-induced early diagenetic overprint by pore waters. We therefore consider a diagenetic influence on samples from 37–23 ka BP through calcite recrystallization possible to explain the occurrence of the tetrahedra-shaped crystals, but rather relate high Mg/Ca ratios in *Nps* to contamination by Mn-bearing minerals or coatings. Nevertheless, the cause of these overgrowths should be further investigated.

# 6. Rapid changes in North Pacific Intermediate Water formation during the last glacial termination

**Based on:** *"Rapid changes in North Pacific Intermediate Water formation during the last glacial termination"* by Lars Max, Lester Lembke-Jene, Jan-Rainer Riethdorf, Ralf Tiedemann, and Dirk Nürnberg (to be submitted to *Nature Geoscience*).

## Abstract

Today the formation of North Atlantic Deep Water (NADW) leads to deep convection in the North Atlantic and no deep convection occurs in the North Pacific, where only intermediate water masses are formed in the Okhotsk Sea that ventilate the North Pacific. Recent studies suggest a switch to deep water formation in the subarctic North Pacific during the last glacial termination in response to a shutdown or weakening of the Atlantic Meridional Overturning Circulation (AMOC) (Okazaki et al., 2010). Here we show detailed records of past ventilation changes from the Okhotsk Sea and Bering Sea spanning the last glacial termination. Compelling evidence for intermediate water formation in these two marginal seas is given by combining marine radiocarbon ages and stable isotope ventilation records, which suggest that only the upper North Pacific (∼1350 m) was better ventilated, whereas data from the deeper portion of the North Pacific (>2130 m) show no evidence for deep water formation during phases of AMOC reductions.

## 6.1. Introduction

A prime mechanism to explain the rise in atmospheric $CO_2$ concentrations during the last deglaciation is the removal of old and deep sequestered carbon from the North Pacific Ocean (Marchitto et al., 2007; Galbraith et al., 2007; Jaccard et al., 2009; Stott et al., 2009). Given that the abyssal North Pacific Ocean today holds the largest quantity of dissolved inorganic carbon, it is of paramount importance to understand its exchange with the atmosphere through changes in ventilation rates in the past. At present, the subarctic North Pacific surface waters are isolated from deeper, nutrient-rich waters by a steep, year-round salinity gradient (halocline). This halocline forms a barrier for heat and gas exchange between the atmosphere and the deep ocean, as well as for the supply of nutrients into the photic zone. As the excessive evasion of nutrients into the photic zone is hampered by the halocline, the subarctic North Pacific is marked by one of the highest modern carbon export efficiencies known in the world oceans and is a net sink of atmospheric $CO_2$ (Honda et al., 2002; Sarmiento et al., 2004). Today,

formation of new water masses in the North Pacific is restricted to the Okhotsk Sea in the northwest Pacific (NW-Pacific), where waters are produced in coastal polynyas by brine rejection during wintertime sea-ice production (Talley, 1993; Shcherbina et al., 2003). These new water masses leave the Okhotsk Sea as Okhotsk Sea Intermediate Water (OSIW) (see supplementary information), mix with water in the NW-Pacific at intermediate depths and form North Pacific Intermediate Water (NPIW). The NPIW spreads eastward through the North Pacific Ocean between ca. 20°N–40°N to the proximity of the California Current region, where it can still be recognized as positive oxygen anomaly between 300–800 m water depth.

It has been proposed that a better ventilated Glacial North Pacific Intermediate Water (GNPIW) formed during the Last Glacial Maximum, leading to deeper convection of the subarctic North Pacific in the upper 2000 m (Boyle and Keigwin, 1985; Keigwin, 1998; Matsumoto et al., 2002). Studies on deep-sea records (deeper than 2000 m) based on benthic carbon isotopes ($\delta^{13}C$) and paired benthic/planktic foraminifera $^{14}C$ measurements (BF-PF ages) show only minor changes in deep convection (Keigwin, 1987; Lund et al., 2011) in the North Pacific or no ventilation changes at all in the deep Pacific Ocean (Broecker et al., 2004; Broecker et al., 2008). However, studies with General Circulation Models (GCMs) point to a more rigorous ventilation of the deglacial North Pacific in response to a shutdown of the AMOC during the Heinrich 1 cold event. Accordingly, this would lead to an onset of a Pacific Meridional Overturning Circulation (PMOC), which transports heat and salt poleward and warms the subpolar North Pacific, while the North Atlantic cools (temperature seesaw) (Bard et al., 2000). An enhanced poleward transport of warm and saline waters by the PMOC would also lead to an onset of deep overturning in the subarctic North Pacific (Okazaki et al., 2010), whereas a sluggish AMOC persisted during Heinrich 1 in the North Atlantic (ventilation seesaw) (Saenko et al., 2004). Strong evidence for mid-depth ventilation changes from BF-PF ages in the western subarctic North Pacific indicate significant changes in intermediate water formation during the last glacial termination (Duplessy et al., 1989; Ahagon et al., 2003; Sagawa and Ikehara, 2008). However, if enhanced ventilation of water masses in the subarctic North Pacific was related to GNPIW, potential source regions are the Okhotsk Sea, the Bering Sea or both. Some evidence for deglacial changes in the ventilation history of these marginal seas stems from studies on microfossil assemblages (Tanaka and Takahashi, 2005) and trace-metals (Horikawa et al., 2010), which point out that the Bering Sea in particular played a more active role in ventilating the North Pacific. Whether an amplified convection from the marginal seas led to changes in the ventilation of the North Pacific when the AMOC was collapsed has remained elusive in the context to understand the role of North Pacific Ocean ventilation changes during rapid climate changes.

## 6.2. Material and methods

We present new results from carbon isotope records in combination with BF-PF ages to give a first comprehensive view on past ventilation changes in the North Pacific to: (1) infer the timing and extent of intermediate or deep water formation in the potential source regions and to: (2) assess the impact of a North Atlantic–North Pacific meridional overturning asymmetry on ventilation changes in the North Pacific during the last glacial termination. Sediment records from the Okhotsk Sea (SO178-13-6;

52°43'N, 144°42'E, 713 m water depth) and the western Bering Sea (SO201-2-85KL; 57°30'N, 170°24'E, 968 m water depth) were selected to provide new insights into the mid-depth ventilation history of the study area (Fig. 6.1a). The stratigraphy is well constrained by multiple AMS-$^{14}$C datings (AMS-$^{14}$C ages, see supplementary Table 6.1 on page 142, and Fig. 6.4 on page 138, and Fig. 6.5 on page 139) and detailed inter-core correlation via high-resolution X-ray fluorescence (XRF) core scanner data (Max et al., in review) (see supplementary methods on page 137). $\delta^{13}$C was measured on epibenthic foraminifera *Cibicidoides lobatulus* (see supplementary Table 6.3 on page 146), proven to be a robust proxy to study changes in past ocean circulation (Curry et al., 1988; Curry and Oppo, 2005). These data are supplemented by a set of six BF-PF ages derived from sediment records of the NW Pacific (see supplementary Table 6.2 on page 143). In addition, we used recently published high-resolution sea surface temperature (SST) data based on alkenone paleothermometry ($U^{k'}_{37}$) from the subarctic NW-Pacific (Max et al., in review) together with previously published northeast Pacific (Barron et al., 2003) and North Atlantic (Bard et al., 2000) SST data to study circulation changes and the AMOC/PMOC relationship to deglacial climate changes (Okazaki et al., 2010).

## 6.3. Results and discussion

In order to assess the timing and nature of ventilation changes in the subarctic North Pacific and its relationship to major reorganizations in the AMOC we compared our western Bering Sea intermediate-depth $\delta^{13}$C record with published $^{231}$Pa/$^{230}$Th data (proposed to reflect the strength of the AMOC) from the North Atlantic (McManus et al., 2004) during the last deglaciation (Fig. 6.1b). The most striking feature is that the western Bering Sea record reveals millennial-scale oscillations in $\delta^{13}$C that indicate repeated intermediate water ventilation changes, which are strictly opposite in sign (ventilation seesaw) compared to the North Atlantic deep circulation history of the last 20 kyr (Fig. 6.1b). In more detail, the western Bering Sea $\delta^{13}$C record shows several pronounced reversals between $\delta^{13}$C minima at 19–17.5 ka BP, 14.8–12.8 ka BP and 11.7–11 ka BP, and alternating maxima in the $\delta^{13}$C at 17–14.9 ka BP and 12.2–11.7 ka BP. The North Atlantic $^{231}$Pa/$^{230}$Th record suggests that the AMOC nearly ceased and North Atlantic Deep Water (NADW) formation became sluggish during Heinrich 1 (17.5–15 ka BP) and the Younger Dryas (12.8–11.8 ka BP) cold phases. In contrast, the western Bering Sea $\delta^{13}$C data show more rigorous ventilation of intermediate waters during the cold phases and times of reduced deep convection in the North Atlantic. Furthermore, when the North Atlantic deep overturning cell was re-established during the Bølling/Allerød (14.7–12.8 ka BP) and at the onset of the Holocene, active ventilation of western Bering Sea intermediate water ceased. From this we infer that the western Bering Sea was better ventilated episodically during phases of AMOC slowdown, forming a ventilation seesaw between the North Pacific and North Atlantic.

Enhanced formation of intermediate water masses in the subarctic North Pacific becomes more apparent from the Okhotsk Sea $\delta^{13}$C record (Fig. 6.2a). Higher $\delta^{13}$C values are associated with Heinrich 1 in the Okhotsk Sea and similar in timing to the western Bering Sea, but reveal much higher amplitudes of up to +1.0‰. This clearly indicates the enhanced formation of fresh, newly formed water masses in the Okhotsk

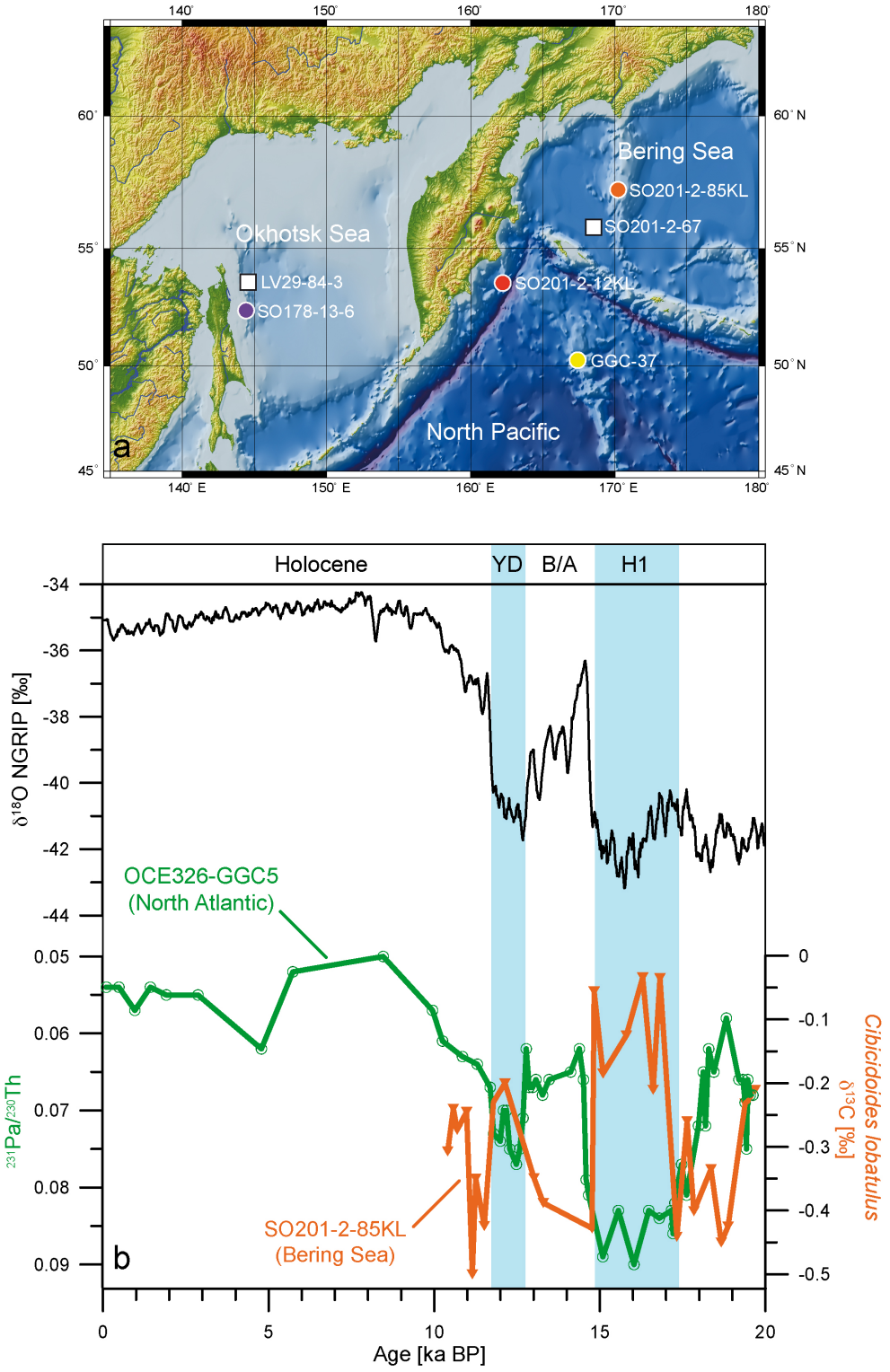


**Figure 6.1.:** (a) Overview map of the subarctic NW Pacific and its marginal seas with sediment core locations for SO201-2-85KL in the western Bering Sea (orange spot), SO178-13-6 in the Okhotsk Sea (purple spot), SO201-2-12KL (red spot) and GGC-3711 (yellow spot) from the NW Pacific as well as location of water profiles of $\delta^{13}C_{DIC}$ (see supplementary Fig. 6.6 on page 141), indicated as white boxes. (b) NGRIP ice core record and Pa/Th ratio (in green; McManus et al., 2004) as a proxy for the AMOC strength in the North Atlantic and $\delta^{13}$C-record (in orange) of the western Bering Sea as proxy for intermediate water ventilation for the last 20 kyr.

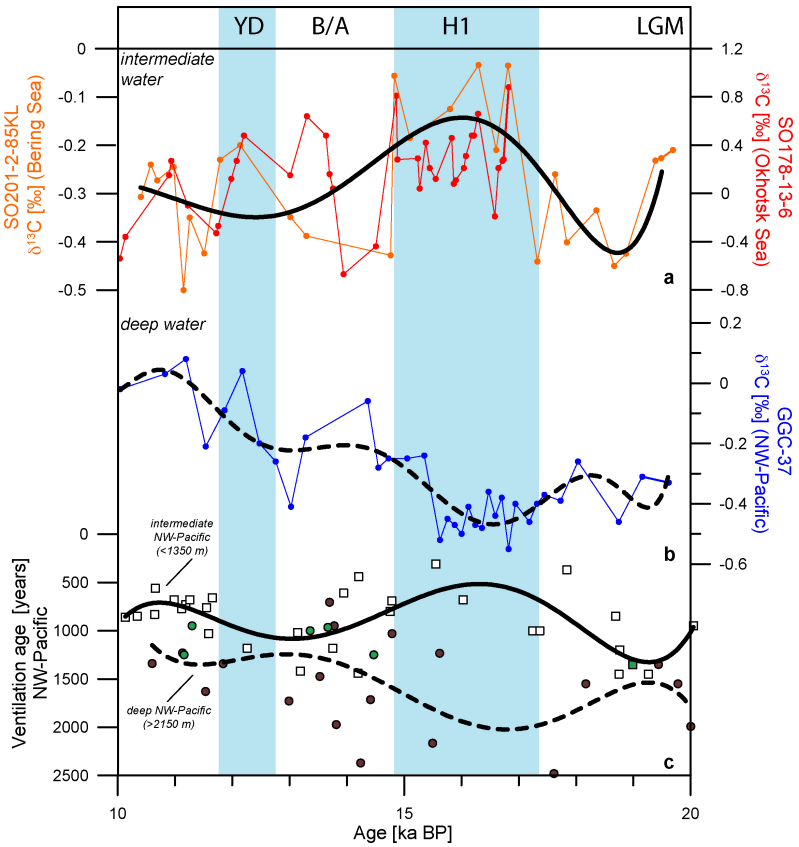


**Figure 6.2.:** Sediment proxy records of past ventilation changes of intermediate (<1366 m) and deep water (>2130 m) in the NW Pacific from 20–10 ka BP with (a) benthic foraminiferal $\delta^{13}$C-records (*C. lobatulus*) from the Okhotsk Sea (red curve) and Bering Sea (orange curve) together with spline-interpolated $\delta^{13}$C-record from the Bering Sea (thick black line) and in (b) $\delta^{13}$C-record from sediment record GGC-37 (in blue) from the deep NW Pacific and spline interpolation (thick stippled line) together with (c) published intermediate (open boxes) and deep water (filled brown circles) BF-PF ages (Duplessy et al., 1989; Ahagon et al., 2003; Sagawa and Ikehara, 2008; Ikehara et al., 2006; Hoshiba et al., 2006; Keigwin, 2002; Minoshima et al., 2007b; Murayama et al., 1992; Sarnthein et al., 2006) and intermediate (filled green boxes) and deep water (filled green circles) BF-PF ages from this study. Calculated splines are derived from whole set of BF-PF ages and given for intermediate (thick black line) and deep water (thick stippled line), respectively.

Sea during Heinrich 1 (17–15 ka BP), the Allerød (13.2–13.5 ka BP) and Younger Dryas (11.8–12.2 ka BP). In particular, during Heinrich 1 the OSIW is characterized by values of up to +1.0‰, which are similar to modern NADW $\delta^{13}$C signatures (+1-1.2‰) in the subarctic North Atlantic (Curry and Oppo, 2005). In turn, most depleted $\delta^{13}$C values (-0.5 to -0.8‰) are recorded during the early Bølling (14.7–14.0 ka BP) and the early Holocene, similar to the western Bering Sea. From this we infer a strengthened formation of NPIW in the subarctic North Pacific during phases of AMOC reductions and vice versa. Both the high magnitude of $\delta^{13}$C values recorded in the Okhotsk Sea (-0.8–1.0‰) and the less pronounced western Bering Sea $\delta^{13}$C values (-0.5–0‰) point to concurrent, rapid changes in ventilation of intermediate water masses in the two marginal seas during the last 20 kyr. Given the difference in $\delta^{13}$C gradients between the two basins we conclude that the Okhotsk Sea was the major source region for young, well-ventilated intermediate water masses (NPIW) in the subarctic North Pacific during the last deglaciation.

We combined available BF-PF ages (see supplementary Table 6.2 on page 143) and $\delta^{13}$C records from the intermediate and deep NW Pacific to assess the extent of ventilation changes during the last glacial termination (Fig. 6.2, a-c). By direct comparison between intermediate and deep ventilation records ($\delta^{13}$C signal and BF-PF ages), it becomes apparent that during Heinrich 1 the intermediate and deep water ventilation changes were opposite in sign and indicate most intensified intermediate water ventilation compared to most decreased ventilation of the deep NW Pacific. Highest gradients in $\delta^{13}$C and ventilation ages between intermediate and deep water during Heinrich 1 suggest the development of a shallow overturning (shallow PMOC) that leaves the North Pacific Deep Water unaffected. The ventilation asymmetry between intermediate and deep water contradicts the onset of deep water formation in the North Pacific (Okazaki et al., 2010), but are in harmony with the evidence for a bathyal front at about 2000 m reported for the glacial North Pacific (Keigwin, 1998; Matsumoto et al., 2002; Duplessy et al., 1988; Herguera et al., 1992) and probably also established during Heinrich 1 of the last deglacial period. The better ventilated volumes and ages in the upper ocean during glacial conditions (<2000 m) were related to the wind stress curl and surface buoyancy fluxes at mid- to high latitudes in the North Pacific, probably driven by enhanced meridional and zonal pressure and temperature gradients. In turn, the deeper portion of the North Pacific (>2000 m) has been proposed to be affected by water masses formed in the Southern Ocean (Herguera et al., 2010). Similar processes could also feature the establishment of the observed ventilation asymmetry between intermediate and deep water during Heinrich 1 in the NW Pacific but are not understood so far.

The strengthening of NPIW formation in response to AMOC reductions (ventilation seesaw) is in harmony with results of several modelling studies (GCMs), which simulate enhanced meridional overturning in the North Pacific during the last glacial termination. However, most studies suggest an establishment of a PMOC and active convection of heat and salt in the subpolar regions of the North Pacific to promote deep overturning (Saenko et al., 2004; Schmittner et al., 2007; Krebs and Timmermann, 2007). This scenario would lead to a more rigorous ventilation of the subarctic North Pacific accompanied with a rise in SST by up to 1.8°C (Okazaki et al., 2010) as response to a weakening of the AMOC (e.g. during Heinrich 1 or the Younger Dryas) and cooling in the North Atlantic (temperature seesaw). On the other hand, some model results proposed a cooling in the subarctic North Pacific due to a shutdown of AMOC (Mikolajewicz et al., 1997; Okumura et al., 2009). There, the simulated shutdown of the Meridional Overturning Circulation in the North Atlantic triggers rapid atmospheric reorganizations in the subarctic North Pacific via an atmospheric bridge and leads to an intensification of low pressure systems (Aleutian Low), which amplifies a cooling in the subarctic North Pacific. Conversely, this mechanism would lead to a similar SST development between the North Atlantic and the North Pacific (no temperature seesaw) and also question the mechanism of PMOC-related warming and deep overturning in the subarctic North Pacific. We used high-resolution SST data from the North Pacific (Max et al., in review; Barron et al., 2003) and the North Atlantic (Bard et al., 2000), together with the North Greenland ice-core record (NGRIP; Rasmussen et al., 2006) to assess the proposed mechanistic links between the shutdown of the AMOC (cooling of the North Atlantic) and an onset of a PMOC (warming of the North Pacific). The comparison of SST data between the North Pacific and the North Atlantic temperature record (Fig. 6.3) exhibits a similar SST development (no temperature seesaw) during the last glacial termination (Max et al., in review). The similar SST development

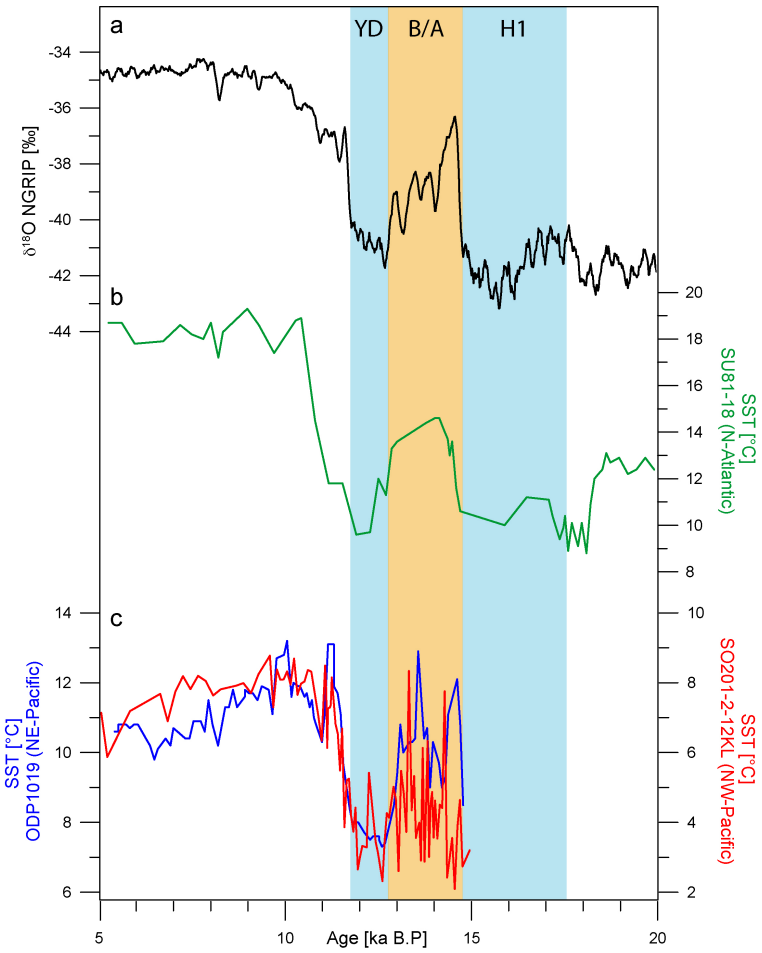


**Figure 6.3.:** Northern Hemisphere climate fluctuations of the past 20 kyr given by (a) NGRIP ice core oxygen isotope record together with (b) alkenone-based sea surface temperature record SU81-18 from the North Atlantic (in green; Bard et al., 2000) and (c) alkenone-based sea surface temperature records from the NE Pacific (in blue; Barron et al., 2003) and NW Pacific (in red; Max et al., in review) for the last 15 kyr.

between the North Atlantic and the North Pacific clearly shows that changes in the PMOC only have a minor influence on the NW Pacific SST development. This calls for other mechanisms to explain enhanced intermediate or deep water formation in the North Pacific during the last glacial termination.

More recently, a study addressed the issue of variability in North Pacific intermediate and deep water ventilation during Heinrich events by using two coupled climate models (MIROC and LOVECLIM) with LGM background conditions (Chikamoto et al., 2012). Both model runs simulated a differing strengths of the PMOC, which resulted in a cooling of the western North Pacific (no temperature seesaw) by 2.2 and 2.6°C, respectively. The largest cooling trend appears in the western North Pacific in association with severe cooling of the overlying atmosphere in the Northern Hemisphere and intensification of the Aleutian Low (Okumura et al., 2009). Interestingly, the model-run with a weak PMOC (MIROC) results in a more pronounced cooling of the western North Pacific and also indicates a cooling in the eastern North Pacific. As a result, the mixed layer deepens near the Kamchatka region and in the western boundary currents, corresponding to strong mixing of surface and subsurface waters and shallow overturning (extending to 2000 m water depth) of the North Pacific in line with our results. On the other hand, an enhanced PMOC (LOVECLIM) would result in deeper

overturning (greater than 3000 m water depth) due to a greater transport of warm and saline equatorial waters to the North Pacific (temperature seesaw) in contrast to our results.

## 6.4. Conclusions

The match between the simulated SST and ventilation changes (MIROC) and our results make a compelling case for the existence of intermediate water formation during H1 and associated onset of shallow overturning in the North Pacific. In turn, no deep water formation occurred in the subarctic North Pacific during Heinrich 1 as given by the largest intermediate to deep water BF-PF age and $\delta^{13}C$ gradients, in contrast to the simulated intensification of a PMOC and related deep overturning (LOVECLIM; Okazaki et al., 2010). Several model studies emphasize the importance of changes in overlying atmospheric pressure regimes in the northern hemisphere during AMOC reductions. Accordingly, the simulated shutdown of the Meridional Overturning Circulation in the North Atlantic triggers rapid atmospheric reorganizations in the subarctic North Pacific via an atmospheric bridge and leads to an intensification of the Aleutian Low and a cooling in the North Pacific. Some studies suggest that in response to a substantial AMOC-weakening tropical Atlantic cooling induces anomalous high pressure that extends to the eastern tropical Pacific, thereby intensifying northeasterly trade winds across the central isthmus of America (Wu et al., 2008). The advection of cold and dry air from the Atlantic to the Pacific would lead to tropical precipitation anomalies in the eastern tropical North Pacific and triggers the propagation of Rossby waves, which influences the strength of the Aleutian Low (Okumura et al., 2009). Other studies emphasize the role of intensified westerly winds due to an AMOC-shutdown. This would lead to enhanced thermal advection of cold air masses to the North Pacific by prevailing westerly winds, which induce a southward shift of the oceanic frontal zones and a deepening of the wintertime Aleutian Low (Manabe and Stouffer, 1988; Mikolajewicz et al., 1997; Vellinga and Wood, 2002). A recent study also claims the sensitivity of the East Asian winter monsoon to AMOC variations by enhanced westerly winds, which are supposed to lead to an overall reduction of humidity and colder temperatures in the Northern Hemisphere (Sun et al., 2012). Altogether, our results confirm the proposed impact of rapid atmospheric teleconnections between the North Atlantic and North Pacific, which led to a cooling and shallow overturning in the western North Pacific during AMOC reductions. We conclude that intermediate water formation in the subarctic North Pacific can be explained by fast atmospheric interactions between the North Atlantic and North Pacific, which led to rapid dynamics in oceanography and circulation during the last glacial termination.

# 6.5. Supplementary information

## 6.5.1. Age model (AMS-$^{14}$C dating and X-ray fluorescence measurements)

AMS-$^{14}$C ages were measured on samples of monospecific planktic foraminifera *Neogloboquadrina pachyderma* (sin.) from the 125–250 $\mu$m size fraction in core SO201-2-85KL. AMS-$^{14}$C ages in core SO178-13-6 were measured on a mix of planktonic foraminifera (*G. bulloides* and *Neogloboquadrina pachyderma* sin.) picked from 150–250 $\mu$m size fraction. The radiocarbon dating (AMS-$^{14}$C) has been performed by the National Ocean Science Accelerator Mass Spectrometry Facility (NOSAMS) at Woods Hole Oceanographic Institute (WHOI) and Leibniz-Laboratory for Radiometric Dating and Isotope Research at Kiel University. Radiocarbon ages have been reported according to the convention outlined by Stuiver and Polach (1977) and Stuiver (1980). All planktic radiocarbon ages were converted into calibrated 1-sigma calendar age ranges using the calibration tool Calib Rev 6.0 (Stuiver and Reimer, 1993) with the Intcal09 atmospheric calibration curve (Reimer et al., 2009) and are given in Table 6.1. For reservoir age correction, reservoir ages of 900 years were applied for core SO178-13-6 and 700 years for core SO201-2-85KL, in line with reported values for the Bering and Okhotsk Sea (Kuzmin et al., 2001; Kuzmin et al., 2007).

Relative sedimentary elemental composition was measured using the Avaatech X-ray Fluorescence (XRF) core scanner at the Alfred Wegener Institute for Polar and Marine Research except Okhotsk Sea cores LV29-114-3 and SO178-13-6, where XRF measurements were conducted at the Center for Marine Environmental Science (MARUM), Bremen. Each core segment was double-scanned for element analysis at 1 mA and tube voltages of 10 kV (Al, Si, S, K, Ca, Ti, Fe) and 50 kV (Ag, Cd, Sn, Te, Ba), using a sampling resolution of 1 cm and 30 s count time.

The deglacial stratigraphy is based on the set of radiocarbon measurements (Table 6.1) (AMS-$^{14}$C ages) and constrained with the X-ray Fluorescence (XRF) core scanner data for inter-core correlation (Fig. 6.4 and 6.5), described in detail by Max et al. (in review). In general, the Ca intensity records (XRF) have been used to correlate prominent similar structures between sediment records. We preferentially dated carbonate maxima (maxima in planktic foraminifera abundance), which are indicated by maxima in Ca intensities (XRF), to avoid age artefacts due to bioturbation effects. Figure 6.4 shows the Ca intensity records and a detailed core-to-core correlation of the core sites. The Ca intensity pattern shows two intervals with high Ca intensities (carbonate maxima) between 13.390–11.950 $^{14}$C years and 10.800–9.570 $^{14}$C years. These pronounced carbonate maxima are well dated in the NW Pacific realm and mark the B/A and the interval of the early Holocene (Keigwin et al., 1992; Keigwin, 1998; Gorbarenko et al., 2002a; Seki et al., 2004b; Gorbarenko et al., 2005; Cook et al., 2005; Seki et al., 2009). Hence, core SO178-13-6 was correlated to the established stratigraphy of Okhotsk Sea core LV129-114-3 (Max et al., in review) via the Ca intensity record (XRF) and available AMS-$^{14}$C dates (Table 6.1 and Fig. 6.5).

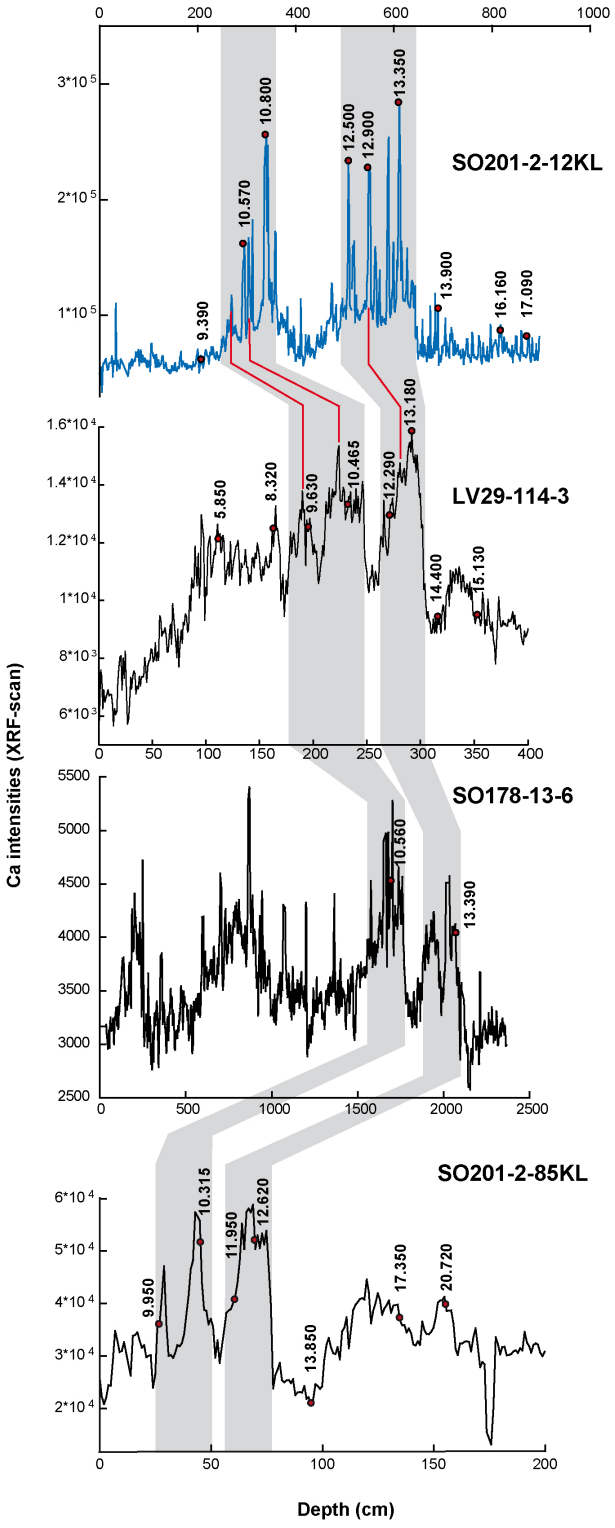


**Figure 6.4.:** Stratigraphic framework of sediment records from the western Bering Sea (SO201-2-85KL) and Okhotsk Sea (LV29-114-3 and SO178-13-6) correlated with high-resolution record SO201-2-12KL record (blue curve) from the subarctic NW-Pacific. The stratigraphy is based on Ca intensities, derived from core logging data (XRF), together with raw AMS-$^{14}$C datings (red spots with vertical numbers). Grey shaded areas mark prominent carbonate maxima, red lines indicate correlation points between the sediment records.

## 6.5.2. Paired benthic/planktic radiocarbon measurements (BF-PF ages)

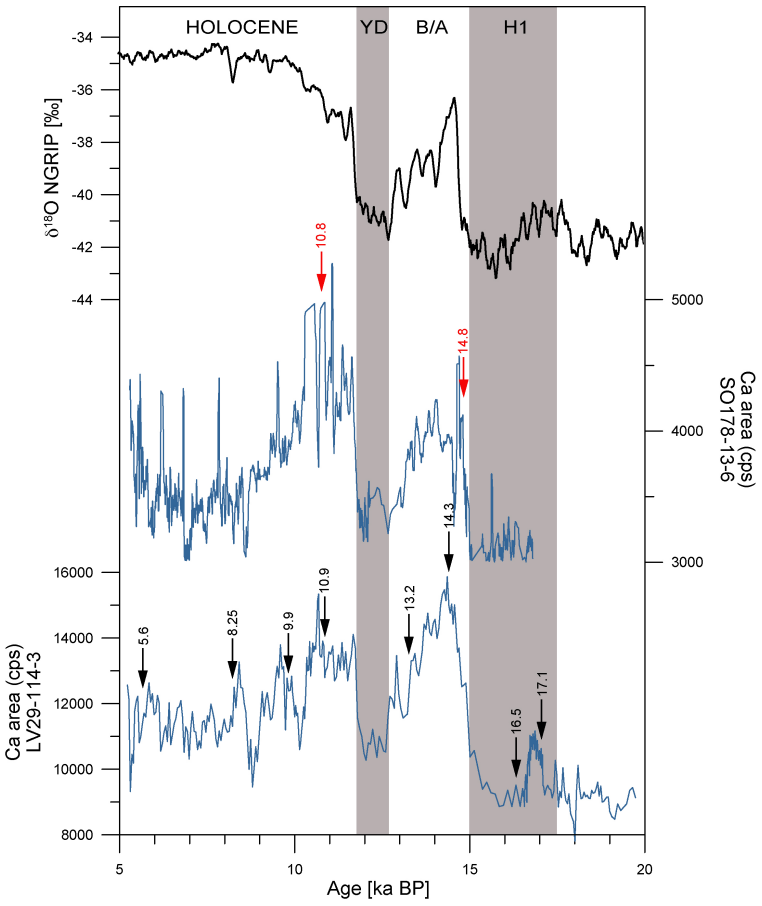


**Figure 6.5.:** Detailed core-to-core correlation for SO178-13-6 to the established age model of LV29-114-3 via AMS-$^{14}$C datings and Ca intensity records (in blue), see also Max et al. (in review) together with NGRIP isotope record in upper panel (in black). For this study, core SO178-13-6 was correlated via Ca intensity studies (XRF) and AMS-$^{14}$C datings to LV29-114-3. Black arrows with vertical numbers indicate calibrated $^{14}$C ages of LV29-114-3, red arrows with vertical numbers indicate calibrated $^{14}$C ages derived from SO178-13-6.

To infer paleo-ventilation ages in the subarctic Pacific we measured mono-specific samples of benthic foraminifera *Uvigerina peregrina* and planktic foraminifera *Neogloboquadrina pachyderma* (sin.) to assess BF-PF age differences on six samples (Table 6.2). Benthic/planktic radiocarbon measurements from this study were compiled together with already published BF-PF ages and used to infer ventilation changes in intermediate- and deep-water of the NW Pacific. Ventilation ages (BF-PF ages) were calculated by the difference of raw $^{14}$C ages between benthic and planktic foraminifera (Table 6.2).

## 6.5.3. Stable isotope measurements

Sediment samples from core SO178-13-6 and SO201-2-85KL were freeze-dried, washed over a 63 $\mu$m screen, dried and separated in sub-fractions (63–150, 150–250, 250–500, >500 $\mu$m). For stable isotope analysis, we picked the species *Cibicidoides lobatulus* (*C. lobatulus*). This species has been observed to preferentially live attached to hard

substrate on or slightly above the sediment surface (Lutze and Thiel, 1989; Schweizer et al., 2009) and studies on live specimen indicated that the species faithfully records the $\delta^{13}C_{\Sigma CO2}$ of overlying bottom waters. Some studies have observed a positive offset in the $\delta^{13}C$ of this species with regard to ambient bottom water for $\delta^{13}C_{DIC}$ at the time of sampling in other high latitude settings. However, this effect was shown to be likely caused by high seasonal variability of the original water $\delta^{13}C_{DIC}$ signal as indicated by time-series measurements of water column $\delta^{13}C_{DIC}$ and according calcification of *C. lobatulus* during time intervals of maximum ventilation (Mackensen et al., 2000). We thus regard *C. lobatulus* to reliably reflect the water mass $\delta^{13}C$ signal. We mostly picked between two and five specimen per sample and restricted our selection to well-preserved specimen with visible pores, clear sutures and unfilled chambers. During some intervals with low foraminifera abundance, we analyzed single specimen with sufficient size and preservation. Samples were cracked open to remove dirt particles from the inside, if necessary cleaned ultrasonically in ethanol p.a. and roasted at 200°C for 24 h. Samples of core SO178-13-6 were measured with a Thermo Finnigan MAT 252 isotope ratio mass spectrometer coupled to an automated KIEL II CARBO preparation device at the Paleoceanography Unit's Stable Isotope Laboratory of the GEOMAR, Kiel. Overall analytical reproducibility is ±0.04‰ for $\delta^{13}C$ and ±0.06‰ for $\delta^{18}O$. Sample measurements of core SO201-2-85KL were measured with a Thermo Finnigan MAT 253 isotope ratio mass spectrometer coupled to an automated KIEL CARBO preparation device at the Stable Isotope Laboratory of the Alfred Wegener Institute for Polar and Marine Research, Bremerhaven. Overall analytical reproducibility is ±0.06‰ for $\delta^{13}C$ and ±0.08‰ for $\delta^{18}O$. Calibration was achieved via National Bureau of Standards NBS19 and NBS20 material as well as through an internal laboratory standard of Solnhofen limestone. All values are reported as against the Vienna Pee Dee Belemnite Standard (expressed as ‰ vs. V-PDB) and given in Table 6.3.

## 6.5.4. Modern hydrography

Two stations proximal to the core sites SO201-2-85KL (for western Bering Sea SO201-2-67; 56°04'N, 169°14'E) and SO178-13-6 (for Okhotsk Sea station LV29-84-3, 52°42'N, 144°13'E) were selected to study the modern distribution of $\delta^{13}C_{DIC}$ (Fig. 6.6).

For the Bering Sea samples, the water column was sampled during the expedition S0201-2 of R/V Sonne in 2009 (Dullo et al., 2009) in eight depth intervals via a water sampling rosette device. Immediately after sub-sampling of Niskin bottles, water samples were poisoned with a saturated solution of mercury, sealed with wax and stored at 4°C temperature until further treatment. On shore, 1 ml of water was injected through a septum into a vial with ca. 3 ml concentrated phosphoric acid flushed with pure helium. After storage at room temperature for complete reaction the resultant $CO_2$ was transferred via a Finnigan Gas Bench II to a Finnigan MAT 252 gas mass spectrometer for determination of stable carbon isotope ratio at the Alfred Wegener Institute for Polar and Marine Research, Bremerhaven. Results are given in $\delta$-notation versus V-PDB. The precision of $\delta^{13}C$ measurements based on an internal laboratory standard has been reported to be better than ±0.1‰.

For the Okhotsk Sea, water samples were collected during the expedition LV29 of R/V Akademik M.A. Lavrentyev in 2002 (Biebow et al., 2003). Samples for carbon

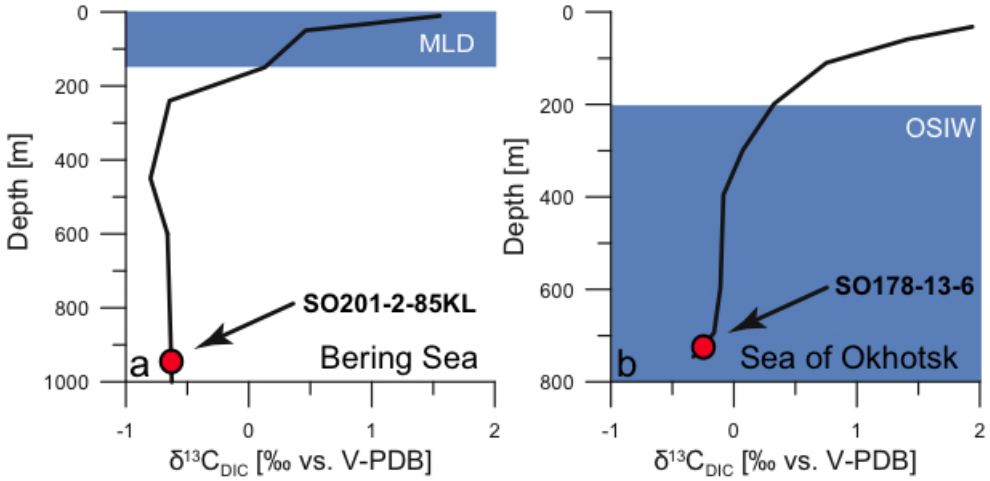


**Figure 6.6.:** Water profiles of $\delta^{13}C_{DIC}$ for the Bering Sea (station SO201-2-67) and Okhotsk Sea (station LV29-84-3) marginal Seas given as (a) $\delta^{13}C_{DIC}$ profile of the Bering Sea together with the depth-interval of SO201-2-85KL (red spot) and (b) $\delta^{13}C_{DIC}$ profile for the Okhotsk Sea together with the depth-interval of SO178-13-6 (red spot). Blue shaded area marks the mixing depth of fresh water masses in the Bering Sea (mixed layer depth = MLD) and Okhotsk Sea (OSIW), respectively.

isotope analysis of dissolved inorganic carbon (DIC) were slowly filled into 100 ml glass bottles directly after retrieval of a combined CTD water rosette sampler equipped with 12 Niskin bottles. 0.2 ml $HgCl_2$ was immediately added to each sample to stop biological activity. Bottles were closed by airtight crimp seals and stored under refrigerated, dark conditions until further treatment. Measurements of the $\delta^{13}C_{DIC}$ were carried out in the Leibniz Laboratory for Radiometric Dating and Isotope Research, Kiel, using an automated Kiel DICI-II device for $CO_2$ extraction and a Finnigan MAT Delta E mass spectrometer for measurements (see also Erlenkeuser and the TRANSDRIFT II Shipboard Scientific Party, 1995; Erlenkeuser et al., 1999). Isotope results are given in the $\delta$-notation and calibration is based on the NBS20 carbonate isotope standard, the measurement precision of the $\delta^{13}C_{DIC}$ is $\pm 0.04‰$.

The modern distribution of $\delta^{13}C_{DIC}$ show large differences between the Okhotsk Sea and Bering Sea marginal seas as indicated in Fig. 6.6. In the Bering Sea, a large gradient in $\delta^{13}C_{DIC}$ is located around 100 m depth, which marks today the mixed layer depth (MLD) by mixing of surface water with underlying water masses in winter (Fig. 6.6a). Beyond the MLD $\delta^{13}C_{DIC}$ values rapidly decline to -0.6 to -0.7‰ and indicate the absence of fresh intermediate-water masses in the western Bering Sea today. Modern values of $\delta^{13}C_{DIC}$ are around -0.6‰ at the depth interval of core SO201-2-85KL.

The $\delta^{13}C_{DIC}$ profile from the Okhotsk Sea show the presence of enriched $\delta^{13}C_{DIC}$ values within the water column between 200–800 m (Fig. 6.6b). Today, newly formed Okhotsk Sea Intermediate Water (OSIW) spreads across the Okhotsk Sea, expressed as positive $\delta^{13}C_{DIC}$ anomaly in the water profile. The modern value of Okhotsk Sea record SO178-13-6 lies at the lower boundary of OSIW with $\delta^{13}C_{DIC}$ values around -0.2‰.

**Table 6.1.:** AMS-$^{14}$C ages of the sediment records with calibrated age $\pm 1\sigma$ (years) and applied reservoir correction used in this study. AMS-$^{14}$C ages in italics have been derived from Max et al. (in review).

| Lab. No. | Core | Core depth (cm) | $^{14}$C age (years) | Cal. age $\pm 1\sigma$ (years) | Res. age (years) |
|---|---|---|---|---|---|
| *OS-85655* | *SO201-2-12KL* | *210* | *9390±40* | *9484-9527* | *900* |
| *KIA44680* | | *295* | *10570±50* | *11080-11191* | *900* |
| *OS-87895* | | *340* | *10800±65* | *11231-11368* | *900* |
| *OS-92047* | | *508* | *12500±50* | *13340-13498* | *900* |
| *OS-87891* | | *550* | *12900±50* | *13782-13918* | *900* |
| *OS-87902* | | *610* | *13350±65* | *14219-14752* | *900* |
| *OS-92150* | | *695* | *13900±55* | *15227-15872* | *900* |
| *KIA44682* | | *820* | *16160±80* | *18491-18666* | *900* |
| *KIA44683* | | *875* | *17090±90* | *19254-19457* | *900* |
| *transferred age* | *LV29-114-3* | *108* | *5850±60* | *5607-5730* | *900* |
| *OS-88042* | | *162* | *8320±40* | *8236-8310* | *900* |
| *KIA30864* | | *197* | *9630±50* | *9764-10067* | *900* |
| *KIA30863* | | *232* | *10465±50* | *10808-11080* | *900* |
| *KIA30867* | | *272* | *12290±55* | *13164-13308* | *900* |
| *KIA30865* | | *292* | *13180±60* | *13960-14457* | *900* |
| *KIA30868* | | *317* | *14400±80* | *16538-16827* | *900* |
| *KIA30866* | | *352* | *15130±80* | *17117-17497* | *900* |
| KIA30872* | SO178-13-6 | 1682.5 | 10560±50 | 10874-11183 | 900 |
| KIA30869* | | 2072.5 | 13390±100 | 14467-14917 | 900 |
| *OS-85665* | *SO201-2-85KL* | *26* | *9950±40* | *10378-10507* | *700* |
| *KIA42231* | | *45* | *10315±65* | *10791-10966* | *700* |
| *OS-85669* | | *60* | *11950±45* | *13104-13217* | *700* |
| *KIA42232* | | *70* | *12620±90* | *13665-13887* | *700* |
| *OS-87896* | | *95* | *13850±55* | *15822-15803* | *700* |
| *OS-87890* | | *135* | *17350±65* | *19575-19895* | *700* |
| *KIA42233* | | *155* | *20720±160* | *23706-24194* | *700* |

*this study

**Table 6.2.:** Radiocarbon measurements on paired benthic/planktic foraminiferas in the NW Pacific. BF-PF ages are given in years and periods are indicated by LGM, H1, B/A, and Holocene, respectively.

| Core | Wt. depth (m) | Cal. age (ka BP) | Core depth (cm) | Planktic $^{14}$C age (kyr) | $\pm1\sigma$ (years) | Benthic $^{14}$C age (kyr) | $\pm1\sigma$ (years) | BF-PF (years) | Period | Reference |
|---|---|---|---|---|---|---|---|---|---|---|
| **North Pacific (intermediate water)** | | | | | | | | | | |
| CH84-14 | 978 | 10.34 | 230 | 10000 | 140 | 10850 | 140 | 850 | Holocene | Duplessy et al. (1989) |
| CH84-14 | 978 | 10.64 | 280 | 10230 | 140 | 11060 | 150 | 830 | Holocene | |
| CH84-14 | 978 | 11.19 | 310 | 10640 | 150 | 11370 | 130 | 730 | Holocene | |
| CH84-14 | 978 | 11.55 | 340 | 10870 | 150 | 11630 | 180 | 760 | Holocene | |
| CH84-14 | 978 | 13.14 | 400 | 12180 | 160 | 13200 | 150 | 1020 | B/A | |
| CH84-14 | 978 | 13.76 | 480 | 12750 | 150 | 13930 | 220 | 1180 | B/A | |
| CH84-14 | 978 | 14.21 | 510 | 13060 | 140 | 13500 | 200 | 440 | B/A | |
| CH84-14 | 978 | 15.55 | 550 | 13830 | 150 | 14140 | 200 | 310 | H1 | |
| CH84-14 | 978 | 17.84 | 690 | 15570 | 210 | 15940 | 190 | 370 | | |
| GH02-1030 | 1212 | 10.13 | 210 | 9840 | 40 | 10700 | 70 | 860 | Holocene | Ikehara et al. (2006), |
| GH02-1030 | 1212 | 10.66 | 220 | 10240 | 60 | 10800 | 70 | 560 | Holocene | Sagawa and Ikehara (2008) |
| GH02-1030 | 1212 | 10.99 | 235 | 10510 | 60 | 11190 | 60 | 680 | Holocene | |
| GH02-1030 | 1212 | 11.26 | 244 | 10690 | 60 | 11370 | 60 | 680 | Holocene | |
| GH02-1030 | 1212 | 11.65 | 261 | 10950 | 60 | 11610 | 70 | 660 | Holocene | |
| GH02-1030 | 1212 | 13.94 | 290 | 12900 | 70 | 13510 | 80 | 610 | B/A | |
| GH02-1030 | 1212 | 14.19 | 323.5 | 13060 | 70 | 14500 | 50 | 1440 | B/A | |
| GH02-1030 | 1212 | 14.78 | 345.5 | 13470 | 40 | 14160 | 40 | 690 | H1 | |
| GH02-1030 | 1212 | 17.25 | 435.5 | 15010 | 80 | 16010 | 90 | 1000 | H1 | |
| GH02-1030 | 1212 | 17.37 | 465.5 | 15140 | 60 | 16140 | 80 | 1000 | H1 | |
| GH02-1030 | 1212 | 18.69 | 523 | 16380 | 60 | 17230 | 100 | 850 | | |
| GH02-1030 | 1212 | 20.05 | 558 | 17780 | 70 | 18730 | 120 | 950 | LGM | |
| GH02-1030 | 1212 | 21.77 | 630 | 19130 | 180 | 20590 | 180 | 1460 | LGM | |
| MR01K03-PC4/5 | 1366 | 11.12 | 231-232 | 10600 | 50 | 11370 | 50 | 770 | Holocene | Ahagon et al. (2003), |
| MR01K03-PC4/5 | 1366 | 11.59 | 262-264 | 10900 | 55 | 11930 | 60 | 1030 | Holocene | Hoshiba et al. (2006) |
| MR01K03-PC4/5 | 1366 | 12.26 | 291-293 | 11420 | 60 | 12600 | 50 | 1180 | YD | |
| MR01K03-PC4/5 | 1366 | 13.19 | 311-313 | 12230 | 50 | 13650 | 100 | 1420 | B/A | |
| MR01K03-PC4/5 | 1366 | 14.76 | 363-365 | 13450 | 85 | 14250 | 120 | 800 | H1 | |

**Table 6.2. (continued)**.

| Core | Wt. depth (m) | Cal. age (ka BP) | Core depth (cm) | Planktic $^{14}$C age (kyr) | $\pm1\sigma$ (years) | Benthic $^{14}$C age (kyr) | $\pm1\sigma$ (years) | BF-PF (years) | Period | Reference |
|---|---|---|---|---|---|---|---|---|---|---|
| MR01K03-PC4/5 | 1366 | 16.03 | 405-407 | 14150 | 55 | 14830 | 60 | 680 | H1 | |
| MR01K03-PC4/5 | 1366 | 18.76 | 540-542 | 16450 | 110 | 17650 | 100 | 1200 | | |
| MR01K03-PC4/5 | 1366 | 20.64 | 642-644 | 18200 | 65 | 19650 | 110 | 1450 | LGM | |
| **Bering Sea** | | | | | | | | | | |
| **SO201-2-101KL** | **630** | **18.99** | **110** | **17310** | **120** | **18630** | **200** | **1350** | **LGM** | **this study** |
| **Okhotsk Sea** | | | | | | | | | | |
| GGC-27 | 995 | 18.75 | 70 | 16750 | 200 | 18200 | 95 | 1450 | | Keigwin (2002) |
| B34-91 | 1227 | 19.26 | 225 | 17200 | 80 | 18650 | 110 | 1450 | LGM | Keigwin (2002) |
| **North Pacific (deep water)** | | | | | | | | | | |
| **SO201-2-12KL** | **2170** | **11.30** | **340** | **10800** | **65** | **11750** | **50** | **950** | **Holocene** | **this study** |
| **SO201-2-12KL** | **2170** | **13.36** | **508** | **12500** | **50** | **13500** | **55** | **1000** | **B/A** | |
| **SO201-2-12KL** | **2170** | **13.78** | **550** | **12900** | **50** | **13850** | **50** | **950** | **B/A** | |
| KR02-15 PC6 | 2215 | 11.13 | 539.2 | 10610 | 90 | 11840 | 60 | 1230 | Holocene | Minoshima et al. (2007b) |
| KR02-15 PC6 | 2215 | 11.54 | 555.1 | 10860 | 70 | 12490 | 110 | 1630 | Holocene | |
| KR02-15 PC6 | 2215 | 14.79 | 575.6 | 13470 | 70 | 14500 | 120 | 1030 | H1 | |
| KT89-18-P4 | 2700 | 10.60 | 185-190 | 9800 | 133 | 11140 | 207 | 1340 | Holocene | Murayama et al. (1992) |
| KT89-18-P4 | 2700 | 11.84 | 200-204 | 10692 | 108 | 12034 | 143 | 1342 | YD | |
| KT89-18-P4 | 2700 | 12.99 | 236-240 | 11622 | 101 | 13350 | 259 | 1728 | YD | |
| KT89-18-P4 | 2700 | 13.82 | 268-272 | 12450 | 91 | 14423 | 254 | 1973 | B/A | |
| KT89-18-P4 | 2700 | 15.62 | 338-342 | 13447 | 113 | 14681 | 153 | 1234 | H1 | |
| KT89-18-P4 | 2700 | 20.00 | 449-453 | 17275 | 478 | 19267 | 734 | 1992 | LGM | |
| KT89-18-P4 | 2700 | 22.87 | 534-538 | 19665 | 303 | 21344 | 366 | 1689 | LGM | |
| MD01-2416 | 2317 | 13.67 | 88 | 12690 | 55 | 13655 | 55 | 965 | B/A | Sarnthein et al. (2006) |
| MD01-2416 | 2317 | 13.53 | 96 | 12555 | 60 | 14030 | 70 | 1475 | B/A | |
| MD01-2416 | 2317 | 14.41 | 115 | 13205 | 55 | 14920 | 70 | 1715 | B/A | |
| MD01-2416 | 2317 | 14.24 | 136 | 13090 | 60 | 15460 | 80 | 2370 | B/A | |
| MD01-2416 | 2317 | 15.50 | 163 | 13795 | 60 | 15960 | 100 | 2165 | H1 | |

**Table 6.2. (continued)**.

| Core | Wt. depth (m) | Cal. age (ka BP) | Core depth (cm) | Planktic $^{14}$C age (kyr) | $\pm1\sigma$ (years) | Benthic $^{14}$C age (kyr) | $\pm1\sigma$ (years) | BF-PF (years) | Period | Reference |
|---|---|---|---|---|---|---|---|---|---|---|
| MD01-2416 | 2317 | 17.62 | 177 | 15380 | 70 | 17860 | 100 | 2480 | | |
| ODP883 | 2385 | 13.70 | 51 | 12715 | 50 | 13420 | 90 | 705 | B/A | Sarnthein et al. (2006) |
| **Bering Sea** | | | | | | | | | | |
| **SO201-2-77KL** | **2163** | **11.16** | **115** | **10450** | **40** | **11650** | **45** | **1250** | **Holocene** | **this study** |
| **SO201-2-77KL** | **2163** | **14.47** | **180** | **13200** | **45** | **14450** | **85** | **1250** | **B/A** | |
| **Okhotsk Sea** | | | | | | | | | | |
| GGC-20 | 1510 | 19.44 | 230 | 17350 | 100 | 18700 | 140 | 1350 | LGM | Keigwin (2002) |
| GGC-18 | 1700 | 18.17 | 214-216 | 16250 | 120 | 17800 | 140 | 1550 | | Keigwin (2002) |
| GGC-15 | 1980 | 19.78 | 170 | 17650 | 80 | 19200 | 110 | 1550 | LGM | Keigwin (2002) |

**Table 6.3.:** Stable isotope measurements on epibenthic foraminifera *Cibicidoides lobatulus*.

| Core | Depth (cm) | Age (ka BP) | $\delta^{18}$O (‰PDB) | $\delta^{13}$C (‰PDB) |
|---|---|---|---|---|
| SO201-2-85KL | 30 | 10.41 | 3.209 | -0.307 |
| (western Bering Sea) | 33 | 10.58 | 3.350 | -0.240 |
| | 35 | 10.69 | 3.249 | -0.273 |
| | 40 | 10.98 | 3.266 | -0.245 |
| | 43 | 11.15 | 3.440 | -0.500 |
| | 45 | 11.26 | 3.228 | -0.350 |
| | 50 | 11.51 | 3.117 | -0.424 |
| | 53 | 11.79 | 3.360 | -0.230 |
| | 55 | 12.14 | 3.387 | -0.200 |
| | 60 | 13.01 | 3.461 | -0.349 |
| | 63 | 13.29 | 3.323 | -0.388 |
| | 80 | 14.76 | 3.307 | -0.428 |
| | 81 | 14.83 | 3.670 | -0.056 |
| | 85 | 15.10 | 3.481 | -0.185 |
| | 95 | 15.80 | 3.988 | -0.125 |
| | 100 | 16.30 | 4.536 | -0.034 |
| | 103 | 16.61 | 3.640 | -0.210 |
| | 105 | 16.81 | 4.231 | -0.035 |
| | 110 | 17.33 | 3.256 | -0.441 |
| | 113 | 17.64 | 3.960 | -0.260 |
| | 115 | 17.84 | 3.817 | -0.401 |
| | 120 | 18.36 | 4.121 | -0.335 |
| | 123 | 18.67 | 3.930 | -0.450 |
| | 125 | 18.87 | 3.965 | -0.425 |
| | 130 | 19.39 | 3.839 | -0.232 |
| | 131 | 19.49 | 3.864 | -0.227 |
| | 133 | 19.69 | 3.900 | -0.210 |
| | 135 | 19.90 | 3.852 | -0.518 |
| | 140 | 20.85 | 3.848 | -0.570 |
| SO178-13-6 | 1632.5 | 10.041 | 3.03 | -0.54 |
| (Okhotsk Sea) | 1642.5 | 10.137 | 3.06 | -0.36 |
| | 1682.5 | 10.896 | 3.54 | 0.15 |
| | 1687.5 | 10.937 | 2.96 | -0.44 |
| | 1687.5 | 10.937 | 3.34 | 0.27 |
| | 1722.5 | 11.226 | 3.55 | -0.10 |
| | 1767.5 | 11.722 | 3.74 | -0.33 |
| | 1772.5 | 11.753 | 3.45 | -0.27 |
| | 1822.5 | 11.984 | 3.59 | 0.12 |
| | 1842.5 | 12.076 | 3.48 | 0.27 |
| | 1857.5 | 12.203 | 3.59 | 0.48 |
| | 1870.5 | 13.011 | 3.66 | 0.15 |
| | 1885.5 | 13.304 | 3.38 | 0.64 |
| | 1912.5 | 13.636 | 3.43 | 0.48 |
| | 1917.5 | 13.698 | 3.22 | 0.16 |
| | 1922.5 | 13.759 | 3.39 | 0.04 |
| | 1937.5 | 13.944 | 3.26 | -0.67 |
| | 1972.5 | 14.507 | 4.07 | -0.44 |
| | 2087.5 | 14.866 | 3.10 | 0.81 |
| | 2092.5 | 14.884 | 3.05 | 0.28 |

**Table 6.3. (continued)**.

| Core | Depth (cm) | Age (ka BP) | $\delta^{18}$O (‰PDB) | $\delta^{13}$C (‰PDB) |
|---|---|---|---|---|
| SO178-13-6 | 2157.5 | 15.237 | 3.81 | 0.29 |
| (Okhotsk Sea) | 2162.5 | 15.272 | 4.04 | 0.04 |
| | 2177.5 | 15.377 | 4.05 | 0.42 |
| | 2187.5 | 15.447 | 3.82 | 0.21 |
| | 2202.5 | 15.552 | 3.88 | 0.12 |
| | 2242.5 | 15.833 | 3.90 | 0.46 |
| | 2247.5 | 15.868 | 3.81 | 0.08 |
| | 2252.5 | 15.903 | 3.86 | 0.11 |
| | 2272.5 | 16.043 | 3.78 | 0.21 |
| | 2277.5 | 16.078 | 3.88 | 0.31 |
| | 2292.5 | 16.183 | 3.64 | 0.48 |
| | 2297.5 | 16.218 | 4.12 | 0.48 |
| | 2307.5 | 16.288 | 3.75 | 0.66 |
| | 2317.5 | 16.583 | 3.11 | -0.19 |
| | 2327.5 | 16.648 | 3.94 | 0.21 |
| | 2342.5 | 16.715 | 3.99 | 0.27 |
| | 2347.5 | 16.737 | 4.31 | 0.28 |
| | 2367.5 | 16.826 | 3.67 | 0.88 |

# 7. Synthesis and perspectives

Within the framework of this thesis proxy records for sediment cores from the western Bering Sea (SO201-2-77KL, -85KL, -101KL), the subarctic NW Pacific off Kamchatka (SO201-2-12KL), and the southern Okhotsk Sea (LV29-114-3) covering the last ∼180 kyr were established and examined. These sediment cores for the first time allowed to reconstruct environmental changes in the western Bering Sea at high temporal resolution, thereby significantly extending previous Bering Sea records into MIS6. Moreover, they provided sufficient $CaCO_3$ contents to perform Mg/Ca-based subsurface temperature and salinity-approximating reconstructions during the last glacial termination and to directly compare these results with alkenone-based SST estimates. According reconstructions have previously not been available for the continental slope off eastern Kamchatka or the western Bering and southern Okhotsk seas. The major conclusions of this thesis as well as perspectives for future work resulting from it are summarized in the following paragraphs.

## 7.1. Stratigraphy

This thesis contributed to the establishment of the age models for the beforementioned sediment cores from the NW Pacific, and the Bering and Okhotsk seas. Age models were tested via spectral analysis and are consistent with the global benthic reference stack LR04 (Lisiecki and Raymo, 2005), the paleomagnetic PISO-1500 reference stack (Channell et al., 2009), and for the last glacial termination are verified by AMS-$^{14}$C dating. High sedimentation rates of these cores allow for paleoceanographic reconstructions at high temporal resolution (from decades to millennia) for the last glacial-interglacial cycle and MIS6. However, changes in sedimention and variability of benthic $\delta^{18}$O values indicate potential erosion at Site 85KL during Termination II.

## 7.2. Late Pleistocene to Holocene changes in marine productivity and terrigenous matter supply

In agreement with previous studies it could be shown that marine productivity remained low in the western Bering Sea, but was maintained during most of the last glacial-interglacial cycle and MIS6. At the same time, the supply of terrigenous matter, which is dominated by silt and clay-sized siliciclastics, was high at the study sites. Only during interglacials, and to a lower extent during MIS5a and MIS5c, marine productivity increased, while lithogenous element concentrations were reduced by ∼30–40%. This anticorrelated behaviour is similar to that observed in the Okhotsk Sea and is attributed to a close coupling of insolation and sea-level changes, which, in turn, influence the strength of atmospheric pressure cells, sea-ice dynamics, and upper-ocean

stratification. In the context of sea-level changes, the opening history of the Bering Strait is considered to play an important role for changes in upper-ocean stratification as well. Moreover, regional differences were found along the Shirshov Ridge core transect, which most probably is the result of changes in the extent of sea-ice rafting and coverage. Sea-ice supposedly not only acts as the primary transport agent for terrigenous matter from mixed geochemical sources, but also as a critical factor for stratification/ventilation and productivity changes. A distinct pattern of environmental changes was found during the last glacial termination, remarkably resembling the deglacial temperature evolution recorded in Greenland ice cores. The Bølling-Allerød warm phase (B/A) was characterized by a higher bottom water calcite saturation state, enhanced marine productivity, strengthened upper-ocean stratification, and higher nitrate utilization. This situation potentially applies to abrupt changes in sediment composition found during MIS3–6 that might be related to N Atlantic D/O-events.

## 7.3. Temperature, salinity, and stratification during the last deglaciation

Deglacial records of subsurface temperature (subSST$_{Mg/Ca}$) and $\delta^{18}O_{ivc-sw}$ were generated by combined $\delta^{18}O$ and Mg/Ca-analyses on calcitic tests of the planktonic foraminifera *Neogloboquadrina pachyderma* (sin.). Results show subsurface conditions in the western Bering Sea, the subarctic NW Pacific off Kamchatka, and the southern Okhotsk Sea, that are different on a regional scale, especially regarding changes in subsurface salinity. In general, changes in subSST$_{Mg/Ca}$ and $\delta^{18}O_{ivc-sw}$ occur synchronously, and cold subSST$_{Mg/Ca}$ characterize the Heinrich Stadial 1 (H1) and the Younger Dryas (YD) cold phase. In contrast, temperature gradients between the surface and subsurface during the warmer B/A indicate changes in upper-ocean (thermal) stratification during the last glacial termination. Sea-ice influence and seasonal contrasts are considered to explain the regionally different development with more enhanced impact by sea-ice on the northern sites restricting the establishment of seasonal thermoclines. It is suggested, that during H1 and the YD advection of low-salinity water from the Alaskan Stream and East Kamchatka Current as well as sea-ice formation were stronger, while reduced dilution by these currents, less sea-ice formation, and enhanced upper-ocean stratification characterized the B/A. Direct comparison with alkenone-derived temperature reconstructions were used to infer deglacial thermocline changes in the mixed layer and to propose scenarios for water mass changes. The deglacial evolution is most likely related to changes in Northern Hemisphere summer insolation which influences the strength of the atmospheric pressure systems, and, thus, seasonal contrasts, sea-ice formation, and upper-ocean stratification. Finally, supporting evidence for a long-term decrease in subsurface temperature and salinity during the early Holocene is presented, implying that the halocline was subject to deglacial changes and that modern conditions in the subarctic N Pacific are a relatively recent feature as suggested by Sarnthein et al. (2004). This notion might indicate that the subarctic NW Pacific and its marginal seas contributed to the deglacial rise in atmospheric $CO_2$ by a weakened halocline during H1 and the YD.

## 7.4. Perspectives

### Was intermediate water formed during past glacial stages?

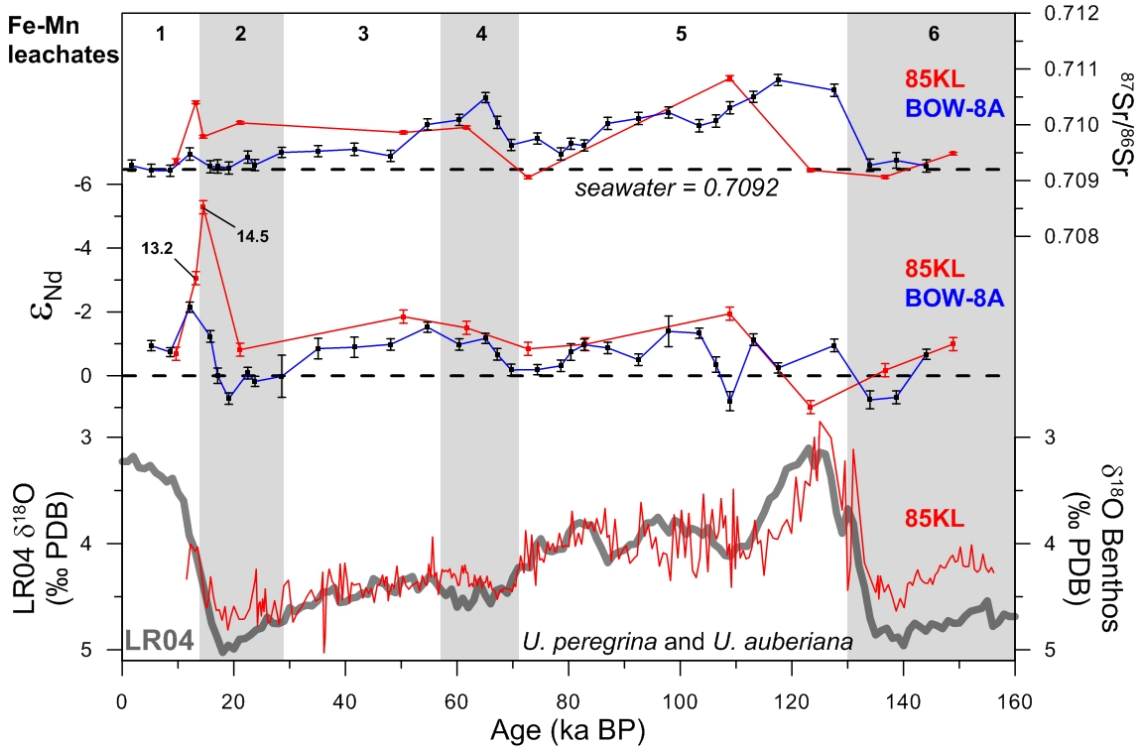


**Figure 7.1.:** This figure shows the radiogenic isotope signatures for neodyme and strontium from early diagenetic ferromanganese (Fe-Mn) oxyhydroxide coatings for Shirshov Ridge core SO201-2-85KL (in red; this study) and Bowers Ridge core BOW-8A (in blue; Horikawa et al., 2010) (for site locations see Fig. 3.1 on page 32). Benthic $\delta^{18}O$ from core SO201-2-85KL are shown in comparison with the LR04 reference stack (Lisiecki and Raymo, 2005). Dashed lines indicate $\varepsilon_{Nd} = 0$ and the Quaternary seawater value ($^{87}Sr/^{86}Sr = 0.7092$; Henderson et al., 1994), respectively. Black numbers mark MIS1-6 (after Lisiecki and Raymo, 2005).

In order to reconstruct intermediate water mass formation in the subarctic N Pacific during glacial periods, Horikawa et al. (2010) investigated core KH99-3-BOW-8A (884 m) from Bowers Ridge. They determined radiogenic isotope signatures in Fe-Mn oxyhydroxides and found a systematic variation between more radiogenic values during cold periods and less radiogenic values during warm periods. Their interpretation of this variability was that during glacial periods surface waters were subducted to intermediate depths due to brine rejection. Further they proposed the northwestern Bering Sea off northeastern Kamchatka to be the possible source region of glacial intermediate water masses. However, $\varepsilon_{Nd}$ signatures from the suggested source area were missing so far. The idea to test the hypothesis of Horikawa et al. (2010) based on measurements in Shirshov Ridge core 85KL led to collaboration with Prof. Dr. M. Frank and Dr. C. Blanchet (both at GEOMAR).

The preliminary results of this investigation are shown in Fig. 7.1 and reveal a general pattern following that of Horikawa et al. (2010). However, more radiogenic values are registered during the Holocene and MIS5e, i.e. warm periods with supposedly no intermediate water mass formation in the Bering Sea. Thus, from our preliminary results,

we can not verify the initial interpretation of enhanced intermediate water formation during glacial stages in the suggested source area. Moreover, extreme unradiogenic values, which compare to Nd isotope signatures from the Yukon River mouth (VanLaningham et al., 2009), are recorded during the B/A and thus could be indicative of a strong deglacial meltwater pulse. Since the $\varepsilon_{Nd}$ signatures indicate the presence of a fundamentally different water mass at Site 85KL during that time this work should clearly be extended. A further goal of future marine expeditions to the Bering Sea should be the determination of water mass signatures via $\varepsilon_{Nd}$.

### How was upper-ocean stratification characterized during MIS6?

The Shirshov Ridge sites provide the possibility for high-resolution proxy studies assessing millennial-scale changes in upper-ocean stratification, thereby allowing to significantly extend existing Bering Sea studies into MIS6.

### Where is sea-ice actually formed?

Although indications exist that Anadyr Bay is the sought-after source area of terrigenous matter in Shirshov Ridge sediments, geochemical provenance and/or IRD component analyses are needed to verify this assumption. In this respect, the B.Sc thesis of Miriam Ibenthal (CAU Kiel) investigated surface sediment samples recovered during SO201-2 and produced according surface distribution maps for lithogenous elements and productivity proxies. This work should be extended to samples from other sites.

### Is there a single source for terrigenous matter?

In Shirshov Ridge cores, Al/Ti and Fe/Al ratios remained fairly constant during the last 180 kyr, neither showing clear glacial-interglacial changes nor differences between sites. Accordingly, comparison with geochemical signatures from other Bering Sea sites is needed to find out whether they are influenced by different sources and/or transport mechanisms.

### Can abrupt environmental changes recorded by XRF core logging be validated?

Sediment records from Shirshov Ridge showed abrupt changes in sediment composition as determined by high-resolution core logging (color b*, XRF). Since these changes might be related to D/O-events, they should be validated by quantitative geochemical analyses (CN-Analytics, $XRF_{Bulk}$), and, if possible, dated via AMS-$^{14}$C dating.

### Where and when does the temperature signal in *Nps* form?

In this thesis it is assumed that in the subarctic NW Pacific and its marginal seas the planktonic foraminifer *Neogloboquadrina pachyderma* (sin.) calcifies in an isopycnal layer in 50–100 m water depth during boreal summer, at the same time the alkenone temperature signal is formed. This should be verified by future expeditions and Mg/Ca-T calibrations should be established for the N Pacific for this species.

### Were SST, subSST, and salinity different during the last interglacial?

Increased marine productivity during MIS5a/c/e indicates the possibility of temperature reconstructions, that would allow for a comparison with deglacial and modern conditions.

### How saline was the Bering Sea during the LGM?

Modern $\delta^{18}O_{sw}$-S relationships should be established for the Bering Sea. Subsequent salinity reconstructions should focus on the LGM to verifiy if the Bering Sea was a glacial source of intermediate water mass formation.

# References

Adkins, J.F., Boyle, E.A., 1997. Changing atmospheric $\Delta^{14}C$ and the record of deep water paleoventilation ages. Paleoceanography 12 (3), 337–344.

Ahagon, N., Ohkushi, K., Uchida, M., Mishima, T., 2003. Mid-depth circulation in the northwest Pacific during the last deglaciation: Evidence from foraminiferal radiocarbon ages. Geophysical Research Letters 30 (21), 2097, doi:10.1029/2003GL018287.

Arzhanova, N.V., Zubarevich, V.L., Sapozhnikov, V.V., 1995. Seasonal variability of nutrient stocks in the euphotic zone and assessment of primary production in the Bering Sea. In: Kotenev, B.N., Sapozhnikov, V.V. (Eds.), Complex studies of the Bering Sea ecosystem. VNIRO, Moscow, pp. 162–179.

Bard, E., Rostek, F., Turon, J.-L., Gendreau, S., 2000. Hydrological impact of Heinrich Events in the subtropical northeast Atlantic. Science 289, 1321–1324.

Bareille, G., Grousset, F.E., Labracherie, M., Labeyrie, L.D., Petit, J.-R., 1994. Origin of detrital fluxes in the southeast Indian Ocean during the last climatic cycles. Paleoceanography 9 (6), 799–819.

Barker, S., Greaves, M., Elderfield, H., 2003. A study of cleaning procedures used for foraminiferal Mg/Ca paleothermometry. Geochemistry Geophysics Geosystems 4 (9), 8407, doi:10.1029/2003GC000559.

Barr, I.D., Clark, C.D., 2011. Glaciers and climate in Pacific Far NE Russia during the Last Glacial Maximum. Journal of Quaternary Science 26 (2), 227–237.

Barron, J.A., Heusser, L., Herbert, T., Lyle, M., 2003. High-resolution climatic evolution of coastal northern California during the past 16,000 years. Paleoceanography 18 (1), 1020, doi:10.1029/2002PA000768.

Bauch, D., Carstens, J., Wefer, G., 1997. Oxygen isotope composition of living *Neogloboquadrina pachyderma* (sin.) in the Arctic Ocean. Earth and Planetary Science Letters 146, 47–58.

Bauch, D., Erlenkeuser, H., Winckler, G., Pavlova, G., Thiede, J., 2002. Carbon isotopes and habitat of polar planktic foraminifera in the Okhotsk Sea: The 'carbonate ion effect' under natural conditions. Marine Micropaleontology 45, 83–99.

Behl, R.J., Kennett, J.P., 1996. Brief interstadial events in the Santa Barbara basin, NE Pacific, during the past 60 kyr. Nature 379, 243–246.

Belt, S.T., Massé, G., Rowland, S.J., Poulin, M., Michel, C., LeBlanc, B., 2007. A novel chemical fossil of palaeo sea ice: $IP_{25}$. Organic Geochemistry 38, 16–27.

Biebow, N., Kulinich, R., Baranov, B. (Eds.), 2003. Cruise Reports: KOMEX (Kurile Okhotsk Sea Marine Experiment) RV Akademik M.A. Lavrentyev Cruise 29, Leg 1 and Leg 2. Vladivostok–Pusan–Okhostsk Sea–Pusan–Okhotsk Sea–Pusan–Vladivostok. May 25–August 05 2002. GEOMAR Report 110, GEOMAR, Kiel, 190 pp.

Bigg, G.R., Clark, C.D., Hughes, A.L.C., 2008. A last glacial ice sheet on the Pacific Russian coast and catastrophic change arising from coupled ice-volcanic interaction. Earth and Planetary Science Letters 265, 559–570.

Bishop, J.K.B., 1988. The barite-opal-organic carbon association in oceanic particulate matter. Nature 332, 341–343.

Blackman, R.B., Tukey, J.W., 1958. The Measurement of Power Spectra from the Point of View of Communication Engineering. Dover Publications, New York, 190 pp.

Blockley, S.P.E., Lane, C.S., Hardiman, M., Rasmussen, S.O., Seierstad, I.K., Steffensen, J.P., Svensson, A., Lotter, A.F., Turney, C.S.M., Ramsey, C.B., INTIMATE members, 2012. Synchronisation of palaeoenvironmental records over the last 60,000 years, and an extended INTIMATE event stratigraphy to 48,000 b2k. Quaternary Science Reviews 36, 2–10.

Boyle, E.A., 1983a. Chemical accumulation variations under the Peru current during the past 130,000 years. Journal of Geophysical Research 88 (C12), 7667–7680.

Boyle, E.A., 1983b. Manganese carbonate overgrowths on foraminifera tests. Geochimica et Cosmochimica Acta 47, 1815–1819.

Boyle, E.A., Keigwin, L.D., 1985. Comparison of Atlantic and Pacific paleochemical records for the last 215,000 years: Changes in deep ocean circulation and chemical inventories. Earth and Planetary Science Letters 76, 135–150.

Brassell, S.C., Eglinton, G., Marlowe, I.T., Pflaumann, U., Sarnthein, M., 1986. Molecular stratigraphy: A new tool for climatic assessment. Nature 320, 129–133.

Brigham-Grette, J., Hopkins, D.M., Ivanov, V.F., Basilyan, E.B., Benson, S.L., Heiser, P.A., Pushkar, V.S., 2001. Last Interglacial (isotope stage 5) glacial and sea-level history of coastal Chukotka Peninsula and St. Lawrence Island, Western Beringia. Quaternary Science Reviews 20, 419–436.

Brigham-Grette, J., Gualtieri, L.M., Glushkova, O.Y., Hamilton, T.D., Mostoller, D., Kotov, A., 2003. Chlorine-35 and $^{14}C$ chronology support a limited last glacial maximum across central Chukotka, northeastern Siberia, and no Beringian ice sheet. Quaternary Research 59, 386–398.

Broecker, W.S., Peng, T.-H., 1987. The role of $CaCO_3$ compensation in the glacial to interglacial atmospheric $CO_2$ change. Global Biogeochemical Cycles 1 (1), 15–29.

Broecker, W., Barker, S., Clark, E., Hajdas, I., Bonani, G., Stott, L., 2004. Ventilation of the glacial deep Pacific Ocean. Science 306, 1169–1172.

Broecker, W., Clark, E., Barker, S., 2008. Near constancy of the Pacific Ocean surface to mid-depth radiocarbon-age difference over the last 20 kyr. Earth and Planetary Science Letters 274, 322–326.

Brunelle, B.G., Sigman, D.M., Cook, M.S., Keigwin, L.D., Haug, G.H., Plessen, B., Schettler, G., Jaccard, S.L., 2007. Evidence from diatom-bound nitrogen isotopes for subarctic Pacific stratification during the last ice age and a link to North Pacific denitrification changes. Paleoceanography 22, PA1215, doi:10.1029/2005PA001205.

Brunelle, B.G., Sigman, D.M., Jaccard, S.L., Keigwin, L.D., Plessen, B., Schettler, G., Cook, M.S., Haug, G.H., 2010. Glacial/interglacial changes in nutrient supply and stratification in the western subarctic North Pacific since the penultimate glacial maximum. Quaternary Science Reviews 29, 2579–2590.

Burov, B.V., Yasonov, P.G., 1979. Introduction into different thermomagnetic analysis of rocks. Kazanian University Press [in Russian].

Caissie, B.E., Brigham-Grette, J., Lawrence, K.T., Herbert, T.D., Cook, M.S., 2010. Last Glacial Maximum to Holocene sea surface conditions at Umnak Plateau, Bering Sea, as inferred from diatom, alkenone, and stable isotope records. Paleoceanography 25, PA1206, doi:10.1029/2008PA001671.

Calvert, S.E., Fontugne, M.R., 2001. On the late Pleistocene-Holocene sapropel record of climatic and oceanographic variability in the eastern Mediterranean. Paleoceanography 16 (1), 78–94.

Calvo, E., Grimalt, J., Jansen, E., 2002. High resolution $U_{37}^{K}$ sea surface temperature reconstruction in the Norwegian Sea during the Holocene. Quaternary Science Reviews 21, 1385–1394.

Channell, J.E.T., Xuan, C., Hodell, D.A., 2009. Stacking paleointensity and oxygen isotope data for the last 1.5 Myr (PISO-1500). Earth and Planetary Science Letters 283, 14–23.

Chen, C.-T.A., 2002. Shelf-vs. dissolution-generated alkalinity above the chemical lysocline. Deep-Sea Research II 49, 5365–5375.

Chikamoto, M.O., Menviel, L., Abe-Ouchi, A., Ohgaito, R., Timmermann, A., Okazaki, Y., Harada, N., Oka, A., Mouchet, A., 2012. Variability in North Pacific intermediate and deep water ventilation during Heinrich events in two coupled climate models. Deep-Sea Research II 61–64, 114–126.

Chow, T.J., Goldberg, E.D., 1960. On the marine geochemistry of barium. Geochimica et Cosmochimica Acta 20, 192–198.

Cohen, A.S., Onions, R.K., Siegenthaler, R., Griffin, W.L., 1988. Chronology of the pressure–temperature history recorded by a granulite terrain. Contributions to Mineralogy and Petrology 98 (3), 303–311.

Cook, M.S., 2006. The paleoceanography of the Bering Sea during the last glacial cycle. PhD thesis, Massachusetts Institute of Technology, Woods Hole Oceanographic Institution, 126 pp.

Cook, M.S., Keigwin, L.D., Sancetta, C.A., 2005. The deglacial history of surface and intermediate water of the Bering Sea. Deep-Sea Research II 52, 2163–2173.

Crusius, J., Pedersen, T.F., Kienast, S., Keigwin, L., Labeyrie, L., 2004. Influence of northwest Pacific productivity on North Pacific Intermediate Water oxygen concentrations during the Bölling-Alleröd interval (14.7–12.9 ka). Geology 32, 633–636.

Curry, W.B., Oppo, D.W., 2005. Glacial water mass geometry and the distribution of $\delta^{13}$C of $\Sigma CO_2$ in the western Atlantic Ocean. Paleoceanography 20, PA1017, doi:10.1029/2004PA001021.

Curry, W.B., Duplessy, J.C., Labeyrie, L.D., Shackleton, N.J., 1988. Changes in the distribution of $\delta^{13}$C of deep water $\Sigma CO_2$ between the last glaciation and the Holocene. Paleoceanography 3 (3), 317–341.

Debret, M., Desmet, M., Balsam, W., Copard, Y., Francus, P., Laj, C., 2006. Spectrophotometer analysis of Holocene sediments from an anoxic fjord: Saanich Inlet, British Columbia, Canada. Marine Geology 229, 15–28.

Dehairs, F., Goeyens, L., Stroobants, N., Bernard, P., Goyet, C., Poisson, A., Chesselet, R., 1990. On suspended barite and the oxygen minimum in the Southern Ocean. Global Biogeochemical Cycles 4 (1), 85–102.

Dehairs, F., Stroobants, N., Goeyens, L., 1991. Suspended barite as a tracer of biological activity in the Southern Ocean. Marine Chemistry 35, 399–410.

Dekens, P.S., Lea, D.W., Pak, D.K., Spero, H.J., 2002. Core top calibration of Mg/Ca in tropical foraminifera: Refining paleotemperature estimation. Geochemistry Geophysics Geosystems 3 (4), doi:10.1029/2001GC000200.

De La Rocha, C.L., 2007. The biological pump. In: Elderfield, H. (Ed.), Treatise on Geochemistry Vol 6, Elsevier, Amsterdam, pp. 83–111.

DeMaster, D., 1981. The supply and accumulation of silica in the marine environment. Geochimica et Cosmochimica Acta 45, 1715–1732.

Derkachev, A., Portnyagin, M., Ponomareva, V., Gorbarenko, S., Malakhov, M., Nürnberg, D., Riethdorf, J.-R., Tiedemann, R., van den Bogaard, C., 2011. Marker tephra layers in the Holocene-Pleistocene deposits of the Bering Sea and the northwestern Pacific Ocean. In: van den Bogaard, C., Dullo, W.-C. (Eds.), KALMAR - Bilateral Workshop on Russian-German Cooperation on Kurile-Kamchatka and the Aleutean Marginal Sea-Island Arc Systems, May 16-20, 2011, Trier, pp. 38–40, IFM-GEOMAR, Kiel.

Dickson, A.G., 1990. Thermodynamics of the dissociation of boric acid in synthetic seawater from 273.15 to 318.15 K. Deep-Sea Research 37 (5), 755–766.

Duce, R.A., Tindale, N.W., 1991. Atmospheric transport of iron and its deposition in the ocean. Limnology and Oceanography 36 (8), 1715–1726.

Dullo, W.-C., Baranov, B., van den Bogaard, C. (Eds.), 2009. FS Sonne Fahrtbericht / Cruise Report SO201-2 KALMAR, Busan/Korea-Tomakomai/Japan, 30.08.-08.10.2009. IFM-GEOMAR Report 35, 233 pp.

Duplessy, J.C., Shackleton, N.J., Fairbanks, R.G., Labeyrie, L., Oppo, D., Kallel, N., 1988. Deepwater source variations during the last climatic cycle and their impact on the global deepwater circulation. Paleoceanography 3 (3), 343–360.

Duplessy, J.-C., Arnold, M., Bard, E., Juillet-Leclerc, A., Kallel, N., Labeyrie, L., 1989. AMS $^{14}$C study of transient events and of the ventilation rate of the Pacific Intermediate Water during the last deglaciation. Radiocarbon 31 (3), 493–502.

Dymond, J., Collier, R., 1996. Particulate barium fluxes and their relationships to biological productivity. Deep-Sea Research II 43 (4-6), 1283–1308.

Dymond, J., Suess, E., Lyle, M., 1992. Barium in deep-sea sediment: a geochemical proxy for paleoproductivity. Paleoceanography 7 (2), 163–181.

Elderfield, H., Ganssen, G., 2000. Past temperature and $\delta^{18}$O of surface ocean waters inferred from foraminiferal Mg/Ca ratios. Nature 405, 442–445.

Elderfield, H., Vautravers, M., Cooper, M., 2002. The relationship between shell size and Mg/Ca, Sr/Ca, $\delta^{18}$O, and $\delta^{13}$C of species of planktonic foraminifera. Geochemistry Geophysics Geosystems 3 (8), doi:10.1029/2001GC000194.

Elderfield, H., Yu, J., Anand, P., Kiefer, T., Nyland, B., 2006. Calibrations for benthic foraminiferal Mg/Ca paleothermometry and the carbonate ion hypothesis. Earth and Planetary Science Letters 250, 633–649.

Elias, S.A., Short, S.K., Nelson, C.H., Birks, H.H., 1996. Life and times of the Bering land bridge. Nature 382, 60–63.

Elias, S.A., Short, S.K., Birks, H.H., 1997. Late Wisconsin environments of the Bering Land Bridge. Palaeogeography, Palaeoclimatology, Palaeoecology 136, 293–308.

Emeis, K.-C., Dawson, A.G., 2003. Holocene palaeoclimate records over Europe and the North Atlantic. The Holocene 13 (3), 305–309.

Emile-Geay, J., Cane, M.A., Naik, N., Seager, R., Clement, A.C., van Geen, A., 2003. Warren revisited: Atmospheric freshwater fluxes and "Why is no deep water formed in the North Pacific". Journal of Geophysical Research 108 (C6), 3178, doi:10.1029/2001JC001058.

Engel, A.E.J., Engel, C.G., Havens, R.G., 1965. Chemical characteristics of oceanic basalts and the upper Miocene. Geological Society of America Bulletin 76, 719–734.

Enkin, R.J., Baker, J., Nourgaliev, D., Iassonov, P., Hamilton, T.S., 2007. Magnetic hysteresis parameters and Day plot analysis to characterize diagenetic alteration in gas hydrate-bearing sediments. Journal of Geophysical Research 112, B06S90, doi:10.1029/2006JB004638.

Eppley, R.W., Peterson, B.J., 1979. Particulate organic matter flux and planktonic new production in the deep ocean. Nature 282, 677–680.

Erlenkeuser, H., and the TRANSDRIFT II Shipboard Scientific Party, 1995. Stable carbon isotope ratios in the waters of the Laptev Sea/Sept. 94. In Kassens, H., Piepenburg, D., Thiede, J., Timokhov, L., Hubberten, H.-W., Priamikov, S.M. (Eds.), "Russian-German Cooperation: Laptev Sea System". Berichte zur Polarforschung/Reports on Polar Research 176, 170–177.

Erlenkeuser, H., Spielhagen, R.F., Taldenkova, E., 1999. Stable isotopes in modern water and bivalve samples from the Kara Sea. In: Matthiessen, J., Stepanets, O.V., Stein, R., Fütterer, D.K., Galimov, E.M. (Eds.), The Kara Sea Expedition of RV Akademik Boris Petrov 1997: First Results of a Joint Russian-German Pilot Study. Berichte zur Polarforschung/Reports on Polar Research 300, 80–90.

Fahl, K., Stein. R., in review. Modern seasonal variability and deglacial/Holocene change of central Arctic Ocean sea-ice cover: New insights from biomarker proxy records. Submitted to Earth and Planetary Science Letters.

Farrell, J.W., Prell, W.L., 1989. Climatic change and $CaCO_3$ preservation: An 800,000 year bathymetric reconstruction from the central equatorial Pacific Ocean. Paleoceanography 4 (4), 447–466.

Feely, R.A., Sabine, C.L., Lee, K., Millero, F.J., Lamb, M.F., Greeley, D., Bullister, J.L., Key, R.M., Peng, T.-H., Kozyr, A., Ono, T., Wong, C.S., 2002. In situ calcium carbonate dissolution in the Pacific Ocean. Global Biogeochemical Cycles 16 (4), 1144, doi:10.1029/2002GB001866.

Fleming, K., Johnston, P., Zwartz, D., Yokoyama, Y., Lambeck, K., Chappell, J., 1998. Refining the eustatic sea-level curve since the Last Glacial Maximum using far- and intermediate-field sites. Earth and Planetary Science Letters 163, 327–342.

Francois, R., Honjo, S., Manganini, S.J., Ravizza, G.E., 1995. Biogenic barium fluxes to the deep sea: Implications for paleoproductivity reconstruction. Global Biogeochemical Cycles 9 (2), 289–303.

Galbraith, E.D., Jaccard, S.L., Pedersen, T.F., Sigman, D.M., Haug, G.H., Cook, M., Southon, J.R., Francois, R., 2007. Carbon dioxide release from the North Pacific abyss during the last deglaciation. Nature 449, 890–893.

Galbraith, E.D., Kienast, M., Jaccard, S.L., Pedersen, T.F., Brunelle, B.G., Sigman, D.M., Kiefer, T., 2008. Consistent relationship between global climate and surface nitrate utilization in the western subarctic Pacific throughout the last 500 ka. Paleoceanography 23, PA2212, doi:10.1029/2007PA001518.

Galer, S.J.G., O'Nions, R.K., 1989. Chemical and isotopic studies of ultramafic inclusions from the San Carlos volcanic field, Arizona: A bearing on their petrogenesis. Journal of Petrology 30 (4), 1033–1064.

Ganeshram, R.S., Calvert, S.E., Pedersen, T.F., Cowie, G.L., 1999. Factors controlling the burial of organic carbon in laminated and bioturbated sediments off NW Mexico: Implications for hydrocarbon preservation. Geochimica et Cosmochimica Acta 63 (11/12), 1723–1734.

Gardner, J.V., Dean, W.E., Vallier, T.L., 1980. Sedimentology and geochemistry of surface sediments, outer continental shelf, southern Bering Sea. Marine Geology 35, 299–329.

Gebhardt, H., Sarnthein, M., Grootes, P.M., Kiefer, T., Kühn, H., Schmieder, F., Röhl, U., 2008. Paleonutrient and productivity records from the subarctic North Pacific for Pleistocene glacial terminations I to V. Paleoceanography 23, PA4212, doi:10.1029/2007PA001513.

Gingele, F., Zabel, M., Kasten, S., Bonn, W.J., Nürnberg, C.C., 1999. Biogenic barium as a proxy for paleoproductivity: Methods and limitations of application. In: Fischer, G., Weger, G. (Eds.), Use of proxies in paleoceanography. Examples from the South Atlantic, Springer, Berlin, pp. 345–364.

Goñi, M.A., Ruttenberg, K.C., Eglinton, T.I., 1998. A reassessment of the sources and importance of land-derived organic matter in surface sediments from the Gulf of Mexico. Geochimica et Cosmochimica Acta 62 (18), 3055–3075.

Gorbarenko, S.A., 1996. Stable isotope and lithologic evidence of late-glacial and Holocene oceanography of the northwestern Pacific and its marginal seas. Quaternary Research 46, 230–250.

Gorbarenko, S.A., Khusid, T.A., Basov, I.A., Oba, T., Southon, J.R., Koizumi, I., 2002a. Glacial Holocene environment of the southeastern Okhotsk Sea: Evidence from geochemical and paleontological data. Palaeogeography, Palaeoclimatology, Palaeoecology 177, 237–263.

Gorbarenko, S.A., Nürnberg, D., Derkachev, A.N., Astakhov, A.S., Southon, J.R., Kaiser, A., 2002b. Magnetostratigraphy and tephrochronology of the Upper Quaternary sediments in the Okhotsk Sea: Implication of terrigenous, volcanogenic and biogenic matter supply. Marine Geology 183, 107–129.

Gorbarenko, S.A., Southon, J.R., Keigwin, L.D., Cherepanova, M.V., Gvozdeva, I.G., 2004. Late Pleistocene–Holocene oceanographic variability in the Okhotsk Sea: Geochemical, lithological and paleontological evidence. Palaeogeography, Palaeoclimatology, Palaeoecology, 209, 281–301.

Gorbarenko, S.A., Basov, I.A., Chekhovskaya, M.P., Southon, J., Khusid, T.A., Artemova, A.V., 2005. Orbital and millenium scale environmental changes in the southern Bering Sea during the last glacial-Holocene: Geochemical and paleontological evidence. Deep-Sea Research II 52, 2174–2185.

Gorbarenko, S.A., Wang, P., Wang, R., Cheng, X., 2010. Orbital and suborbital environmental changes in the southern Bering Sea during the last 50 kyr. Palaeogeography, Palaeoclimatology, Palaeoecology 286, 97–106.

Greaves, M., Caillon, N., Rebaubier, H., Bartoli, G., Bohaty, S., Cacho, I., Clarke, L., Cooper, M., Daunt, C., Delaney, M., deMenocal, P., Dutton, A., Eggins, S., Elderfield, H., Garbe-Schoenberg, D., Goddard, E., Green, D., Groeneveld, J., Hastings, D., Hathorne, E., Kimoto, K., Klinkhammer, G., Labeyrie, L., Lea, D.W., Marchitto, T., Martinez-Boti, M.A., Mortyn, P.G., Ni, Y., Nuernberg, D., Paradis, G., Pena, L., Quinn, T., Rosenthal, Y., Russell, A., Sagawa, T., Sosdian, S., Stott, L., Tachikawa, K., Tappa, E., Thunell, R., Wilson, P.A., 2008. Interlaboratory comparison study of calibration standards for foraminiferal Mg/Ca thermometry. Geochemistry Geophysics Geosystems 9 (8), Q08010, doi:10.1029/2008GC001974.

Groeneveld, J., Nürnberg, D., Tiedemann, R., Reichart, G.-J., Steph, S., Reuning, L., Crudeli, D., Mason, P., 2008. Foraminiferal Mg/Ca increase in the Caribbean during the Pliocene: Western Atlantic Warm Pool formation, salinity influence, or diagenetic overprint? Geochemistry Geophysics Geosystems 9 (1), Q01P23, doi:10.1029/2006GC001564.

Gromet, L.P., Dymek, R.F., Haskin, L.A., Korotev, R.L., 1984. The "North American shale composite": Its compilation, major and trace element characteristics. Geochimica et Cosmochimica Acta 48, 2469–2482.

Grootes, P.M., Stuiver, M., White, J.W.C., Johnsen, S., Jouzel, J., 1993. Comparison of oxygen isotope records from the GISP2 and GRIP Greenland ice cores. Nature 366, 552–554.

Grosswald, M.G., Hughes, T.J., 2002. The Russian component of an Arctic Ice Sheet during the Last Glacial Maximum. Quaternary Science Reviews 21, 121–146.

Gutjahr, M., Frank, M., Stirling, C.H., Klemm, V., van de Flierdt, T., Halliday, A.N., 2007. Reliable extraction of a deepwater trace metal isotope signal from Fe–Mn oxyhydroxide coatings of marine sediments. Chemical Geology 242, 351–370.

Harada, N., Shin, K.H., Murata, A., Uchida, M., Nakatani, T., 2003. Characteristics of alkenones synthesized by a bloom of *Emiliania huxleyi* in the Bering Sea. Geochimica et Cosmochimica Acta 67 (8), 1507–1519.

Harada, N., Sato, M., Shiraishi, A., Honda, M.C., 2006a. Characteristics of alkenone distributions in suspended and sinking particles in the northwestern North Pacific. Geochimica et Cosmochimica Acta 70, 2045–2062.

Harada, N., Ahagon, N., Sakamoto, T., Uchida, M., Ikehara, M., Shibata, Y., 2006b. Rapid fluctuation of alkenone temperature in the southwestern Okhotsk Sea during the past 120 ky. Global and Planetary Change 53, 29–46.

Harada, N., Sato, M., Seki, O., Timmermann, A., Moossen, H., Bendle, J., Nakamura, Y., Kimoto, K., Okazaki, Y., Nagashima, K., Gorbarenko, S.A., Ijiri, A., Nakatsuka, T., Menviel, L., Chikamoto, M.O., Abe-Ouchi, A., Schouten, S., 2012. Sea surface temperature changes in the Okhotsk Sea and adjacent North Pacific during the last glacial maximum and deglaciation. Deep-Sea Research II 61-64, 93–105.

Hartnett, H.E., Keil, R.G., Hedges, J.I., Devol, A.H., 1998. Influence of oxygen exposure time on organic carbon preservation in continental margin sediments. Nature 391, 572–574.

Haug, G.H., Sigman, D.M., Tiedemann, R., Pedersen, T.F., Sarnthein, M., 1999. Onset of permanent stratification in the subarctic Pacific Ocean. Nature 401, 779–782.

Haug, G.H., Ganopolski, A., Sigman, D.M., Rosell-Mele, A., Swann, G.E.A., Tiedemann, R., Jaccard, S.L., Bollmann, J., Maslin, M.A., Leng, M.J., Eglinton, G., 2005. North Pacific seasonality and the glaciation of North America 2.7 million years ago. Nature 433, 821–825.

Healy-Williams, N., 1992. Stable isotope differences among morphotypes of *Neogloboquadrina pachyderma* (Ehrenberg): implications for high-latitude palaeoceanographic studies. Terra Nova 4, 693–700.

Hedges, J.I., Clark, W.A., Quay, P.D., Richey, J.E., Devol, A.H., de M. Santos, U., 1986. Compositions and fluxes of particulate organic material in the Amazon River. Limnology and Oceanography 31 (4), 717–738.

Hedges, J.I., Baldock, J.A., Gélinas, Y., Lee, C., Peterson, M., Wakeham, S.G., 2001. Evidence for non-selective preservation of organic matter in sinking marine particles. Nature 409, 801–804.

Henderson, G.M., Martel, D.J., O'Nions, R.K., Shackleton, N.J., 1994. Evolution of seawater $^{87}Sr/^{86}Sr$ over the last 400 ka: The absence of glacial/interglacial cycles. Earth and Planetary Science Letters 128, 643–651.

Hendy, I.L., Kennett, J.P., 2000. Dansgaard-Oeschger cycles and the California Current System: Planktonic foraminiferal response to rapid climate change in Santa Barbara Basin, Ocean Drilling Program hole 893A. Paleoceanography 15 (1), 30–42.

Herguera, J.C., Jansen, E., Berger, W.H., 1992. Evidence for a bathyal front at 2000-m depth in the glacial Pacific, based on a depth transect on Ontong Java Plateau. Paleoceanography 7 (3), 273–288.

Herguera, J.C., Herbert, T., Kashgarian, M., Charles, C., 2010. Intermediate and deep water mass distribution in the Pacific during the Last Glacial Maximum inferred from oxygen and carbon stable isotopes. Quaternary Science Reviews 29, 1228–1245.

Honda, M.C., Imai, K., Nojiri, Y., Hoshi, F., Sugawara, T., Kusakabe, M., 2002. The biological pump in the northwestern North Pacific based on fluxes and major components of particulate matter obtained by sediment-trap experiments (1997–2000). Deep-Sea Research II 49, 5595–5625.

Horikawa, K., Asahara, Y., Yamamoto, K., Okazaki, Y., 2010. Intermediate water formation in the Bering Sea during glacial periods: Evidence from neodymium isotope ratios. Geology 35 (5), 435–438.

Horwitz, E.P., Chiarizia, R., Dietz, M.L., 1992. A novel strontium-selective extraction chromatographic resin. Solvent Extraction and Ion Exchange 10 (2), 313–336.

Hoshiba, M., Ahagon, N., Ohkushi, K., Uchida, M., Motoyama, I., Nishimura, A., 2006. Foraminiferal oxygen and carbon isotopes during the last 34 kyr off northern Japan, northwestern Pacific. Marine Micropaleontology 61, 196–208.

Hu, A., Meehl, G.A., Otto-Bliesner, B.L., Waelbroeck, C., Han, W., Loutre, M.-F., Lambeck, K., Mitrovica, J.X., Rosenbloom, N., 2010. Influence of Bering Strait flow and North Atlantic circulation on glacial sea-level changes. Nature Geoscience 3, 118–121.

Huang, R.X., Cane, M.A., Naik, N., Goodman, P., 2000. Global adjustment of the thermocline in response to deepwater formation. Geophysical Research Letters 27 (6), 759–762.

Hut, G., 1987. Consultants group meeting on stable isotope reference samples for geochemical and hydrological investigations. Report to the Director General, International Atomic Energy Agency, Vienna, 42 pp.

Ikehara, K., Ohkushi, K., Shibahara, A., Hoshiba, M., 2006. Change of bottom water conditions at intermediate depths of the Oyashio region, NW Pacific over the past 20,000 yrs. Global and Planetary Change 53, 78–91.

Itaki, T., Uchida, M., Kim, S., Shin, H.-S., Tada, R., Khim, B.-K., 2009. Late Pleistocene stratigraphy and palaeoceanographic implications in northern Bering Sea slope sediments: Evidence from the radiolarian species *Cycladophora davisiana*. Journal of Quaternary Science 24 (8), 856–865.

Jaccard, S.L., Haug, G.H., Sigman, D.M., Pedersen, T.F., Thierstein, H.R., Röhl, U., 2005. Glacial/interglacial changes in subarctic North Pacific stratification. Science 308, 1003–1008.

Jaccard, S.L., Galbraith, E.D., Sigman, D.M., Haug, G.H., Francois, R., Pedersen, T.F., Dulski, P., Thierstein, H.R., 2009. Subarctic Pacific evidence for a glacial deepening of the oceanic respired carbon pool. Earth and Planetary Science Letters 277, 156–165.

Jaccard, S.L., Galbraith, E.D., Sigman, D.M., Haug, G.H., 2010. A pervasive link between Antarctic ice core and subarctic Pacific sediment records over the past 800 kyrs. Quaternary Science Reviews 29, 206–212.

Jacobsen, S.B., Wasserburg, G.J., 1980. Sm-Nd isotopic evolution of chondrites. Earth and Planetary Science Letters 50, 139–155.

Jansen, J.H.F., Van der Gaast, S.J., Koster, B., Vaars, A.J., 1998. CORTEX, a shipboard XRF-scanner for element analyses in split sediment cores. Marine Geology 151, 143–153.

Jansen, H., Zeebe, R.E., Wolf-Gladrow, D.A., 2002. Modeling the dissolution of settling $CaCO_3$ in the ocean. Global Biogeochemical Cycles 16 (2), 1027, doi:10.1029/2000GB001279.

Jenkins, R., De Vries, J.L., 1970. Practical X-ray Spectrometry. Macmillan, London.

Jouzel, J., Masson-Delmotte, V., Cattani, O., Dreyfus, G., Falourd, S., Hoffmann, G., Minster, B., Nouet, J., Barnola, J.M., Chappellaz, J., Fischer, H., Gallet, J.C., Johnsen, S., Leuenberger, M., Loulergue, L., Luethi, D., Oerter, H., Parrenin, F., Raisbeck, G., Raynaud, D., Schilt, A., Schwander, J., Selmo, E., Souchez, R., Spahni, R., Stauffer, B., Steffensen, J.P., Stenni, B., Stocker, T.F., Tison, J.L., Werner, M., Wolff, E.W., 2007. Orbital and millennial Antarctic climate variability over the past 800,000 years. Science 317, 793–796.

Karhu, J.A., Tschudi, S., Saarnisto, M., Kubik, P., Schlüchter, C., 2001. Constraints for the latest glacial advance on Wrangel Island, Arctic Ocean, from rock surface exposure dating. Global and Planetary Change 31, 447–451.

Katsuki, K., Takahashi, K., 2005. Diatoms as paleoenvironmental proxies for seasonal productivity, sea-ice and surface circulation in the Bering Sea during the late Quaternary. Deep-Sea Research II 52, 2110–2130.

Katsuki, K., Khim, B.-K., Itaki, T., Harada, N., Sakai, H., Ikeda, T., Takahashi, K., Okazaki, Y., Asahi, H., 2009. Land-sea linkage of Holocene paleoclimate on the Southern Bering Continental Shelf. The Holocene 19 (5), 747–756.

Katsumata, K., Yasuda, I., 2010. Estimates of non-tidal exchange transport between the Sea of Okhtosk and the North Pacific. Journal of Oceanography 66, 489–504.

Kaufman, D.S., Forman, S.L., Lea, P.D., Wobus, C.W., 1996. Age of pre-late-Wisconsin glacial-eastuarine sedimentation, Bristol Bay, Alaska. Quaternary Research 45, 59–72.

Kaufman, D.S., Ager, T.A., Anderson, N.J., Anderson, P.M., Andrews, J.T., Bartlein, P.J., Brubaker, L.B., Coats, L.L., Cwynar, L.C., Duvall, M.L., Dyke, A.S., Edwards, M.E., Eisner, W.R., Gajewski, K., Geirsdóttir, A., Hu, F.S., Jennings, A.E., Kaplan, M.R., Kerwin, M.W., Lozhkin, A.V., MacDonald, G.M., Miller, G.H., Mock, C.J., Oswald, W.W., Otto-Bliesner, B.L., Porinchu, D.F., Rühland, K., Smol, J.P.,

Steig, E.J., Wolfe, B.B., 2004. Holocene thermal maximum in the western Arctic (0–180°W). Quaternary Science Reviews 23, 529–560.

Keigwin, L.D., 1987. North Pacific deep water formation during the latest glaciation. Nature 330, 362–364.

Keigwin, L.D., 1998. Glacial-age hydrography of the far northwest Pacific Ocean. Paleoceanography 13 (4), 323–339.

Keigwin, L.D., 2002. Late Pleistocene-Holocene paleoceanography and ventilation of the Gulf of California. Journal of Oceanography 58, 421–432.

Keigwin, L.D., Jones, G.A., 1990. Deglacial climatic oscillations in the Gulf of California. Paleoceanography 5 (6), 1009–1023.

Keigwin, L.D., Jones, G.A., Froelich, P.N., 1992. A 15,000 year paleoenvironmental record from Meiji Seamount, far northwestern Pacific. Earth and Planetary Science Letters 111, 425–440.

Keigwin, L.D., Donnelly, J.P., Cook, M.S., Driscoll, N.W., Brigham-Grette, J., 2006. Rapid sea-level rise and Holocene climate in the Chukchi Sea. Geology 34 (10), 861–864, doi:10.1130/G22712.1.

Kennett, J.P., Ingram, B.L., 1995. A 20,000-year record of ocean circulation and climate change from the Santa Barbara basin. Nature 377, 510–514.

Kennett, J.P., Cannariato, K.G., Hendy, I.L., Behl, R.J., 2000. Carbon isotopic evidence for methane hydrate instability during Quaternary interstadials. Science 288, 128–133.

Khim, B.-K., Kim, S., Uchida, M., Itaki, T., 2010. High organic carbon deposition in the northern margin of the Aleutian Basin (Bering Sea) before the last deglaciation. Ocean Science Journal 45 (4), 203–211.

Kiefer, T., 2010. When still waters ran deep. Science 329, 290–291.

Kiefer, T., Kienast, M., 2005. Patterns of deglacial warming in the Pacific Ocean: A review with emphasis on the time interval of Heinrich event 1. Quaternary Science Reviews 24, 1063–1081.

Kiefer, T., Sarnthein, M., Erlenkeuser, H., Grootes, P.M., Roberts, A.P., 2001. North Pacific response to millennial-scale changes in ocean circulation over the last 60 kyr. Paleoceanography 16 (2), 179–189.

Kienast, S.S., McKay, J.L., 2001. Sea surface temperatures in the subarctic northeast Pacific reflect millennial-scale climate oscillations during the last 16 kyrs. Geophysical Research Letters 28 (8), 1563–1566.

Kienast, S.S., Hendy, I.L., Crusius, J., Pedersen, T.F., Calvert, S., 2004. Export production in the subarctic North Pacific over the last 800 kyrs: No evidence for iron fertilization? Journal of Oceanography 60, 189–203.

Kim, J.-H., Rimbu, N., Lorenz, S.J., Lohmann, G., Nam, S.-I., Schouten, S., Rühlemann, C., Schneider, R.R., 2004. North Pacific and North Atlantic sea-surface temperature variability during the Holocene. Quaternary Science Reviews 23, 2141–2154.

Kim, S., Khim, B.K., Uchida, M., Itaki, T., Tada, R., 2011. Millennial-scale paleoceanographic events and implication for the intermediate-water ventilation in the northern slope area of the Bering Sea during the last 71 kyrs. Global and Planetary Change 79, 89–98.

Klump, J., Hebbeln, D., Wefer, G., 2000. The impact of sediment provenance on barium-based productivity estimates. Marine Geology 169, 259–271.

Kohfeld, K.E., Fairbanks, R.G., Smith, S.L., Walsh, I.D., 1996. *Neogloboquadrina pachyderma* (sinistral coiling) as paleoceanographic tracers in polar oceans: Evidence from Northeast Water Polynya plankton tows, sediment traps, and surface sediments. Paleoceanography 11 (6), 679–699.

Kowalik, Z., Luick, J.L., Royer, T.C., 1994. On the dynamics of the Alaska Coastal Current. Continental Shelf Research 14 (7/8), 831–845.

Kozdon, R., Eisenhauer, A., Weinelt, M., Meland, M.Y., Nürnberg, D., 2009. Reassessing Mg/Ca temperature calibrations of *Neogloboquadrina pachyderma* (sinistral) using paired $\delta^{44/40}$Ca and Mg/Ca measurements. Geochemistry Geophysics Geosystems 10 (3), Q03005, doi:10.1029/2008GC002169.

Krebs, U., Timmermann, A., 2007. Tropical air-sea interactions accelerate the recovery of the Atlatnic Meridional Overturning Circulation after a major shutdown. Journal of Climate 20, 4940–4956.

Kuroyanagi, A., Kawahata, H., 2004. Vertical distribution of living planktonic foraminifera in the seas around Japan. Marine Micropaleontology 53, 173–196.

Kuzmin, Y.V., Burr, G.S., Jull, A.J.T., 2001. Radiocarbon reservoir correction ages in the Peter The Great Gulf, Sea of Japan, and eastern coast of the Kunashir, southern Kuriles (northwestern Pacific). Radiocarbon 43 (2A), 477–481.

Kuzmin, Y.V., Burr, G.S., Gorbunov, S.V., Rakov, V.A., Razjigaeva, N.G., 2007. A tale of two seas: Reservoir age correction values ($R$, $\Delta R$) for the Sakhalin Island (Sea of Japan and Okhotsk Sea). Nuclear Instruments and Methods in Physics Research B 259, 460–462.

Laskar, J., Robutel, P., Joutel, F., Gastineau, M., Correia, A.C.M., Levrard, B., 2004. A long-term numerical solution for the insolation quantities of the Earth. Astronomy & Astrophysics 428, 261–285, doi:10.1051/0004-6361:20041335.

Latimer, J.C., Filippelli, G.M., 2001. Terrigenous input and paleoproductivity in the Southern Ocean. Paleoceanography 16 (6), 627–643.

Le, J., Shackleton, N.J., 1992. Carbonate dissolution fluctuations in the western equatorial Pacific during the late Quaternary. Paleoceanography 7 (1), 21–42.

Lea, D.W., Pak, D.K., Spero, H.J., 2000. Climate impact of Late Quaternary equatorial Pacific sea surface temperature variations. Science 289, 1719–1724.

Leduc, G., Schneider, R., Kim, J.-H., Lohmann, G., 2010. Holocene and Eemian sea surface temperature trends as revealed by alkenone and Mg/Ca paleothermometry. Quaternary Science Reviews 29, 989–1004.

Lisiecki, L., Raymo, M., 2005. A Pliocene-Pleistocene stack of 57 globally distributed benthic $\delta^{18}$O records. Paleoceanography 20, PA1003, doi:10.1029/2004PA001071.

Lisitzin, A.P., 2002. Sea ice and iceberg sedimentation in the ocean: Recent and past. Springer-Verlag, Berlin, 563 pp.

Locarnini, R.A., Mishonov, A.V., Antonov, J.I., Boyer, T.P., Garcia, H.E., 2010. World Ocean Atlas 2009, Volume 1: Temperature. In: Levitus, S. (Ed.), NOAA Atlas NESDIS 68, U.S. Government Printing Office, Washington, D.C., 184 pp.

Lund, D.C., Mix, A.C., Southon, J., 2011. Increased ventilation age of the deep northeast Pacific Ocean during the last deglaciation. Nature Geoscience 4, 771–774.

Lutze, G. F., Thiel, H., 1989. Epibenthic foraminifera from elevated microhabitats; *Cibicidoides wuellerstorfi* and *Planulina ariminensis*. Journal of Foraminiferal Research 19, 153–158.

Mackensen, A., Schumacher, S., Radke, J., Schmidt, D.N., 2000. Microhabitat preferences and stable carbon isotopes of endobenthic foraminifera: Clue to quantitative reconstruction of oceanic new production? Marine Micropaleontology 40, 233–258.

Mahowald, N.M., Baker, A.R., Bergametti, G., Brooks, N., Duce, R.A., Jickells, D., Kubilay, N., Prospero, J.M., Tegen, I., 2005. Atmospheric global dust cycle and iron inputs to the ocean. Global Biogeochemical Cycles 19, GB4025, doi:10.1029/2004GB002402.

Malakhov, M.I., Gorbarenko, S.A., Malakhova, G.Y., Harada, N., Vasilenko, Y.P., Bosin, A.A., Goldberg, E.L., Derkachev, A.N., 2009. Petromagnetic parameters of bottom sediments as indicators of the climatic and environmental changes in the central zone of the Sea of Okhotsk during the last 350 kyr. Russian Geology and Geophysics 50, 973-982, doi:10.1016/j.rgg.2009.10.006.

Manabe, S., Stouffer, R.J., 1988. Two stable equilibria of a coupled ocean–atmosphere model. Journal of Climate 1 (9), 841–866.

Mantua, N.J., Hare, S.R., Zhang, Y., Wallace, J.M., Francis, R.C., 1997. A Pacific interdecadal climate oscillation with impacts on salmon production. Bulletin of the American Meteorological Society 78 (6), 1069–1079.

Marchal, O., Cacho, I., Stocker, T.F., Grimalt, J.O., Calvo, E., Martrat, B., Shackleton, N., Vautravers, M., Cortijo, E., van Kreveld, S., Andersson, C., Koc, N., Chapman, M., Sbaffi, L., Duplessy, J.-C., Sarnthein, M., Turon, J.-L., Duprat, J., Jansen, E., 2002. Apparent long-term cooling of the sea surface in the northeast Atlantic and Mediterranean during the Holocene. Quaternary Science Reviews 21, 455–483.

Marchitto, T.M., Lynch-Stieglitz, J., Hemming, S.R., 2005. Deep Pacific $CaCO_3$ compensation and glacial–interglacial atmospheric $CO_2$. Earth and Planetary Science Letters 231, 317–336.

Marchitto, T.M., Lehman, S.J., Ortiz, J.D., Flückiger, J., van Geen, A., 2007. Marine radiocarbon evidence for the mechanism of deglacial atmospheric $CO_2$ rise. Science 316, 1456–1459.

Mashiotta, T.A., Lea, D.W., Spero, H.J., 1999. Glacial–interglacial changes in subantarctic sea surface temperature and $\delta^{18}$O-water using foraminiferal Mg. Earth and Planetary Science Letters 170, 417–432.

Matsumoto, K., Oba, T., Lynch-Stieglitz, J., Yamamoto, H., 2002. Interior hydrography and circulation of the glacial Pacific Ocean. Quaternary Science Reviews 21, 1693–1704.

Matul, A., Abelmann, A., Tiedemann, R., Kaiser, A., Nürnberg, D., 2002. Late Quaternary polycystine radiolarian datum events in the Sea of Okhotsk. Geo-Mar. Lett. 22, 25–32.

Max, L., Riethdorf, J.-R., Tiedemann, R., Smirnova, M., Lembke-Jene, L., Fahl, K., Nürnberg, D., Matul, A., Mollenhauer, G., in review. Sea surface temperature variability and sea-ice extent in the subarctic Northwest Pacific during the past 15,000 years. Submitted to Paleoceanography.

McDonald, D., Pedersen, T.F., Crusius, J., 1999. Multiple late Quaternary episodes of exceptional diatom production in the Gulf of Alaska. Deep-Sea Research II 46, 2993–3017.

McKay, J.L., Pedersen, T.F., Kienast, S.S., 2004. Organic carbon accumulation over the last 16 kyr off Vancouver Island, Canada: Evidence for increased marine productivity during the deglacial. Quaternary Science Reviews 23, 261–281.

McLennan, S.M., 1995. Sediments and soils: Chemistry and abundances. In: Ahrens, T.J. (Ed.), Rock physics and phase relations: A handbook of physical constants, AGU Reference Shelf 3, AGU, Washington, pp. 8–20.

McManus, J.F., Francois, R., Gherardi, J.-M., Keigwin, L.D., Brown-Leger, S., 2004. Collapse and rapid resumption of Atlantic meridional circulation linked to deglacial climate changes. Nature 428, 834–837.

McNeely, R., Dyke, A.S., Southon, J.R., 2006. Canadian marine reservoir ages, preliminary data assessment. Geological Survey Canaca, 3 pp.

Menviel, L., Timmermann, A., Elison Timm, O., Mouchet, A., Abe-Ouchi, A., Chikamoto, M.O., Harada, N., Ohgaito, R., Okazaki, Y., 2012. Removing the North Pacific halocline: Effects on global climate, ocean circulation and the carbon cycle. Deep-Sea Research II 61–64, 106–113.

Middelburg, J.J., Soetaert, K., Herman, P.M.J., 1997. Empirical relationships for use in global diagenetic models. Deep-Sea Research I 44 (2), 327–344.

Mikolajewicz, U., Crowley, T.J., Schiller, A., Voss, R., 1997. Modelling teleconnections between the North Atlantic and North Pacific during the Younger Dryas. Nature 387, 384–387.

Millo, C., Sarnthein, M.., Erlenkeuser, H., Frederichs, T., 2005a. Methane-driven late Pleistocene $\delta^{13}$C minima and overflow reversals in the southwestern Greenland Sea. Geology 33 (11), 873–876.

Millo, C., Sarnthein, M., Erlenkeuser, H., Grootes, P.M., Andersen, N., 2005b. Methane-induced early diagenesis of foraminiferal tests in the southwestern Greenland Sea. Marine Micropaleontology 58, 1–12.

Minoshima, K., Kawahata, H., Ikehara, K., 2007a. Changes in biological production in the mixed water region (MWR) of the northwestern North Pacific during the last 27 kyr. Palaeogeography, Palaeoclimatology, Palaeoecology 254, 430–447.

Minoshima, K., Kawahata, H., Irino, T., Ikehara, K., Aoki, K., Uchida, M., Yoneda, M., Shibata, Y., 2007b. Deep water ventilation in the northwestern North Pacific during the last deglaciation and the early Holocene (15-5 cal. kyr B.P.) based on AMS $^{14}$C dating. Nuclear Instruments and Methods in Physics Research B 259, 448–452.

Miura, T., Suga, T., Hanawa, K., 2002. Winter mixed layer and formation of dichothermal water in the Bering Sea. Journal of Oceanography 58, 815–823.

Mohiuddin, M.M., Nishimura, A., Tanaka, Y., 2005. Seasonal succession, vertical distribution, and dissolution of planktonic foraminifera along the Subarctic Front: Implications for paleoceanographic reconstruction in the northwestern Pacific. Marine Micropaleontology 55, 129–156.

Mulitza, S., Boltovskoy, D., Donner, B., Meggers, H., Paul, A., Wefer, G., 2003. Temperature:$\delta^{18}$O relationships of planktonic foraminifera collected from surface waters. Palaeogeography, Palaeoclimatology, Palaeoecology 202, 143–152.

Müller, P., 1977. C/N ratios in Pacific deep-sea sediments: effect of inorganic ammonium and organic nitrogen compounds sorbed by clays. Geochimica et Cosmochimica Acta 41, 765–776.

Müller, P., Schneider, R., 1993. An automated leaching method for the determination of opal in sediments and particulate matter. Deep-Sea Research I 40, 425–444.

Müller, P.J., Kirst, G., Ruhland, G., von Storch, I., Rosell-Melé, A., 1998. Calibration of the alkenone paleotemperature index $U^K_{37}$ based on core-tops from the eastern South Atlantic and the global ocean (60°N-60°S). Geochimica et Cosmochimica Acta 62 (10), 1757–1772.

Müller, J., Massé, G., Stein, R., Belt, S.T., 2009. Variability of sea-ice conditions in the Fram Strait over the past 30,000 years. Nature Geoscience 2, 772–776.

Müller, J., Wagner, A., Fahl, K., Stein, R., Prange, M., Lohmann, G., 2011. Towards quantitative sea ice reconstructions in the northern North Atlantic: A combined biomarker and numerical modelling approach. Earth and Planetary Science Letters 306, 137–148.

Murayama, M., Taira, A., Matsumoto, E., Iwakura, H., Nakamura, T., 1992. Northwest Pacific deep water ventilation rate during the past 35,000 years using the AMS $^{14}$C foraminifera ages. Summaries of Researches Using AMS at Nagoya University 3, 114–121. *(in Japanese with English abstract).*

Murray, R.W., Leinen, M., Knowlton, C.W., 2012. Links between iron input and opal deposition in the Pleistocene equatorial Pacific Ocean. Nature Geoscience 5, 270–274.

Nakatsuka, T., Watanabe, K., Handa, N., Matsumoto, E., Wada, E., 1995. Glacial to interglacial surface nutrient variations of Bering deep basins recorded by $\delta^{13}$C and $\delta^{14}$N of sedimentary organic matter. Paleoceanography 10 (6), 1047–1061.

Nameroff, T.J., Calvert, S.E., Murray, J.W., 2004. Glacial-interglacial variability in the eastern tropical North Pacific oxygen minimum zone recorded by redox-sensitive trace metals. Paleocanography 19, PA1010, doi:10.1029/2003PA000912.

Narita, H., Sato, M., Tsunogai, S., Murayama, M., Ikehara, M., Nakatsuka, T., Wakatsuchi, M., Harada, N., Ujiié, Y., 2002. Biogenic opal indicating less productive northwestern North Pacific during the glacial ages. Geophysical Research Letters 29 (15), 1732, doi:10.1029/2001GL014320.

Nelson, D.M., Tréguer, P., Brzezinski, M.A., Leynaert, A., Quéguiner, B., 1995. Production and dissolution of biogenic silica in the ocean: Revised global estimates, comparison with regional data and relationship to biogenic sedimentation. Global Biogeochemical Cycle 9 (3), 359–372.

Niebauer, H.J., 1988. Effects of El Nino–Southern Oscillation and North Pacific weather patterns on interannual variability in the subarctic Bering Sea. Journal of Geophysical Research 93 (C5), 5051–5068.

Niebauer, H.J., 1998. Variability in Bering Sea ice cover as affected by a regime shift in the North Pacific in the period 1947-1996. Journal of Geophysical Research 103 (C12), 27717–27737.

Niebauer, H.J., Alexander, V., Henrichs, S.M., 1995. A time-series study of the spring bloom at the Bering Sea ice edge I. Physical processes, chlorophyll and nutrient chemistry. Continental Shelf Research 15 (15), 1859–1877.

Niebauer, H.J., Bond, N.A., Yakunin, L.P., Plotnikov, V.V., 1999. An update on the climatology and sea ice of the Bering Sea. In: Loughlin, T.R., Ohtani, K. (Eds.), Dynamics of the Bering Sea, University of Alaska Sea Grant, pp. 29–59.

North Greenland Ice Core Project members, 2004. High-resolution record of northern hemisphere climate extending into the last interglacial period. Nature 431, 147–151.

Nürnberg, C.C., 1995a. Bariumfluss und Sedimentation im südlichen Südatlantik–Hinweise auf Produktivitätsänderungen im Quartär. GEOMAR Reports 38, Research Center for Marine Geosciences (GEOMAR), Kiel, 105 pp.

Nürnberg, C.C., Bohrmann, G., Schlüter, M., Frank, M., 1997. Barium accumulation in the Atlantic sector of the Southern Ocean: Results from 190,000-year records. Paleoceanography 12 (4), 594–603.

Nürnberg, D., 1995b. Magnesium in tests of *Neogloboquadrina pachyderma* sinistral from high northern and southern latitudes. Journal of Foraminiferal Research 25 (4), 350-368.

Nürnberg, D., Tiedemann, R., 2004. Environmental change in the Sea of Okhotsk during the last 1.1 million years. Paleoceanography 19, PA4011, doi:10.1029/2004PA001023.

Nürnberg, D., Wollenburg, I., Dethleff, D., Eicken, H., Kassens, H., Letzig, T., Reimnitz, E., Thiede, J., 1994. Sediments in Arctic sea ice: Implications for entrainment, transport and release. Marine Geology 119, 185–214.

Nürnberg, D., Bijma, J., Hemleben, C., 1996. Assessing the reliability of magnesium in foraminiferal calcite as a proxy for water mass temperatures. Geochimica et Cosmochimica Acta 60 (5), 803-814.

Nürnberg, D., Dethleff, D., Tiedemann, R., Kaiser, A., Gorbarenko, S.A., 2011. Okhotsk Sea ice coverage and Kamchatka glaciation over the last 350 ka – Evidence from ice-rafted debris and planktonic $\delta^{18}$O. Palaeogeography, Palaeoclimatology, Palaeoecology 310, 191–205.

Ohkushi, K., Itaki, T., Nemoto, N., 2003. Last glacial–Holocene change in intermediate-water ventilation in the northwestern Pacific. Quaternary Science Reviews 22, 1477–1484.

Ohkushi, K., Uchida, M., Ahagon, N., Mishima, T., Kanematsu, T., 2004. Glacial intermediate water ventilation in the northwestern Pacific based on AMS radiocarbon dating. Nuclear Instruments and Methods in Physics Research B 223–224, 460–465.

Ohtani, K., Akiba, Y., Takenouti, A.Y., 1972. Formation of western subarctic water in the Bering Sea. In: Takenouti, A.Y. (Ed.), Biological oceanography of the northern North Pacific Ocean. Idemitsu Shoten Publ. Co, pp. 32–44.

Okada, M., Takagi, M., Narita, H., Takahashi, K., 2005. Chronostratigraphy of sediment cores from the Bering Sea and the subarctic Pacific based on paleomagnetic and oxygen isotopic analyses. Deep-Sea Research II 52, 2092–2109.

Okazaki, Y., Takahashi, K., Asahi, H., Katsuki, K., Hori, J., Yasuda, H., Sagawa, Y., Tokuyama, H., 2005a. Productivity changes in the Bering Sea during the late Quaternary. Deep-Sea Research II 52, 2150–2162.

Okazaki, Y., Takahashi, K., Katsuki, K., Ono, A., Hori, J., Sakamoto, T., Uchida, M., Shibata, Y., Ikehara, M., Aoki, K., 2005b. Late Quaternary paleoceanographic changes in the southwestern Okhotsk Sea: Evidence from geochemical, radiolarian, and diatom records. Deep-Sea Research II 52, 2332–2350.

Okazaki, Y., Timmermann, A., Menviel, L., Harada, N., Abe-Ouchi, A., Chikamoto, M.O., Mouchet, A., Asahi, H., 2010. Deepwater formation in the North Pacific during the Last Glacial Maximum. Science 329, 200–204.

Okumura, Y.M., Deser, C., Hu, A., Timmermann, A., Xie, S.-P., 2009. North Pacific climate response to freshwater forcing in the subarctic North Atlantic: Oceanic and atmospheric pathways. Journal of Climate 22, 1424–1445.

O'Neil, J.R., Clayton, R.N., Mayeda, T.K., 1969. Oxygen isotope fractionation in divalent metal carbonates. Journal of Chemical Physics 51 (12), 5547–5558.

Orians, K.J., Bruland, K.W., 1986. The biogeochemistry of aluminium in the Pacific Ocean. Earth and Planetary Science Letters 78, 397–410.

Ortiz, J.D., O'Connell, S.B., DelViscio, J., Dean, W., Carriquiry, J.D., Marchitto, T., Zheng, Y., van Geen, A., 2004. Enhanced marine productivity off western North America during warm climate intervals of the past 52 k.y. Geology 32 (6), 521–524.

Overland, J.E., Adams, J.M., Bond, N.A., 1999. Decadal variability of the Aleutian Low and its relation to high-latitude circulation. Journal of Climate 12 (5), 1542–1548.

Overland, J.E., Bond, N.A., Adams, J.M., 2002. The relation of surface forcing of the Bering Sea to large-scale climate patterns. Deep-Sea Research II 49, 5855–5868.

Paillard, D., Labeyrie, L., Yiou, P., 1996. Macintosh program performs time-series analysis. EOS Transactions 77, 379.

Pierrot, D., Lewis, E., Wallace, D.W.R., 2006. MS Excel program developed for CO2 system calculations. ORNL/CDIAC-105a. Carbon Dioxide Information Analysis Center, Oak Ridge National Laboratory, U.S. Department of Energy, Oak Ridge, Tennessee, doi:10.3334/CDIAC/otg.CO2SYS_XLS_CDIAC105a.

Pisias, N.G., Mix, A.C., Heusser, L., 2001. Millennial scale climate variability of the northeast Pacific Ocean and northwest North America based on radiolaria and pollen. Quaternary Science Reviews 20, 1561–1576.

Pondaven, P., Ragueneau, O., Tréguer, P., Hauvespre, A., Dezileau, L., Reyss, J.L., 2000. Resolving the 'opal paradox' in the Southern Ocean. Nature 405, 168–172.

Prahl, F.G., Wakeham, S.G., 1987. Calibration of unsaturation patterns in long-chain ketone compositions for palaeotemperature assessment. Nature 330, 367–369.

Prahl, F.G., Muehlhausen, L., Zahnle, D.L., 1988. Further evaluation of long-chain alkenones as indicators of paleoceanographic conditions. Geochimica et Cosmochimica Acta 52, 2303–2310.

Pushkar, V.S., Roof, S.R., Cherepanova, M.V., Hopkins, D.M., Brigham-Grette, J., 1999. Paleogeographic and paleoclimatic significance of diatoms from middle Pleistocene marine and glaciomarine deposits on Baldwin Peninsula, northwestern Alaska. Palaeogeography, Palaeoclimatology, Palaeoecology 152, 67–85.

Pye, K., 1987. Aeolian dust and dust deposits. Academic Press, London, 334 pp.

Ragueneau, O., Tréguer, P., Leynaert, A., Anderson, R.F., Brzezinski, M.A., DeMaster, D.J., Dugdale, R.C., Dymond, J., Fischer, G., Francois, R., Heinze, C., Maier-Reimer, E., Martin-Jézéquel, V., Nelson, D.M., Quéguiner, B., 2000. A review of the Si cycle in the modern ocean: recent progress and missing gaps in the application of biogenic opal as a paleoproductivity proxy. Global and Planetary Change 26, 317–365.

Rahmstorf, S., 1995. Bifurcations of the Atlantic thermohaline circulation in response to changes in the hydrological cycle. Nature 378, 145–149.

Rasmussen, S.O., Andersen, K.K., Svensson, A.M., Steffensen, J.P., Vinther, B.M., Clausen, H.B., Siggaard-Andersen, M.-L., Johnsen, S.J., Larsen, L.B., Dahl-Jensen, D., Bigler, M., Röthlisberger, R., Fischer, H., Goto-Azuma, K., Hansson, M.E., Ruth, U., 2006. A new Greenland ice core chronology for the last glacial termination. Journal of Geophysical Research 111, D06102, doi:10.1029/2005JD006079.

Redfield, A.C., Ketchum, B.H., Richards, F.A., 1963. The influence of organisms on the composition of seawater. In: Hill, M.N. (Ed.), The Sea, Vol. 2, Wiley-Interscience, New York, pp. 26–77.

Reed, R.K., Khen, G.V., Stabeno, P.J., Verkhunov, A.V., 1993. Water properties and flow over the deep Bering Sea basin, summer 1991. Deep-Sea Research I (11/12), 2325–2334.

Regenberg, M., Nürnberg, D., Steph, S., Groeneveld, J., Garbe-Schönberg, D., Tiedemann, R., Dullo, W.-C., 2006. Assessing the effect of dissolution on planktonic foraminiferal Mg/Ca ratios: Evidence from Caribbean core tops. Geochemistry Geophysics Geosystems 7 (7), Q07P15, doi:10.1029/2005GC001019.

Reimer, P.J., Baillie, M.G.L., Bard, E., Bayliss, A., Beck, J.W., Blackwell, P.G., Bronk Ramsey, C., Buck, C.E., Burr, G.S., Edwards, R.L., Friedrich, M., Grootes, P.M., Guilderson, T.P., Hajdas, I., Heaton, T.J., Hogg, A.G., Hughen, K.A., Kaiser, K.F., Kromer, B., McCormack, F.G., Manning, S.W., Reimer, R.W., Richards, D.A., Southon, J.R., Talamo, S., Turney, C.S.M., van der Plicht, J., Weyhenmeyer, C.E., 2009. IntCal09 and Marine09 radiocarbon age calibration curves, 0-50,000 years cal BP. Radiocarbon 51 (4), 1111–1150.

Richter, T., van der Gaast, S., Koster, B., Vaars, A., Gieles, R., de Stigter, H., De Haas, H., van Weering, T., 2006. The Avaatech XRF core scanner: technical description and applications to NE Atlantic sediments. Geological Society Special Publication 267, 39–50.

Riethdorf, J.-R., Max, L., Nürnberg, D., Lembke-Jene, L., Tiedemann, R., in prep. Deglacial development of (sub) sea surface temperature and salinity in the subarctic NW Pacific: Implications for upper-ocean stratification. For submission to Paleoceanography.

Ronov, A.B., Migdisov, A.A., 1971. Geochemical history of the crystalline basement and the sedimentary cover of the Russian and North American platforms. Sedimentology 16, 137–185.

Rosenthal, Y., Lohmann, G.P., Lohmann, K.C., Sherrell, R.M., 2000. Incorporation and preservation of Mg in Globigerinoides sacculifer: Implications for reconstructing the temperature and 18O/16O of seawater. Paleoceanography 15 (1), 135-145.

Rosenthal, Y., Perron-Cashman, S., Lear, C.H., Bard, E., Barker, S., Billups, K., Bryan, M., Delaney, M.L., deMenocal, P.B., Dwyer, G.S., Elderfield, H., German, C.R., Greaves, M., Lea, D.W., Marchitto Jr., T.M., Pak, D.K., Paradis, G.L., Russell, A.D., Schneider, R.R., Scheiderich, K., Stott, L., Tachikawa, K., Tappa, E., Thunell, R., Wara, M., Weldeab, S., Wilson, P.A., 2004. Interlaboratory comparison study of Mg/Ca and Sr/Ca measurements in planktonic foraminifera for paleoceanographic research. Geochemistry Geophysics Geosystems 5 (4), Q04D09, doi:10.1029/2003GC000650.

Rösler, H.J., Lange, H., 1972. Geochemical tables. Elsevier, New York, 468 pp.

Roy, R.N., Roy, L.N., Vogel, K.M., Porter-Moore, C., Pearson, T., Good, C.E., Millero, F.J., Campbell, D.M., 1993. The dissociation constants of carbonic acid in seawater at salinities 5 to 45 and temperatures 0 to 45 C. Marine Physical Chemistry 44 (2–4), 249–267.

Saenko, O.A., Schmittner, A., Weaver, A.J., 2004. The Atlantic–Pacific seasaw. Journal of Climate 17 (11), 2033–2038.

Sagawa, T., Ikehara, K., 2008. Intermediate water ventilation change in the subarctic northwest Pacific during the last deglaciation. Geophysical Research Letters 35, L24702, doi:10.1029/2008GL035133.

Sakamoto, T., Ikehara, M., Uchida, M., Aoki, K., Shibata, Y., Kanamatsu, T., Harada, N., Iijima, K., Katsuki, K., Asahi, H., Takahashi, K., Sakai, H., Kawahata, H., 2006. Millennial-scale variations of sea-ice expansion in the southwestern part of the Okhotsk Sea during the past 120 kyr: Age model and ice-rafted debris in IMAGES Core MD01-2412. Global and Planetary Change 53, 58–77.

Sancetta, C., 1983. Effect of Pleistocene glaciation upon oceanographic characteristics of the North Pacific Ocean and Bering Sea. Deep-Sea Research 30 (8A), 851–869.

Sancetta, C., 1992. Primary production in the glacial North Atlantic and North Pacific oceans. Nature 360, 249–151.

Sancetta, C., Robinson, S.W., 1983. Diatom evidence on Wisconsin and Holocene events in the Bering Sea. Quaternary Research 20, 232–245.

Sarmiento, J.L., Gruber, N., Brzezinski, M.A., Dunne, J.P., 2004. High-latitude controls of thermocline nutrients and low latitude biological productivity. Nature 427, 56–60.

Sarnthein, M., Stattegger, K., Dreger, D., Erlenkeuser, H., Grootes, P., Haupt, B.J., Jung, S., Kiefer, T., Kuhnt, W., Pflaumann, U., Schäfer-Neth, C., Schulz, H., Schulz, M., Seidov, D., Simstich, J., van Kreveld, S., Vogelsang, E., Völker, A., Weinelt, M., 2001. Fundamental modes and abrupt changes in North Atlantic circulation and climate over the last 60 ky–Concepts, reconstruction and numerical modeling. In: Schäfer, P., Ritzrau, W., Schlüter, M., Thiede, J. (Eds.), The northern North Atlantic: A changing environment, Springer, Berlin, pp. 365–410.

Sarnthein, M., Gebhardt, H., Kiefer, T., Kucera, M., Cook, M., Erlenkeuser, H., 2004. Mid Holocene origin of the sea-surface salinity low in the subarctic North Pacific. Quaternary Science Reviews 23, 2089–2099.

Sarnthein, M., Kiefer, T., Grootes, P.M., Elderfield, H., Erlenkeuser, H., 2006. Warmings in the far northwestern Pacific promoted pre-Clovis immigration to America during Heinrich Event 1. Geology 34 (3), 141–144, doi:10.1130/G22200.1.

Sarnthein, M., Grootes, P.M., Kennett, J.P., Nadeau, M.-J., 2007. $^{14}$C Reservoir ages show deglacial changes in ocean currents and carbon cycle. In: Schmittner, A., J.C.H. Chiang, S.R. Hemming (Eds.), Past and Future Changes of the Oceanic Meridional Overturning Circulation: Mechanisms and Impacts, AGU Monograph Series 173, AGU, Washington, pp. 175–196.

Sato, M.M., Narita, H., Tsunogai, S., 2002. Barium increasing prior to opal during the last termination of glacial ages in the Okhotsk Sea sediments. Journal of Oceanography 58, 461–467.

Sawada, K., Handa, N., 1998. Variability of the path of the Kuroshio ocean current over the past 25,000 years. Nature 392, 592–595.

Schlitzer, R., 2011. Ocean Data View. http://odv.awi.de

Schmidt, M.W., Spero, H.J., Lea, D.W., 2004. Links between salinity variation in the Caribbean and North Atlantic thermohaline circulation. Nature 428, 160–163.

Schmittner, A., Saenko, O.A., Weaver, A.J., 2003. Coupling of the hemispheres in observations and simulations of glacial climate change. Quaternary Science Reviews 22, 659–671.

Schmittner, A., Galbraith, E.D., Hostetler, S.W., Pedersen, T.F., Zhang, R., 2007. Large fluctuations of dissolved oxygen in the Indian and Pacific oceans during Dansgaard-Oeschger oscillations caused by variations of North Atlantic Deep Water subduction. Paleoceanography 22, PA3207, doi:10.1029/2006PA001384.

Schmitz, B., 1987. The $TiO_2/Al_2O_3$ ratio in the Cenozoic Bengal abyssal fan sediments and its use as a paleostream energy indicator. Marine Geology 76, 195–206.

Schneider, R.R., Price, B., Müller, P.J., Kroon, D., Alexander, I., 1997. Monsoon related variations in Zaire (Congo) sediment load and influence of fluvial silicate supply on marine productivity in the east equatorial Atlantic during the last 200,000 years. Paleoceanography 12 (3), 463–481.

Schulz, M., 2002. On the 1470-year pacing of Dansgaard-Oeschger warm events. Paleoceanography 17 (2), doi:10.1029/2000PA000571.

Schweizer, M., Pawlowski, J., Kouwenhoven, T., van der Zwaan, B., 2009. Molecular phylogeny of common cibicidids and related rotaliida (foraminifera) based on small subunit rDNA sequences. Journal of Foraminiferal Research 39 (4), 300–315.

Seki, O., Ishiwatari, R., Matsumoto, K., 2002. Millennial climate oscillations in NE Pacific surface waters over the last 82 kyr: New evidence from alkenones. Geophysical Research Letters 29 (23), 2144, doi:10.1029/2002GL015200.

Seki, O., Kawamura, K., Nakatsuka, T., Ohnishi, K., Ikehara, M., Wakatsuchi, M., 2003. Sediment core profiles of long-chain n-alkanes in the Sea of Okhotsk: Enhanced transport of terrestrial organic matter from the last deglaciation to the early Holocene. Geophysical Research Letters 30 (1), 1001, doi:10.1029/2001GL014464.

Seki, O., Kawamura, K., Ikehara, M., Nakatsuka, T., Oba, T., 2004a. Variation of alkenone sea surface temperature in the Sea of Okhotsk over the last 85 kyrs. Organic Geochemistry 35, 347–354.

Seki, O., Ikehara, M., Kawamura, K., Nakatsuka, T., Ohnishi, K., Wakatsuchi, M., Narita, H., Sakamoto, T., 2004b. Reconstruction of paleoproductivity in the Sea of Okhotsk over the last 30 kyr. Paleoceanography 19, PA1016, doi:10.1029/2002PA000808.

Seki, O., Nakatsuka, T., Kawamura, K., Saitoh, S.-I., Wakatsuchi, M., 2007. Time-series sediment trap record of alkenones from the western Sea of Okhotsk. Marine Chemistry 104, 253–265.

Seki, O., Sakamoto, T., Sakai, S., Schouten, S., Hopmans, E.C., Sinninghe Damste, J.S., Pancost, R.D., 2009. Large changes in seasonal sea ice distribution and productivity in the Sea of Okhotsk during the deglaciations. Geochemistry Geophysics Geosystems 10 (10), Q10007, doi:10.1029/2009GC002613.

Shackleton, N.J., 1974. Attainment of isotopic equilibrium between ocean water and the benthonic foraminifera genus *Uvigerina*: Isotopic changes in the ocean during the last glacial. Colloques Internationaux du C.N.R.S. 219 – Les Méthodes Quantitatives D'étude des Variations du Climat au Cours du Pléistocène, 203–209.

Shackleton, N.J., Hall, M.A., 1984. Oxygen and carbon isotope stratigraphy of Deep Sea Drilling Project Hole 552A: Plio-Pleistocene glacial history. In: Roberts, D.G., Schnitker, D., et al., Init. Repts. DSDP, 81, Washington (U.S. Govt. Printing Office), pp. 599–609.

Shcherbina, A.Y., Talley, L.D., Rudnick, D.L., 2003. Direct observations of North Pacific ventilation: Brine rejection in the Okhotsk Sea. Science 302, 1952–1955.

Shigemitsu, M., Narita, H., Watanabe, Y.W., Harada, N., Tsunogai, S., 2007. Ba, Si, U, Al, Sc, La, Th, C and $^{13}C/^{12}C$ in a sediment core in the western subarctic Pacific as proxies of past biological production. Marine Chemistry 106, 442–455.

Sigman, D.M., Boyle, E.A., 2000. Glacial/interglacial variations in atmospheric carbon dioxide. Nature 407, 859–869.

Sigman, D.M., Haug, G.H., 2003. The biological pump in the past. In: Elderfield, H. (Ed.), Treatise on Geochemistry, Vol. 6: The Oceans and Marine Geochemistry, Elsevier-Pergamon, pp. 491–528.

Sigman, D.M., Jaccard, S.L., Haug, G.H., 2004. Polar ocean stratification in a cold climate. Nature 428, 59–63.

Sigman, D.M., Hain, M.P., Haug, G.H., 2010. The polar ocean and glacial cycles in atmospheric $CO_2$ concentration. Nature 466, 47–55.

Sikes, E.L., Volkman, J.K., Robertson, L.G., Pichon, J.-J., 1997. Alkenones and alkenes in surface waters and sediments of the Southern Ocean: Implications for paleotemperature estimation in polar regions. Geochimica et Cosmochimica Acta 61 (7), 1495–1505.

Simstich, J., Sarnthein, M., Erlenkeuser, H., 2003. Paired $\delta^{18}O$ signals of *Neogloboquadrina pachyderma* (s) and *Turborotalia quinqueloba* show thermal stratification structure in Nordic Seas. Marine Micropaleontology 48, 107–125.

Southon, J.R., Nelson, D.E., Vogel, J.S., 1990. A record of past ocean-atmosphere radiocarbon differences from the northeast Pacific. Paleoceanography 5 (2), 197–206.

Springer, A.M., McRoy, C.P., Flint, M.V., 1996. The Bering Sea green belt: shelf-edge processes and ecosystem production. Fisheries Oceanography 5 (3-4), 205–223.

Stabeno, P.J., Schumacher, J.D., Ohtani, K., 1999. The physical oceanography of the Bering Sea. In: Loughlin, T.R., Ohtani, K. (Eds.), Dynamics of the Bering Sea, University of Alaska Sea Grant, pp. 1–28.

Stein, R., 2008. Arctic Ocean sediments: Processes, proxies, and paleoenvironment. Developments in Marine Geology Vol. 2, Chamley, H. (Ed.), Elsevier, Amsterdam, 592 pp.

Stott, L., Southon, J., Timmermann, A., Koutavas, A., 2009. Radiocarbon age anomaly at intermediate water depth in the Pacific Ocean during the last deglaciation. Paleoceanography 24, PA2223, doi:10.1029/2008PA001690.

Stuiver, M., 1980. Workshop on $^{14}C$ data reporting. Radiocarbon 22 (3), 964–966.

Stuiver, M., Polach, H.A., 1977. Discussion - Reporting of $^{14}C$ data. Radiocarbon 19 (3), 355–363.

Stuiver, M., Reimer, P.J., 1993. Extended $^{14}$C data base and revised Calib 3.0 $^{14}$C age calibration program. Radiocarbon 35 (1), 215–230.

Sun, Y., Clemens, S.C., Morrill, C., Lin, X., Wang, X., An, Z., 2011. Influence of Atlantic meridional overturning circulation on the East Asian winter monsoon. Nature Geoscience 5, 46–49.

Szeremeta, N., Bassinot, F., Balut, Y., Labeyrie, L., Pagel, M., 2004. Oversampling of sedimentary series collected by giant piston corer: Evidence and corrections based on 3.5-kHz chirp profiles. Paleoceanography 19, PA1005, doi:10.1029/2002PA000795.

Takahashi, K., 1998. The Bering and Okhotsk Sea: Modern and past paleoceanographic changes and gateway impact. Journal of Asian Earth Sciences 16, 49–58.

Takahashi, K., 1999. Paleoceanographic changes and present environment of the Bering Sea. In: Loughlin, T.R., Ohtani, K. (Eds.), Dynamics of the Bering Sea, University of Alaska Sea Grant, pp. 365–385.

Takahashi, K., 2005. The Bering Sea and paleoceanography. Deep-Sea Research II 52, 2080–2091.

Takahashi, K., Fujitani, N., Yanada, M., 2002a. Long term monitoring of particle fluxes in the Bering Sea and the central subarctic Pacific Ocean, 1990-2000. Progress in Oceanography 55, 95–112.

Takahashi, T., Sutherland, S.C., Sweeney, C., Poisson, A., Metzl, N., Tilbrook, B., Bates, N., Wanninkhof, R., Feely, R.A., Sabine, C., Olafsson, J., Nojiri, Y., 2002b. Global sea–air $CO_2$ flux based on climatological surface ocean $pCO_2$ and seasonal biological and temperature effects. Deep-Sea Research II 49, 1601–1622.

Talley, L.D., 1993. Distribution and formation of North Pacific Intermediate Water. Journal of Physical Oceanography 23, 517–537.

Tanaka, S., Takahashi, K., 2005. Late Quaternary paleoceanographic changes in the Bering Sea and the western subarctic Pacific based on radiolarian assemblages. Deep-Sea Research II 52, 2131–2149.

Tanaka, T., Togashi, S., Kamioka, H., Amakawa, H., Kagami, H., Hamamoto, T., Yuhara, M., Orihashi, Y., Yoneda, S., Shimizu, H., Kunimaru, T., Takahashi, K., Yanagi, T., Nakano, T., Fujimaki, H., Shinjo, R., Asahara, Y., Tanimizu, M., Dragusanu, C., 2000. JNdi-1: A neodymium isotopic reference in consistency with LaJolla neodymium. Chemical Geology 168, 279–281.

Taylor, S.R., 1964. Abundance of chemical elements in the continental crust: a new table. Geochimica et Cosmochimica Acta 28, 1273–1285.

Taylor, S.R., McLennan, S.M., 1995. The geochemical evolution of the continental crust. Reviews of Geophysics 33 (2), 241–265.

Taylor, S.R., McLennan, S.M., McCulloch, M.T., 1983. Geochemistry of loess, continental crust composition and crustal model ages. Geochimica et Cosmochimica Acta 47, 1897–1905.

Ternois, Y., Kawamura, K., Ohkouchi, N., Keigwin, L., 2000. Alkenone sea surface temperature in the Okhotsk Sea for the last 15 kyr. Geochemical Journal 34, 283–293.

Ternois, Y., Kawamura, L., Keigwin, L., Ohkouchi, N., Nakatsuka, T., 2001. A biomarker approach for assessing marine and terrigenous inputs to the sediments of Sea of Okhotsk for the last 27,000 years. Geochimica et Cosmochimica Acta 65 (5), 791–802.

Thunell, R.C., Varela, R., Llano, M., Collister, J., Muller-Karger, F., Bohrer, R., 2000. Organic carbon fluxes, degradation, and accumulation in an anoxic basin: Sediment trap results from the Cariaco Basin. Limnology and Oceanography 45 (2), 300–308.

Timmermann, A., Menviel, L., Okumura, Y., Schilla, A., Merkel, U., Timm, O., Hu, A., Otto-Bliesner, B., Schulz, M., 2010. Towards a quantitative understanding of millennial-scale Antarctic warming events. Quaternary Science Reviews 29, 74–85.

Tjallingii, R., 2006. Application and quality of X-Ray Fluorescence core scanning in reconstructing late Pleistocene NW African continental margin sedimentation patterns and paleoclimate variations. Dissertation, Universität Bremen, Bremen, Germany, 114 pp.

Tjallingii, R., Röhl, U., Kölling, M., Bickert, T., 2007. Influence of the water content on X-ray fluorescence core-scanning measurements in soft marine sediments. Geochemistry Geophysics Geosystems 8(2), Q02004, doi:10.1029/2006GC001393.

Tomczak, M., Godfrey, J.S., 1994. Regional oceanography: An introduction. Elsevier Science Ltd., Oxford, 391 pp.

Tyrrell, T., Merico, A., Waniek, J.J., Wong, C.S., Metzl, N., Whitney, F., 2005. Effect of seafloor depth on phytoplankton blooms in high-nitrate, low-chlorophyll (HNLC) regions. Journal of Geophysical Research 110, G02007, doi:10.1029/2005JG000041.

van Andel, T., Heath, G., Moore jr, T., 1975. Cenozoic history and paleoceanography of the central equatorial Pacific Ocean. Geological Society of America Memoir 143, 134 pp.

van Geen, A., Zheng, Y., Bernhard, J.M., Cannariato, K.G., Carriquiry, J., Dean, W.E., Eakins, B.W., Ortiz, J.D., Pike, J., 2003. On the preservation of laminated sediments along the western margin of North America. Paleoceanography 18 (4), 1098, doi:10.1029/2003PA000911.

VanLaningham, S., Pisias, N.G., Duncan, R.A., Clift, P.D., 2009. Glacial–interglacial sediment transport to the Meiji Drift, northwest Pacific Ocean: Evidence for timing of Beringian outwashing. Earth and Planetary Science Letters 277, 64–72.

Vellinga, M., Wood, R.A., 2002. Global climatic impacts of a collapse of the Atlantic thermohaline circulation. Climatic Change 54 (3), 251–267.

Verardo, D.J., Froelich, P.N., McIntyre, A., 1990. Determination of organic carbon and nitrogen in marine sediments using the Carlo Erba NA-1500 Analyzer. Deep-Sea Research 37 (1), 157–165.

Waelbroek, C., Labeyrie, L., Michel, E., Duplessy, J.C., McMannus, J.F., Lambeck, K., Balbon, E., Labracherie, M., 2002. Sea-level and deep water temperature changes derived from benthic foraminifera isotopic records. Quaternary Science Reviews 21, 295–305.

Wang, Y.J., Cheng, H., Edwards, R.L., An, Z.S., Wu, J.Y., Shen, C.-C., Dorale, J.A., 2001. A high-resolution absolute-dated Late Pleistocene monsoon record from Hulu cave, China. Science 294, 2345–2348.

Warner, M.J., Roden, G.I., 1995. Chlorofluorocarbon evidence for recent ventilation of the deep Bering Sea. Nature 373, 409–412.

Warren, B., 1983. Why is no deepwater formed in the North Pacific? Journal of Marine Research 41, 327–347.

Wedepohl, K.H., 1971. Environmental influences on the chemical composition of shales and clays. In: Ahrens, L., Press, K., Runcorn, S., Urey, H. (Eds.), Physics and chemistry of the Earth, Pergamon Press, Oxford, pp. 307–333.

Weingartner, T.J., Danielson, S.L., Royer, T.C., 2005. Freshwater variability and predictability in the Alaska Coastal Current. Deep-Sea Research II 52, 169–191.

Welch, P.D., 1967. The use of fast Fourier transform for the estimation of power spectra: A method based on time averaging over short, modified periodograms. IEEE Transactions on Audio Electroacoustics AU-15, 70–73.

Wu, L., Li, C., Yang, C., Xie, S.-P., 2008. Global teleconnections in response to a shutdown of the Atlantic Meridional Overturning Circulation. Journal of Climate 21 (12), 3002–3019.

Yamamoto, M., Tanaka, N., Tsunogai, S., 2001. Okhotsk Sea intermediate water formation deduced from oxygen isotope systematics. Journal of Geophysical Research 106 (C12), 31075–31084.

Yamamoto, M., Watanabe, S., Tsunogai, S., Wakatsuchi, M., 2002. Effects of sea ice formation and diapycnal mixing on Okhotsk Sea intermediate water clarified with oxygen isotopes. Deep-Sea Research I 49, 1165–1174.

Yarincik, K.M., Murray, R.W., Peterson, L.C., 2000. Climatically sensitive eolian and hemipelagic deposition in the Cariaco Basin, Venezuela, over the past 578,000 years: Results from Al/Ti and K/Al. Paleoceanography 15 (2), 210–228.

Yasonov, P.G., Nourgaliev, D.C., Bourov, B.V., Heller, F., 1998. A modernized coercivity spectrometer. Geologica Carpathica 49 (3), 224–226.

Yasuda, I., 1997. The origin of the North Pacific Intermediate Water. Journal of Geophysical Research 102 (C1), 893–909.

Yin, J., Stouffer, R.J., 2007. Comparison of the stability of the Atlantic thermohaline circulation in two coupled atmosphere–ocean general circulation models. Journal of Climate 20 (17), 4293–4315.

Yokoyama, Y., Lambeck, K., De Deckker, P., Johnston, P., Fifield, L.K., 2000. Timing of the Last Glacial Maximum from observed sea-level minima. Nature 406, 713–716.

Yoneda, M., Uno, H., Shibata, Y., Suzuki, R., Kumamoto, Y., Yoshida, K., Sasaki, T., Suzuki, A., Kawahata, H., 2007. Radiocarbon marine reservoir ages in the western Pacific estimated by pre-bomb molluscan shells. Nuclear Instruments and Methods in Physics Research B 259, 432–437.

You, Y., 2003. Implications of cabbeling on the formation and transformation mechanism of North Pacific Intermediate Water. Journal of Geophysical Research 108, C5, 3134, doi:10.1029/2001JC001285.

Yu, J., Elderfield, H., 2008. Mg/Ca in the benthic foraminifera *Cibicidoides wuellerstorfi* and *Cibicidoides mundulus*: Temperature versus carbonate ion saturation. Earth and Planetary Science Letters 276, 129–139.

Zhang, R., Delworth, T.L., 2005. Simulated tropical response to a substantial weakening of the Atlantic thermohaline circulation. Journal of Climate 18 (12), 1853–1860.

Zhang, J., Woodgate, R., Moritz, R., 2010. Sea ice response to atmospheric and oceanic forcing in the Bering Sea. Journal of Physical Oceanography 40 (8), 1729–1747.

Zheng, Y., van Geen, A., Anderson, R.F., Gardner, J.V., Dean, W.E., 2000. Intensification of the northeast Pacific oxygen minimum zone during the Bölling-Alleröd warm period. Paleoceanography 15 (5), 528–536.

Ziegler, M., Jilbert, T., de Lange, G.J., Lourens, L.J., Reichart, G.-J., 2008. Bromine counts from XRF scanning as an estimate of the marine organic carbon content of sediment cores. Geochemistry Geophysics Geosystems 9 (5), Q05009, doi:10.1029/2007GC001932.

# A. Appendix

## A.1. Ph.D. Publications

### *Submitted and in review*

Max, L., **Riethdorf, J.-R.**, Tiedemann, R., Smirnova, M., Lembke-Jene, L., Fahl, K., Nürnberg, D., Matul, A., Mollenhauer, G., in review. Sea surface temperature variability and sea-ice extent in the subarctic northwest Pacific during the past 15,000 years. Submitted to Paleoceanography.

**Riethdorf, J.-R.**, Max, L., Nürnberg, D., Tiedemann, R., Lembke-Jene, L., submitted. Deglacial variability of sea surface temperature and salinity in the subarctic North Pacific and its marginal seas. GV & Sediment Meeting, Hamburg, Germany, 23/09-28/02/2012, Poster.

### *2011*

Derkachev, A., Portnyagin, M., Ponomareva, V., Gorbarenko, S., Malakhov, M., Nürnberg, D., **Riethdorf, J.-R.**, Tiedemann, R., van den Bogaard, C., 2011. Marker tephra layers in the Holocene-Pleistocene deposits of the Bering Sea and the north-western Pacific Ocean. Second Bilateral KALMAR Project Workshop, Trier, Germany, 16/05-20/05/2011, Poster.

Gottschalk, J., Tiedemann, R., Schulz, M., **Riethdorf, J.-R.**, Max, L., 2011. Laminierte Sedimentintervalle offenbaren Timing und Antrieb von Klimawandel in der Beringsee während der letzten Deglaziation. Statusseminar Meeresforschung mit FS Sonne 2011, Hannover, Germany, 09/02-10/02/2011, Poster.

Ivanova, E., Ovsepyan, E., Murdmaa, I., Max, L., **Riethdorf, J.-R.**, Nürnberg, D., Tiedemann, R., Alekseeva, T., 2011. Millennial environmental variability on Shirshov Ridge, Bering Sea, during the penultimate and last glacial cycles. AGU Fall Meeting, San Francisco, USA, 05/12-09/12/2011, Poster.

Malakhov, M., Gorbarenko, S., Nürnberg, D., Tiedemann, R., MalakhovA, G., **Riethdorf, J.-R.**, 2011. Geomagnetic relative paleointensity of sediment cores of the western Bering Sea and NW Pacific. Second Bilateral KALMAR Project Workshop, Trier, Germany, 16/05-20/05/2011, Poster.

Malakhov, M., Gorbarenko, S., Nürnberg, D., Tiedemann, R., MalakhovA, G., **Riethdorf, J.-R.**, Bosin, A., CHEREPANOVA, M., 2011. Climate change, sea ice and productivity responses in magnetic parameters of sediments from western Bering Sea and NW Pacific. Second Bilateral KALMAR Project Workshop, Trier, Germany, 16/05-20/05/2011, Poster.

Max, L., **Riethdorf, J.-R.**, Tiedemann, R., Nürnberg, D., Abelmann, A., 2011. Late Pleistocene to Holocene sea surface temperature development in the NW-Pacific and its marginal seas. AGU Fall Meeting, San Francisco, USA, 05/12-09/12/2011, Poster.

**Riethdorf, J.-R.**, Max, L., Nürnberg, D., Tiedemann, R., 2011. Late Pleistocene to Holocene changes in sea surface temperature, marine productivity and terrigenous fluxes in the western Bering Sea. Second Bilateral KALMAR Project Workshop, Trier, Germany, 16/05-20/05/2011, Talk.

**Riethdorf, J.-R.**, Max, L., Nürnberg, D., Tiedemann, R., 2011. Rekonstruktion der Oberflächentemperaturen, marinen Produktivität und TerrigenflÜsse im westlichen Beringmeer während des Spätpleistozäns und Holozäns (Sonne 201-2). Statusseminar Meeresforschung mit FS Sonne 2011, Hannover, Germany, 09/02-10/02/2011, Talk.

**Riethdorf, J.-R.**, Max, L., Nürnberg, D., Tiedemann, R., Gorbarenko, S., Malakhov, M., 2011. Millennial-scale climate variability in the subarctic NW-Pacific during the last 150 kyr and implications for upper-ocean stratification. AGU Fall Meeting, San Francisco, USA, 05/12-09/12/2011, Talk.

Tiedemann, R., Nürnberg, D., Max, L., **Riethdorf, J.-R.**, Gottschalk, J., Abelmann, A., Gorbarenko, S., Ivanova, E., Matul, A., 2011. Oceanic and atmospheric teleconnections between the North Pacific and the North Atlantic during the past 25 ka. Second Bilateral KALMAR Project Workshop, Trier, Germany, 16/05-20/05/2011, Talk.

## *2010*

Gottschalk, J., **Riethdorf, J.-R.**, Tiedemann, R., Schulz, M., 2010. Deglacial climate change in the western Bering Sea derived from laminated sediment units. Fifth German KALMAR Project Workshop, Kiel, Germany, 27/09-28/09/2010, Poster.

Max, L., **Riethdorf, J.-R.**, Lembke-Jene, L., Tiedemann, R., Nürnberg, D., 2010. Changes in sea surface and (sub)sea surface temperatures in the Bering Sea and Sea of Okhotsk from Termination I into the Holocene. 10th International Conference on Paleoceanography, San Diego, USA, 29/08-03/09/2010, Poster.

Max, L., **Riethdorf, J.-R.**, Lembke-Jene, L., Tiedemann, R., Nürnberg, D., 2010. Changes in sea surface and (sub)sea surface temperatures in the Bering Sea and Sea of Okhotsk from Termination I into the Holocene. Fifth German KALMAR Project Workshop, Kiel, Germany, 27/09-28/09/2010, Poster.

Ovsepyan, E.A., Ivanova, E.V., Max, L., **Riethdorf, J.-R.**, Tiedemann, R., Nürnberg, D., 2010. Reconstruction of bottom water ventilation and export production based on benthic foraminiferal assemblages from the Shirshov Ridge (Bering Sea) during MS1-3. FORAMS 2010, Bonn, Germany, 05/09-10/09/2010, Poster.

Ovsepyan, E.A., Ivanova, E.V., Max, L., **Riethdorf, J.-R.**, Tiedemann, R., Nürnberg, D., 2010. Reconstruction of bottom water ventilation and export production based on benthic foraminiferal assemblages from the Shirshov Ridge (Bering Sea) during MS1-3. Fifth German KALMAR Project Workshop, Kiel, Germany, 27/09-28/09/2010, Poster.

**Riethdorf, J.-R.**, Max, L., Nürnberg, D., Tiedemann, R., 2010. Sea surface temperature, marine productivity and terrigenous fluxes in the western Bering Sea during

the last 150 ka. 10th International Conference on Paleoceanography, San Diego, USA, 29/08-03/09/2010, Poster.

**Riethdorf, J.-R.**, Max, L., Nürnberg, D., Tiedemann, R., 2010. Sea surface temperature, marine productivity and terrigenous fluxes in the western Bering Sea during the last 150 ka. Fifth German KALMAR Project Workshop, Kiel, Germany, 27/09-28/09/2010, Poster.

**Riethdorf, J.-R.**, Max, L., Nürnberg, D., Tiedemann, R., Lembke-Jene, L., 2010. Late Pleistocene to Holocene paleoceanographic reconstructions at Shirshov Ridge, western Bering Sea. GeoDarmstadt2010, Darmstadt, Germany, 10/10-13/10/2010, Poster.

### *2009*

**Riethdorf, J.-R.**, Max, L., Nürnberg, D., Tiedemann, R., Dullo, W.-Chr., 2009. Reconstruction of late Pleistocene-Holocene climate and oceanography in the subarctic NW-Pacific. First Bilateral Workshop on Russian-German Cooperation on Kurile-Kamchatka and the Aleutean Marginal Sea-Island Arc Systems, Petropavlovsk-Kamchatsky, Russia, 27/04-01/05/2009, Talk.

## A.2. Data management

All data presented in this thesis will be made electronically available via the PANGAEA Data Publisher for Earth & Environmental Science (http://www.pangaea.de/).